



INAOE

Enhancing the sensitivity of a phase-based plasmonic sensor for biomolecular sensing: from theory to experiment

by:

Juan Pablo Cuanalo Fernández
M.Sc., INAOE

A Dissertation Submitted to the Program in Optics,
Optics Department
in partial fulfillment of the requirements for the degree of

DOCTOR OF SCIENCE IN OPTICS

at the
Instituto Nacional de Astrofísica, Óptica y Electrónica
June, 2024
Tonantzintla, Puebla

Advisors:
Dra. Svetlana Mansurova
Optics department at INAOE
Dr. Rubén Ramos García
Optics department at INAOE

©INAOE 2024
All rights reserved

The author hereby grants to INAOE permission to reproduce and
to distribute copies of this thesis document in whole or in part



Agradecimientos

Durante mis estudios para obtener el grado de Doctor en Ciencias en Óptica conté con el apoyo y la guía de numerosas personas a quienes quiero expresar mi agradecimiento. En primer lugar, quiero agradecer al CONAHCYT, por haberme otorgado una beca durante mis estudios de doctorado, lo cual permitió dedicarme a desarrollar este proyecto de investigación de tiempo completo. También quiero agradecer el INAOE por haberme brindado las instalaciones, el equipo y los recursos necesarios para desarrollar mi investigación.

A mis directores de tesis, la Dra. Svetlana Mansurova y el Dr. Rubén Ramos García, les expreso mi más sincero agradecimiento por su invaluable guía, paciencia y apoyo durante todo mi doctorado. Me dieron su total confianza para desarrollar un proyecto en un área nueva para sus grupos de investigación. También les agradezco por darme su confianza y resplaldo para presentar mis resultados de investigación en diversas conferencias nacionales e internacionales. Sus conocimientos y experiencia fueron fundamentales para el desarrollo de mi proyecto. Finalmente, quiero agradecer la excelente relación personal y profesional que he tenido con ambos. Su amabilidad, paciencia y buen humor han creado un ambiente de trabajo excepcional.

A mis sinodales de tesis, Dra. Claudia Betanzo, Dr. Nikolai Korneev, Dr. Ismael Cosme, Dr. Gabriel Martínez y Dr. Alejandro Reyes, por haber dedicado su tiempo y conocimientos a la evaluación de este trabajo. Sus comentarios, sugerencias y observaciones han sido de gran utilidad para mejorar la calidad de la investigación.

A mi familia, en especial a mis padres y hermana les agradezco por su apoyo y comprensión a lo largo de toda mi vida, especialmente en esta última etapa. Ellos fueron testigos de todo el trabajo realizado en estos años. Sin ellos no hubiera sido posible haber obtenido este logro en mi vida.

A Alba Joselin, le expreso mi más profundo agradecimiento por su apoyo incondicional, paciencia, comprensión y amor durante todo este proceso. Especialmente en aquellos momentos en los que la carga de trabajo y las exigencias del doctorado fueron abrumadores. Le agradezco por sus palabras de motivación para seguir adelante y enfocarme en alcanzar mis metas. Su presencia ha sido un pilar fundamental en mi vida personal y profesional, impulsándome a seguir adelante en los momentos más desafiantes. Sin duda, hemos formado un gran equipo.

A mis amigos, Pedro, Sergio y Rodrigo, con quien he compartido varios años de amistad y nos hemos visto crecer personal y profesionalmente. Sin duda, las tardes de *Champions*, serán muy bien recordadas. También quiero agradecer a Carla, Manuel, Dora, Efrain, Irving, Karem y Mireya por su amistad, apoyo, motivación y por crear un ambiente agradable durante mi etapa en el INAOE.

Finalmente, quiero agradecer a todas las personas que de una u otra forma contribuyeron en el desarrollo de este trabajo.

¡Gracias a todos por su invaluable apoyo!

Abstract

Plasmonic biosensors have emerged as powerful tools for label-free sensing offering indispensable attributes such as high sensitivity, real-time monitoring capabilities, and reliable detection, all of which are crucial for diverse biomedical and environmental applications. However, commercial Surface Plasmon Resonance (SPR) based systems are complex and costly, while Localized Surface Plasmon Resonance (LSPR) systems, though easier to use, exhibit lower sensitivity. Phase measurements of the plasmonic response of SPR and LSPR transducer are a promising alternative to enhance the sensitivity.

This dissertation describes the development and characterization of a plasmonic phase-based biosensor, aiming to enhance the device performance parameters such as sensitivity, refractive index resolution, and the limit of detection of biomolecular interactions using SPR and LSPR phenomena. Theoretical and experimental analysis explore and compare both intensity and phase interrogation modes (focusing on the last one) with different resonance markers.

Theoretical analysis for SPR transducer was performed using the transfer matrix method to calculate the intensity and phase response of the reflectance spectra for a four-layered system composed of glass–thin titanium film–thin gold film–surrounding medium. The island film theory was computationally implemented for calculating the intensity and phase response of the reflectance spectrum for LSPR transducer represented by a random array of identical metallic nanoparticles supported on a glass substrate. Both analysis were performed under Attenuated Total Reflection (ATR) conditions.

In experiment, the SPR transducer consisted of a gold film deposited through magnetron sputtering on a glass substrate. While the LSPR transducer is composed by a self-assembled array of gold NanoIslands (Au NI), fabricated through thermal annealing of ultra thin gold films. Scanning Electron Microscopy (SEM) and Atomic Force Microscopy (AFM) were used for morphological characterization of the metasurfaces.

Experimental measurements of the reflectance spectrum under different angles of incidence and for different refractive indexes of the surrounding were performed using the Kretschmann configuration for both intensity and phase interrogation modes. Along this, the LabVIEW interfaces for both intensity and phase interrogation modes were developed for real-time acquisition, processing, and display of signals.

In the SPR approach, our experimental findings reveal that the 50 nm thick gold NanoFilm (Au NF) exhibited the highest sensitivity in both intensity and phase interrogations, achieving values of 9970 nm RIU^{-1} and 6360 nm RIU^{-1} , respectively. However, phase interrogation provides an improved refractive index resolution, reaching values of $5.2 \times 10^{-8} \text{ RIU}$ for wavelength marker, $4.3 \times 10^{-7} \text{ RIU}$ for phase marker, and $3.7 \times 10^{-6} \text{ RIU}$ for phase derivative marker. Due to its superior refractive index resolution, phase interrogation was utilized for the detection of various biological systems. This method demonstrated improved limit of detection values for biotin and oligonucleotides of severe acute respiratory syndrome coronavirus 2 (SARS-CoV-2) detection, reaching 6.6 nM and 5.2 pM, respectively.

In the LSPR approach, the sensing properties of the Au NI were evaluated using both intensity and phase interrogation modes. A significant observation is that the resonance wavelength shifts to smaller wavelengths (blueshift) in response to an increase in the refractive index of the surrounding medium. This behaviour contrasts with the typical SPR response and previously reported LSPR results at normal incidence (both from literature and our experimental observations), where the resonance wavelength is shifted to longer wavelengths (redshift).

Furthermore, both analytical and experimental demonstrations of the topological darkness phenomenon in random metasurface composed of Au NI arrays were achieved. While topological darkness has been observed in ordered arrays of nanoparticles with complex shapes and materials, its observation in a random array of Au NI under ATR conditions is novel. Sensitivity measurements conducted around the phase singularity, characteristic of the topological darkness phenomenon, exhibited high values of refractive index resolution, reaching values of 2.1×10^{-6} RIU and 2.7×10^{-7} RIU for the phase and phase derivative detection modes, respectively. The obtained value of refractive index resolution exceeds typical values reported in the literature for the LSPR sensing mode and it is comparable with record values reported for SPR sensing mode. The detection of the deposition of poly-electrolytes on the surface of an Au NI array was successfully performed. Our findings in this domain, demonstrate that the phase derivative detection mode is more sensitive to bioreceptor-analyte binding events compared to the wavelength detection mode.

Overall, this dissertation demonstrates the advantages of using a phase-based plasmonic biosensor for sensing applications, in particular, for monitoring biomolecular interactions. In addition, it provides guidance for fabricating random metasurfaces on a glass substrate with maximized sensitivity for advanced sensing applications, with implications for the development of novel biosensing technologies.

Resumen

Los biosensores plasmónicos han surgido como herramientas poderosas para la detección sin etiquetas, ofreciendo atributos indispensables como alta sensibilidad, capacidades de monitoreo en tiempo real y detección confiable, todos los cuales son cruciales para diversas aplicaciones biomédicas y ambientales. Sin embargo, los sistemas comerciales basados en Resonancia de Plasmones Superficiales (SPR) son complejos y costosos, mientras que los sistemas basados en Resonancia de Plasmones Superficiales Localizados (LSPR), aunque más fáciles de usar, exhiben una sensibilidad menor. Las mediciones de fase de la respuesta plasmónica de los transductores SPR y LSPR son una alternativa prometedora para mejorar la sensibilidad.

Esta disertación describe el desarrollo y caracterización de un biosensor plasmónico basado en fase, con el objetivo de mejorar los parámetros de rendimiento del dispositivo, como la sensibilidad, la resolución del índice de refracción y el límite de detección de interacciones biomoleculares utilizando fenómenos SPR y LSPR. Se realizan análisis teóricos y experimentales para explorar y comparar ambos modos de interrogación, intensidad y fase (centrándose en este último), con diferentes marcadores de resonancia.

El análisis teórico del transductor SPR se realizó utilizando el método de la matriz de transferencia para calcular la intensidad y la respuesta de fase de los espectros de reflectancia para un sistema de cuatro capas compuesto por vidrio – película delgada de titanio – película delgada de oro – medio circundante. La teoría de películas insulares se implementó computacionalmente para calcular la intensidad y la respuesta de fase del espectro de reflectancia para el transductor LSPR representado por una matriz aleatoria de nanopartículas metálicas idénticas soportadas en un sustrato de vidrio. Ambos análisis se realizaron bajo condiciones de Reflexión Total Atenuada (ATR).

En el experimento, el transductor SPR consistió en una película de oro depositada mediante pulverización por magnetrón sobre un sustrato de vidrio. Mientras que el transductor LSPR está compuesto por una matriz autoensamblada de NanoIsla de oro (Au NI), fabricada mediante recocido térmico de películas ultradelgadas de oro. La Microscopía Electrónica de Barrido (SEM) y la Microscopía de Fuerza Atómica (AFM) se utilizaron para la caracterización morfológica de las metasuperficies.

Se realizaron mediciones experimentales del espectro de reflectancia bajo diferentes ángulos de incidencia y para diferentes índices de refracción del medio circundante utilizando la configuración de Kretschmann para ambos modos de interrogación, intensidad y fase. Además, se desarrollaron interfaces de LabVIEW para ambos modos de interrogación, intensidad y fase, para la adquisición, procesamiento y visualización en tiempo real de señales.

En el enfoque SPR, nuestros hallazgos experimentales revelan que la NanoPelícula de oro (Au NF) de 50 nm de espesor exhibió la mayor sensibilidad en ambos modos de interrogación, intensidad y fase, logrando valores de 9970 nm RIU^{-1} y 6360 nm RIU^{-1} , respectivamente. Sin embargo, la interrogación de fase proporciona una mejor resolución del índice de refracción, alcanzando valores de $5.2 \times 10^{-8} \text{ RIU}$ para el marcador de longitud de onda, $4.3 \times 10^{-7} \text{ RIU}$ para el marcador de fase y $3.7 \times 10^{-6} \text{ RIU}$ para el marcador de derivada de fase. Debido a su superior resolución del índice de refracción, la interrogación de fase se utilizó para la detección de varios sistemas biológicos. Este método demostró valores mejorados de límite de detección para biotina y oligonucleótidos en la detección del coronavirus 2 del síndrome respiratorio agudo severo (SARS-CoV-2), alcanzando 6.6 nM y 5.2 pM, respectivamente.

En el enfoque LSPR, las propiedades de detección del Au NI se evaluaron utilizando ambos modos de interrogación, intensidad y fase. Una observación significativa es que la

longitud de onda de resonancia se desplaza a longitudes de onda más pequeñas (desplazamiento al azul) en respuesta a un aumento en el índice de refracción del medio circundante. Este comportamiento contrasta con la respuesta típica de SPR y los resultados de LSPR previamente reportados en incidencia normal (tanto de la literatura como de nuestras observaciones experimentales), donde la longitud de onda de resonancia se desplaza a longitudes de onda más largas (desplazamiento al rojo).

Además, se lograron demostraciones tanto analíticas como experimentales del fenómeno de oscuridad topológica en una metasuperficie aleatoria compuesta por matrices de Au NI. Mientras que la oscuridad topológica se ha observado en matrices ordenadas de nanopartículas con formas y materiales complejos, su observación en una matriz aleatoria de Au NI bajo condiciones de ATR es novedosa. Las mediciones de sensibilidad realizadas alrededor de la singularidad de fase, característica del fenómeno de oscuridad topológica, exhibieron altos valores de resolución del índice de refracción, alcanzando valores de 2.1×10^{-6} RIU y 2.7×10^{-7} RIU para los modos de detección de fase y derivada de fase, respectivamente. El valor obtenido de resolución del índice de refracción supera los valores típicos reportados en la literatura para el modo de detección LSPR y es comparable con los valores récord reportados para el modo de detección SPR. La detección de la deposición de polielectrolitos en la superficie de una matriz de Au NI se realizó con éxito. Nuestros hallazgos en este dominio demuestran que el modo de detección de derivada de fase es más sensible a los eventos de unión bioreceptor-analito en comparación con el modo de detección de longitud de onda.

En general, esta tesis demuestra las ventajas de usar un biosensor plasmónico basado en fase para aplicaciones de detección, en particular, para monitorear interacciones biomoleculares. Además, proporciona una guía para fabricar metasuperficies aleatorias sobre un sustrato de vidrio con sensibilidad maximizada para aplicaciones avanzadas de detección, con implicaciones para el desarrollo de nuevas tecnologías de biosensores.

Contents

Acknowledgements	I
Abstract	II
1 Introduction	1
1.1 Motivation	1
1.2 Background	2
1.2.1 Nanoscience and Nanotechnology	2
1.2.2 Biosensors	2
1.2.3 Surface Plasmon Resonance	4
1.2.4 Localized Surface Plasmon Resonance	5
1.3 Problem statement	8
1.4 Objectives	9
1.5 Tasks	9
1.6 Scientific contribution	10
1.7 Outline	11
2 Basic Concepts and State of the Art	13
2.1 Electromagnetic waves	13
2.1.1 Maxwell equations	13
2.1.2 Fresnel coefficients	15
2.1.3 Total internal reflection	18
2.1.4 Transfer matrix method for calculating the reflectance of a multilayered system	20
2.2 Optical properties of metals	22
2.2.1 Drude model	23
2.2.2 Real metals	25
2.3 Surface Plasmon Polaritons	26
2.3.1 Excitation of SPPs	29
2.4 Localized Surface Plasmons	31
2.4.1 Island film theory in the low coverage limit	34
2.5 Biosensors	36
2.5.1 Other techniques for detection of biomolecular binding events	36
2.5.2 Classification of biosensors	37
2.5.3 SPR based biosensors	38
2.5.4 LSPR based biosensors	39
2.5.5 Performance parameters of biosensors	40
2.5.6 Interrogation modes in plasmonic sensors	42
2.6 Literature Review	43
2.6.1 SPR-based biosensors	43
2.6.2 LSPR-based biosensors	44

3 Materials and Methods	47
3.1 Fabrication of transducers	47
3.1.1 Fabrication of Au NF	47
3.1.2 Fabrication of Au NI	48
3.2 Morphological and optical characterization of Au NI	49
3.2.1 Scanning Electron Microscopy	49
3.2.2 Atomic Force Microscopy	50
3.2.3 Optical spectroscopy	51
3.3 Microfluidic device fabrication	52
3.4 Experimental setup	54
3.4.1 Kretschmann configuration in phase interrogation mode	54
3.4.2 Kretschmann configuration	55
3.5 LabVIEW interface	56
3.6 Bulk RIS and RIR measurements	59
3.7 Chemical preparation of detection samples	59
3.7.1 Sodium chloride solutions preparation	59
3.7.2 Polyelectrolytes preparation	60
3.7.3 Streptavidin - biotin preparation	61
3.7.4 Oligonucleotides preparation	62
3.8 Functionalization and hybridization of transducers	64
4 SPR: Results and Discussion	67
4.1 Reflectance spectrum of Au NFs under ATR condition	67
4.1.1 Main parameters for reflectance spectrum simulation	67
4.1.2 Theoretical calculations	68
4.1.3 Experimental measurements	69
4.1.4 Discussion	71
4.2 Bulk refractive index sensitivity of Au NFs using the intensity interrogation mode	72
4.2.1 Theoretical calculations	72
4.2.2 Experimental measurements	74
4.2.3 Discussion	78
4.3 Experimental measurements of bulk refractive index sensitivity using the phase interrogation mode	78
4.3.1 Discussion	81
4.4 SPR sensing of various analytes	81
4.4.1 Polyelectrolytes LbL system detection	81
4.4.2 Streptavidin-biotin binding event detection	84
4.4.3 Conjugated oligonucleotides binding event detection	85
4.4.4 Discussion	86
5 LSPR: Results and Discussion	89
5.1 Morphological characterization of the Au NI arrays	90
5.1.1 SEM analysis of Au NI arrays	90
5.1.2 AFM analysis of Au NI arrays	91
5.1.3 Discussion	92
5.2 Island film theory-based analysis of reflectance spectra for Au NI arrays	92
5.2.1 General remarks	92
5.2.2 Size and shape influence on the reflectance spectra of Au NI	94
5.2.3 Discussion	97

5.3	Transmittance spectrum of Au NI arrays at normal incidence	97
5.3.1	Theoretical calculations	98
5.3.2	Experimental measurements	98
5.3.3	Discussion	99
5.4	Reflectance spectrum of Au NI arrays under ATR condition	100
5.4.1	Theoretical calculations	100
5.4.2	Experimental measurements	101
5.4.3	Discussion	103
5.5	Bulk refractive index sensitivity of Au NI arrays	104
5.5.1	Theoretical calculations	104
5.5.2	Experimental measurements	107
5.5.3	Discussion	110
5.5.4	Experimental measurements of bulk refractive index sensitivity using the phase interrogation mode	112
5.5.5	Discussion	115
5.6	Zero reflectance and phase singularity in a random array of Au NI	115
5.6.1	Reflectance spectra under <i>p</i> and <i>s</i> polarized light for different angles of incidence	117
5.6.2	Reflectance spectra for <i>p</i> and <i>s</i> polarized light for different refractive indices	118
5.6.3	Phase response	118
5.6.4	Localized surface plasmon resonance phase sensitivity	119
5.6.5	Discussion	121
5.7	Polyelectrolytes binding detection using LSPR effect	122
5.7.1	Discussion	123
6	Conclusions	125
6.1	Surface Plasmon Resonance Approach	125
6.2	Localized Surface Plasmon Resonance Approach	126
6.3	Perspectives	126
A	Derivation of the dielectric function using the Lorentz-Drude model	129
B	Derivation of SPPs dispersion relation	133
	Bibliography	137

List of acronymes

AFM	Atomic Force Microscopy
ATR	Attenuated Total Reflection
Au NI	Gold NanoIslands
Au NF	Gold NanoFilm
CCD	Charge-Coupled Device
DNA	Deoxyribonucleic Acid
DTT	Dithiothreitol
ELISA	Enzyme-Linked Immunosorbent Assay
FOM	Figure Of Merit
FWHM	Full Width at Half Maximum
HMM	Hyperbolical Metamaterial
LbL	Layer-by-Layer
LOD	Limit Of Detection
LSPR	Localized Surface Plasmon Resonance
MLWA	Modified Long-Wavelength Approximation
PAH	Polyallylamine Hydrochloride
PCR	Polymerase Chain Reaction
PDMS	Polydimethylsiloxane
PSS	Polystyrene Sulfonate
RIR	Refractive Index Resolution
RIS	Refractive Index Sensitivity
RIU	Refractive Index Units
RNA	Ribonucleic Acid
SARS-CoV-2	Severe Acute Respiratory Syndrome Coronavirus 2
SERS	Surface-Enhanced Raman Spectroscopy
SEM	Scanning Electron Microscopy
SPP	Surface Plasmon Polariton
SPR	Surface Plasmon Resonance
TE	Transverse Electric
TM	Transverse Magnetic
TIR	Total Internal Reflection
Ti NF	Titanium NanoFilm
TMDC	Transition Metal Dichalcogenides Monolayer
WHO	World Health Organization

Chapter 1 | Introduction

1.1 Motivation

The emergence of new viral diseases, marked by mutations, recombination, or the resurgence of previously known viruses, is the worldwide concern. The potential for a pandemic emergence lies in the characteristics of the disease such as mortality rates, severity, transmissibility, and ability to spread remotely. One significant factor contributing to the emergence of new viruses is the ongoing contact with, or consumption of non-domestic animals. This is presumably the case of the severe acute respiratory syndrome coronavirus 2 (SARS-CoV-2) that caused the COVID-19 pandemic.^[1]

Due to global society in which we are immersed, the spread of the virus occurred rapidly across the world. After first detection in China in December 2019 the virus was present in practically all parts of the world. According to the European Centre for Disease Prevention and Control and WHO, the incubation time of SARS-CoV-2 spans from 2 to 14 days, with an average of five days. Moreover, they indicate that individuals infected with COVID-19 may potentially transmit the virus before experiencing significant symptoms.

Due to the global health crisis caused by SARS-CoV-2, borders have been closed, economies paralyzed, and most tragically, hundreds of thousands of human lives have been lost. The lingering economic fallout continues to cast a shadow over societies worldwide. This unprecedented crisis underscores the critical need for early and accurate pathogen detection to prevent the escalation of outbreaks into full-blown pandemics. However, current detection methods often fall short in meeting the demands of early and accurate pathogen identification.

Existing biosensors, while valuable tools, often lack the necessary sensitivity, response time, and specificity to effectively combat emerging threats like COVID-19. The limitations of current biosensors necessitate the development of next-generation detection technologies that can address these shortcomings.

Nanoscience and nanotechnology, with their ability to manipulate matter at the atomic and molecular levels, offer a promising avenue for achieving this goal. Biosensors based on nanotechnology have the potential to detect pathogens with high sensitivity, high specificity, and low detection time, enabling early identification to prevent the spread of infectious diseases.

The development of this doctoral dissertation was made in a framework of the project entitled “Plasmonic Biosensor for the Detection of the SARS-CoV-2” approved and partially funded by “Proyecto Nacional de Investigación e Incidencia” of CONACYT.

1.2 Background

1.2.1 Nanoscience and Nanotechnology

Nanoscience, defined as the study of structures and molecular configurations on the scale of nanometers (ranging between 1 and 100 nm), forms the foundational basis for nanotechnology, a field that applies this understanding in practical applications. [2, 3] This discipline was first conceptualized by the American physicist and Nobel laureate Richard Feynman in 1959. During the annual meeting of the American Physical Society, Feynman delivered a seminal lecture titled “There’s Plenty of Room at the Bottom” at the California Institute of Technology (Caltech), establishing the theoretical underpinnings of nanotechnology. [4] It was not until 1974 that the term “nanotechnology” was formally introduced and defined by Norio Taniguchi, a Japanese scientist, as “the processing of separation, consolidation, and deformation of materials by one atom or one molecule.” [5]

The interest in studying materials at the nanometric scale is driven by their unique properties, which markedly differ from those of bulk materials. [6] At the macrometric scale, material properties are uniform, influenced by the symmetrical forces exerted by interactions among bulk atoms. However, atoms at the nanoscale experience anisotropic forces due to less coordination and greater surface exposure, as a result of a considerable increase in the surface-to-volume ratio. Moreover, at nanometric scale the discretization of electronic states occurs, resulting in distinct optical, thermal, mechanical, magnetic, and electrical properties that diverge substantially from bulk characteristics.

Metamaterials, artificially engineered materials composed of subwavelength-scale nanostructures, exemplify a further advancement in material science at nanoscale. The term “metamaterial” originates from the Greek prefix “meta”, indicating a transcendence beyond the conventional. By manipulating the arrangement and size of these nanostructures, scientists can tailor the material’s response to electromagnetic, acoustic, and optical waves, achieving behaviors that expand the possibilities of material applications and functionalities. [7, 8]

Metasurfaces, essentially two-dimensional analogues of metamaterials, are easier to fabricate, and have better integration with ultra-compact optical devices. Emerging prominently as platforms for diverse applications, metasurfaces have been employed in the development of metalenses, [9] advanced color printing, [10] image multiplexing, [11] perfect absorbers, [12] optical cloaking, [13] and, notably, biosensing technologies. [14]

Over recent decades, nanotechnology’s applications have become crucial in sectors ranging from industry to medicine, with innovations such as diagnostic biosensors, drug delivery systems. [14–19] The intersection of nanotechnology with biosensing underscores the profound potential of nanoscale phenomena to transform the landscape of medical diagnostics and analytical systems through enhanced sensitivity and specificity.

1.2.2 Biosensors

Biosensing encompasses a broad and interdisciplinary field focused on detecting various biological agents such as bacteria, viruses, Deoxyribonucleic Acid (DNA), Ribonucleic Acid (RNA) and proteins, etc. Detecting these elements holds essential importance in diverse domains including medical diagnostics, environmental monitoring, food control, and biomedical research.

A biosensor is a device designed to monitor biological signals via a transducer, producing

a distinctive signal proportional to the concentration of a specific biological or chemical substance. [20] While biosensors may consist of various components, five essential elements constitute their structure:

Analyte: the specific biological or chemical agent targeted for detection.

Bioreceptor: a biological or chemical entity capable of recognizing the analyte. Bioreceptors and analytes may share the same nature (e.g., protein-protein, DNA-DNA), or they can represent combinations thereof. For example, analytes can be biotinylated to bind with streptavidin molecules.

Transducer: This component converts the interaction between the bioreceptor and analyte into a measurable signal.

Signal processor: The signal is acquired and processed typically using electronics. Electronic circuits are employed to amplify and filter the signal, although filtering can also be done digitally.

Display: The output signal is presented by a designed interface, typically on a computer screen.

Biosensors are classified based on the type of analyte they detect (e.g., protein sensors, glucose sensors, etc.) and their applications or signal transduction mechanisms, which include electrochemical, optical, acoustic, and piezoelectric biosensors, among others. Optical biosensors have significantly advanced the field of biosensing, offering non-invasive detection in real time that maintains the integrity of the sample post-analysis. [21–23] Within the broad category of optical sensors, several types exist, each with unique mechanisms and applications. These include optical waveguides, photonic crystals, optical fibers, fluorescence sensors, refractometric sensors, colorimetric sensors, and Surface-Enhanced Raman Spectroscopy (SERS). Additionally, Surface Plasmon Resonance (SPR) and Localized Surface Plasmon Resonance (LSPR) based biosensors have gained prominence due to the unique benefits they offer.

Plasmonic biosensors, the focus of this thesis, exploit the interactions between light and free electrons in metallic nanomaterials, primarily noble metals like gold and silver. Gold is particularly favored over silver for these applications due to its biocompatibility and lower toxicity; silver nanoparticles can disrupt cellular membranes and induce toxicity, making gold the preferred choice for *in vivo* applications. [24] Other materials such as palladium, metal alloys, and graphene-based structures are also explored to enhance the functionality and sensitivity of plasmonic sensors. Recently, the exploration of plasmonic materials and plasmonic biosensors has become a trend within research community (see Figure 1.1).

SPR and LSPR biosensors are recognized for their sensitivity and specificity, derived from their ability to detect changes in the refractive index at the sensor surface. This sensitivity, while substantial, has room for improvement to meet the increasing demands of modern biosensing applications, as will be demonstrated in this thesis. These biosensors enable real-time monitoring of biomolecular interactions without the need for labels, a feature that simplifies the detection process and reduces the complexity of assays. Moreover, SPR and LSPR technologies are well-suited for integration into lab-on-chip systems, facilitating the development of compact, efficient diagnostic tools. This adaptability is essential for advancing point-of-care diagnostics and other applications where space and efficiency are at a premium.

The following section will describe in detail the main principles of SPR and LSPR, explaining how these technologies operate and why they represent a significant advance in the field of biosensing. [21–23]

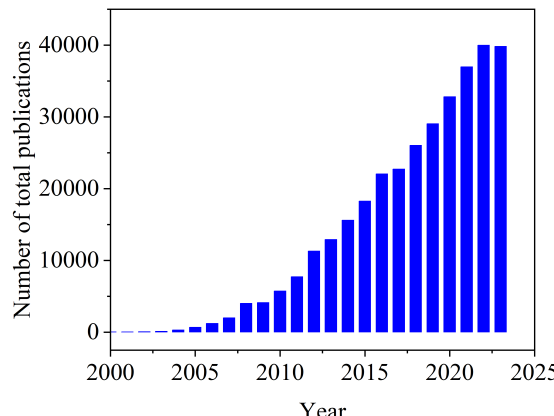


Figure 1.1: Number of publications from 2000 to 2023 from the website "Dimensions" (www.dimensions.ai) using *Plasmonics* as topic subject

1.2.3 Surface Plasmon Resonance

SPR is an optical phenomenon that occurs when polarized light excites free electrons at the interface between a metal film and a dielectric medium, leading to the generation of surface plasmon waves. The resonance condition depends crucially on the polarization and frequency of the incident light, the angle of incidence, the electronic properties of the metal, and the refractive index of the surrounding medium. The usual manifestation of SPR is a sharp dip in the reflected light intensity at a specific angle and wavelength, corresponding to the energy transfer from the light to the surface plasmons.

The discovery of SPR dates back to 1902 when Wood identified distinct thin dark bands in the reflection spectrum of a white light source using metallic gratings, a phenomenon that suggested unique optical interactions at the metal-dielectric interface.^[25] It was not until Fano's theoretical analysis in 1941, that these bands were formally linked to surface waves known as surface plasmon polaritons.^[26] This foundational work laid the groundwork for the later practical realization of SPR observation techniques. It was the Kretschmann, Raether, and Otto configurations in the 1960s and 1980s that demonstrated the excitation of surface plasmons via Attenuated Total Reflection (ATR) method, cementing it as the standard technique for SPR studies.^{[27] [28]}

The sensitivity of SPR to slight changes in the refractive index near the metal surface makes it particularly effective for biosensing applications. This capability allows for the detection of molecular interactions, such as the binding events between a bioreceptor and an analyte, by observing shifts in the resonance condition. SPR can monitor these shifts through various interrogation modes, specifically intensity or phase interrogation modes, each detecting different resonance markers like angle, wavelength, intensity (within intensity mode), or phase (within phase mode).

Refractive Index Sensitivity (RIS) is used to quantify the performance of these interrogation modes, measuring the change in a detectable signal (ΔX) per unit change in refractive index (Δn), with ΔX representing intensity, wavelength, angle, or phase. Conversely, Refractive Index Resolution (RIR) indicates the sensor's ability to discern the smallest refractive index change, calculated as the ratio of the standard deviation of noise to the RIS.

The significant breakthrough in SPR for biosensing emerged from Liedberg et al. 1983 proposal, which exploited SPR's responsiveness to variations in the dielectric constant at

the metal interface to detect bioreceptor-analyte bindings.^[29] This innovation spurred extensive research into SPR applications across various biological substances including proteins, enzymes, RNA, bacteria, and viruses, demonstrating the versatility of SPR sensors.^[30-35]

The robust research interest in SPR-based biosensors has catalyzed the development of sophisticated commercial devices, particularly those by Biacore, which have set the standard for studying molecular interactions. These systems primarily employ angle as the resonance marker within the intensity interrogation mode to detect shifts in resonance conditions induced by molecular binding. However, despite the advancements and widespread use of SPR systems in biosensing, challenges remain, primarily in enhancing sensitivity and specificity beyond the capabilities of current angle-based detection techniques.

There is an increasing interest in phase-based interrogation methods, which have been shown to offer a significantly higher sensitivity, achieving detection limits at least two orders of magnitude more sensitive than those possible with commercially available systems like Biacore. Pioneering studies by Nikitin et al.^[36] and Kabashin et al.^[37, 38] have demonstrated that phase detection provides substantial advantages over amplitude detection.

Besides the high-sensitive detection of biomolecular interactions, phase detection also benefits from its differential nature, which compensates for common noise sources such as fluctuations in light source intensity or environmental disturbances. Importantly, phase signals typically exhibit lower noise compared to amplitude signals, further enhancing the signal-to-noise ratio. Furthermore, phase interrogation is compatible with advanced signal processing techniques like lock-in amplification, which isolates the desired signal from background noise, thereby improving the detection accuracy and reliability. These features collectively highlight the potential of phase detection to significantly improve the performance of biosensors and expand their applications in various fields.

1.2.4 Localized Surface Plasmon Resonance

The phenomenon of localized surface plasmon resonance has been observable for centuries, as evidenced by the vibrant colors of stained glass in historical sites like the Sainte-Chapelle in Paris. These colors, which range from deep blues to vivid reds and purples, result from the interaction of light with metallic nanoparticles embedded in the glass. Elements such as cobalt, copper, manganese, or antimony, used during the manufacturing process, contribute to the wide spectrum of hues seen in these glasses. Despite such historical manifestations, it was only in recent decades that the formal scientific study of LSPR began, unlocking a deeper understanding of its underlying mechanisms and potential applications,^[39] as depicted in Figure 1.2.

LSPR occurs when incident light interacts with metallic nanoparticles, inducing the collective oscillation of conduction electrons at the nanoparticle surface.^[48] This resonance is highly sensitive to the size, shape, composition of the nanoparticles, as well as their surrounding environment. Unlike SPR, which requires momentum matching typically achieved through a prism, LSPR can be excited directly under normal incident light conditions. This characteristic allows LSPR to be utilized in simpler and more compact biosensing setups. The interaction of light with these nanoparticles results in sharp peaks in the absorption and scattering spectra, known as the LSPR peak, which shifts in response to changes in the local refractive index caused by biomolecular interactions near the nanoparticle surface. This shift provides a sensitive measure of molecular binding events, making LSPR particularly effective for biosensing applications.^[14] LSPR sensors have successfully detected a diverse array of molecules and pathogens, including RNA,^[49] DNA from virus,^[45] antigens,^[47] enzymes,^[50]

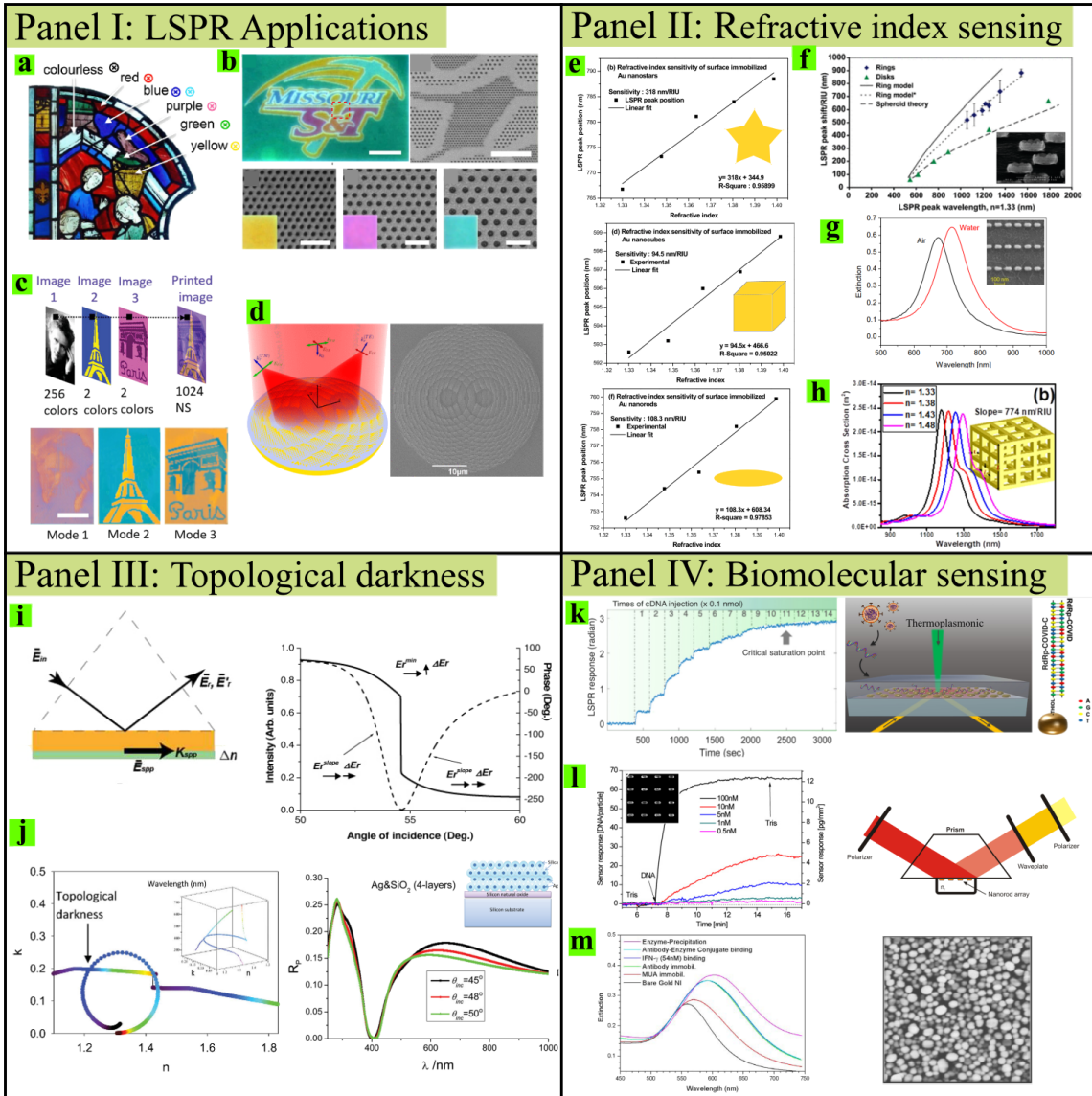


Figure 1.2: Panel I: **a.** Coloured stained glass of Sainte-Chapelle due to presence of metallic nanoparticles, image adapted from [39]. Examples of nanoparticle applications using the LSPR phenomenon, including **b.** high-quality colour printing, **c.** image multiplexing, and **d.** metasenses. Images adapted from [10], [11] and [9] respectively. Panel II: Bulk refractive index sensing using various nanoparticles shapes. **e.** LSPR peak position of surface immobilized gold nanostars, nanocubes, and nanorods with increase in glucose concentration from 0 % to 20 %. Image adapted from [40] **f.** Plasmon peak position dependence of the refractive index using gold nanorings. Image adapted from [41] **g.** Extinction spectra of gold nanorod chains measured in air and in water. Image adapted from [42] **h.** Absorption cross section of etched core-texture shell optimized cubic nanocage versus refractive index of surrounding medium. Image adapted from [43] Panel III: **i.** Intensity and phase manifestation of topological darkness phenomenon using a gold thin film. Image adapted from [38] **j.** Calculated p polarized zero-reflection curve and the dispersion curve for a four-layer core-shell metamaterial. Image adapted from [44] Panel IV: Examples of LSPR biosensing using metasurfaces. **k.** Sensogram of gold nanoparticles functionalization using the common-path spectral interferometer. The purpose of this biosensor is to detect SARS-CoV-2 through complementary oligonucleotides. Image adapted from [45] **l.** LSPR sensor response for five different concentrations of target oligonucleotides. Image adapted from [46] **m.** Extinction spectra changes due to molecular binding between an antigen and an antibody on gold nano-island surfaces. Image adapted from [47]

proteins, [51] biotinylated molecules, [52] among others.

LSPR can be observed in two primary configurations: with nanoparticles dispersed in colloidal solutions or with nanoparticles anchored to a solid substrate, such as glass, forming what is known as a plasmonic metasurface. In colloidal solutions configuration, nanoparticles are freely suspended in a liquid medium, which allows for dynamic interactions between the nanoparticles and target analytes in solution, providing rapid response times and easy integration into various assay formats. However, colloidal solutions can suffer from issues such as particle aggregation or sedimentation over time, which may lead to inconsistencies in sensor responses and challenges in long-term stability and repeatability.

When nanoparticles are fixed onto a substrate, they create a plasmonic metasurface. This configuration offers several advantages over colloidal solutions. Firstly, it provides enhanced stability and repeatability of the biosensing system, as the fixed nanoparticles do not aggregate or sediment. This arrangement allows for precise control over the nanoparticle environment, leading to more uniform and reproducible responses. Additionally, plasmonic metasurfaces can be used in ATR configuration, thus increasing the sensitivity and specificity of the biosensor. Finally, plasmonic metasurfaces also facilitate the integration of biosensors into more complex, miniaturized systems, such as lab-on-a-chip devices.

One major challenge that hinders the advancement of plasmonic metasurface-based transducers in biosensing is the inherent limitations in sensitivity [53] mainly due to intrinsic losses in metallic nanostructures. Conventional spectroscopic techniques based solely on intensity or wavelength interrogation have proven to be insufficient in addressing this sensitivity issue. In this context, a promising solution to achieve ultra-high sensitive LSPR transducers lies in the phase interrogation mode. [54–56] The advantages of phase detection has been discussed in previous subsection.

However, the phase detection sensitivity can be increased even further by exploiting the concept of topological darkness as proposed by Kravets et al. [57] It refers to a phenomenon in which complete suppression of reflection occurs under certain conditions. [57] Topological darkness provides enhanced sensitivity for LSPR-based sensing due to its unique phase behaviour. When the conditions for no reflection are met, the zero amplitude of the light yields a phase singularity since the later is undefined in this scenario. Around the singularity point, the phase reveals bifurcation behaviour which manifests itself as abrupt $\pm\pi$ jumps with a sudden change of sign in the phase slope when plotted as a function of wavelength. The position of this abrupt phase change depends on the refractive index of the surroundings of the nanostructures, among other parameters, and thus has been exploited for biosensing, where it has allowed highly sensitive detection of analytes. [44, 57–59] Furthermore, the topological nature of the curve associated with zero reflection ensures that this enhanced sensitivity is robust against imperfections in the internal geometry of the nanostructures used.

In recent years, two main approaches have emerged for the implementation of topological darkness: the thin film approach [59–61] and the nanostructuring approach. [44, 57, 58, 62–64] The thin film approach encompasses a range of systems, including atomically thin high-refractive index materials, [59] Hyperbolical MetaMaterials (HMMs), [60] and plasmonic heterostructures based on thin layers of metals and dielectrics. [61] This approach offers simplicity and ease of fabrication, requiring fewer processing steps compared to nanostructuring. However, achieving zero reflection in continuous thin films can be challenging due to the limited number of degrees of freedom to tune the necessary optical constants.

The second option, which involves carefully engineered metallic nanostructures, allows for precise control over optical properties and field distributions by creating highly precise 2D patterns at the nanoscale on a substrate surface. Zero reflection can be achieved by fine

tuning the size and shape of the nanostructure as well as the surface coverage of the array. The nanostructures encompass a variety of shapes, including spheres, [63] rods, [62] dots, [57, 58] and layers of core shell nanoparticles. [44, 64] Techniques such as electron beam lithography, nanoimprinting and photolithography are commonly used for nanopatterning, [65–67] but they are complex, costly, and have limitations in terms of scalability, making them less accessible for a widespread implementation.

An alternative approach involves the use of random metasurfaces, which can be fabricated using cost-effective methods such as thermal annealing of ultrathin gold films. [68] However, the properties of random metasurfaces in relation to topological darkness and phase singularity remain largely unexplored. Investigating these aspects holds great promise for developing practical and scalable solutions in the field of ultrasensitive optical biosensing.

1.3 Problem statement

Plasmonic biosensors hold promise potential for label-free, highly sensitive detection of biomolecules due to their ability to exploit the SPR and LSPR effects. However, despite significant advancements, several challenges and gaps persist, impeding the widespread adoption and practical implementation of plasmonic biosensing platforms.

1. Limitations of Current Interrogation Modes:

Current interrogation modes predominantly focus on angular or intensity measurements, which may not provide the required sensitivity or specificity for detecting small changes in biomolecular interactions. The potential of alternative interrogation methods, such as phase and phase derivative techniques, has not been fully explored, leaving a gap in achieving optimal detection capabilities.

2. Influence of Nanostructure Properties:

In LSPR mode, the effectiveness of plasmonic biosensors is significantly influenced by the physical characteristics of the nanostructures used, such as size, shape, and distribution. Yet, the complex relationship between these morphological parameters and the LSPR transducer optical response—particularly under variations in the refractive index of the surrounding medium—remains poorly understood.

3. Non-linear Dependence of the LSPR Response on the Refractive Index:

In SPR the shift in the resonance wavelength has a more predictable linear correlation with changes in refractive index. In contrast, LSPR exhibits a complex, nonlinear dependence, complicating the interpretation and utilization of these shifts for sensitive measurements. The mechanisms underlying this nonlinear behavior in LSPR systems are poorly understood and underexplored in the literature, indicating a significant gap in the fundamental understanding of plasmonic interactions and their practical applications in biosensing.

4. Phenomenon of Topological Darkness:

The occurrence of topological darkness in plasmonic metasurfaces presents a unique optical behavior that could significantly enhance biosensing sensitivity but has not been extensively studied in random metasurfaces. The associated phase singularities in such conditions indicate a promising avenue for research yet are not well-explored within the context of biosensing technologies.

This dissertation aims to address these unresolved issues within the domain of plasmonic biosensing by investigating the potential of using a phase interrogation mode under ATR conditions. The research will explore two approaches for the plasmonic biosensor: *i*) using the SPR phenomenon with an Au NF transducer; and *ii*) exploiting LSPR excited from Au NI randomly distributed onto a glass substrate (random metasurface). Specifically, for the LSPR case, the sensitivity will be investigated for gold random metasurfaces with varying sizes. Additionally, the research will explore advanced methods for enhancing the sensitivity using disordered gold metasurfaces, particularly those that exhibit topological darkness.

1.4 Objectives

The primary objective of this research is to theoretically and experimentally investigate and optimize the phase response of SPR and LSPR transducers, with an emphasis on enhancing the sensitivity of biosensing applications. The effectiveness of the phase-based detection mode was demonstrated through the detection of several biological analytes, including SARS-CoV-2 RNA fragments. Additionally, this thesis will explore the concept of topological darkness and its potential to improve the sensitivity of plasmonic biosensors.

To achieve the main objective, the specific objectives were formulated as:

- Fabrication and characterization of SPR and LSPR transducers using magnetron sputtering and solid state thermal dewetting process;
- Development of theoretical and experimental methodological tools to study plasmonic response of SPR and LSPR transducers;
- Theoretical and experimental study and optimization of
 - SPR transducer in intensity and phase interrogation mode. Application of optimised transducer for sensing experiments using biological analytes;
 - LSPR transducer in intensity and phase interrogation mode;
 - Topological darkness and phase singularity phenomena and its use for refractive index sensing.

1.5 Tasks

To achieve the objectives, the following tasks were performed:

- ◊ Design and set up the sensor experimental arrangement.
- ◊ Design and fabricate a microfluidic device with one input and one output channel for transducer functionalization.
- ◊ Characterize morphologically and optically the metasurfaces.
- ◊ Implement a computational code for analytically obtain the reflectance and transmittance spectrum of a system composed by four layers using the transfer matrix method.

- ◊ Implement a computational code based on the island film theory to obtain analytical reflectance and transmittance spectrum of a random arrays of metallic nanospheroids and nanospheres.
- ◊ Develop a LabVIEW homemade interface for acquire, process and display the SPR and LSPR response in real time.
- ◊ Calibrate the transducers by measuring the sensor response shifts under variations of the refractive index of the surrounding medium for the SPR and LSPR modalities.
- ◊ Determine experimentally the interrogation mode (intensity or phase) which exhibits the highest sensitivity to refractive index changes.
- ◊ Determine experimentally the optimal thickness of a gold NanoFilm (Au NF) for sensing applications.
- ◊ Determine experimentally the optimal size of gold NanoIslands (Au NI) for sensing applications.
- ◊ Explore the intensity and phase response of Au NI arrays which exhibits topological darkness phenomenon.
- ◊ Detect the binding between bioreceptor and analyte of three systems: polyelectrolytes LbL system, streptavidin-biotin system and conjugated oligonucleotides system.

1.6 Scientific contribution

Throughout this research work, various significant scientific contributions have been made, which are summarized below.

Firstly, a plasmonic biosensor was developed, characterized, and optimized using both SPR and LSPR techniques, employing both intensity and phase interrogation modes for the detection of biomolecular interactions.

Secondly, it was determined how the size, shape, and distribution of Au NI on a substrate affect the reflectance spectrum. Moreover, it was demonstrated that changes in the refractive index of the sensing medium induce a non-linear blueshift in the resonance wavelength of the reflectance spectrum. This behavior contrasts with traditional experiments conducted under normal incidence using intensity interrogation. Furthermore, we identified the morphological parameters of the random metasurfaces to achieve the highest sensitivity possible under our experimental conditions.

Thirdly, novel detection modes were proposed for the phase interrogation mode, including wavelength, phase, and phase derivative detection modes. Among these, the phase derivative method exhibited the highest sensitivity for detecting biomolecular interactions.

Finally, the phenomenon of topological darkness was investigated both theoretically and experimentally in a random metasurface composed of spheroidal nanoparticles. Using the phase interrogation mode, topological darkness was observed by varying the refractive index of the surrounding medium, showing an associated phase singularity in the measurements of the differential phase.

1.7 Outline

This dissertation has six chapters. The first chapter contains a general introduction of the nanoscience applied to optical biosensing, also presenting the research gap and remaining challenges. Finally, the justification and objectives of this work are presented.

Chapter 2 introduces fundamental concepts for comprehending the topics covered in this dissertation. Initially, the Maxwell's equations are described to understand how the light propagates and interacts with matter, particularly with metals. Subsequently, Fresnel coefficients are given to explain the behaviour of light when interacting with an interface under external and internal incidence. To study the optical properties of metals the Drude model and its derivatives are reviewed. Additionally, analytical and experimental conditions for exciting SPR and LSPR are reviewed. Additionally, biosensors are introduced, followed by a review of key parameters. Finally, this chapter concludes by reviewing the most relevant works in optical sensing using metallic films and nanostructures establishing context and providing a foundation for the research conducted in this dissertation.

Chapter 3 outlines the materials and methods used in this research. First, the methodology for fabricating and characterizing Au NFs and Au NIs supported on a glass substrate is presented. To complete the fabrication of the chip, the microfluidic device design and fabrication is discussed. Furthermore, the chapter presents the experimental setups employed for reflectance spectra and sensitivity measurements, along with the development of LabVIEW interfaces. Finally, it provides detailed descriptions of the preparation procedures for sensing samples, encompassing the polyelectrolytes Layer-by-Layer (LbL) system, biotin-streptavidin system, and oligonucleotide conjugation system.

Chapter 4 presents the analytical and experimental findings of the SPR-based biosensor approach in parallel. This chapter begins with the theoretical calculation of the reflectance spectrum for a four-layered system (glass – Titanium NanoFilm (Ti NF) – Au NF – dielectric medium) using the transfer matrix method. The experimental counterpart involves measuring the reflectance spectrum under oblique incidence using the Kretschmann configuration. Next, the reflectance spectra are obtained for various refractive index values of the surrounding medium. This allows us to determine the dependence of the resonance wavelength on the refractive index. Subsequently, the bulk refractive index sensitivity, refractive index resolution, and figure of merit are obtained and compared with analytical calculations. Furthermore, the chapter presents an experimental characterization of the sensing properties of Au NF using the Kretschmann configuration but employing the phase interrogation mode. Finally, the chapter demonstrates the successful detection of three biological systems through phase interrogation.

The Chapter 5 contains the analytical and experimental results of the LSPR biosensor approach. This chapter begins by analyzing SEM and AFM micrographs to obtain the morphological parameters of self-assembled Au NI through statistical methods. The transmittance spectrum under normal incidence as well as the reflectance spectrum under oblique incidence of a random metasurface with oblate spheroid shape is calculated using the island film theory in the low coverage limit under *p* and *s* polarized light. The experimental counterparts involve measuring the transmittance and reflectance spectra using the corresponding experimental setups. The experimental transmittance and reflectance spectrum are also measured. Next, the dependence of the resonance wavelength on the refractive index of the surrounding medium is obtained analytically and experimentally . Refractive index sensitivity and resolution are subsequently calculated. Furthermore, the chapter highlights the experimental demonstration of the topological darkness phenomenon

in a random gold metasurface, supported by the corresponding theoretical results. Finally, the chapter presents the detection of polyelectrolytes deposited on the surface of the Au NI.

As a complementary information, Appendix A shows a detailed derivation of the dielectric function using the Lorentz-Drude model, while Appendix B shows the derivation of the dispersion relation of surface plasmon polaritons.

Chapter 2 | Basic Concepts and State of the Art

In this chapter, the basic concepts for understanding the topics covered in this dissertation are presented. First, the Maxwell's equations are presented to understand the light propagation and its interaction with matter, including metals. Then, Fresnel coefficients are given to explain the behaviour of light when interacting with an interface between two media under external and internal incidence.

The Drude model analytically introduces the interaction between an electric field and electrons in materials, particularly in metals. Subsequently, the Lorentz-Drude model, an extension of the Drude model, provides a more comprehensive description of how light interacts with metals, considering bound electrons and damping effects.

Additionally, the necessary conditions for observing surface plasmon polaritons are analytically obtained. Furthermore, localized surface plasmon resonance conditions are also given for understanding how light interacts with metallic nanoparticles. Later, a short description of biosensors and its subfield, optical biosensors, is followed by the main parameters that characterize them. Finally, this chapter concludes by reviewing the most relevant works in optical sensing using metallic films and nanostructures establishing context and providing a foundation for the research conducted in this dissertation.

2.1 Electromagnetic waves

2.1.1 Maxwell equations

The unification of the electric and magnetic theory was established by James Clerk Maxwell in the third part of the paper titled "*A dynamical theory of the electromagnetic field*". Using modern mathematical concepts for that time, now known as vector calculus, he was able to mathematically establish the relationship between the electric \vec{E} and magnetic \vec{H} fields described by Michael Faraday and André-Marie Ampère. The Maxwell equations in their differential form in a medium are [69]

$$\nabla \cdot \vec{D} = \rho, \quad (2.1)$$

$$\nabla \cdot \vec{B} = 0, \quad (2.2)$$

$$\nabla \times \vec{E} = -\frac{\partial \vec{B}}{\partial t}, \quad (2.3)$$

$$\nabla \times \vec{H} = \vec{J} + \frac{\partial \vec{D}}{\partial t}. \quad (2.4)$$

$\vec{D} = \epsilon \vec{E}$ and $\vec{B} = \mu \vec{H}$ are the constitutive relations and relate the electric and magnetic flux densities \vec{D} , \vec{B} to the field intensities \vec{E} , \vec{H} , respectivamente. \vec{D} is also known as the electric displacement. The electric and magnetic permeability of the medium are represented by ϵ and μ , respectively. $\vec{J} = \mu \sigma \vec{E}$ stands for the volumetric electric current density. The scalar quantities ρ and σ are the volumetric electric charge density and the volumetric electric conductivity, respectively.

Let us consider an isotropic media that exhibit linear response to an external electromagnetic field. Additionally, we will consider materials whose interaction with a magnetic field is negligible, rendering them nonmagnetic. Then, the electric permeability is related to the electric susceptibility χ as follows

$$\epsilon = \epsilon_0(1 + \chi), \quad (2.5)$$

where ϵ_0 stands for the electric permittivity in free space. Thus, the electric displacement, the electric field and the electric susceptibility are given by

$$\vec{D} = \epsilon_0(1 + \chi)\vec{E}. \quad (2.6)$$

The description of the electric field includes polarization effects, which are related by

$$\vec{P} = \epsilon_0 \chi \vec{E}, \quad (2.7)$$

where \vec{P} is the electric dipole moment per unit volume inside the material.

Now, for a non-conductive medium, $\sigma = 0$, taking the curl of both sides of Faraday's law [Equation (2.3)] and combining it with Ampère's law [Equation (2.4)], the wave equation for the electric field is [69]

$$\nabla^2 \vec{E} = \frac{1}{c^2} \frac{\partial^2 \vec{E}}{\partial t^2}, \quad (2.8)$$

where $c = 1/\sqrt{\mu\epsilon}$ is the speed of light. The relative permittivity and permeability are defined as

$$\epsilon_r = \frac{\epsilon}{\epsilon_0}, \quad \mu_r = \frac{\mu}{\mu_0}, \quad (2.9)$$

and

$$n = \sqrt{\epsilon_r \mu_r}, \quad (2.10)$$

is the refractive index of the medium. Using Equation (2.10), the speed of light in a medium can be expressed in terms of the speed of light in free space c_0 by

$$c = \frac{c_0}{n} \quad (2.11)$$

It can be shown that the differential spatial and temporal operators can be transformed in the Fourier domain in the following way:

$$\nabla \rightarrow i\vec{k}, \quad \frac{\partial}{\partial t} \rightarrow -i\omega. \quad (2.12)$$

Then, the wave equation becomes

$$ik^2 \vec{E} = \frac{-i\omega^2}{c^2} \vec{E}, \quad (2.13)$$

or

$$k = \frac{\omega}{c_0} n. \quad (2.14)$$

Equation (2.14) is known as dispersion relation; and it is true for transverse waves propagating in a medium with refractive index n .

Let us now consider a solution of the wave equation where the electric field is described by a mathematical function where the spatial and temporal dependencies are separated in the form

$$\vec{E}(\vec{r}, t) = \vec{E}_0(\vec{r}) e^{i\omega t}. \quad (2.15)$$

After substituting Equation (2.15) in Equation (2.8) and then simplifying, we obtain the relation

$$(\nabla^2 + k^2) \vec{E}_0 = 0. \quad (2.16)$$

Equation (2.16) is known as the Helmholtz equation and it represents a time-independent form of the wave equation.

2.1.2 Fresnel coefficients

We shall consider an interface composed between two homogeneous and isotropic dielectrics where absorption or other types of losses are not considered. An incident electromagnetic field with wavevector \vec{k}_i propagates in a medium with electric permittivity of ϵ_1 reaches an interface with another medium with electric permittivity of ϵ_2 . Then, the electromagnetic field is reflected with wavevector of \vec{k}_r and at the same time the electromagnetic field is partially transmitted with wavevector \vec{k}_t . Here, the magnetic permeability of both media is negligible, consequently $\mu_1 = \mu_2 = 1$. Additionally, the direction of the reflected wave is determined by the reflection law, $\theta_i = \theta_r$, while for the transmitted wave is determined for the Snell's law, $n_1 \sin \theta_i = n_2 \sin \theta_t$. As depicted in Figure 2.1, the plane of incidence is the xz plane, and the xy plane is taken as the boundary.

The general expression for the incident, reflected and transmitted plane waves are

$$\vec{E}_{i,r,t} = \vec{E}_{0,i,r,t} e^{-i(\vec{k}_i,r,t \cdot \vec{r} - \omega t)}. \quad (2.17)$$

At the boundary of both media, the tangential components of the electric and magnetic fields must be continuous, hence

$$\begin{aligned} \vec{E}_{1 \text{ tangential}} &= \vec{E}_{2 \text{ tangential}}, \\ \vec{H}_{1 \text{ tangential}} &= \vec{H}_{2 \text{ tangential}}. \end{aligned} \quad (2.18)$$

Additionally, the normal components of the electric field displacement and the magnetic field should be also continuous across the interface, then

$$\begin{aligned} \vec{D}_{1 \text{ normal}} &= \vec{D}_{2 \text{ normal}}, \\ \vec{B}_{1 \text{ normal}} &= \vec{B}_{2 \text{ normal}}. \end{aligned} \quad (2.19)$$

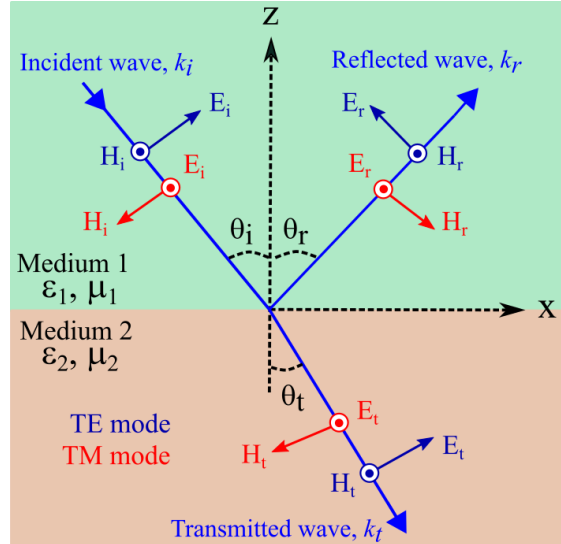


Figure 2.1: Incident electromagnetic field (\vec{E}_i, \vec{H}_i) at an interface composed by a medium 1 with permittivity (ε_1) and permeability (μ_1) and a medium 2 with permittivity (ε_2) and permeability (μ_2). Subsequently, the electromagnetic field is reflected (\vec{E}_r, \vec{H}_r) in the medium 1 with wave vector \vec{k}_r , while simultaneously being transmitted (\vec{E}_t, \vec{H}_t) into the medium 2 with wave vector \vec{k}_t . The directions of reflected and transmitted electromagnetic field are governed by the reflection and Snell's laws, respectively. The TE mode is represented by navy blue, while the TM mode is represented by red.

Now, let us explore two distinct scenarios. The first case arises when the magnetic field vector aligns perpendicular to the plane of incidence, hence known as the Transverse Magnetic (TM) mode or transverse magnetic polarization. The second case occurs when the electric field oscillates perpendicular to the plane of incidence, denoted as the Transverse Electric (TE) mode or transverse electric polarization.

Applying the boundary conditions for TM polarization, we derive

$$\begin{aligned} \vec{E}_i + \vec{E}_r &= \vec{E}_t, \\ \vec{B}_i + \vec{B}_r &= \vec{B}_t. \end{aligned} \quad (2.20)$$

Rewriting the magnetic field boundary conditions in terms of the x -components, we obtain

$$B_i \cos \theta_i - B_r \cos \theta_r = B_t \cos \theta_t. \quad (2.21)$$

In addition, the amplitudes of the magnetic and electric fields are related by the relation

$$B = \frac{n}{c} E. \quad (2.22)$$

By combining from Equation (2.20) to Equation (2.22) and solving for $\frac{E_{r,s}}{E_{i,s}}$, the reflection coefficient yields [69]

$$r_s = \frac{n_1 \cos \theta_i - n_2 \cos \theta_t}{n_1 \cos \theta_i + n_2 \cos \theta_t}, \quad (2.23)$$

and the ratio between the transmitted and incident electric field, $\frac{E_{t,s}}{E_{i,s}}$, represents the transmission coefficient, which is expressed as [69]

$$t_s = \frac{2n_1 \cos \theta_i}{n_1 \cos \theta_i + n_2 \cos \theta_t}. \quad (2.24)$$

Equations (2.23) and (2.24) are called the Fresnel coefficients for the TM polarization or also called *s* polarized light. In a similar way, the Fresnel coefficients for the TE polarization are obtained. Now, applying the boundary conditions for the TE polarization

$$\begin{aligned} \vec{E}_i + \vec{E}_r &= \vec{E}_t, \\ \vec{B}_i + \vec{B}_r &= \vec{B}_t, \end{aligned} \quad (2.25)$$

and rewriting the electric field in terms of the *x*-components we obtain

$$E_i \cos \theta_i - E_r \cos \theta_r = E_t \cos \theta_t. \quad (2.26)$$

Using Equations (2.22), (2.25) and (2.26) the ratio between the parallel components of the reflected and the incident electric wave $\frac{E_{r,p}}{E_{i,p}}$ is [69]

$$r_p = \frac{n_2 \cos \theta_i - n_1 \cos \theta_t}{n_1 \cos \theta_t + n_2 \cos \theta_i}. \quad (2.27)$$

Similarly, solving for the ratio between the parallel components of the transmitted and the incident electric wave $\frac{E_{t,p}}{E_{i,p}}$, the transmission is given by [69]

$$t_p = \frac{2n_1 \cos \theta_i}{n_1 \cos \theta_t + n_2 \cos \theta_i}. \quad (2.28)$$

Equations (2.27) and (2.28) are called reflection and transmission Fresnel coefficients, respectively, for the TE polarization or also called *p* polarized light.

Moreover, the reflectivity is defined as

$$R_{s,p} = |r_{s,p}|^2, \quad (2.29)$$

with the corresponding phase as

$$\phi_{s,p} = \arg(r_{s,p}). \quad (2.30)$$

And the transmittance is

$$T_{s,p} = \frac{n_2 \cos \theta_t}{n_1 \cos \theta_i} |t_{s,p}|^2. \quad (2.31)$$

As an example, let us consider an interface composed of water ($n_{\text{water}} = 1.33$) and glass ($n_{\text{glass}} = 1.52$), where incident light goes from the medium with a lower refractive index to one with a higher refractive index, a condition known as external incidence. The reflectance and transmittance dependence on the angle of incidence, for both *s* and *p* polarization components, are depicted in Figure 2.2a and Figure 2.2b, respectively.

At a specific angle of incidence, the incident light polarized parallel to the plane of incidence becomes completely polarized perpendicular to the plane of incidence upon reflection ($r_p = 0$). This angle, known as the angle of polarization or Brewster angle, is 48.81° for the water-glass interface, as depicted in Figure 2.2a.

As previously mentioned, a non-absorbent and lossless medium was considered, then from Figure 2.2 it can be confirmed that the relation $R + T = 1$ is fulfilled.

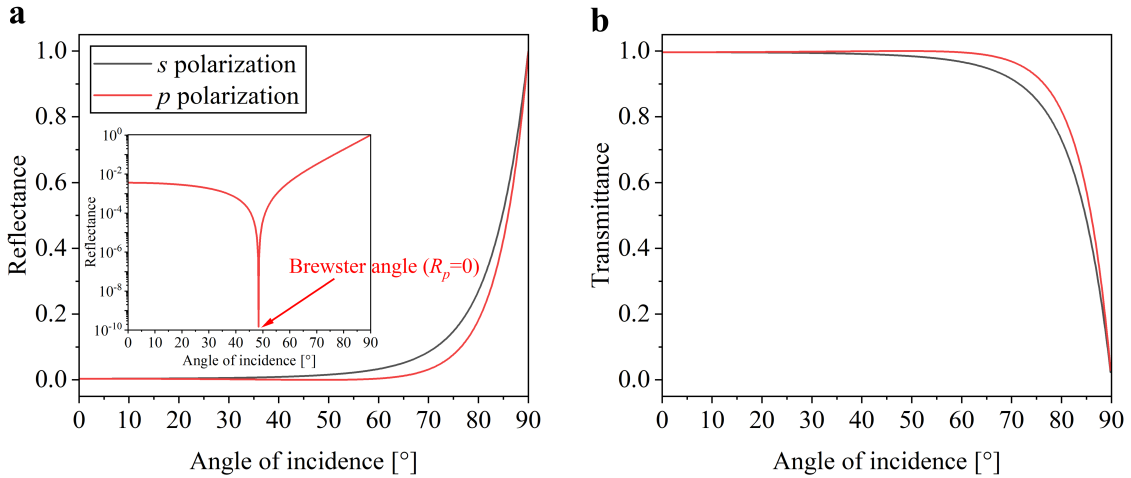


Figure 2.2: a. Reflectance and b. transmittance calculated using the Fresnel coefficients for s (black) and p (red) polarization components. The interface consists of water and glass media, under external incidence. Inset in a. shows R_p in logarithmic scale. The red arrow indicates Brewster angle with value of 48.81°

2.1.3 Total internal reflection

Total Internal Reflection (TIR) is a phenomenon that occurs when an incidence wave propagates from a denser medium to a less dense one ($n_1 > n_2$), also called internal incidence. At a particular angle of incidence, instead of refracting into the second medium, the wave is reflected back into the original medium. According to the Snell's law, the critical angle is defined as [69]

$$\theta_c = \arcsin\left(\frac{n_2}{n_1}\right). \quad (2.32)$$

Figure 2.3 illustrates the reflectance Fresnel coefficients as a function of the angle of incidence for the glass-water interface for both p and s polarization components. In both cases, the reflectance reaches its maximum at the angle of incidence with a value of 61.05° . Above this angle, the reflectance remains with a value of one.

Though none of the wave is transmitted to the second medium, there is a flow of energy across the boundary. The electric wave which propagates along the interface in the plane of incidence is described by

$$E = E_0 e^{-i(kz \cos \theta_t + kx \sin \theta_t)}. \quad (2.33)$$

Separating the terms related to the spatial coordinates x and z , and assuming total internal reflection the following expression is obtained

$$E = E_0 e^{-k\beta z} e^{-ikx(1+\beta^2)^{1/2}}, \quad (2.34)$$

where the factor $\beta = \left(\frac{n_1^2}{n_2^2} \sin^2 \theta_i - 1\right)^{1/2}$ is called attenuation constant. Equation (2.34) represents a non-propagating wave and is usually referred as evanescent wave. The term $E_0 e^{-k\beta z}$ in Equation (2.34) shows that the amplitude of the evanescent wave decreases exponentially with distance from the interface. The characteristic penetration depth or the skin depth is the distance where the amplitude of the electric field at the interface decays at $1/e$ and is defined as $1/k\beta$.

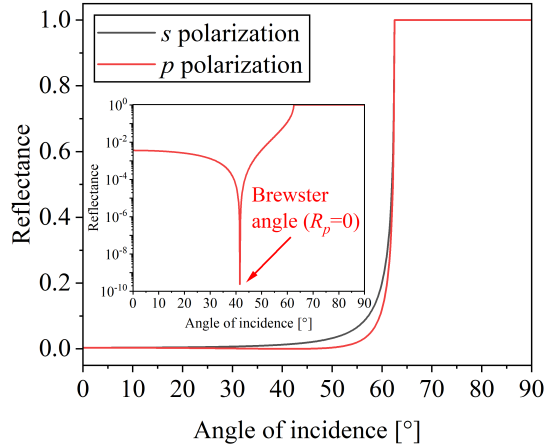


Figure 2.3: Reflectance as function of the angle of incidence for an interface composed of water and glass under internal of incidence. The inset shows R_p in logarithmic scale. The Brewster angle is 41.19° , while the critical angle is 61.05°

In addition, the evanescent field penetration depth can be expressed in terms of the angle of incidence as follows [70]

$$L_{pd} = \frac{\lambda}{4\pi\sqrt{n_2^2 \sin^2 \theta_i - n_1^2}}, \quad (2.35)$$

where λ is the incident wavelength in vacuum and θ_i is the angle of incidence which is greater than the critical angle.

In Figure 2.4a, a schematic representation of the penetration depth of the evanescent field is depicted. As an example of typical values of the penetration depth of the evanescent field, let's consider an incident electric field propagating from glass to water with a wavelength of 532 nm. Figure 2.4b presents various penetration depth values as a function of the angle of incidence calculated using Equation (2.35).

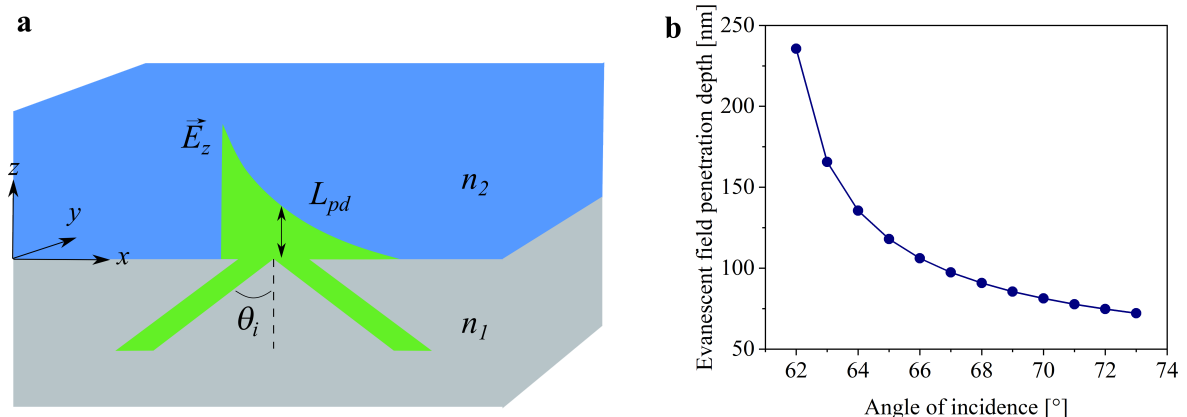


Figure 2.4: a. Graphical illustration of an interface between glass and water, with refractive indexes of $n_1 = 1.52$ and $n_2 = 1.33$, respectively. The interface is illuminated by an incident electric field with wavelength of 532 nm and an angle of incidence of θ_i . The penetration depth of the evanescent field is illustrated by a horizontal arrow, where amplitude of the evanescent field decays to $1/e$. b. Penetration depth as a function of the angle of incidence

It demonstrates a significant dependence of the penetration depth on the angle of incidence. As the angle of incidence increases beyond the critical angle, a reduction in penetration is evident. For instance, at an angle of 62° , the penetration depth is 236 nm, whereas for a more oblique angle (73°), it reduces to 72 nm. This indicates that the evanescent field decays more rapidly as the light deviates further from the critical angle for TIR.

The excitation of the evanescent wave in TIR conditions has several important and diverse applications, for example in optical waveguides and fibres, TIR fluorescence microscopy and SPR sensors, among others.

2.1.4 Transfer matrix method for calculating the reflectance of a multilayered system

The transfer matrix method is widely used theory for analysing the propagation of light in a stratified system. Therefore, it is necessary to extend the previous formulation of the reflection and transmission Fresnel coefficients for a multilayered system. For multiple films, the reflectance and transmission coefficients are mathematically described using 2×2 matrices.

We shall consider a multilayered system composed by N layers with thickness d_j , where the light propagates from the medium j to a medium $j + 1$, as depicted in Figure 2.5. Additionally, the thickness of the first and the last medium are assumed to be semi-infinite.

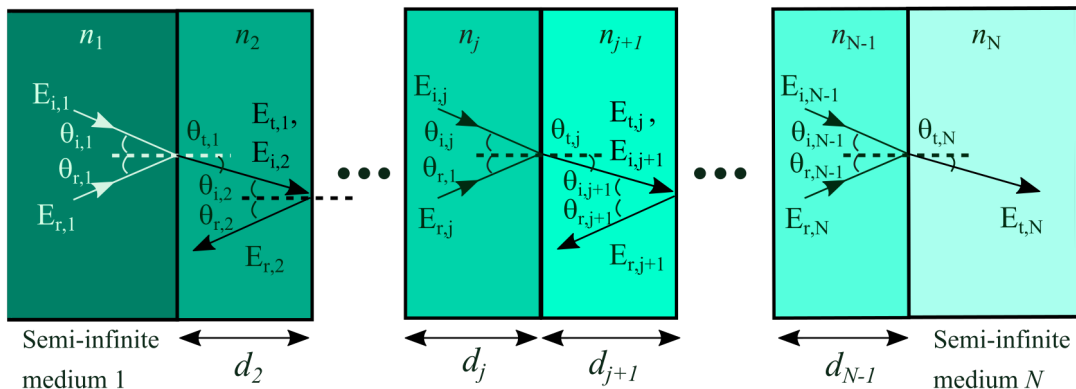


Figure 2.5: Geometry of a stratified system comprising N layers with refractive index n . Each layer has a thickness d , except for the first and last layers, which are considered as semi-infinite media. The angles of incidence θ_i and reflection θ_r are related by the reflection law, while the incident and transmitted angles θ_t follow Snell's law. The paths of the optical incident, reflected, and transmitted rays are indicated by arrows

Similarly, the boundary conditions for the tangential electric and magnetic fields, must be also satisfied in each interface. Then, the boundary conditions for s polarized electric field are

$$\begin{aligned} \vec{E}_{i,j} + \vec{E}_{r,j} &= \vec{E}_{t,j+1}, \\ B_{i,j} \cos \theta_{i,j} - B_{r,j} \cos \theta_{r,j} &= B_{t,k} \cos \theta_{t,j+1}. \end{aligned} \quad (2.36)$$

Here $\theta_{i,j}$ is the angle of incidence from the medium with refractive index n_j and $\theta_{t,j+1}$ is the transmitted angle to the medium with refractive index n_{j+1} .

For the p polarized electric field, the boundary conditions are

$$\begin{aligned} E_i \cos \theta_i - E_r \cos \theta_r &= E_t \cos \theta_t, \\ \vec{B}_i + \vec{B}_r &= \vec{B}_t. \end{aligned} \quad (2.37)$$

From the boundary conditions, the electric field can be written in a matrix in the form

$$V_j \begin{pmatrix} E_{i,j} \\ E_{r,j} \end{pmatrix} = V_k \begin{pmatrix} E_{i,j+1} \\ E_{r,j+1} \end{pmatrix}, \quad (2.38)$$

where $V_{j,k}$ are 2×2 matrices. For s polarized light, we obtain

$$V_j^s = \begin{pmatrix} 1 & 1 \\ n_j \cos \theta_j & -n_j \cos \theta_j \end{pmatrix}, \quad (2.39)$$

and for p polarized light

$$V_j^p = \begin{pmatrix} \cos \theta_j & \cos \theta_j \\ n_j & -n_j \end{pmatrix}. \quad (2.40)$$

Now, rewriting the electric field in terms of V_j and V_{j+1}

$$\begin{pmatrix} E_{i,j} \\ E_{r,j} \end{pmatrix} = V_j^{-1} V_{j+1} \begin{pmatrix} E_{i,j+1} \\ E_{r,j+1} \end{pmatrix}, \quad (2.41)$$

where the transfer matrix $T_{j,j+1}$ is defined as $T_{j,j+1} = V_j^{-1} V_{j+1}$. Then, it can be written for the s polarization component as

$$T_{j,j+1}^s = \frac{1}{2} \begin{pmatrix} 1 & \frac{1}{n_j \cos \theta_j} \\ 1 & -\frac{1}{n_j \cos \theta_j} \end{pmatrix} \begin{pmatrix} 1 & 1 \\ n_{j+1} \cos \theta_{j+1} & -n_k \cos \theta_{j+1} \end{pmatrix}, \quad (2.42)$$

and for the p polarization component as

$$T_{j,j+1}^p = \frac{1}{2} \begin{pmatrix} \frac{1}{\cos \theta_j} & \frac{1}{n_j} \\ \frac{1}{\cos \theta_j} & -\frac{1}{n_j} \end{pmatrix} \begin{pmatrix} \cos \theta_{j+1} & \cos \theta_{j+1} \\ n_{j+1} & -n_{j+1} \end{pmatrix}. \quad (2.43)$$

Considering that the light is propagating in a homogeneous medium, the propagation matrix before reaching the medium $j+1$ is defined as

$$P_j = \begin{pmatrix} e^{i\phi_j} & 0 \\ 0 & e^{-i\phi_j} \end{pmatrix} \quad (2.44)$$

where the phase is defined as

$$\phi_j = \left(\frac{\omega}{c} \right) d_j n_j \cos \theta_j. \quad (2.45)$$

The resulting electric field amplitudes are then obtained by alternately multiplying the transfer matrix $T_{j,j+1}^{s,p}$ with its respective propagation matrix P_j . Then, the two sets of electric field coefficients are related by

$$\begin{pmatrix} E_{i,1} \\ E_{r,1} \end{pmatrix} = T_{01}^{s,p} P_1 T_{12}^{s,p} \cdots P_N T_{N+1}^{s,p} \begin{pmatrix} E_{i,N+1} \\ E_{r,N+1} \end{pmatrix}, \quad (2.46)$$

where the product of the transfer and propagation matrices can be defined as $M = T_{01}^{s,p} P_1 T_{12}^{s,p} \cdots P_N T_{N+1}^{s,p}$, and M is usually referred to as the system transfer matrix. Since M is a 2×2 matrix, it can be rewritten as

$$M = \begin{pmatrix} m_{11} & m_{12} \\ m_{21} & m_{22} \end{pmatrix}. \quad (2.47)$$

Finally, the reflected and the transmitted amplitude coefficients for the multilayered system can be calculated as [71, 72]

$$\begin{aligned} r^{s,p} &= \frac{m_{21}}{m_{11}}, \\ t^{s,p} &= \frac{1}{m_{11}}. \end{aligned} \quad (2.48)$$

2.2 Optical properties of metals

Metals, which are characterized by excellent mechanical, thermal and optical properties, efficiently transport electricity due to the presence of big number of freely moving electrons. The dielectric constant of materials ϵ , including metals, is a fundamental optical parameter for describing the response of the material under an applied electric field. As the material response depends on the frequency of the electric field, ϵ is more commonly referred to as the dielectric function.

The Drude-Lorentz model is a classical theory that describes the interaction of light with materials. This theory combines the Drude model, [73] which describes the motion of free electrons in a metal, with the Lorentz model, [74] which is an extension of the Drude model for a more complete description of the interaction of atoms under an applied electric field.

In the Drude-Lorentz model electrons, with mass m_e , are attached to the atomic nucleus through a spring-like force with a restitutive constant Γ . The analysis of forces using the Newton's second law is then

$$\vec{F}_{\text{electric}} + \vec{F}_{\text{restoring}} + \vec{F}_{\text{damping}} = \vec{F}_{\text{net}}. \quad (2.49)$$

By explicitly writing the value of each force we obtain

$$q\vec{E} + m_e\omega_0^2\vec{r} + m_e\Gamma\frac{\partial\vec{r}}{\partial t} = m_e\frac{\partial^2\vec{r}}{\partial t^2}. \quad (2.50)$$

Thus, when applying an external electric field \vec{E} with frequency ω to the atom-electron system, forces on the electron are induced, leading to a displacement of charges, also known as dipole moment. The dipole moment \vec{p} is proportional to the incident electric field, and relating it to the electric susceptibility χ , through the electric polarizability \vec{P} , the dielectric permittivity, denoted as ϵ_m , is [48]

$$\epsilon_m(\omega) = 1 + \frac{\omega_p^2}{(\omega_0^2 - \omega)^2 - i\Gamma\omega}, \quad (2.51)$$

where ω_0 stands for the resonant frequency of the string, q is the fundamental charge of electron and $\omega_p^2 = \frac{N_e q^2}{\epsilon_0 m_e}$ is known as plasma frequency of the free electron gas. The term N_e is the electron density. The plasma energy is characteristic of each metal; however, the typical values go from $\hbar\omega_p \approx 2$ eV to 15 eV, see Table 2.1.

From Equation (2.51), we conclude that electrons in the metal oscillate in phase with the incident electric field. Additionally, as the dielectric function is related to the refractive

Table 2.1: Plasma energy values of various metals [75]

Metal	Symbol	Plasma energy [eV]
Gold	Au	9.026
Silver	Ag	9.013
Aluminium	Al	14.750
Copper	Cu	8.760
Platinum	Pt	5.145
Iron	Fe	4.091
Titanium	Ti	2.517
Palladium	Pd	5.455

index, it is concluded that a dependence of the complex refractive index on the frequency of the incident electric field.

The complete mathematical derivation of the dielectric function is provided in Appendix A.

2.2.1 Drude model

The Lorentz model can be extended to metals by considering its electronic structure as free electrons gas, where no restoring forces act on the atom-electron system under the influence of an electric field. The Drude model is a reduced case of the Lorentz model, by considering the resonant frequency of the string as $\omega_0 = 0$. Additionally, it is assumed that the damping force is proportionally to the velocity of electron, and it is due to consecutive collisions between them.

Similarly, as demonstrated in the calculations presented in Appendix A, an equation relating the electric permittivity and the frequency of the incident light can be derived. Analysing the forces acting on the system using Newton's second law yields the expression.

$$-q\vec{E} - m_e \Gamma \frac{\partial \vec{r}}{\partial t} = m_e \frac{\partial^2 \vec{r}}{\partial t^2}. \quad (2.52)$$

The solution of the differential equation is

$$\vec{r}(\omega) = -\frac{q}{m_e} \frac{\vec{E}(\omega)}{\omega^2 + i\Gamma\omega}. \quad (2.53)$$

Following a similar procedure for obtaining the dielectric function using the Drude-Lorentz model, the dielectric permittivity is [48, 76]

$$\varepsilon_m(\omega) = 1 - \frac{\omega_p^2}{\omega^2 + i\Gamma\omega}. \quad (2.54)$$

Similarly, ε_m can be expressed in terms of their real and imaginary part as $\varepsilon_m(\omega) = \varepsilon'_m + i\varepsilon''_m$. Then

$$\varepsilon'_m(\omega) = 1 - \frac{\omega_p^2}{\omega^2 + \Gamma^2}, \quad (2.55)$$

$$\varepsilon''_m(\omega) = \frac{\omega_p^2 \Gamma}{\omega(\omega^2 + \Gamma^2)}. \quad (2.56)$$

Figure 2.6 illustrates the real and imaginary part of the dielectric function using the free electron gas model. For light with frequencies much smaller than the plasma frequency ($\omega \ll \omega_p$), the real part of the dielectric function is negative. Consequently, metals exhibit opacity at shorter wavelengths, reflecting light rather than transmitting it. Conversely, when the frequency of an electromagnetic wave far exceeds the plasma frequency ($\omega \gg \omega_p$), both the imaginary and real parts of the dielectric constant are positive, with $\varepsilon'_m \approx 1$. This indicates that electromagnetic waves can effectively propagate through the metal. Additionally, ε''_m approaches zero indicating that the metal weakly absorbs. In other words, the metal becomes transparent to the electromagnetic waves, allowing them to penetrate into the metal.

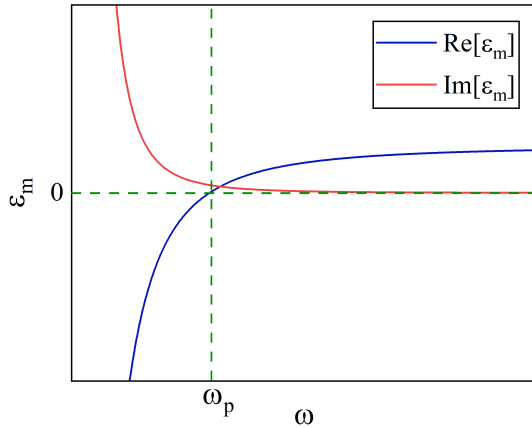


Figure 2.6: Real and imaginary part of the dielectric function ε_m of a metal using the Drude model

Using Equation (2.14), the dispersion relation of the free electron gas is [48, 76]

$$k = \frac{\omega}{c} \sqrt{1 - \frac{\omega_p^2}{\omega^2 + i\Gamma\omega}}. \quad (2.57)$$

Finally, the simplest version of the free electron gas model is obtained by not considering damping in the electron motion, i.e. $\Gamma = 0$. Then, the dielectric permittivity becomes real and it is expressed as [48, 76]

$$\varepsilon_m(\omega) = 1 - \frac{\omega_p^2}{\omega^2}. \quad (2.58)$$

From Equation (2.57), the behavior of ε_m as a function of the light frequency is similar to that represented by the real part of Equation (2.54), as depicted in the blue plot of Figure 2.6. For frequencies of the incident light lower than the plasma frequency ($\omega < \omega_p$), ε_m is negative, at the same time k is imaginary, indicating that the wave decays exponentially with distance inside the metal. On the contrary, when the frequency of the incident light

is above the plasma frequency, ε_m is positive; while k is real and it indicates that the wave propagates through the metal without decay.

By substituting Equation (2.58) into Equation (2.14), the dispersion relation in a free electron gas is [48, 76]

$$k = \frac{\omega}{c} \sqrt{1 - \frac{\omega_p^2}{\omega^2}}. \quad (2.59)$$

Figure 2.7 shows the dispersion relation in the free space (black line) and in a free electron gas (red line). The equation in red is derived by expressing k in terms of ω . As it can be seen both dispersion relations do not intersect for any frequency of the incident light.

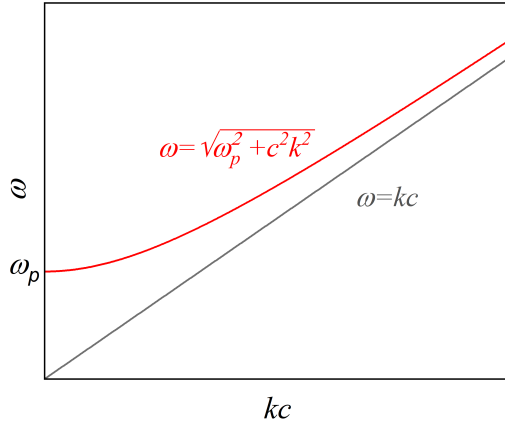


Figure 2.7: Dispersion relation of an electromagnetic field propagating in a free electron gas (red line), based on the Drude model. The grey line represents the dispersion relation of a wave propagating in the free space

Another optical constant of matter is the index of refraction. As discussed everywhere, the refractive index is a dimensionless quantity which indicates how fast an electromagnetic wave travels in a material, respect to the propagation in the vacuum. The complex refractive index is related to the dielectric function by [69]

$$\tilde{n} = \sqrt{\varepsilon_m} = (n + i\kappa). \quad (2.60)$$

The real part of the complex refractive index is known as the refractive index and it is responsible for the dispersion in the medium. The imaginary part determines the absorption of the medium.

2.2.2 Real metals

Drude model is useful to understand the fundamental optical properties of metals. Nevertheless, in deriving the relationship for the dielectric function of a metal, certain simplifications were necessary. For example, factors such as the contributions of additional electrons in the conduction band and electron-phonon interactions were omitted from consideration. Johnson, P.B. and Christy, R.W. experimentally obtained the optical properties of various metals, over a wide spectral range. [77] Their work provides accurate information about the dielectric function of metals.

Figure 2.8 illustrates the real and imaginary components of ε_m for gold and silver, respectively, as determined through two approaches: the Drude model (depicted in dark) and experimental data provided by Johnson and Christy (depicted in red). The parameters for the Drude model to both gold and silver were taken from the work of Zeman, E.J. and Schatz, G.C. [78]. Typically, these parameters are defined in terms of photon energy in electron volts (eV), with the plasma frequency of gold standing at 9.026 eV and that of silver at 9.6 eV. Moreover, the damping frequencies for gold and silver are 26.7 meV and 22.8 meV, respectively.

Discrepancies between the Drude model and experimental data in the dielectric function are evident. For gold, the imaginary component of ε_m (Figure 2.8a) exhibits a good agreement in the near-infrared range yet displays contrasting behaviour in the ultraviolet (UV) region. Furthermore, while both plots of the real component of ε_m show similar trends, a gap exists between them. This disparity arises because the Drude model does not account for interband transitions within metals.

Likewise, the real component of ε_m for silver (Figure 2.8b) demonstrates a consistent behaviour between both approaches. However, notable differences arise in the imaginary component of ε_m for wavelengths below 400 nm, where the experimental data indicate significantly higher losses compared to those predicted by the Drude model.

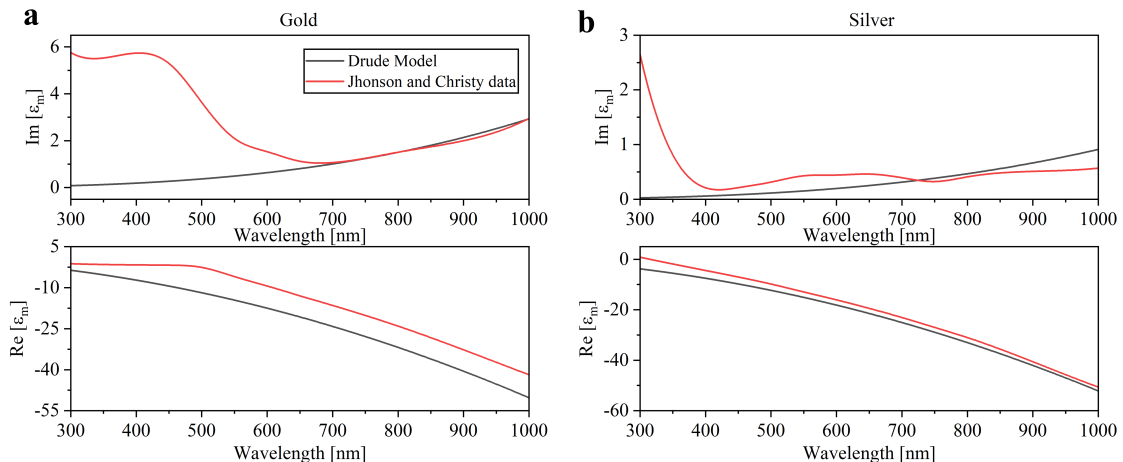


Figure 2.8: Comparison of the real and imaginary parts of dielectric function of **a.** gold and **b.** silver using the Drude model (dark) and the experimental data from Johnson and Christy (red)

2.3 Surface Plasmon Polaritons

Surface Plasmon Polaritons (SPPs) are collective oscillation of conduction electrons at an interface between a dielectric and a flat metal when illuminated by *p* polarized electric field. Experimental excitation of SPPs requires a specific momentum matching condition between the incident photons and the electrons. Various methods can be employed to excite SPPs, with prism coupling, grating, and metallic nanostructures being the most used techniques.

Indirect observation of SPPs is typically achieved using the surface plasmon resonance spectroscopy, which involves reflected or transmitted electric field measurements. When the SPP conditions are met, there is a significant absorption of light at the metal surface, signifying an efficient transfer of energy from the incident photons to the collective oscillations of free electrons at the metal surface. Consequently, a sharp dip in the reflectance spectrum

or a peak in the transmittance spectrum is observed. This phenomenon is referred to as SPR.

The angular or spectral position of the SPR depends on several factors including the plasma frequency of the metal, the angle and wavelength of the incident light as well as the refractive index of the surrounding dielectric. Variations in the refractive index of the surrounding medium near the metal surface lead to shifts in the resonance angle, intensity, wavelength, or phase of the SPR signal. This phenomenon is exploited for surface-sensitive techniques for sensing and biosensing applications, where SPR shifts are induced by bimolecular interactions.

In this context, the basic concepts, principles and the conditions to excite SPP are presented. The dispersion relation of an electromagnetic wave propagating in a medium provides crucial information about its propagation, concerning its angular and spatial frequency as well as its direction. Consequently, the dispersion relation for SPPs must be determined. Its derivation is based on solving the boundary conditions at the interface between a metal and a dielectric interface.

Therefore, we now shall consider an interface comprising two media: thin metallic film and a non-absorbing dielectric medium, as shown in Figure 2.1. In this context, medium 1 represents the dielectric medium with a dielectric constant of ε_d while the medium 2 represents the thin metallic film with a dielectric function ε_m .

The incident electric and magnetic fields can be mathematically described as $\vec{E}(\vec{r}) = \vec{E}(z)e^{ik_x z}$ and $\vec{H}(\vec{r}) = \vec{H}(z)e^{ik_x z}$, respectively. By substituting these equations into the Helmholtz equation [Equation (2.16)] and using Maxwell's equations, we can describe the electric and magnetic fields on both sides of the interface. Then, by applying boundary conditions and doing some algebra manipulations, we derive the propagation constant [48, 76]

$$k_{\text{SPP}} = \frac{\omega}{c} \sqrt{\frac{\varepsilon_m \varepsilon_d}{\varepsilon_m + \varepsilon_d}}, \quad (2.61)$$

where k_{SPP} is known as the dispersion relation for SPPs. This equation is only valid when the interface is illuminated under a *p* polarized electric field. In cases where the interface is illuminated under a *s* polarized electric field, no dispersion relation is mathematically obtained, indicating that SPPs can only be excited under *p* polarized incident electric fields. A detailed derivation of the dispersion relation for SPPs is shown in Appendix B.

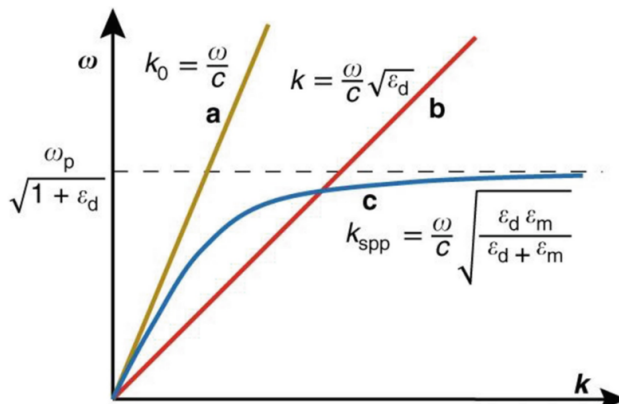


Figure 2.9: Dispersion relation of an electromagnetic field propagating in the **a.** free space and **b.** a medium with dielectric constant of ε_d . **c.** Dispersion relation of surface plasmon polaritons propagating. ε_d is the dielectric function of the metal and ω_p is the plasma frequency. Image taken from [79]

As an example, the SPP dispersion relation [Equation (2.61)] is plotted for an interface composed of a dielectric and a metal with plasma frequency of ω_p , as shown in Figure 2.9. Additionally, the dispersion relation for an electromagnetic wave propagating in free space and a dielectric medium is also presented.

From Figure 2.9, SPPs cannot be excited by direct illumination, as energy and momentum conservation ($\omega_i = \omega_{\text{SPP}}$ and $k_i = k_{\text{SPP}}$) cannot be fulfilled, meaning that the blue curve does not intersect with the gold curve. Instead, excitation of SPPs necessitates a high refractive index medium for fulfilling the momentum transfer condition, leading to the intersection between the blue and red curves.

Another essential parameter is the propagation length L_{pd} of the SPPs wave, which refers to the distance over which the SPP can propagate along the metal-dielectric interface before its intensity decreases significantly by a factor of $1/e$. L_{pd} is described by the following expression [48, 76]

$$L_{\text{pd}} = (2 \text{Im}[k_{\text{SPP}}])^{-1}. \quad (2.62)$$

The typical values of L_{pd} go from 10 to 100 nm, depending upon the experimental conditions used such as the type of metal, dielectric, wavelength, angle of incidence, etc.

Due to the evanescent wave nature of the SPPs, the electric field penetrates into both metal and dielectric media. The distance at which the SPPs electric field decays by a factor of $1/e$, in a direction normal to the interface, is referred to as the skin depth or penetration depth. Then, the penetration depth in the dielectric δ_d and in the metal δ_m are defined as [79]

$$\delta_{d,m} = \frac{1}{k} \sqrt{\left| \frac{\varepsilon_d + \varepsilon_m}{-\varepsilon_{d,m}^2} \right|}, \quad (2.63)$$

Let us consider the interface composed of gold and water media. The penetration depth into the gold and water are analytically calculated using Equation (2.63). In Figure 2.10, the penetration depth of the electric field SPPs into the water and gold are depicted by the black and red lines, respectively.

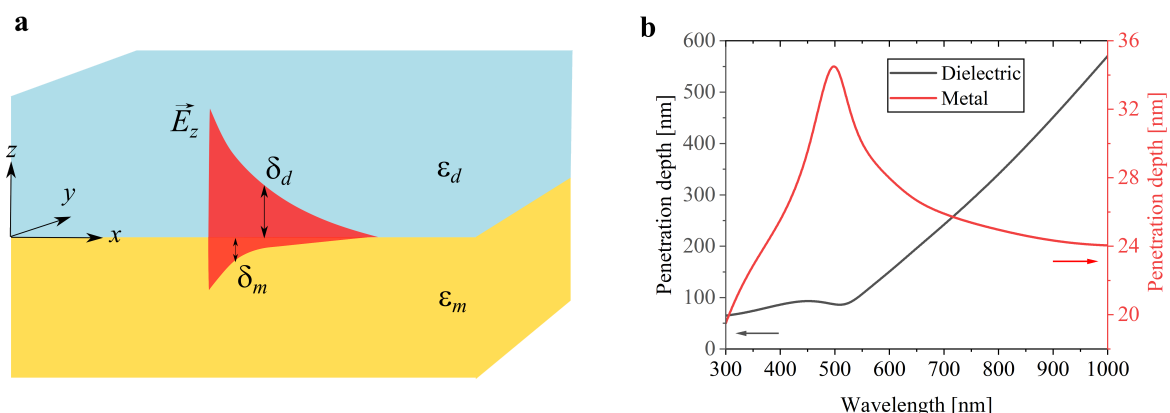


Figure 2.10: a. Schematic representation of the penetration depth of the evanescent field (L_{pd}), as well as the penetration depth of the SPPs into the dielectric (δ_d) and the metal (δ_m) media. b. Penetration depth of the SPPs into water as dielectric and gold as metal. The dielectric constant of water is $\varepsilon_d = 1.7689$ and the dielectric function of gold is obtained from experimental data of Johnson and Christy [77].

It is evident that the electric field of SPPs penetrates more deeply into the dielectric than into the metal. As an example, the dielectric constant of gold and water are $\varepsilon_m = -15.051 + 1.0516i$ and $\varepsilon_d = 1.7689$, respectively, for incident light with a wavelength of 680 nm. Thus, the penetration depth into the gold and water are $\delta_m = 26.2$ nm and $\delta_d = 223.3$ nm, respectively.

2.3.1 Excitation of SPPs

The SPP dispersion relation demonstrates that the SPPs cannot be excited by direct illumination on the metal-dielectric interface mainly because the momentum of the incident photons and the momentum of surface charges on the metal does not match. Figure 2.11 illustrates the main techniques to achieve SPP excitation, including prism coupling, grating coupling and fibre coupling, which are discussed in the following sections.

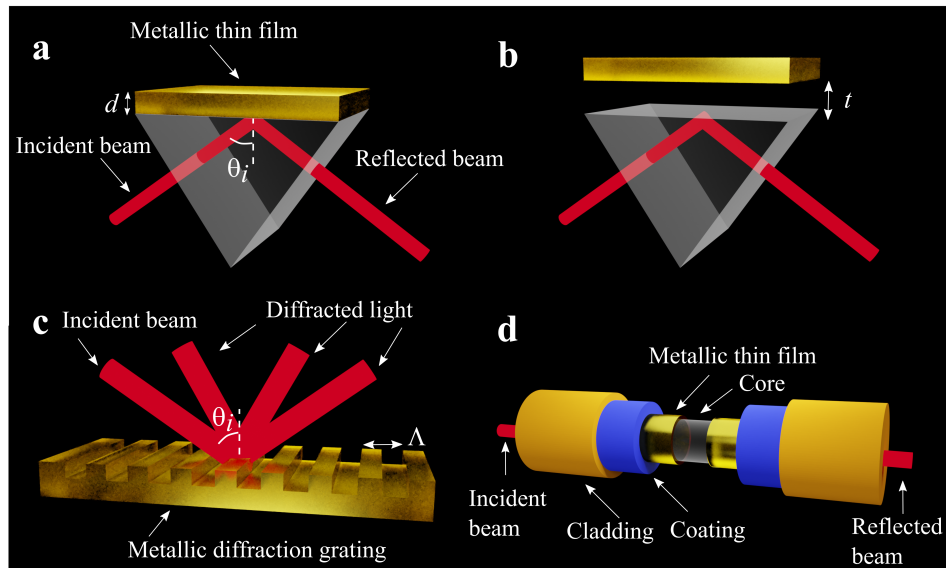


Figure 2.11: Geometrical configurations of SPPs excitation techniques. Prism coupling using **a.** Kretschmann and **b.** Otto configuration. **c.** Excitation of SPPs using a metallic diffraction grating with grating period of Λ . **d.** Optical fibre coupling, where the fibre core is coated with a metallic thin film and directly exposed to the sensing medium

2.3.1.1 Prism coupling

One of the main ways to excite SPP is by coupling the incident photons to the metallic film using a glass prism. This method is mainly achieved under two geometries: Kretschmann [27] and Otto [28] configurations.

E. Kretschmann and H. Raether proposed the exciting of SPPs using a glass prism with a thin metallic film, typically around 50 nm thick, in the top face, see Figure 2.11a. The dielectric-metallic interface is illuminated by light above the critical angle, reaching ATR condition. For this configuration the SPP excitation cannot be achieved for thicker metallic films, since the skin penetration of the evanescent wave is shorter than the film thickness. This problem can be overcome using the Otto configuration. In this case, the prism and the metallic film are separated by a thin gap of air, as depicted in Figure 2.11b. Experimentally, this configuration is impractical as the distance between the prism and the metallic film must

be displaced precisely, so the most used prism coupler geometry for sensing purposes is the Kretschmann configuration.

The excitation of SPP occurs when the wave vector of the propagation constant of evanescent wave exactly matches with that of the SPP of similar frequency, $k_i = k_{\text{SPP}}$. Then

$$\frac{\omega}{c} \sqrt{\varepsilon_p} \sin \theta_R = \frac{\omega}{c} \sqrt{\frac{\varepsilon_m \varepsilon_d}{\varepsilon_m + \varepsilon_d}}. \quad (2.64)$$

Solving for θ_R [48, 76]

$$\theta_R = \sin^{-1} \left(\sqrt{\frac{\varepsilon_m \varepsilon_d}{\varepsilon_p (\varepsilon_m + \varepsilon_d)}} \right). \quad (2.65)$$

This particular angle of incidence is known as resonance angle θ_R . The excitation of SPP is seen by a drastic reduction in the intensity of light reflected by the three-layered system composed of prism-metallic film-dielectric interface, as illustrated in Figure 2.12.

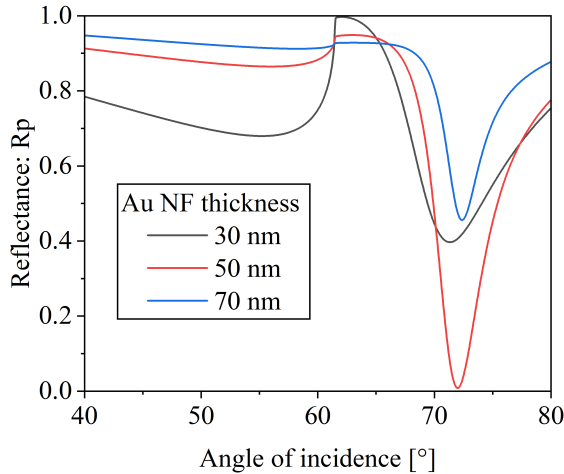


Figure 2.12: Analytical SPR curves of an Au NF using the transfer matrix method. The thickness of the Au NF is 30 nm, 50 nm and 70 nm. The surrounding medium is water, and the incident wavelength is 633 nm

As the angle of incidence increases, the reflectance decreases until it reaches the critical angle for the glass-water interface. Subsequently, the intensity of the reflectance drastically drops, reaching its minimum at the resonance angle. With further increases in angle, the reflectance increases again. Specifically, the 50 nm thick Au NF exhibits the lowest reflectance (0.008) at the resonance angle of $\sim 72^\circ$.

2.3.1.2 Grating coupling

Another way to fulfil the SPP excitation condition is by compensating the momentum mismatch using diffraction effects. For this purpose, the metallic surface is nanopatterned composed of gratings, holes or other structures, see Figure 2.11c. The shape, depth and periodicity of the grating is determinant for the position of the plasmonic response in the electromagnetic spectrum. Let's consider a one-dimensional grating with period Λ . At resonance, the diffracted wave vector is equal to the wave vector of incident light, then

$$\frac{\omega}{c} \sqrt{\varepsilon_p} \sin \theta + \frac{m2\pi}{\Lambda} = \frac{\omega}{c} \sqrt{\frac{\varepsilon_m \varepsilon_d}{\varepsilon_m + \varepsilon_d}}. \quad (2.66)$$

After simplification, the resonance angle is

$$\theta_R = \sin^{-1} \left(\sqrt{\frac{\varepsilon_m \varepsilon_d}{\varepsilon_p(\varepsilon_m + \varepsilon_d)}} - \frac{m\lambda}{n_p^2 \Lambda} \right). \quad (2.67)$$

From Equation (2.67), the resonance angle not only depends on the dielectric function of the metal and the surrounding medium, but also on the grating period. The grating period must be carefully designed to match the momentum of the incident light wave with the SPPs mode, which could limit the flexibility of the system. Moreover, the efficiency of SPPs excitation may be affected due to scattering losses from the grating.

2.3.1.3 Optical fibre coupling

The excitation of SPPs on optical fibres or waveguides is similar to the configuration of the Kretschmann geometry. In this setup, the cladding of the fibre is removed, exposing the core which replaces the prism in the Kretschmann configuration, see Figure 2.11d. The core fibre is then coated with a metallic thin film, allowing direct exposure to the dielectric medium. The resonance condition for exciting surface plasmon waves on optical fibres resembles Equation (2.65), where $\sqrt{\varepsilon_p}$ stands for the refractive index of the fibre core.

SPR fibre sensors offer a practical solution for sensing applications, characterized by a simple, flexible, and compact optical design. However, their sensitivity and resolution are restricted by the signal-to-noise ratio, being a persistent challenge. Furthermore, multimode fibers are susceptible to mechanical disturbances, which can affect the output signal. Additionally, bending the fiber probe has a considerable impact on the sensor's sensitivity. [80]

In summary, the SPP occurs at the interface between a metal and a dielectric. Metals are particularly chosen for their property of having a negative dielectric constant in a determined optical frequency region. This negative dielectric constant enables the formation of surface plasmons. Gold, silver and aluminium are the primary metals used for SPP excitation due to the strong plasmonic responses, tunability, and compatibility with various fabrication techniques. However, the choice of metal depends on the specific requirements of the application, including the desired spectral range, sensitivity, and environmental conditions.

Additionally, the SPR position depends on the dielectric function of the metal, the refractive index of the prism but it mainly depends on the refractive index of the dielectric medium. This is the basic principle of the SPR biosensing; when molecules bind to the surface, the effective refractive index changes, results in a shift in the SPR position.

2.4 Localized Surface Plasmons

Nanoparticles have become increasingly important in recent years due to their diverse biomedical applications such as drug delivering, health diagnosis and therapy.

Localized surface plasmon are non-propagating waves of the free electrons in the surface of metallic nanostructures when illuminated with light. Figure 2.13a shows a schematic representation of localized plasmons in a metallic nanosphere.

The LSPR is produced in nanoparticles composed by noble metals as Au, Ag, Pt, Pd, semi noble metals as Cu, metal oxides such as ZnO, TiO₂, SnO₂ and MnO₂ and other metals

such as Co, Fe and Bi.^[81] The LSPR is typically observed in the visible and infrared range of the electromagnetic spectrum. Beyond the way plasmons are excited the main difference between the SPR and LSPR phenomena is that the near field is highly confined to the surface of nanostructures.

In Figure 2.13b, the near-field pattern of the electric field intensity around Au nanosphere with radius of 20 nm is illustrated. The electric field distribution was computed using the open-access program *Mie calculator*,^[82] with water considered as the surrounding medium. The colour bar indicates the normalized electric field value, ranging from 0 indicating the absence of electric field to 1 representing the maximum amplitude of the electric field.

Figure 2.13c shows a line profile extracted from the normalized electric field distribution around an Au nanoparticle. The line profile is taken at $y = 0$ as indicated by the dashed white line in Figure 2.13b. There are sharp peaks in the electric field at the boundaries of the nanosphere (approximately at $x = -20$ nm and $x = 20$ nm). This indicates that the electric field is strongly enhanced near the surface of the nanoparticle due to the LSPR phenomenon. Moving away from the nanoparticle surface, the electric field strength quickly decreases, indicating that the field enhancement is highly localized near the nanosphere.

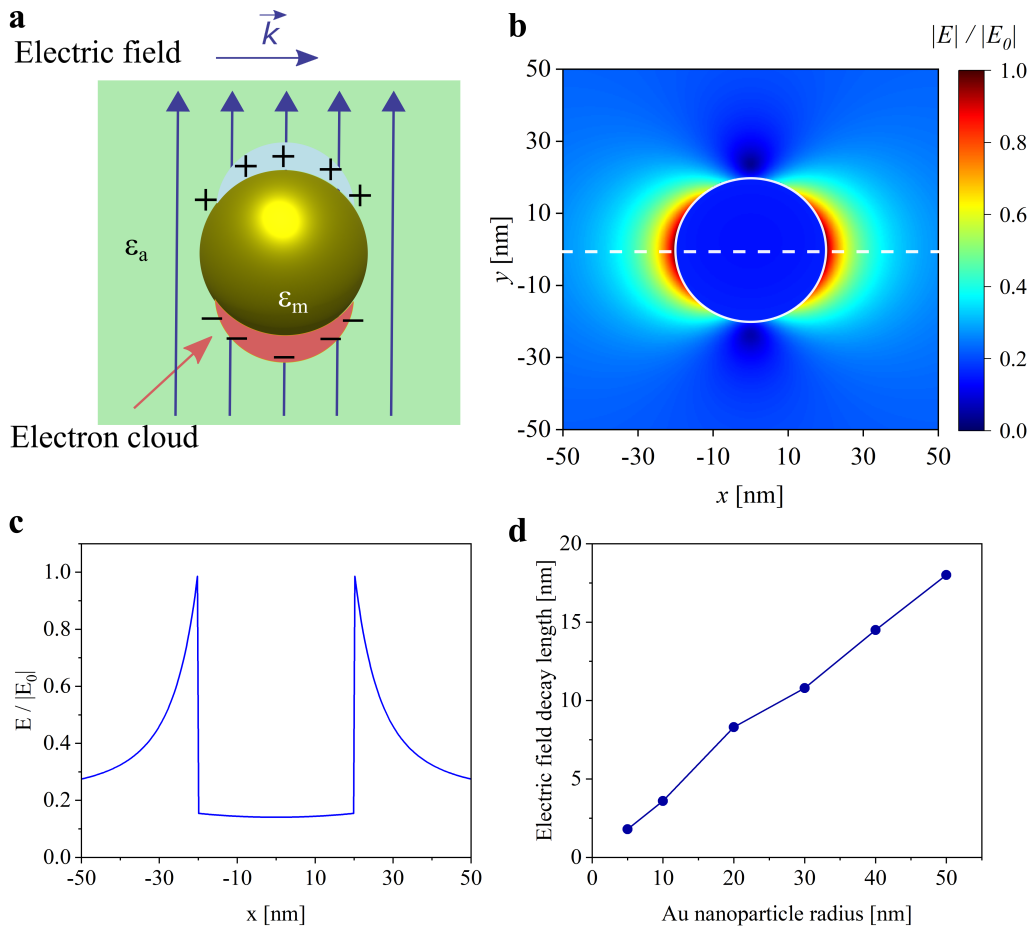


Figure 2.13: **a.** Schematic representation of LSPR phenomenon on a metallic nanosphere with dielectric function ϵ_m surrounded by a medium with dielectric function ϵ_a . The electron cloud, depicted as a red quarter moon, is oscillating perpendicular to the wave vector \vec{k} . **b.** Normalized electric field distribution of an Au nanosphere with a radius of 20 nm, surrounded by water. The near field was computed using the *Mie calculator*.^[82] **c.** Line profile extracted from **b.** at $y = 0$, as indicated by the dashed white line. **d.** Calculated decay length of the LSPR electric field as a function of the nanoparticle radius.

The decay length of the electric field close to the nanoparticle is mainly determined by the size of the nanoparticles, typically spanning tens of nanometres. Figure 2.13d depicts the linear relationship between the decay length of the LSPR electric field and the radius of an Au nanoparticle. For an Au nanosphere with radius of 5 nm, the decay length measures 1.8 nm, whereas for a 50 nm radius nanoparticle, it measures 18.0 nm.

Unlike SPR, the LSPR position depends on the size and shape of the nanoparticle and the composition of the nanoparticle. However, the LSPR strongly depends on the refractive index of the surrounding medium. Consequently, the nanostructures can be used for biosensing applications using the LSPR phenomenon. Like the SPR case, a brief analysis of the optical properties of nanosized particles is presented.

Let us consider the simplest system where a spherical nanoparticle with radius R and dielectric function ε_m is surrounded by an isotropic and non-absorbing medium with dielectric function ε_a . Let's also consider the size of the nanoparticle to be smaller than the incidence wavelength. Additionally, the nanoparticle is illuminated with a linearly polarized electric wave propagating along the z axis which is described by $\vec{E} = E_0 \hat{z}$. As the nanoparticle was assumed to be smaller than the incident wavelength, from the quasistatic approach, the Laplace equation describes their electric potential. From this equation, the electric field can be calculated instead of solving the whole Maxwell's equations.

After solving the Laplace equation and considering the appropriate boundary conditions (here not shown), the electric potential inside Φ_{inside} ($r < R$) and outside Φ_{outside} ($r > R$) the nanosphere can be written as

$$\Phi_{\text{inside}} = -\frac{3\varepsilon_d}{\varepsilon_m + 2\varepsilon_d} E_0 r \cos \theta, \quad (2.68)$$

$$\Phi_{\text{outside}} = -E_0 r \cos \theta + \frac{\varepsilon_m - \varepsilon_d}{\varepsilon_m + 2\varepsilon_d} \frac{E_0 R^3 \cos \theta}{r^2}. \quad (2.69)$$

The first term of the electric potential outside the nanoparticle, Equation (2.69), describes the applied electric field, while the second term describes the dipole located at the center of the particle. Then, Equation (2.69) can be rewritten in terms of the dipole moment \vec{p} as

$$\Phi_{\text{outside}} = -E_0 r \cos \theta + \frac{1}{4\pi\varepsilon_0\varepsilon_d} \frac{\vec{p} \cdot \vec{r}}{r^3}, \quad (2.70)$$

where

$$\vec{p} = 4\pi\varepsilon_0\varepsilon_d R^3 \frac{\varepsilon_m - \varepsilon_d}{\varepsilon_m + 2\varepsilon_d} \vec{E}_0. \quad (2.71)$$

Additionally, the dipole moment is proportional to the electric field, $\vec{p} = \varepsilon_0\varepsilon_d\alpha\vec{E}_0$, where α is the polarizability. Then

$$\alpha = 4\pi R^3 \frac{\varepsilon_m - \varepsilon_d}{\varepsilon_m + 2\varepsilon_d}. \quad (2.72)$$

Equation (2.72) is known as the Clausius-Mossotti relation. The polarizability experiences a resonance when $\varepsilon_m + 2\varepsilon_d$ is minimum, this phenomenon is known as Fröhlich condition. For small changes in the imaginary part of ε_m , the LSPR is located at $\text{Re}[\varepsilon_m(\omega)] = -2\varepsilon_d$.

Nevertheless, this polarizability approach is not sufficient because it considers an isolated spherical nanoparticle with subwavelength dimension. In case of large particles, the

quasistatic approximation, which assumes that the wavelength of the incident light is much larger than the size of the nanoparticles, becomes inadequate.

The Modified Long-Wavelength Approximation (MLWA) describes the polarizability of larger nanoparticles by including the dynamic depolarization and surface damping effects by expanding the dipole radiation up to the third power [83–85]

$$\alpha_{\text{MLWA},\parallel} = \left(\frac{1}{\alpha_{\parallel}} - \frac{k^2}{4\pi a} - \frac{ik^3}{6\pi} \right)^{-1}, \quad (2.73)$$

The second term of Equation (2.73) is the depolarization of the radiation across the particle surface due to the finite ratio of the particle size to the wavelength, while the third term is related to radiation losses due to spontaneous emission by the induced dipole.

Another important optical parameter of a small metallic nanoparticle is the efficiency of how it absorbs and scatters the light. The cross section for absorption is defined as

$$C_{\text{absorption}} = k \text{Im}[\alpha], \quad (2.74)$$

and the cross section for scattering is given by

$$C_{\text{scattering}} = \frac{k^4}{6\pi} |\alpha|^2. \quad (2.75)$$

The extinction cross section is defined as

$$C_{\text{extinction}} = C_{\text{absorption}} + C_{\text{scattering}}. \quad (2.76)$$

The extinction cross section of a spherical nanoparticles with radius R and dielectric function ε_m , mainly depends on polarizability, which in turn depends on the dielectric constant of the surrounding medium. In sensing and detection applications, the nanoparticle cross-extinction is used to design highly sensitive LSPR sensors. Changes in cross-extinction, such as those caused by the binding of target molecules to the nanoparticle surface, can be detected and quantified, enabling accurate detection of analytes in biological, environmental, or chemical samples.

2.4.1 Island film theory in the low coverage limit

The aim of this section is to study the optical properties of an array of metallic nanoparticles supported on a glass substrate. The thin island film model was used to calculate reflectance and transmittance of the metasurface composed by randomly distributed array of identical metallic sphere or oblate particles with the size smaller than light's wavelength supported on a glass substrate ($n_s = \sqrt{\varepsilon_s}$), and in contact with an ambient matrix medium ($n_a = \sqrt{\varepsilon_a}$), as shown in Figure 2.14.

The formalism, proposed by Bedeaux et al. [86], simplifies the complex interaction of electromagnetic fields within an inhomogeneous thin layer containing discrete islands by introducing a dividing surface and uses the concept of the excess fields—the difference between expected bulk fields and actual fields—to characterize surface properties. Boundary conditions at the interface are defined by excess polarization (non-magnetic materials are assumed) which is coupled to the electric field and the electric field displacement through constitutive relations.

Thus, the electromagnetic properties of the system can be described using four susceptibilities: γ , β , τ , and δ , where γ accounts for the surface polarization parallel to the interface

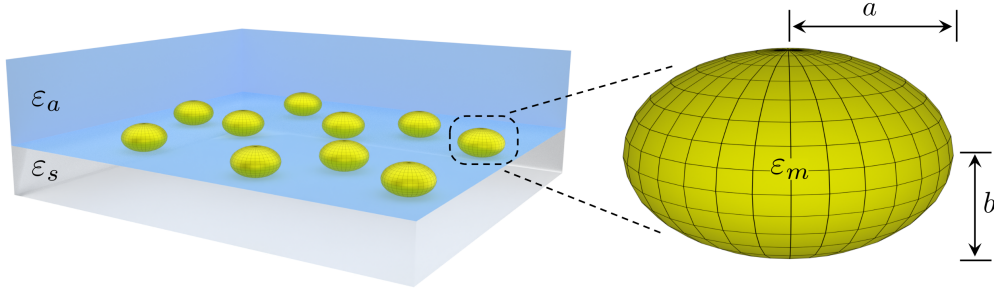


Figure 2.14: Schematic representation of the metasurface studied in this work. It is composed by a random array of Au NI, supported on a glass substrate with dielectric constant ϵ_s and in contact with an ambient matrix medium with dielectric constant ϵ_a . The nanoparticles are modelled as oblate spheroids, characterized by a major semi-axis a and minor semi-axis b

$\gamma = \rho\alpha_{||}$, while β relates to polarization perpendicular to it $\beta = \rho\alpha_{\perp}/\epsilon_s^2$. The terms τ and δ dive the quadrupolar order of the surface polarization parallel and normal to the interface, respectively. These expressions are valid for the case of identical non-interacting nanoparticles, i.e. in low coverage limit or small surface density, ρ . Using this approach, the modified Fresnel coefficients can be expressed as [86]

$$r_s = \frac{r_i e^{-i\zeta_+} [n_s \cos \theta_i - n_a \cos \theta_t + (\frac{\omega}{c})^2 I_\tau (n_s \cos \theta_i + n_a \cos \theta_t)]}{e^{-i\zeta_-} [n_s \cos \theta_i + n_a \cos \theta_t + (\frac{\omega}{c})^2 I_\tau (n_s \cos \theta_i + n_a \cos \theta_t)]}, \quad (2.77)$$

$$r_p = \frac{r_i e^{-i\zeta_+} [n_a \cos \theta_i - n_i \cos \theta_t - i(\frac{\omega n_s}{cn_a}) I_e \sin^2 \theta_i - (\frac{\omega}{c})^2 (I_\tau - I_\delta \epsilon_s \sin^2 \theta_i) \kappa_+]}{e^{-i\zeta_-} [n_a \cos \theta_i + n_i \cos \theta_t + i(\frac{\omega n_s}{cn_a}) I_e \sin^2 \theta_i - (\frac{\omega}{c})^2 (I_\tau - I_\delta \epsilon_s) \kappa_-]}, \quad (2.78)$$

where θ_i and θ_t are the angles of incidence and transmission, respectively, ω is the frequency of the incident light, c is the speed of light and I_τ , I_e , I_δ are invariants combinations of the surface electric susceptibilities γ , β and δ . The terms $\zeta_{\pm} = (\omega/c)(\gamma/(\epsilon_a - \epsilon_s))(n_s \cos \theta_i - n_a \cos \theta_t)$ and $\kappa_{\pm} = [n_a \cos \theta_i \pm n_s \cos \theta_t] [1 - (\omega^2/(4c^2))\epsilon_s \gamma \beta \sin^2 \theta_i]$ were introduced to reduce the notation.

For an array of oblate spheroids with semi-axes a and b , simplifications in Equation (2.77) and Equation (2.78) result in the following expressions [86, 87]

$$r_s = \frac{n_s \cos \theta_i - n_a \cos \theta_t + i(\omega/c)\gamma}{n_s \cos \theta_i + n_a \cos \theta_t - i(\omega/c)\gamma}, \quad (2.79)$$

$$r_p = \frac{\kappa_- - i(\omega/c)\gamma \cos \theta_i \cos \theta_t + i(\omega/c)n_s n_a \epsilon_s \beta \sin^2 \theta_i}{\kappa_+ - i(\omega/c)\gamma \cos \theta_i \cos \theta_t - i(\omega/c)n_s n_a \epsilon_s \beta \sin^2 \theta_i}. \quad (2.80)$$

Equation (2.79) and Equation (2.80) are reduced to the well-known Fresnel coefficients when the surface density of Au NI goes to zero (substrate-ambient interface). The choice of this shape was determined by the characteristics of the fabricated nanoparticles. Subsequently, the polarizability can be written as [88]

$$\alpha_{||,\perp} = \frac{4\pi a^2 b}{3} \frac{\epsilon_s (\epsilon_m - \epsilon_s)}{\epsilon_s + L_{||,\perp} (\epsilon_m - \epsilon_s)}, \quad (2.81)$$

where ε_m is the gold dielectric function. The depolarization factors L_{\parallel} and L_{\perp} are determined by the eccentricity of the oblate spheroids, $e = (a^2/b^2 - 1)^{-1/2}$, and they are given by

$$L_{\parallel} = l_{\parallel} + \frac{1}{2} (1 + e^2) \left(\frac{\varepsilon_s - \varepsilon_a}{\varepsilon_s + \varepsilon_a} \right) \left(e \arctan \left(\frac{1}{e} \right) - \left(e^2 + \frac{3}{2} \right) e^2 \ln \left(1 + \frac{1}{e^2} \right) + e^2 \right), \quad (2.82)$$

$$L_{\perp} = l_{\perp} + (1 + e^2) \left(\frac{\varepsilon_s - \varepsilon_a}{\varepsilon_s + \varepsilon_a} \right) \left(e \arctan \left(\frac{1}{e} \right) - \left(e^2 + \frac{3}{2} \right) e^2 \ln \left(1 + \frac{1}{e^2} \right) + e^2 \right), \quad (2.83)$$

with

$$\begin{aligned} l_{\perp} &= (1 + e^2)(1 - e \arctan(1/e)), \\ l_{\parallel} &= \frac{1}{2} (1 - l_{\perp}). \end{aligned} \quad (2.84)$$

In Equation (2.84), $l_{\parallel,\perp}$ denotes static depolarization factors [85] and the terms proportional to $(\varepsilon_s - \varepsilon_a)/(\varepsilon_s + \varepsilon_a)$ describes the interaction of dipole with its image charges in the substrate. For larger Au nanoparticles, the polarizability α_{\parallel} along the major semi-axis a is corrected using the MLWA theory. Then, the surface susceptibility is $\gamma = \rho \alpha_{\text{MLWA},\parallel}$.

2.5 Biosensors

A biosensor is an analytical tool that detects and responds to changes in biological systems to generate a measurable signal. The importance of biosensors is growing every day as it is necessary to monitor different variables with rapid detection time, high precision and with as small quantity of biological material as possible. Biosensors find applications in large fields such as healthcare, environmental science, agriculture, biotechnology, food safety and biomolecule detection in clinical diagnostics. Among the most important examples is the glucose sensor, which quantifies the glucose concentration in the blood as an electronic signal. An other example are pregnancy tests that detect the presence of human chorionic gonadotropin hormone in a woman's urine or blood. During the COVID-19 pandemic, Polymerase Chain Reaction (PCR) tests or antigen testing were widely used for the SARS-CoV-2 detection.

Despite the wide variety of biosensors, their core components typically comprise a bioreceptor, an analyte, a transducer and a device able to acquire, process and display the signal. In the following, we will review some alternative techniques for detecting biomolecular binding interaction, as well as a more detailed classification of the most used biosensors.

2.5.1 Other techniques for detection of biomolecular binding events

According to the focus of this thesis, in this section some detection techniques focused on viruses are presented.

The virus detection can be made by employing recognition units such as antibodies, enzymes, nucleic acids, and molecularly imprinted polymers to specifically target viral protein, genetic material, or the whole virus. The most used and effective way to detect the virus is the use of real-time PCR. This technique shows high sensitivity and specificity to detect small quantities of genetic material. Nevertheless, PCR is costly due to the price of

reagents, equipment and specialized training required to carry out the experiments. In addition, as observed during the 2019 pandemic of SARS-CoV-2, the PCR can provide results in a question of hours, in the best-case scenario.

Immunochemical assays are outstanding for being portable, easy to use, low-cost and show a short response time, making them suitable for clinical diagnosis. Immunoassays use antibodies to recognize the antigens.^[89] Antibody-antigen techniques can be used as a complementary tool to methods like PCR, since they may not be sensitive enough to detect low levels of virus in samples. Additionally, antibodies may cross-react with other antigens, which may generate false-positive or false-negative results.

Enzyme-Linked Immunosorbent Assay (ELISA) is an immunoassay technique widely used to detect the presence of specific antigens or antibodies in a biological sample. ELISA can be used to detect a wide range of antigens or antibodies, making it useful in a variety of biomedical and research applications with a specificity and sensitivity.^[90] ELISA disadvantages are the same as PCR, it requires special equipment, professional operators, the detection is slow, and the cost of the technique is high.

2.5.2 Classification of biosensors

Biosensors can be classified under different criteria, one of which is the nature of the biological components used for the detection. For example, enzymatic biosensor, immunosensors, aptamer-based biosensor, nucleic acid-based biosensors, microbial-based biosensors or whole-cell biosensors among others.

Another classification is based on the transducer used or the action principle. Based on this categorization, the main types of biosensors will be discussed in more detail below.

Electrochemical Biosensors. These biosensors are the most widely investigated and used biosensors whose operating principles rely on the electrochemical properties of the analyte and transducer. Electrochemical biosensors^[91] detect biological molecules through electrochemical reactions. They typically involve electrodes and measure changes in electrical properties, such as voltage, current, impedance or capacitance, resulting from biomolecular interactions. These biosensors exhibit high sensitivity, selectivity, and the capability of detection. However, some electrochemical sensors may experience degradation over time due to corrosion or accumulation of reaction products on the sensor surfaces. This can affect the long-term stability of the sensor and its lifetime. Additionally, due to the nature of the sensor, in many cases the samples are destroyed.

Piezoelectric Biosensors. The sample is subjected to a mechanical stress producing an electrical signal. Piezoelectric biosensors^[92] detect changes in mass or viscoelastic properties of a surface due to biomolecular interactions. They measure the change in resonant frequency or amplitude of a piezoelectric crystal.

Acoustic Biosensors. Acoustic biosensors^[93] measure changes in acoustic properties, such as frequency or velocity, resulting from biomolecular interactions. This type of sensors can be classified as a subgroup of piezoelectric sensors because piezoelectric materials are commonly used for sensor transducers. For acoustic wave propagation, the optimum resonant frequency is highly dependent on the physical dimensions and properties of the piezoelectric crystal.

Optical Biosensors. Optical biosensors^[21] utilize light to detect biological molecules. They may rely on principles such as SPR, LSPR, fluorescence or Raman scattering. They usually detect changes in the absorption, transmission, intensity, frequency, phase, or light polarization, in response to physical or chemical changes caused by biomolecular binding events. For example, the fluorescence biosensors are widely used in medical diagnosis, envi-

ronmental monitoring, and food quality assessment due to selectivity, sensitivity, and rapid response. The operational principle involves fluorescent molecules to detect biomolecular binding events. Upon binding, changes in fluorescence intensity, wavelength, or lifetime occur, allowing for sensitive detection of target molecules.

Among the optical biosensors, the colorimetric biosensors rely on changes in colour or absorption spectra to detect biomolecular interactions. They often involve indicators or nanoparticles that undergo a colour change upon binding to target molecules. Colorimetric sensors are usually simple to use and do not require expensive equipment or specialized techniques for operation. Furthermore, they can provide fast, real-time results, making them useful for applications that require continuous monitoring. Many colorimetric sensors are compact and portable, making them ideal for field applications or situations where mobility is needed.

Despite these notable advantages, colorimetric sensors can have limited sensitivity compared to more sensitive detection techniques such as spectroscopy. In some cases, colorimetric sensors may provide qualitative rather than quantitative results, which may limit their usefulness in applications requiring precise concentration measurements.

2.5.3 SPR based biosensors

Integration of nanotechnology with biosensors has shown the development path for the novel sensing mechanisms and biosensors as they enhance the performance and sensing ability of the currently used biosensors. The most extensively employed optical biosensors are those based on SPR phenomenon. Even though SPR and LSPR-based biosensors belong to the optical biosensors, they deserve a separate description because it is the basis of this work.

The SPR based biosensors detect local changes in the refractive index near a metal surface due to biomolecular binding. This change alters the resonance angle, wavelength or phase providing real-time information about biomolecular interactions. The main advantage of SPR sensors lies in their ability to detect biomolecular interactions in real time and without the need for fluorescent or colorimetric markers.

The high sensitivity and selectivity of SPR based biosensors allows accurate detection in a wide range of applications of biomolecular interactions, such as bacteria,^[94] human hepatitis B virus,^[95] Escherichia coli,^[96] pharmaceutical analysis,^[97] avian influenza A H7N9 virus,^[98] among others. Additionally, the commercial SPR base biosensor has been developed, Biacore is the most important brand in this field, however there are other commercial brands that also offer SPR based systems. Table 2.2 shows some examples of SPR based systems including their main parameters.

SPR-based biosensors offer numerous advantages for studying biomolecular interactions, yet they also present certain limitations. Commercial SPR systems are costly to acquire, operate, and maintain. Moreover, the cost of consumables like sensor chips and reagents can be substantial. Operating an SPR system requires trained personnel capable of both running the equipment and analysing the acquired data. Furthermore, despite advancements, SPR systems still tend to be bulky, impeding their use for portable clinical analysis of diagnosis. These factors collectively contribute for the low commercialization and use of SPR technology. Overall, while commercial SPR systems are powerful tools for studying biomolecular interactions that offers high control of the conditions of the experiment, low molecular mass detection or multiplexing detection.

Table 2.2: Commercial SPR based systems for biosensing with their principal operational parameters

Manufacturer	System	Performance
BIACORE	BIACORE 1K+	Refractive index range: 1.33 to 1.39 Analysis temperature: 25 °C to 37 °C Association rate constant: up to 3×10^9 M ⁻¹ s ⁻¹ for proteins Sample concentration \geq 1 pM Sample flow rate: 1 to 100 $\mu\text{L min}^{-1}$ Molecular weight detection: no lower limit for organic molecules
AMETEK Reichert	Reichert's SR7500DC	Refractive index range: 1.32 to 1.52 Analysis temperature: 10 °C below ambient to 70°C Refractive Index Resolution: 10 ⁻⁷ RIU Association constant: 10 ³ to 10 ⁷ M ⁻¹ s ⁻¹ Sample concentration: 1 mM to 1 pM Molecular weight detection limit: 100 Da
Bio-Rad Laboratories	ProteOn SPR 36	Analysis temperature: 15 °C to 40 °C Association constant: 3×10^3 - 3×10^6 M ⁻¹ s ⁻¹ Sample flow rate: 25 – 200 $\mu\text{L min}^{-1}$ Sample concentration > 10 pM Molecular mass detection limit: 95 Da
Nicoya	Alto	Analysis temperature: Off, 25 °C, 37 °C Association constant: up to 10 ⁹ M ⁻¹ s ⁻¹

2.5.4 LSPR based biosensors

LSPR based biosensors are a promising tool for the detection and characterization of biomolecules. Because the penetration depth of the evanescent field is of an order of tens of nanometres, the bioreceptor-analyte conjugation bound to the nanoparticles surface occupy a large portion of the field producing an improved LSPR signal. Unlike SPR based biosensors, a great variety of LSPR based biosensor can be designed, because the nanoparticle shape, size, and composition can be optimized. Their potential applications are found mainly in technology and science. Some examples of biomolecular detection include biotin-streptavidin system using Au spherical nanoparticle for detection, [99] antibody-antigen using Au nanorods, [100] avian influenza H5N1 using Au spike-like nanoparticle, [101] DNA using Au nanospheres, [102] RNA using Au nanoparticles, [103] among other pathogens.

To my knowledge, commercial technology has been not developed yet, however some research groups have developed platforms or lab-on-chips. For example, Suthanthiraraj, P.P.A and Sen, A.K. developed a biosensor that integrates a membrane-based blood-plasma separation to develop a lab-on-chip device to diagnosis dengue NS1 antigen in the whole blood. [104] Additionally, Ortega, M.A. et al. developed an organ-on-chip to monitor in situ the insulin secretion in pancreatic islets. [105]

One of the main reasons why LSPR technology has not been introduced into the industry is the low sensitivity for detecting changes in the bulk refractive index, as well as biomolecular interactions. In this direction, several research teams have explored different shapes of nanoparticles, metals or alloys, or integrating other sensor components to enhance the sensitivity of LSPR transducers.

Additionally, techniques for synthesizing ordered nanoparticle arrays with precise shape and size control are time-consuming and require costly equipment. Conversely, the synthesis of random arrays of nanoparticles requires a high degree of care in the fabrication parameters to achieve reproducible nanoparticles arrays.

Addressing these challenges is crucial to enhance the sensitivity and expanding the utilization of LSPR sensors in commercial applications.

2.5.5 Performance parameters of biosensors

Performance indicators and comparison between different biosensor technologies are quantified by the following characteristics and parameters. [14, 106, 107]

Refractive index sensitivity. The Refractive Index Sensitivity (RIS) refers to the capability of a biosensor to detect small changes in the refractive index of the medium surrounding the transducer. The RIS is defined as

$$\text{RIS} = \frac{\Delta X}{\Delta n}, \quad (2.85)$$

where ΔX is the change of sensing variable, it could be the resonance angle (θ_R), intensity (I), wavelength (λ) or phase (ϕ), according with the interrogation used. While Δn stands for the change of the refractive index of the sensor.

Figure 2.15 shows the principle of RIS measurements. In this case, the resonance angle for each reflectance spectrum produced by the surrounding medium is determined. Then, the RIS is calculated as $\text{RIS} = \frac{\Delta\theta_R}{\Delta n}$.

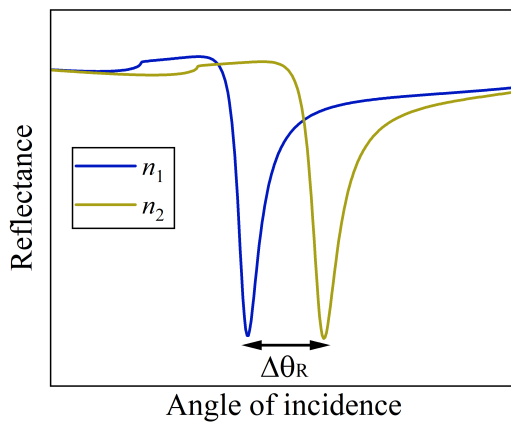


Figure 2.15: Reflectance of a SPR sensor when the metallic film is surrounded by a dielectric medium with refractive index n_1 (blue) and n_2 (gold). The resonance angle shift is due to a change in the refractive index of the ambient medium is represented by $\Delta\theta_R$

In biosensing applications, the sensitivity is also defined in terms of the number of molecules adsorbed on the transducer, this parameter is known as surface sensitivity and

its unit is expressed in terms of mass per area, typically pg mm^{-2} . The overall performance of a biosensor should be evaluated not only in terms of RIS but also in terms of robustness and reliability of the detection.

Refractive index resolution. The Refractive Index Resolution (RIR) refers to the smallest detectable change in refractive index that a measurement system or sensor can accurately discern. It is described by the expression

$$\text{RIR} = \frac{\sigma}{\text{RIS}}, \quad (2.86)$$

where σ stands for the standard deviation of noise in a measurement. A lower refractive index resolution means that the sensor can detect smaller changes in the refractive index of the sample.

In general terms, biosensors operate in different interrogation modes, then their RIS units are different, so that a direct comparison between them cannot be made. Consequently, the RIR becomes a fundamental parameter to evaluate the performance of biosensor because their units are refractive index units (RIU) regardless of the interrogation scheme.

Specificity. The Specificity (S) of a plasmonic biosensor refers to its capacity to detect a particular analyte among a mixture containing diverse materials. It is defined by

$$S = \frac{\Delta X}{\Delta C}, \quad (2.87)$$

where ΔC is the change in the analyte concentration.

Full width at half maximum. Besides the sensing parameters, the spectral response of the biosensors, especially for the SPR and LSPR based biosensors, must be quantified. The most important parameter is the Full Width at Half Maximum (FWHM), defined as the width of the plasmonic peak at half of its amplitude. A narrow plasmonic band facilitate the detection of minimum displacements of the peak position at resonance, while a wider plasmonic peak could introduce a higher inaccuracy in the detection of the sensed variable, typically the resonance angle or wavelength.

Figure 2.16 illustrates a reflectance spectrum where the width of a plasmonic peak is represented by the horizontal red line and it is quantified by the FWHM.

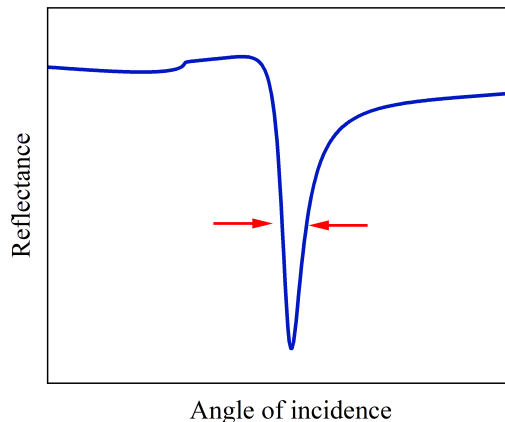


Figure 2.16: Full width at half maximum of a plasmonic dip

Figure of merit. The Figure Of Merit (FOM), also called the quality factor, combines the spectral width and the RIS. It is defined as the ratio of the RIS to the FWHM of the reflectance spectrum

$$\text{FOM} = \frac{\text{RIS}}{\text{FWHM}}. \quad (2.88)$$

The unit of the FOM is RIU⁻¹.

Limit of detection. The Limit Of Detection (LOD) is defined as the lowest concentration or amount of an analyte that can be reliably distinguished from the background noise of a measurement system. It represents the smallest quantity of analyte that can be detected with a certain level of confidence. In this work the 3σ criterion of the baseline noise is chosen. The LOD is given by

$$\text{LOD} = \frac{3\sigma}{\text{RIS}}. \quad (2.89)$$

Dynamic range. Dynamic range defines the range of analyte concentrations over which the biosensor can accurately measure and quantify the biosensor response. A wide dynamic range allows the biosensor to detect both low and high concentrations of analytes with precision.

Response Time. Response time indicates how quickly the biosensor can generate a measurable signal in response to changes in analyte concentration. A shorter response time allows for rapid detection and analysis of analytes.

2.5.6 Interrogation modes in plasmonic sensors

The detection of the SPR and LSPR signal include different detection modalities, also called interrogation modes, depending on the variable being monitored. [108]

The angular interrogation is the most common technique in SPR sensors, including those commercially available. In this interrogation, the plasmonic transducer is illuminated using a monochromatic source, such as laser. Subsequently, the prism coupler is gradually rotated, increasing the angle of incidence while simultaneously measuring the intensity of the reflected beam using a power detector or a Charge-Coupled Device (CCD). Figure 2.17a shows the typical response using the angular interrogation for measuring the SPR or LSPR signal. The dynamic range of this interrogation is limited to the angles of incidence, which ranges from normal incidence (0°) to grazing incidence ($\sim 90^\circ$).

Another widely employed approach is SPR imaging, where the intensity distribution obtained from the reflected beam is captured through a CCD camera. Unlike capturing the intensity of a single point in the sample, this method enables the acquisition of images across a large surface of the sensor.

In the intensity interrogation, or wavelength interrogation, the plasmonic transducer is illuminated with a polychromatic source, such as a stabilized with light source or a LED. The reflected or transmitted beam is captured by a spectrometer. Figure 2.17b illustrates the plasmonic response using the spectral interrogation, where the variable being monitored is the wavelength at the minimal reflectance. In addition, the dynamic range of a sensor under the spectral interrogation is limited by the width of the source spectrum.

Finally, the phase interrogation mode is based on the measurement of changes in the phase of light interacting with the transducer of the sensor. Phase measurements are typically achieved by using ellipsometry techniques, [109] however, interferometric methods can also be used. The typical response using this interrogation is showed in Figure 2.17c. The

phase interrogation mode is the one that shows the lowest RIR among the other interrogation modes. [110] However, its dynamic range is smaller than in the previous examples because it is limited by the linear region of the phase response, indicated by the green rectangle in Figure 2.17c.

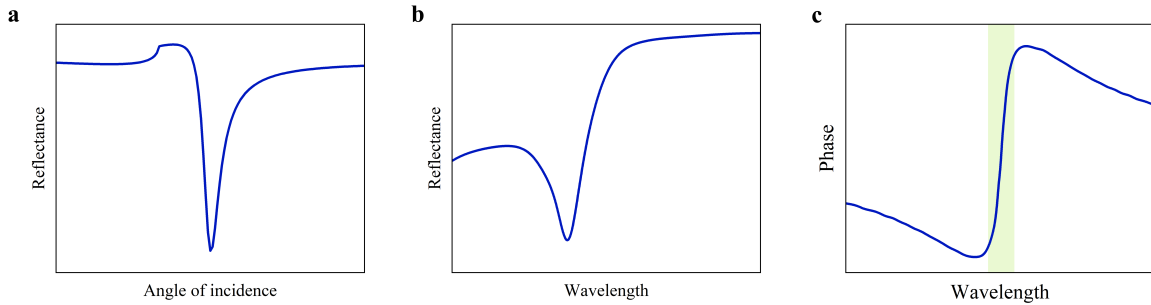


Figure 2.17: Methodologies for measuring the signal of a plasmonic sensor. **a.** Angular, **b.** intensity and **c.** phase interrogation modes. The dynamic range of a plasmonic sensor using phase interrogation is represented by the green rectangle in **c.**

Table 2.3 presents a summary of the key performance indicators, RIS and RIR, of SPR based biosensors operating in different methods such as intensity, angular, spectral and phase interrogation modes. These metrics underscore the detection capabilities of each interrogation mode and is useful for choosing the most appropriate approach based on the sensitivity requirements for a particular application.

Table 2.3: Typical RIS and RIR values of SPR based sensors in different interrogation modes. Data adapted from [110]

Interrogation scheme	Intensity	Angular	Wavelength	Phase
Typical RIS	$1.5 \times 10^4 \text{ \% RIU}^{-1}$	$200^\circ \text{ RIU}^{-1}$	10^4 nm RIU^{-1}	$10^5^\circ \text{ RIU}^{-1}$
Typical RIR	$1 \times 10^{-5} \text{ RIU}^{-1}$	$5 \times 10^{-7} \text{ RIU}^{-1}$	$1 \times 10^{-6} \text{ RIU}^{-1}$	$4 \times 10^{-8} \text{ RIU}^{-1}$

2.6 Literature Review

This section provides context of this research by reviewing the most relevant works related with the main topic of this dissertation, as well as identifying gaps and open questions. Specifically, this section focuses on the investigation of the performance parameters of plasmonic sensors using both approaches: thin metallic films and metasurfaces. Furthermore, the detection interrogations and techniques were also reviewed.

2.6.1 SPR-based biosensors

In the first approach, thin metallic films have been used in different studies over time. The research group of Liedberg, B. was the first to experimentally demonstrate the use of SPR for biosensing applications. [29] They used a thin metallic film to detect anaesthetic gas halothane. Subsequently, they use a silver film to successfully detect changes in the

resonance angle due to antigen-antibody human globulin binding events. As discussed in the previous subsection, the angular interrogation is the most used detection mode in the commercial systems. Tang, Y. et al. [111] presented a homemade SPR device for detecting rabbit antibody-antigen binding events through angular interrogation. However, their approach involves measuring the resonance angle only every 15 minutes, thereby limiting their ability to observe the kinetics of the binding interaction.

The wavelength interrogation is an alternative used to avoid this handicap because the signal is continuously measured. More recently, Sinha, R.K. [112] has detected cardiac marker proteins, cardiac troponin I (CTnI), and cardiac troponin T (CTnT), achieving a LOD of $0.03125 \text{ ng mL}^{-1}$ for CTnI and $0.0625 \text{ pg mL}^{-1}$.

Li, Y.C et al. [113] have demonstrated the detection of complementary oligonucleotides. The process involves the initial functionalization of the gold surface using 11 - mercaptoundecanoic acid, ethanolamine, and streptavidin to immobilize the bioreceptor oligonucleotide. Subsequently, the biotinylated oligonucleotide is immobilized due to the biotin-streptavidin binding, followed by the hybridization of the target oligonucleotide. The LOD achieved in this experiment is 0.5 pM.

Kabashin, V. and Nikitin, P.I. have demonstrated for the first time, the phase detection mode using a SPR system, based on an Au film for detecting refractive index changes due to the injection of Ar and N₂ above the Au film. They have found the LOD being of 4×10^{-8} RIU. [37] Later, Wu, S.Y. and coworkers used a Mach-Zender interferometric SPR system to detect refractive index changes due to variations of glycerine in water solutions. They used as transducer a silver/gold coating. The LOD obtained was 5.5×10^{-8} RIU. [114]

Monzon and Villatoro developed a fibre based SPR sensor by depositing a thin gold film on single-mode optical fibre. The transmission spectra show multiple interference peaks and they are sensible to the refractive index of the medium surrounding the gold film. By varying the refractive index using Cargille oils, they have experimentally found a RIR with value of 7×10^{-7} RIU. [115] In addition, Moayyed, H. et al. [98], has theoretically studied the performance of a fiber based SPR sensor using the transfer matrix theory for stratified optical media. The transducer was composed by a combination of a 50 nm thick silver inner layer with a dielectric titanium oxide layer, showing a resonance peak at approximately 1550 nm.

Although the SPR fibre sensors show a high-performance phase sensitivity the resonance wavelength is situated in the infrared region, where a conventional white lamp source cannot be used.

One area for improvement of SPR-based sensors is their cost. The high cost of purchasing and maintaining the equipment can limit accessibility for laboratories or institutions with limited budgets. In addition, SPR sensors require functional surfaces suitable for the immobilization of biomolecules or analytes of interest. The preparation of these surfaces can be complex and requires optimization for each specific application. Furthermore, the RIS, RIR and LOD should be yet improved.

2.6.2 LSPR-based biosensors

Subwavelength nanostructured transducers are a promising alternative to increase the LOD of pathogens binding events by tuning the characteristics of the nanoparticles array. In this approach, spectroscopy is the most used technique for sensing applications.

Hegde et al. [40] studied the refractometric sensing properties of three gold nanostructures (nanocubes, nanostars and nanorods) in aqueous solutions and immobilized in a glass

substrate. They used different glucose concentrations to modify the refractive index surrounding the nanoparticles achieving RIS values of 318 nm RIU^{-1} , 94.5 nm RIU^{-1} and $108.3 \text{ nm RIU}^{-1}$, for the respectively geometries.

Li, Q. et al. [116] characterized the RIS of Au nanobipyramids in a colloidal solution. They measured changes in extinction spectra due to changes in the refractive index of glycerol solutions, obtaining a RIS of 362 nm RIU^{-1} .

Larsson et al. [42] have investigated the RIS of Au nanorings by measuring the extinction spectra peak shift due to changes in concentrations of ethylene glycol solutions.

Other nanostructures with complicated shapes have been also studied, e.g. Song et al. [117] proposed an LSPR U-shaped fibre sensor composed of graphene oxide/triangular Ag nanoparticles. By measuring the transmission spectroscopy, they have shown a remarkable RIS of $1116.8 \text{ nm RIU}^{-1}$.

In addition to experimental studies, metasurfaces have been also analytically studied. Das, A. et al. [118] have theoretical and experimental studied the sensing properties of a metasurface composed by Au crossed-bowties, obtaining a RIS value of 1753 nm RIU^{-1} .

Phase-sensitive optical biosensing emerges as an alternative to angular or wavelength interrogation, offering an improvement in the RIS and unique optical properties of nanostructures. Li et al. [119] compared the RIR in both wavelength and phase detection methods. The metasurface used was composed by gold nanodisks and other composed by nanorods. They used a common path spectral interferometer to detect phase changes due to changes in glucose concentrations. The RIR found is $1.83 \times 10^{-6} \text{ RIU}$, which is two orders of magnitude higher sensing resolution than extinction spectra among the same nanostructures, at that time. Later, Li et al. [120] used a metasurface composed by X shaped nanoparticles. They change the refractive index of the surrounding medium using glucose concentrations. The RIR obtained is $1.15 \times 10^{-6} \text{ RIU}$, showing an improvement in the RIR of the value obtained in the aforementioned work.

Qui, G. et al. [121] have performed theoretical and experimental studies of sensing properties of a random gold nanoisland array using phase interrogation through a common path spectral interferometer. They obtained a RIR of $9.75 \times 10^{-8} \text{ RIU}$. Additionally, Qui, G. et al. [45] used a two-dimensional Au nanoislands array for detecting SARS-CoV-2 through functionalization and hybridization the transducer with complementary DNA chains. They used the plasmonic photothermal effect to increase hybridization temperature and improve the discrimination of similar sequences in a multigene mixture. This study highlights high sensitivity showing a low LOD of 0.22 pM .

As can be seen, many research groups have focused in improving the RIS of transducer composed of metasurfaces. Optimizing the shape of nanoparticles emerges as a straightforward method to enhance RIS. Nanostructures with peaks or spikes have shown improve RIS among other nanoparticle geometries. However, the extinction peak is typically observed in the near-infrared region, and the methods for fabricating these nanoparticles commonly involve electron beam lithography or nanoimprint techniques. [65–67] These techniques require specialized equipment such as high-power lasers, involve time-consuming and complex procedures, and are limited in patterning to a few μm^2 .

Dewetting is an alternative approach for fabricating random arrays of nanoparticles from thin films previously deposited on a glass substrate. Although the dewetting offers size control of the nanoparticles, it does not achieve the precision of electron beam lithography techniques. However, dewetting stands out as a cost-effective process and it can be potentially scaled for larger area production. These advantages position the dewetting technique as a promising option for fabricating random metasurfaces for LSPR-based sensors.

2.6.2.1 Topological darkness in metasurfaces

Topological darkness, firstly discussed by Kravets et al. [57], is a recent phenomenon observed in ordered metasurfaces which ensures nearly zero reflection or transmission of light. Along nearly zero reflection of incident light, topological darkness is also characterized by a phase singularity. High phase sensitive biosensing emerges as a significant application of topological darkness, benefiting from its distinctive phase behaviour at the point of darkness.

Experimental demonstration of topological darkness has been achieved employing periodic nanostructures manufactured via electron beam lithography. [44, 122, 123]

Kravets et al. [57] designed plasmonic metamaterials consisting of Au double-dots fabricated by e-lithography, covered by a graphene crystal layer, which exhibit topological darkness. By measuring the phase ellipsometry parameters, the authors detect binding events of streptavidin–biotin, achieving an impressive LOD on the order of 1 fg mm^{-2} . This sensitivity is approximately 1000 times higher than that achieved by plasmonic sensors based on conventional techniques.

Topological darkness has also been explored in other nanostructures like HMMs, [60] Transition Metal Dichalcogenides Monolayers (TMDCs), [124] three-dimensional plasmonic metamaterials using Ag-SiO₂ nanoparticles [44] have experimentally demonstrated the achievement of topological darkness in by constructing N layers of core-shell nanoparticles, Au nanorods [62] or Au nanodots, [58] among others.

Furthermore, Svedendahl et al. [125] investigated topological darkness with the associated phase flips in Au nanodisks under oblique incidence. Their experimental data, obtained using ellipsometry techniques under non-total internal reflection conditions, highlighted the potential of nanodisks for biosensing applications, specifically in detecting NeutrAvidin–Biotin binding events through wavelength interrogation.

In summary, topological darkness has been experimentally and analytically demonstrated in various ordered metamaterials, including metallic metasurfaces, as well as HMMs and TMDCs. The most used technique for fabricating these types of metamaterials is the electron beam lithography. While this technique is a powerful tool for fabricating nanoparticles with high precision, electron beam systems are costly and typically have a small writing field, representing a challenge for fabricating large areas of nanoparticles.

An alternative method for fabricating metallic metasurfaces is the dewetting technique, where nanoparticles are randomly self-assembled. However, the properties of random metasurfaces concerning topological darkness and phase singularity remain largely unexplored, demonstrating a gap in this field.

As previously discussed, metasurfaces exhibiting topological darkness demonstrate high sensitivity. Therefore, exploring these aspects holds promise for developing practical and scalable solutions in ultrasensitive optical biosensing utilizing the phenomenon of topological darkness in random metasurfaces.

Chapter 3 |

Materials and Methods

This chapter outlines the methodologies employed in the fabrication of biosensor's transducers, which encompass two distinct modalities. For SPR detection, the transducer features an Au NF, whereas for LSPR detection, it comprises an array of Au NI randomly dispersed on a glass substrate. This section delves into the comprehensive optical and morphological characterization of the Au NI.

This section also describes the various experimental setups utilized for the plasmonic characterization of the transducers, including detailed explanations of the equipment used for both SPR and LSPR detection. Additionally, it provides detailed insights into the experimental setups employed for the calibration and sensitive detection of molecular samples.

Finally, a description is given for the preparation procedures associated with the sensing samples, including the polyelectrolytes LbL system, streptavidin-biotin system and the conjugation of complementary oligonucleotides of SARS-CoV-2.

3.1 Fabrication of transducers

The biosensor transducers were fabricated through the deposition of thin gold films onto corning glass 2947N substrates, chosen for their accessibility and cost. Initially, the substrates were cut into approximately 2.5 cm × 2.5 cm pieces and carefully cleaned. The cleaning process involved immersing the substrates in an ultrasonic bath (Bransonic 3510R-MT) with acetone, followed by a second ultrasonic bath using isopropanol for thorough cleaning. Subsequently, the substrates were rinsed with deionized water and dried using a centrifuge machine.

The metal deposition on the glass substrates was performed through the magnetron sputtering technique. Figure 3.1 illustrates the working principle of this technique, involving the creation of plasma, which is a gas that has been ionized, and then using the plasma to bombard the target material within a vacuum chamber. This bombardment causes atoms from the target material to be ejected or sputtered, and these atoms then travel across the vacuum chamber and gradually condense on the substrate surface, forming a thin film. Notable advantages of this technique include good reproducibility in sample thickness, high deposition rates, surface uniformity in the film, and the production of high-purity films.

3.1.1 Fabrication of Au NF

In this study, the DCXS-750-4 Aja International DC magnetron sputtering system for depositing gold onto glass substrates was used. The ultra-high purity gold target possesses

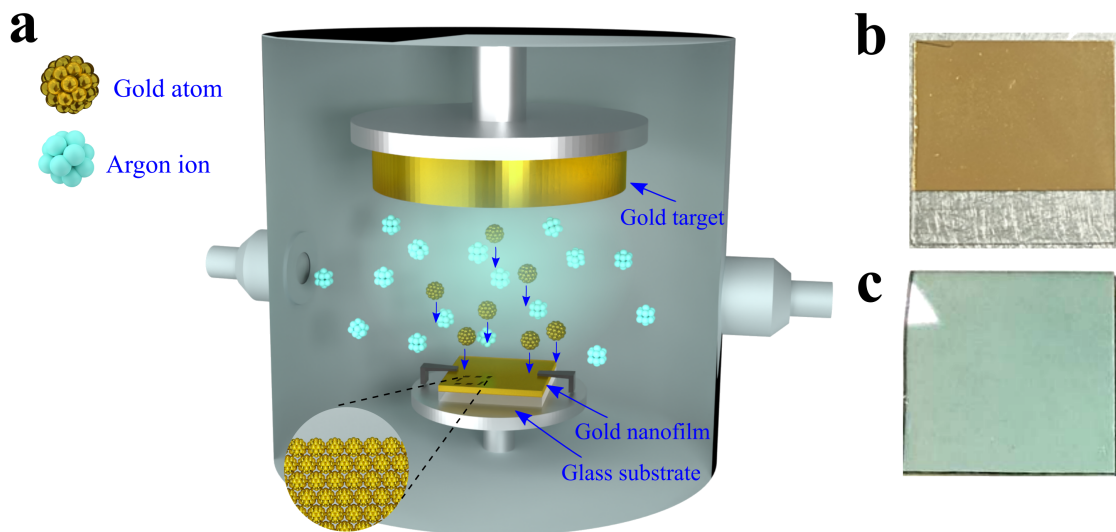


Figure 3.1: a. Schematic illustration of magnetron sputtering deposition of a Au NF onto a glass substrate. A high-purity gold target is bombarded by argon ions generated by a magnetron cathode. The impact sputters gold atoms, which travel across the plasma and deposit onto the glass substrate, forming a thin Au NF. Photograph of an Au NF with thickness of approximately b. 50 nm and c. 11 nm

purity of 99.99 %.

The adhesion of gold to non-metallic surfaces is not good, including glass, but that of titanium to glass is stronger. For this reason, a very thin film, approximately 1 nm, of titanium was firstly deposited on the glass surface. Then, the thin gold film is deposited on the top of the titanium film. The thickness of the gold films deposited onto the surface of the glass substrate was determined by the sputtering operation time. The system demonstrated a deposition rate of 0.2 nm s^{-1} . Consequently, to achieve an Au NF with thickness of 50 nm, the sputtering system needed to operate for 250 seconds. Figure 3.1b shows a photograph of obtained Au NF with thickness of 50 nm. To measure the reference reflectance of a blank substrate and prevent gold deposition at one end of the substrate, a sticker was initially placed and later removed to leave a blank reference.

3.1.2 Fabrication of Au NI

Nanoparticles synthesis is mainly divided into two approaches: bottom-up and top-down methods. [126] In the bottom-up approach, the synthesis of metallic nanoparticles involves the fabrication of nanomaterials from precursor atoms or molecules, typically in gaseous or liquid state, that come together to the formation of desired nanostructures, atom-by-atom, or molecule-by-molecule.

On the other hand, the top-down method involves reducing bulk materials into small particles through chemical or physical methods like micropatterning, laser ablation, chemical or physical vapor deposition. Lithography is a widely used technique to create ordered metallic nanoparticle arrays by imprinting a resist onto a substrate and then depositing metal on top. This method allows for the controlled manipulation of nanoparticle size, shape, and distribution.

The solid-state dewetting technique is a method where a thin film is deposited onto a substrate, typically silicon or glass. Controlled thermal annealing subsequently causes the

thin film to break, resulting in the formation of distinct Au NI. The efficiency of this method mainly depends on factors such as the film thickness, substrate type, annealing duration, and temperature, which critically influences the final characteristics of the Au NI, including size, shape, and spacing. Solid-state dewetting stands out for its ability to produce nanoparticles with well-defined properties, offering tuneable and reproducible samples. [68, 127]

In order to investigate the plasmonic properties of Au NI in relation to their size, Au NF with varying initial nominal thicknesses, ranging from 3 nm to 17 nm in increments of 2 nm, were deposited onto the surface of Corning glass 2947N substrates using the magnetron sputtering technique. Subsequently, all the samples underwent a thermal treatment at 550°C for a duration of 3 hours in the Caisa DTT434 oven. The glass transition temperature of the substrate was determined to be 530°C by placing the substrates with mechanical loads at various temperatures and finding the temperature when the substrate softened. Consequently, at the annealing temperature used in the fabrication process, the Au NI became partially embedded in the substrate, enhancing the mechanical stability of the metasurface. Figure 3.2 presents a photograph of the obtained arrays of Au NI, distinctly labelled with their respective initial nominal thicknesses.

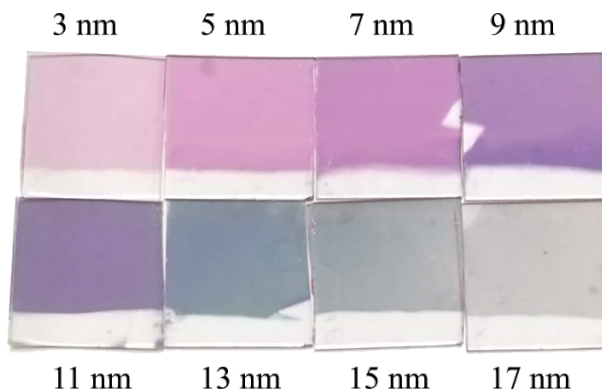


Figure 3.2: Au NI arrays fabricated from different Au NF initial nominal thickness, ranging from 3 nm to 17 nm in steps of 2 nm. Then subjected to a thermal treatment of 550°C for 3 hours

Both Au NF and Au NI types of transducers were fabricated by MSc Guerra-Hernández, S.F and MSc Gazga-Gurrión, I. A more detailed description of the fabrication of both types of transducers are available in their thesis.[128, 129]

3.2 Morphological and optical characterization of Au NI

Characterizing Au NI is fundamental for comprehending their optical and plasmonic properties in relation to key features such as size, shape, surface coverage and the degree of embedding into the substrate contribute significantly to the overall understanding of Au NI arrays. For this reason, the characterization of the Au NI is divided into a morphological and optical characterization.

3.2.1 Scanning Electron Microscopy

Scanning Electron Microscopy (SEM) is a powerful technique for acquiring high-resolution images that reveal the morphological characteristics of a sample, ranging from the micrometre to the nanometre scale. In this method, an electron gun vertically bombards the sample,

leading to multiple interactions such as the generation of backscattered electrons and secondary electron emission. The primary detector focuses on collecting secondary emission electrons, which play a key role in imaging the surface of the sample. Moreover, SEM can produce topographic images based on the detection of backscattered electrons. [130]

The samples studied in this work are composed by conductive metals, thus the samples do not require preparation before being analysed. The SEM images were processed and analysed with an open-source software (Gwyddion) to extract key parameters of the Au NI array, such as the nanoparticle shape, size distribution, and the surface coverage. Figure 3.3 presents an obtained SEM micrograph using the FEI Scios Dual-Beam microscope.

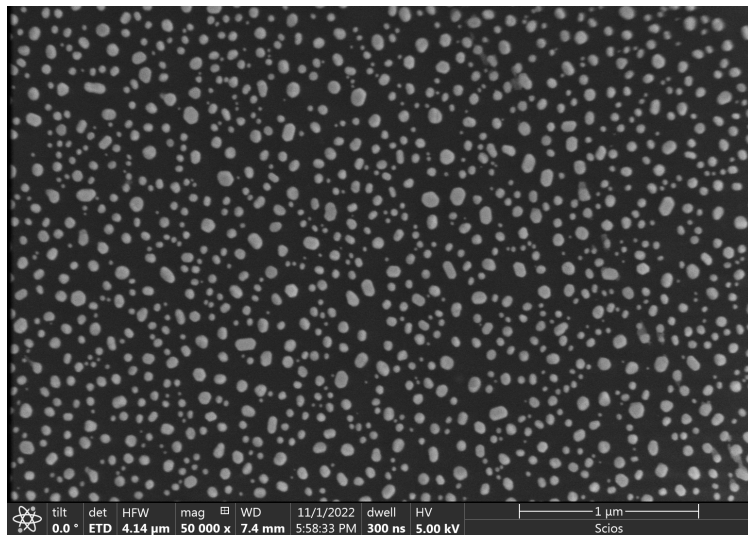


Figure 3.3: Representative SEM micrograph of self-assembled Au NI monolayer

3.2.2 Atomic Force Microscopy

Atomic Force Microscopy (AFM) is a powerful technique that allows us to image and analyse surfaces at the atomic level. Unlike traditional optical microscopes limited by diffraction, AFM can provide stunningly detailed images with resolutions over 1,000 times better, delving into the realm of individual atoms and molecules. AFM operates by establishing interactions between a sharp tip and the atoms on the sample surface. This tip is affixed to a large, flexible cantilever that moves across the samples. A monitoring laser beam is directed onto the cantilever and reflected onto a position-sensitive detector. As the cantilever reacts to the surface roughness of the sample, the photodetector registers changes in position of the laser beam. The collected signal enables the generation of a 3D map or topographical image of the sample surface. AFM is not limited to just imaging. It can also reveal various material properties, encompassing friction, adhesion, and viscoelastic forces. [131]

AFM operates in various modes, including:

Contact mode: The tip physically touches the surface, suitable for hard materials.

Non-contact mode: The tip vibrates slightly above the surface, ideal for soft materials or minimizing tip-sample interaction.

Tapping mode: The tip intermittently touches the surface, useful for fragile samples or imaging high-aspect-ratio structures.

Force spectroscopy: Measures the interaction force between the tip and the sample, providing insights into adhesion, elasticity, and other properties.

Both SEM and AFM techniques offer the advantage of providing detailed imaging at significantly higher magnifications compared to optical microscopy. Moreover, these techniques are non-destructive and minimally invasive in nature.

The topographic characteristics of the Au NI were acquired using the NT-MDT NTEGRA Probe AFM microscope in the semi-contact mode. Additionally, to assess the degree of embedding of the Au NI into the glass substrate, Au NI were removed from the substrate by immersing the substrate into a mixture of hydrochloric acid and nitric acid, with ratio of 3:1, commonly referred as aqua regia. The substrates were immersed for 10 minutes followed by a carefully rinsing with deionized water.

Analogous to the analysis of SEM micrographs, the AFM images underwent processing using Gwyddion software to obtain the morphology and the depth of craters. Figure 3.4a illustrates the height of the Au NI above the substrate, while in Figure 3.4b some sinkholes in the substrate can be observed, confirming the partial embedding of the Au NI into the substrate.

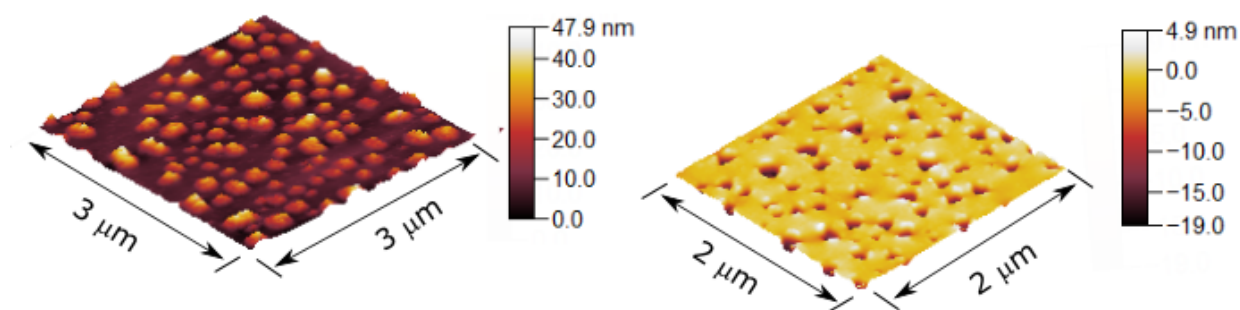


Figure 3.4: Representative AFM images of Au NI **a.** height and **b.** craters

3.2.3 Optical spectroscopy

The interaction between electromagnetic waves and matter occurs through various mechanisms, wherein light can be transmitted, absorbed, scattered, or reflected by a material. Optical spectroscopy plays a crucial role in quantifying these interactions, measuring the transmittance, reflectance, or extinction spectra of a sample. This technique is non-invasive and notably simpler than the aforementioned techniques, as it does not necessitate sophisticated equipment. However, it does not provide quantitative information about nanostructures. Despite this limitation, it serves as an excellent complementary tool to SEM and AFM techniques.

Optical spectroscopy measurements in this study utilized the Thorlabs SLS201L stabilized lamps as the light source with a broad spectrum (ranging from 400 nm to 1000 nm). The incident beam interacts with the sample, and the resulting outgoing beam is captured by the Ocean Optics HR4000 spectrometer. Figure 3.5 illustrates a schematic representation of the experimental setup for measuring the extinction spectrum of an Au NI array under normal incidence.

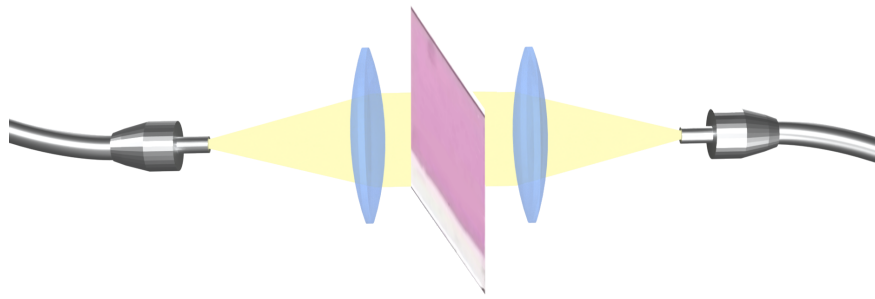


Figure 3.5: Experimental setup for measuring the extinction spectrum of an Au NI array under normal incidence

3.3 Microfluidic device fabrication

Due to the hydrophobic nature of the nanoparticle-composed chip surface, it is essential to confine the surrounding medium onto the Au NI for precise control over reflectance and sensitivity measurements.

In the field of microfluidics, the manipulation of small volumes, typically in the range of mL or μL , requires controlled procedures within minute cavities or microchannels. Polydimethylsiloxane (PDMS), a widely used polymer, is chosen for fabricating microfluidic devices due to its favourable properties. PDMS, being optically transparent, facilitates real-time visualization and analysis of fluids and particles within microfluidic devices. This property is especially valuable for applications such as microscopy and fluorescence-based assays. Additionally, PDMS is non-toxic and chemically inert, rendering it compatible with various biological and biomedical applications. Unlike other materials used in microfluidics such as glass, PDMS offers flexibility, simplifying the fabrication of devices with intricate designs. This flexibility is particularly crucial for effective sealing and bonding to surfaces, such as a glass substrate. PDMS proves relatively easy to work, it can be shaped using a master mold typically fabricated by soft lithography techniques. Its adaptability to diverse shapes and sizes makes PDMS suitable for various microfluidic designs and applications.

The detailed fabrication process of the microfluidic devices employed in this study is outlined below.

The microfluidic device design comprises a square chamber each side measuring 1 cm with a height of 160 μm . The master mold is created by gluing coverslips to a glass petri dish, with the dimensions specified earlier. The PDMS SYLGARD 182 elastomer kit is prepared by blending the base and curing agents at a ratio of 10:1. The resulting mixture is then degassed using a vacuum pump until all bubbles are removed. Subsequently, the PDMS is poured into the master mold and promptly cured in an oven at 85°C for 1.5 hours. Following this, the PDMS is carefully peeled off from the master mold and cut into squares, each side measuring approximately 1.7 cm.

The inlet and outlet channels leading to the microfluidic device chamber are established by drilling the chamber using a 2 mm diameter hole puncher. Subsequently, the PDMS-based devices undergo a cleaning process, which includes immersion in acetone and isopropyl alcohol, followed by a 3 minute soak in an ultrasonic water bath. After this, they are dried with compressed air and carefully stored in a protective box to shield against potential contamination, such as dust.

The bonding between the PDMS microfluidic device and the substrate is achieved through an oxygen plasma treatment using the BD-10AS system. Both the PDMS and

the glass substrate surfaces undergo a one-minute plasma treatment separately. The duration of the plasma treatment is critical for effective bonding. If it is too short, the surfaces remain unaffected, and with a prolonged treatment, the surfaces become rougher, compromising the bonding properties. Immediately following the plasma treatment, the PDMS device and the glass substrate are lightly pressed against each other for a few seconds, and to ensure correct bonding of the two surfaces. Heating the device at 80-90°C during 15 min-30 min on a hot plate is advisable for achieving an enhanced bonding quality between the PDMS device and glass substrate. After cooling the chip to room temperature, plastic tubes with a 2 mm diameter are incorporated into the channels of the microfluidic device, rendering the chip ready for use. Figure 3.6 shows a schematic illustration of the microfluidic device fabrication process employed in this study.

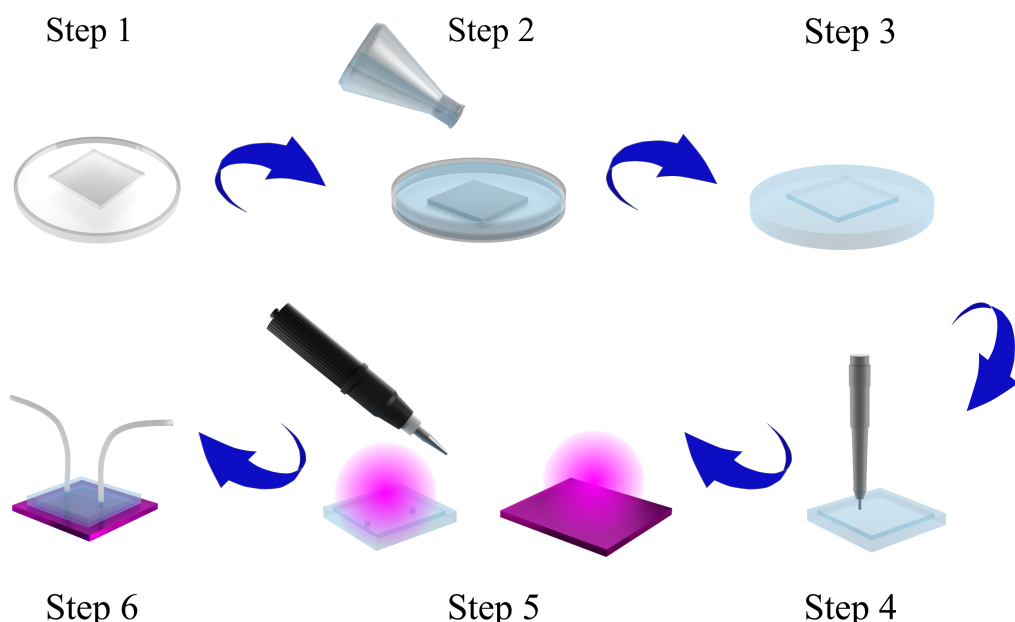


Figure 3.6: Step by step scheme of the microfluidic device fabrication using PDMS polymer

For calibration of the transducers, a microfluidic device with a simple design suffices. It comprises a PDMS square of approximately 1.2 cm × 1.2 cm, featuring a central hole with a radius of approximately 0.4 cm. The PDMS mixture is poured directly into a petri dish, and the Steps from 3 to 5 are repeated. Drilling of the microfluidic device is executed using a clamp-type drill. A photograph of both microfluidic devices is displayed in Figure 3.7.

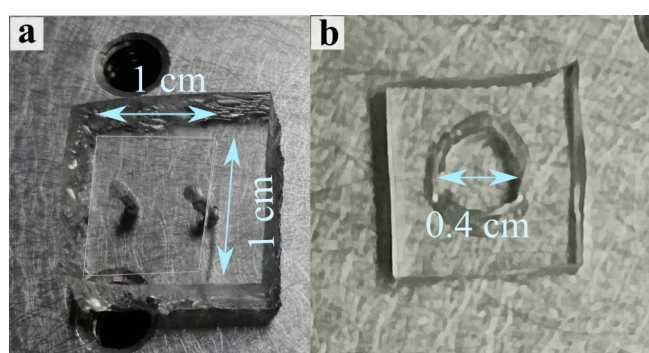


Figure 3.7: Photograph of microfluidic device for **a.** detection of binding events experiments and for **b.** calibration of transducers

3.4 Experimental setup

3.4.1 Kretschmann configuration in phase interrogation mode

A common-path spectral interferometer [121, 132] was implemented to measure the phase shift induced by LSPR. Figure 3.8 shows a schematic diagram of the experimental configuration.

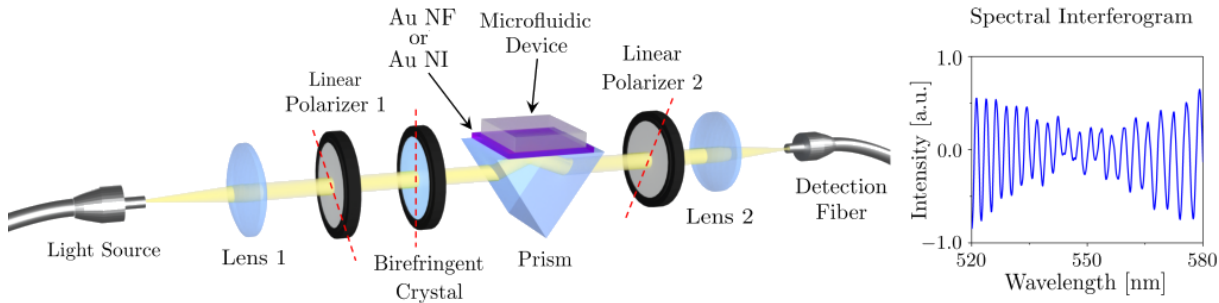


Figure 3.8: a. Optical configuration of the common path spectral interferometer. The red-dash line represents the optical axis of birefringent crystal and the transmission axis of the linear polarizers. b. The typical response of the experimental setup is a spectral interferogram, which exhibits SPR or LSPR-induced phase changes occurring at approximately 550 nm wavelength

A fibre-coupled halogen lamp with a broad spectrum ranging from 400 nm to 1000 nm, was used as the Light Source. The white light beam was collimated by Lens 1 and then linearly polarized by the Linear Polarizer 1 with a transmission axis positioned at 45° to vertical direction. A Birefringent Crystal (undoped Yttrium orthovanadate, YVO₄) with its optical axis oriented at 45° with respect to Linear Polarizer 1, was used to introduce a phase shift between the *s* and *p* polarization components. The dependence of the refractive index on the incident wavelength of the YVO₄ was obtained from the Sellmeier equation, as shown in Figure 3.9.

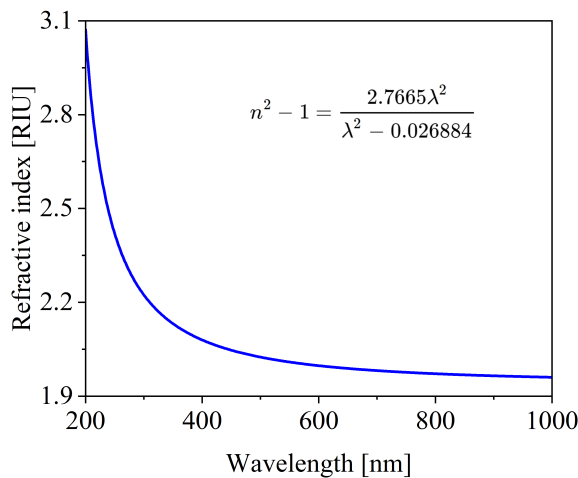


Figure 3.9: Dispersion relation of the YVO₄ obtained from the Sellmeier equation

To reach ATR conditions, a BK7 right angle Prism was used to couple the evanescent field to the SPR or LSPR. The transducer is placed on the top of the Prism and to avoid

an air gap between them, immersion oil (Leitz, $n = 1.5180$) is placed on the top surface of the Prism.

To enable the interference of the two orthogonal linearly polarized beams, the transmission axis of the Linear Polarizer 2, was crossed with respect to Linear Polarizer 1. The transmitted beam after passing through the Linear Polarizer 2, was collected by a Lens 2 and then coupled to the Detection Fiber to the UV-vis spectrometer. To extract the phase information from the spectral interferogram, a custom LabVIEW-based interface was implemented using the Fourier series method. Basically, the acquired spectral interferogram, denoted as $I(\lambda)$, can be mathematically described by a periodic function. This function is expanded in a sine and cosine Fourier series. Additionally, $I(\lambda)$ is centred with respect to the horizontal axis, as shown in Figure 3.8. Consequently, the phase is retrieved as follows

$$\phi(\lambda) = \arctan \left(\frac{Im[I(\lambda)]}{Re[I(\lambda)]} \right). \quad (3.1)$$

The phase retrieval involves the calculation of 150 terms within the expansion series, so this process does not represent a significant computational time.

The interface allowed real time monitoring of the differential LSPR or SPR phase response of the Au NF metasurface or Au NI, respectively. The signal processing for noise reduction was performed using Savitzky–Golay filtering [133] and averaging over twenty points acquired. In essence, the Savitzky–Golay filter entails a local fitting of a signal using a polynomial function of n-th order. The parameters used for filtering are the polynomial order and the side points of the local window.

3.4.2 Kretschmann configuration

The experimental setup mentioned above can be easily adjusted for intensity interrogation mode (Figure 3.10) by removing the Birefringent Crystal and the Linear Polarizer 2. This modification allows for the measurement of the reflectance spectra for both p and s polarization components using the same setup, where polarization change is accomplished by rotating the Linear Polarizer 1.

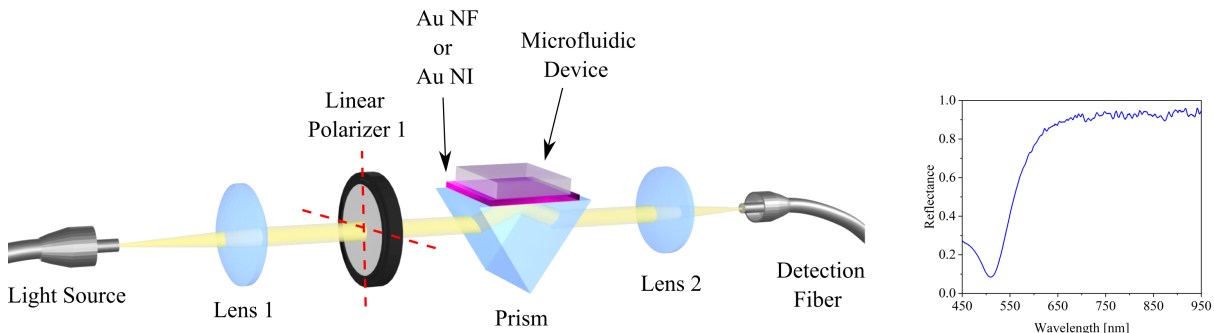


Figure 3.10: a. Optical configuration of the Kretschmann configuration in intensity mode. The red-dash line represents the transmission axis of the linear polarizer. b. The typical response of the experimental setup is a reflectance spectrum of the transducer where a plasmonic dip is observed at the resonance wavelength, with a value of approximately 530 nm

3.5 LabVIEW interface

The acquisition, processing, and display of the optical system signal are executed through a custom LabVIEW 2020 interface. Two distinct interfaces were designed and programmed based on the biosensor's interrogation mode, either wavelength or phase detection mode.

In Figure 3.11, a screenshot of the LabVIEW interface for the wavelength interrogation mode is presented. The most important elements of the interface are highlighted by regions I to V with yellow circles. Window I display the signal acquired directly from the spectrometer. Following this, windows II and III exhibit the calculated reflectance for the *p* and *s* polarization components, respectively. First, to diminish the noise from external light sources, a dark spectrum denoted as S_{dark} , is acquired by blocking the path of the light source and pressing “Store Dark”. Subsequently, a reference spectrum, S_{ref} , is captured with the light source directed at a blank region of the substrate. The reference spectrum must be taken for each polarization component, and it is saved using the buttons “Save Reference *P*” and “Save Reference *S*” for the *p* and *s* polarization component, respectively. The reflectance spectrum of the sample, S_{sample} , is then calculated as follows

$$R_{s,p} = \frac{S_{\text{sample}} - S_{\text{dark}}}{S_{\text{ref}} - S_{\text{dark}}}. \quad (3.2)$$

The Linear Polarizer 1 must be rotated 90° to obtain the reflectance spectrum of each polarization component. For smoothing these graphs, the Savitzky-Golay filter was applied. After experimental observation, it was determined that the optimal parameters for filtering are the polynomial order with value of 1 and the side points of the local window with value of 45. For noisy signal, the side points value must be increased.

The second section of the interface is designed for sensing applications. In the intensity interrogation, determining the position of the plasmonic dip is essential for each polarization component. The process involves delimiting the graph some points around the minimum in graphs of windows II and III, followed by a second-order polynomial regression. This method was chosen for its effectiveness over alternatives like direct determination of the minimum, centroid calculation, among others.

Windows IV and V display real-time monitoring of the SPR or LSPR wavelength for the *p* and *s* polarizations, respectively, under refractive index variations of the surrounding medium. To smooth the sensogram, twenty consecutive resonance wavelengths are averaged. The acquisition time for each point is 0.36 seconds.

Finally, the sensogram under *p* and *s* polarization illumination is saved by pressing the button “Save Sensogram *P*” and “Save Sensogram *S*”, respectively.

The second interface developed is designed for the phase interrogation mode, as depicted in Figure 3.12. Similar to the previous interface, key elements are highlighted by regions I to VII, marked with green circles. The windows marked with circles from I to VI correspond to acquisition data from the spectrometer and signal processing. A brief description of these windows is provided below:

- Window I: Signal obtained from the spectrometer.
- Window II: Calculated reflectance of the spectral interferogram.
- Window III: Spectral differential phase.
- Window IV: Derivative of the differential phase.

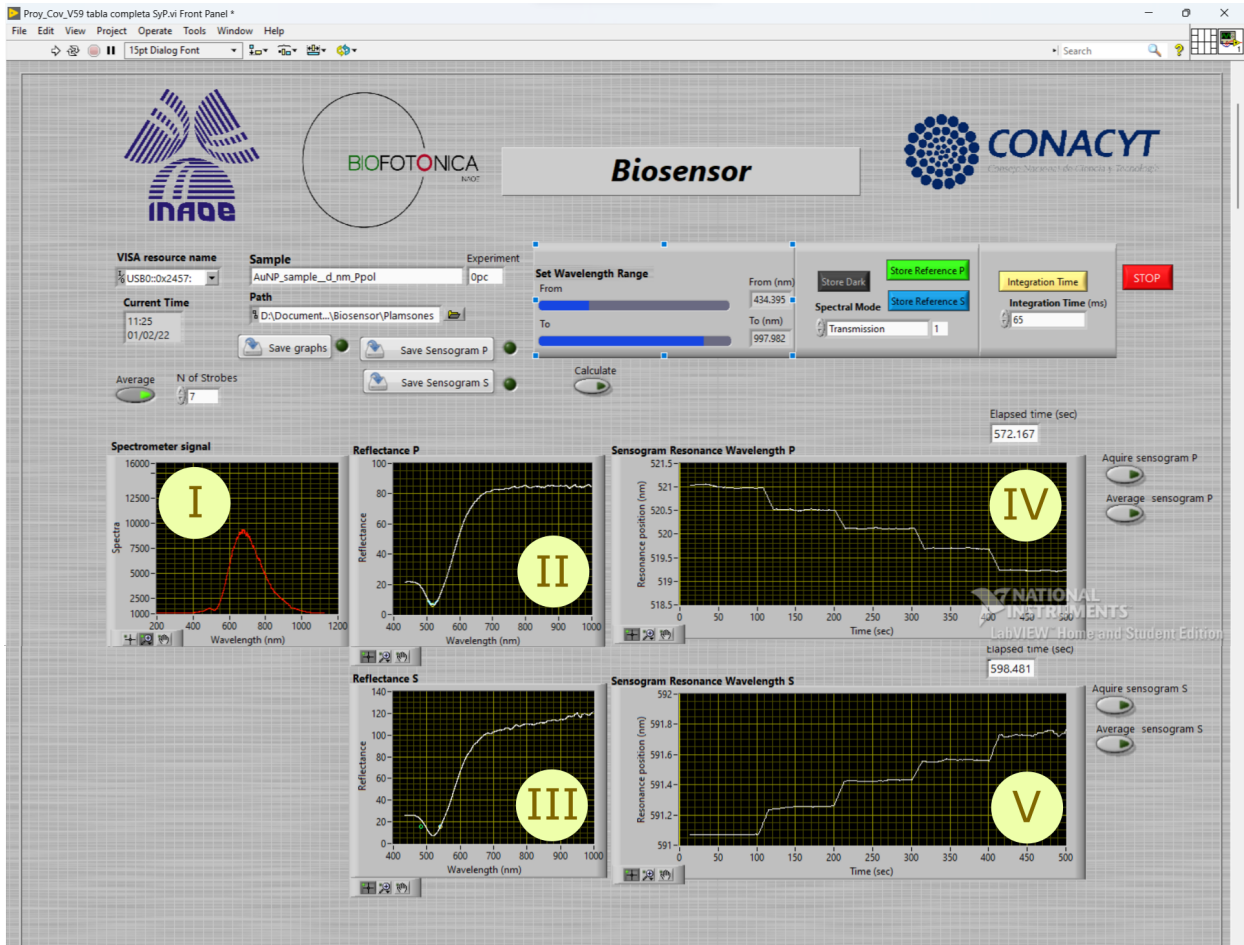


Figure 3.11: Screenshot of custom LabVIEW interface for the intensity interrogation mode

The intensity of the spectral interferogram, $I(\lambda)$, is periodic signal which can be represented as a linear combination of sines and cosines. Therefore, the Fourier series expansion of the spectral interferogram is

$$I(\lambda) = \frac{a_0}{2} + \sum_{n=1}^N \left(a_n \cos \left(\frac{n\pi\lambda}{L} \right) + b_n \sin \left(\frac{n\pi\lambda}{L} \right) \right), \quad (3.3)$$

where a_n and b_n are the Fourier cosine and sine coefficient, respectively, L is the period and λ the spatial coordinate. N stands for the number of terms expanded in the series. It was experimentally determined that 150 terms are sufficient to satisfactorily reconstruct the signal. Therefore, the phase is retrieved as

$$\phi(\lambda) = \arctan \left(\frac{a_n}{b_n} \right). \quad (3.4)$$

Following a straightforward procedure, the phase is unwrapped. The differential phase, shown in Window III of Figure 3.12, is calculated as the difference between the phase reference and the phase induced by the SPR or LSPR transducer.

By deriving the differential phase, the graph in Window IV of Figure 3.12 is obtained. From this graph, three key parameters of the spectral interferogram at resonance can be extracted. Firstly, the peak's position indicates the resonance wavelength. Secondly, the phase at resonance aligns with the maximum steepness of the linear region in the differential

phase. Thirdly, a novel detection scheme is proposed, involving the monitoring of the magnitude of the steepness in the linear region of the differential phase, specifically, the amplitude of the differential phase derivative. Both the differential phase and its derivative are smoothed using the Savitzky-Golay filtering.

Windows V to VII display real-time monitoring of the SPR or LSPR response using the resonance wavelength, differential phase, and its derivative, respectively. In summary, a brief description of the sensing aspect of the interface is provided below:

- Window V: Sensogram of the resonance wavelength.
- Window VI: Sensogram of the resonance differential phase.
- Window VII: Sensogram of the differential phase derivative at resonance.

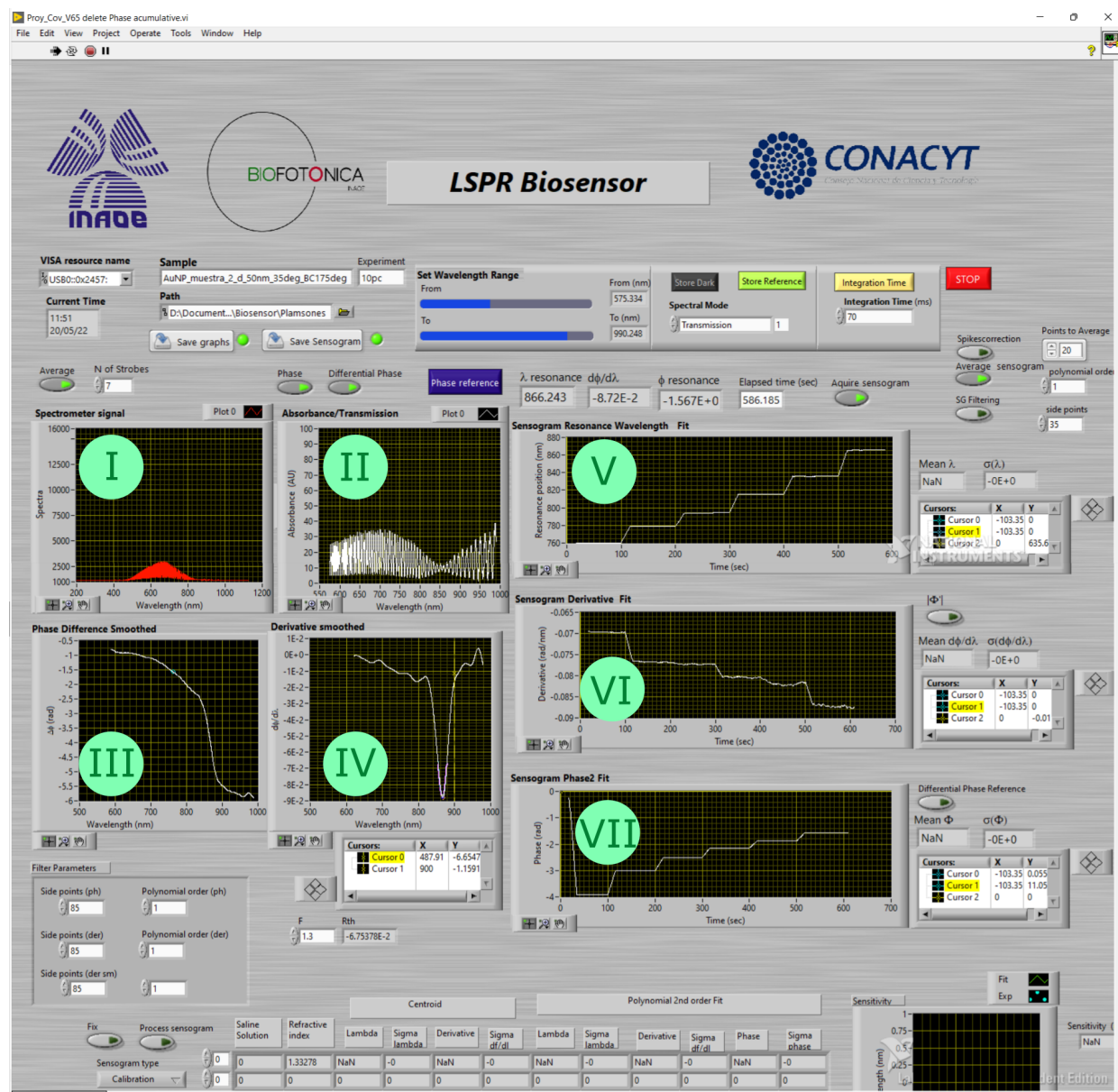


Figure 3.12: Custom LabVIEW interface for the phase interrogation mode

3.6 Bulk RIS and RIR measurements

To calibrate the transducer and determine the performance of the SPR or LSPR-based sensor, both RIS and RIR were determined for both intensity and phase detection schemes, using Equation (2.85) and Equation (2.86), respectively. The RIS was measured by evaluating the SPR or LSPR response shift in intensity or phase interrogation mode due to changes in the refractive index of the surrounding media the transducer. Variations in the refractive index of the surrounding media were achieved by adjusting the salt concentrations in sodium chloride (NaCl) solutions, as detailed in Section 3.7.1. The microfluidic device depicted in Figure 3.7a was used for the transducer calibration. The introduction and removal of water or NaCl solutions onto the Au NI surface were conducted using a micropipette.

After determining the RIS and in accordance with the RIR definition [Equation (2.86)], the standard deviation of the SPR and LSPR system must be established. To evaluate the standard deviation for the three detection modes (wavelength, phase, and phase derivative), continuous recording of the SPR or LSPR signals was conducted for some minutes while the microfluidic device was filled with only water. Subsequently, the acquired data underwent processing, enabling the determination of both the mean value and the standard deviation. In the intensity interrogation mode, the analysis shows a wavelength standard deviation of 4.2×10^{-3} nm, while for the phase interrogation mode, the analysis yielded a wavelength standard deviation of 3.3×10^{-4} nm, a phase standard deviation of 6.0×10^{-4} rad and a phase derivative standard deviation of 3.5×10^{-6} rad nm $^{-1}$.

3.7 Chemical preparation of detection samples

This subsection outlines the procedure for preparing saline solutions with varying sodium chloride concentrations for transducer calibration. Additionally, it details the preparation procedure for different types of bioreceptors and analytes employed in this study, namely polyelectrolytes LbL system, biotin-streptavidin system, and conjugated oligonucleotides. The preparation of these three systems was conducted in a laminar flow hood. It is recommended to use new materials to prevent cross-contamination. Alternatively, all equipment can be sterilized in an autoclave, followed by sterilization in an ultraviolet light chamber for 5 minutes.

The preparation of all sensing samples described in this section was undertaken by MSc Díaz-Failach, C.I. and Ramirez-Cordero, A. For more comprehensive details on the procedures and protocols, refer to their respective theses.[134, 135]

3.7.1 Sodium chloride solutions preparation

A solution is a uniform mixture comprising two or more substances, where the solute is the substance being dissolved, and the solvent is the medium in which the solute dissolves. To characterize the RIS of the transducers, solutions with varying concentrations of NaCl (Omnichem) dissolved in water were employed as the surrounding medium. The relation to calculate the mass of NaCl to be dissolved in water is

$$m_{\text{NaCl}} = \frac{m_{\text{water solution}}}{100 - m_p} \quad (3.5)$$

where $m_{\text{water solution}}$ is the mass of water and m_p is the mass percentage of NaCl to be dissolved. In this study, the NaCl mass percentage was varied from 0.5 % to 15 %, resulting

in a range from 50.25 mg to 1764.71 mg dissolved 10 ml of water. The refractive index of these solutions was determined using an Abbe refractometer (WY1A MG Scientific, ± 0.0003 RIU). The results are summarized in Table 3.1.

Table 3.1: NaCl mass needed for preparation of saline solutions with concentrations from 0.5 % to 15 %, diluted in 10 mL of water. Measured refractive indexes of water and NaCl using an Abbe refractometer

NaCl mass [mg]	NaCl concentration [%]	Refractive index [RIU]
0	0	1.3328
50.25	0.5	1.3339
101.01	1	1.3343
152.28	1.5	1.3353
204.08	2	1.3362
256.41	2.5	1.3372
309.28	3	1.3381
362.69	3.5	1.3387
416.67	4	1.3397
638.30	6	1.3431
869.57	8	1.3458
1111.11	10	1.3488
1764.71	15	1.3591

Figure 3.13 better depicts the linear dependence of the refractive index on their NaCl concentration.

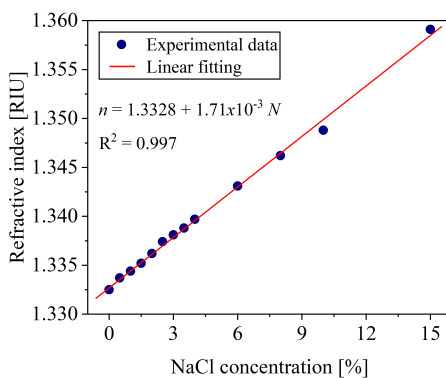


Figure 3.13: Refractive index of saline solutions dependence on the NaCl concentration

3.7.2 Polyelectrolytes preparation

Prior to detecting binding events of SARS-CoV-2 oligonucleotides, some proof-of-concept experiments were conducted. A well-established method for this purpose is the LbL system,

involving the successive deposition of thin layers of molecules atop a biosensor transducer. This approach aims to demonstrate the linear dependence of the signal response on the layer growth, thereby enabling the measurement of the thickness of these molecular layers. Additionally, it seeks to demonstrate the capability of the biosensor to detect small variations in the local refractive index near the transducer surface.

In this study, Polyallylamine Hydrochloride (PAH) and Polystyrene Sulfonate (PSS), from Sigma Aldrich, were chosen as the molecules for the LbL system. The unique characteristic of these polyelectrolytes lies in their opposite average electric charges, allowing for their alternate deposition and binding through electrostatic interactions, as depicted in Figure 3.14. Additionally, the thickness of each layer is highly influenced by the ionic strength of the buffer solution, with higher ionic strengths resulting in thicker layers. [136, 137]

Initially, the NaCl solution was prepared as described in Section 3.7.1, using a mass concentration of 0.3 M. Subsequently, 12 mg of PAH and PSS, both in powder form, were precisely weighed using a precision balance (Ohaus PX Pioneer). Each polyelectrolyte was then immersed in the saline solution within 15 mL Falcon tubes. To ensure thorough mixing of both compounds, the polyelectrolyte solutions underwent gentle vortexing for a few minutes. After this, the resulting polyelectrolyte solutions are now ready for use; otherwise, they should be tightly sealed with parafilm to prevent external contaminants and stored in a refrigerator at 4°C.

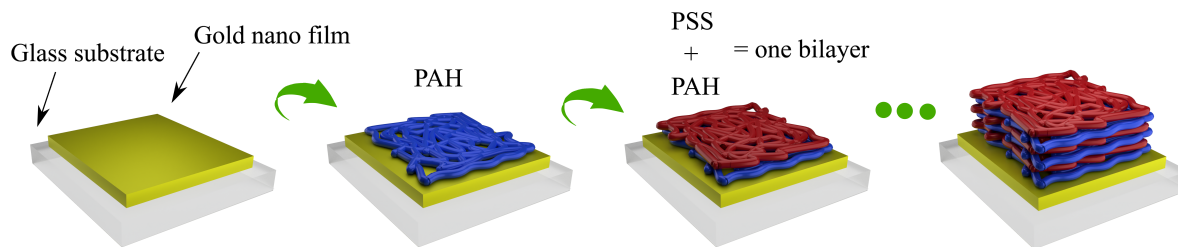


Figure 3.14: Schematic representation of the LbL detection method using polyelectrolytes. Initially, PAH is deposited onto the Au NF surface, followed by the deposition of PSS onto the PAH layer. The electrostatic forces facilitate the bonding between both layers, forming a bilayer. Subsequently, PAH and PSS are successively deposited onto the surface

3.7.3 Streptavidin - biotin preparation

Biotin, also known as vitamin B7, is a commonly used component in biomolecular research, due to its strong binding affinity for the streptavidin molecule. This robust and specific interaction forms the basis of the streptavidin-biotin system, where biotinylated molecules are used. Streptavidin-biotin system is a commonly used tool in various biological assays and techniques, including immunoassays, protein detection, and DNA/RNA hybridization studies.

Biotin, being the smallest molecule of the two, has a molecular weight of 244.3 g M^{-1} . [138] Streptavidin, a tetrameric protein with a molecular weight of 52.8 kDa, exhibits an exceptionally high biotin binding affinity ($K_a \approx 1014 \text{ M}$) and can bind up to four biotin molecules. Streptavidin also exhibits remarkable thermostability (with a T_m of 73°C for apo-SA and 112°C for biotin-SA) and high resistance against extreme pH, denaturing agents, and enzymatic degradation. [138]

Neish, C. et al. [139] employed AFM to quantify the volume of unoccupied streptavidin molecules. Their findings revealed a volume of $105 \pm 3 \text{ nm}^3$, corresponding to a diameter

of 11.3 ± 0.2 nm. Additionally, for a streptavidin-biotin conjugated molecule, resulted in a volume increase to 141 ± 11 nm³, corresponding to a diameter of 11.1 ± 0.1 nm. Figure 3.15 depicts a simplified scheme of the streptavidin and biotin molecules, as well as the binding between them.

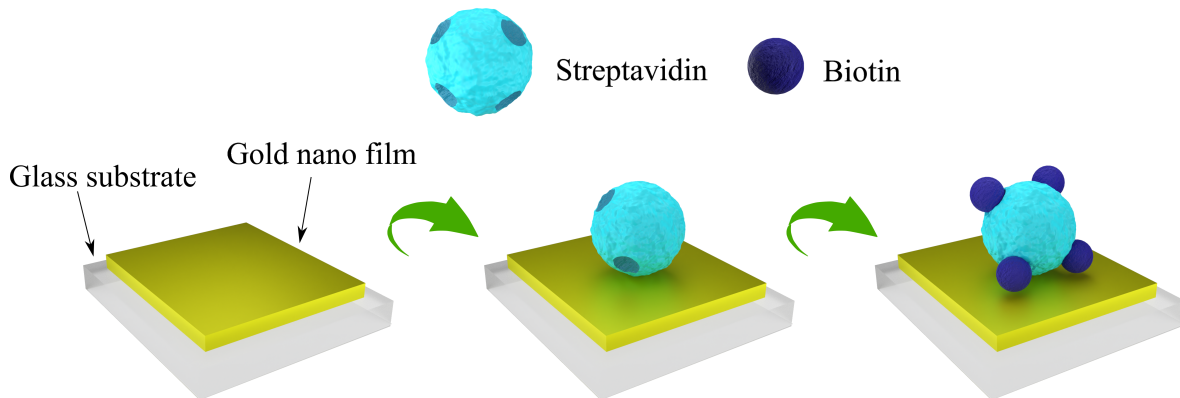


Figure 3.15: Simplified schematic representation of biotin detection. Initially, the streptavidin molecule binds to the Au NF surface through electrostatic forces. Subsequently, the biotin molecule bonds to the streptavidin molecule

Various streptavidin-based applications require the biotinylation of target molecules, enabling their selective binding to streptavidin-coated surfaces or conjugation with other biomolecules. The resultant biotin-streptavidin interaction is highly specific and stable, facilitating the detection and immobilization of various biological molecules.

Biotin and streptavidin were prepared as aqueous solutions from lyophilized forms by separate dilutions in nuclease-free water. Initially, to prepare an aqueous solution of 1 mM concentration of biotin diluted in 50 mL of nuclease-free water, 12.2 mg of biotin is required. Subsequently, the solution was gently vortexed for a few minutes.

The preparation of the streptavidin solution mirrored that of biotin. For a 10 µM concentration of streptavidin diluted in 50 mL of nuclease-free water, it requires 37.5 mg of streptavidin, which was precisely weighed on the precision balance. The streptavidin solution was then vortexed for few minutes. Both biotin and streptavidin solutions were thoroughly sealed with parafilm and stored in a refrigerator at 4°C.

3.7.4 Oligonucleotides preparation

Oligonucleotides are short, single-stranded molecules composed of nitrogenous basis, a ribose sugar, and a phosphate group. Most oligonucleotide modalities engage with their cognate target molecules through complementary Watson–Crick base pairing. [140] This inherent specificity plays a crucial role in various molecular biology applications, including PCR, gene cloning, and RNA interference. Characterized by nanoscale dimensions, oligonucleotides typically range from a few to several tens of nanometers in length. The compact size of these molecules facilitates their manipulation and application in nanotechnology and biotechnology, allowing for precise targeting and modulation of genetic information. [141]

As previously outlined, the primary aim of this study is to detect SARS-CoV-2 oligonucleotide binding events. Then, RdRp-COVID and RdRp-COVID-C oligonucleotides were synthesized and acquired from Microsynth and T4 Oligo companies, respectively, in a lyophilized state.

These specific oligonucleotide sequences were chosen from the DNA strand of SARS-CoV-2 due to the high similarity between the sequences of SARS-CoV-2 and SARS-CoV (RdRp-SARS), with differences in only a few bases.^[45] Table 3.2 provides the main characteristics of the oligonucleotides selected for this study, along with the sequence of the SARS-CoV oligonucleotide.

Table 3.2: Main characteristics of the SARS-CoV-2 oligonucleotides used in this study. To visualize the differences in the bases, the sequence of the SARS-CoV oligonucleotide is presented

Oligonucleotide	Manufacturer	Sequence 5' to 3'	Quantity available	Molecular weight [g M ⁻¹]
RdRp-COVID	Microsynth (Germany)	GCATCTCCTG ATGAGGTTC ACCTG	1.0 μM	7805
RdRp-COVID-C	T4 Oligo (México)	CAGGTGGAC CTCATCAGGA GATGC	347.9 nM	7716.1
RdRp-SARS	—	CAGGTGGAA CATCATCCGGT GATGC	—	7996.2

The detection of the binding of both oligonucleotides involves two key steps.

Firstly, in the surface functionalization process, the oligonucleotide RdRp-COVID is fixed to the plasmonic transducer. The chosen oligonucleotide incorporates a modification at its 5' end, introducing a thiol group that acts as the gold ligand, facilitating the functionalization process. Thiol groups are susceptible to oxidation, leading to the formation of disulfide bonds (-S-S-) either between different oligonucleotide molecules or within the same molecule. These disulfide bonds can potentially result in the cross-linking of oligonucleotides, impacting the functionalization process. To mitigate this, Dithiothreitol (DTT) is often included in reactions involving thiol-containing oligonucleotides to prevent undesired disulfide bond formation. The inclusion of DTT in the buffer helps maintain the thiol groups in their original state.

Secondly, the next step involves the detection of the binding of the complementary oligonucleotide, denoted as RdRp-COVID-C, to the one previously bound to the surface; this process is termed hybridization. Successful hybridization results in the formation of a double-bonded structure between the two oligonucleotides.

Figure 3.16 shows a schematic representation of both functionalization and hybridization processes. It is important to note that adenine binds to thymine, while cytosine binds to guanine.

Due to the limited availability of material, precise weighing and handling are essential for the preparation of both oligonucleotides. Initially, the lyophilized oligonucleotides (1 mM) are diluted in nuclease-free water (50 μL) and stored in separate pellets. To enhance oligonucleotide availability, centrifugation and heating are applied for 5 minutes at 65°C.

Following vortexing for a few minutes, the dilutions are vigorously resuspended using a micropipette and stored in distinct Eppendorf tubes. These tubes are sealed with Parafilm paper and stored at temperatures between -25°C and -15°C, in accordance with the manufacturer's recommendations, which ensures the preservation of their properties for a duration ranging from 6 months to 2 years in the liquid state.

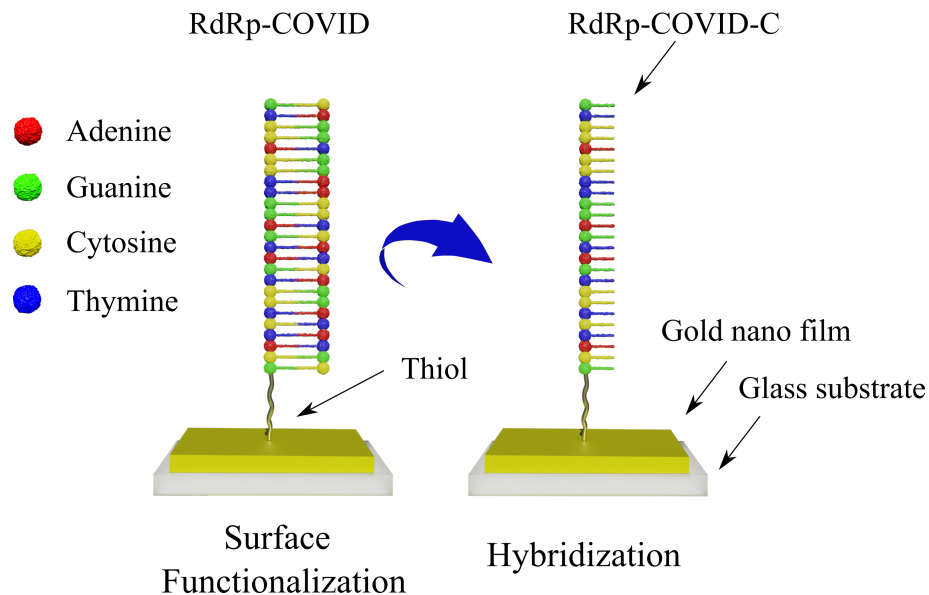


Figure 3.16: Schematic representation of the surface functionalization with the thiolated RdRp-COVID oligonucleotide. Following this, the binding is competed by placing the complementary RdRp-COVID-C oligonucleotide. On the top right the nitrogenous bases are depicted

For oligonucleotide usage, they are thawed and heated in an incubator to approximately 25 °C, then left in the laboratory to reach room temperature. Subsequently, they are vortexed and continuously resuspended to maximize the availability of oligonucleotides.

If the thiolated oligonucleotides are not utilized within 5 days of preparation, DTT should be added to the buffer. Through experimental exploration to identify the optimal DTT concentration, it was determined that for SPR detection experiments, the optimal DTT concentration is 100 nM, while for LSPR detection experiments, the optimal concentration is 20 nM.

3.8 Functionalization and hybridization of transducers

The successful detection of the functionalization and hybridization processes on the transducer is fundamental to this study. Therefore, meticulous cleaning of the transducer is imperative. Initially, the transducer undergoes thorough spraying and vortexing with distilled water for one minute. Subsequently, it undergoes sterilization in a UV chamber for 5 minutes to eliminate any microbial life on the substrate. Afterward, the transducer is dried and becomes ready for attachment to the microfluidic device, as mentioned in Section 3.3.

Another crucial factor in detecting binding events between molecules or between a molecule and the substrate is the method by which bioreceptors and analytes are introduced into the microfluidic device. To facilitate this process, the Chemyx Fusion 100 pump (see Figure 3.17) is employed. This pump allows for the controlled injection and extrusion of fluids through a syringe at a specified speed. Given the limited quantity of bioreceptor and polyelectrolyte material available, these substances are housed in BD U-100 insulin syringes for injection, each with a volume of 0.5 mL.

A primary challenge is the formation of air bubbles within the microfluidic device chamber. This issue disrupts the sensing signal, hindering the continuous detection of binding events. To avoid this problem, meticulous sealing measures were implemented. The syringe

and injection tube were carefully sealed with parafilm. Furthermore, the injection tube connected to the microfluidic device was sealed with parafilm and subsequently heated above the parafilm's melting point (60°C) to ensure more effective sealing.



Figure 3.17: Photograph of Chemyx 100 infusion pump for injecting aqueous solutions with controlled velocity

Chapter 4 |

SPR: Results and Discussion

This chapter presents the results of theoretical and experimental investigation of plasmonic properties of an Au NF for sensing applications. Initially, the reflectance spectrum of a stratified four-layer system—comprising glass, Ti NF, Au NF, and a dielectric medium—was determined through the calculation of Fresnel coefficients employing the transfer matrix method in an attenuated total reflectance configuration. The reflectance spectra were computed across varying Au NF thicknesses and under different incident angles. Furthermore, the refractive index sensitivity and the figure of merit were calculated to evaluate the system’s performance.

The theoretical reflectance spectra of this multilayer system were corroborated by experimental measurements, validating the analytical approach. The sensing parameters, namely RIS, RIR, and FOM, of the Au NF were quantified in both intensity and phase interrogation modes. Based on these analyses, the optimal experimental conditions—including the angle of incidence, Au NF thickness, and interrogation mode—for detecting binding events were identified. Ultimately, the detection of three distinct types of biological binding events was successfully executed, affirming the efficacy of our approach.

4.1 Reflectance spectrum of Au NFs under ATR condition

4.1.1 Main parameters for reflectance spectrum simulation

The reflectance spectrum of an Au NF was calculated using a MATLAB script based on the multilayer transfer method matrix approach. The script was adapted from the free software package available on the Mathworks File Exchange site [142] developed by Guske. [72] To initiate the computational script, several parameters must be specified: the range of the angle of incidence, the spectrum of wavelengths or frequencies, the dielectric constant of the substrate, the thickness of the metallic film along with its dielectric function, and the dielectric constant of the ambient medium. In this dissertation, the investigated system comprises a configuration of glass, Ti NF, Au NF, and the surrounding medium. Consequently, the initial parameters specified are as follows:

- ◊ Angle of incidence range: from 30° to 80°.
- ◊ Wavelength range: from 300 nm to 1000 nm.

- ◊ The BK7 substrate and the water dielectric constants were taken from the RefractiveIndex Info data base.
- ◊ The dielectric function of Au was taken from data of Jhonson and Christy. [77]
- ◊ The dielectric function of Ti was obtained using the Lorentz-Drude model, where the titanium constants were taken from the experimental measurements of Wells et al. [143]

4.1.2 Theoretical calculations

The calculated reflectance spectra of Au NFs, with thicknesses ranging from 40 nm to 58 nm in increments of 2 nm, are depicted in Figure 4.1a. These calculations were performed at a fixed angle of incidence of 70°, employing *p* polarized incident electric fields. The Au NF are in contact with water with a refractive index of $n = 1.3328$.

The reflectance spectra of AuNFs demonstrates consistent behavior. As the wavelength increases, the reflectance grows, peaking at approximately 570 nm. This peak undergoes a redshift when the thickness of the Au NFs increases. Subsequently, a significant reduction in reflectance marks the SPR dip at a resonance wavelength of about 669.0 nm. This resonance wavelength initially shows a blueshift from 669.8 nm to 668.4 nm as the Au NF thickness increases from 40 nm to 50 nm. Further increasing the thickness to 58 nm induces a redshift, settling the resonance wavelength at 669.9 nm, as observed in Figure 4.1b. Such behavior illustrates the effect of Au NF thickness on the plasmonic coupling conditions and the system's effective refractive index.

The resonance strength, as deduced by the minimum reflectance value at the SPR wavelength, increases with increasing Au NF thickness up to 50 nm, reaching a very small reflection of 1.2×10^{-3} at this thickness, indicative of the most efficient energy transfer from light to plasmon. For thicknesses exceeding 50 nm, the reflectance at resonance begins to increase, signaling a decline in energy transfer efficiency. Additionally, the FWHM of the SPR dip, a measure of the spectral precision of the resonance, narrows as the Au NF thickness increases, as shown in Figure 4.1b, indicating a sharper resonance for thicker samples.

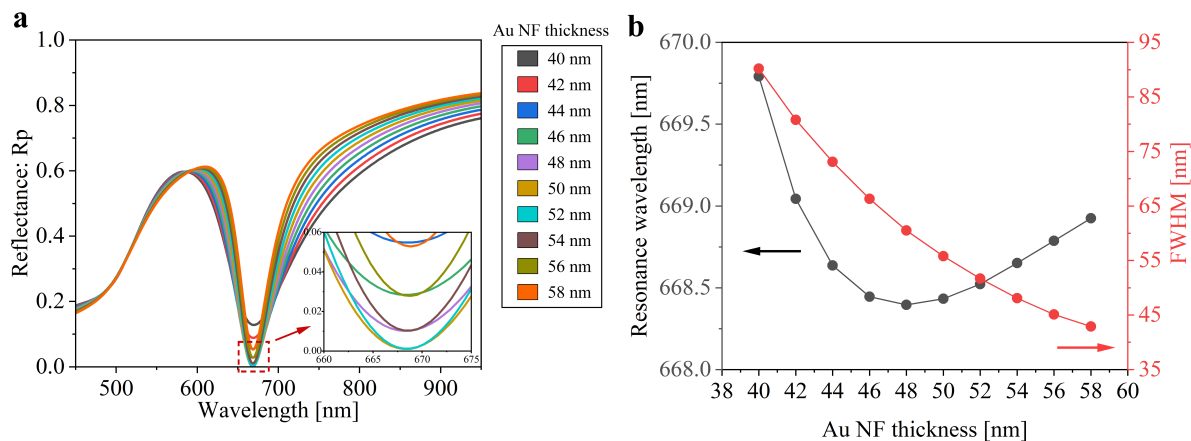


Figure 4.1: a. Analytical reflectance spectrum of a four-layer system (glass – Au NF – Ti NF – surrounding medium). The Au NF thickness range from 40 nm to 58 nm. b. Resonance wavelength and FWHM of Au NFs reflectance spectra in function of the Au NF thickness. The surrounding medium is water, and the angle of incidence is 70°

Beyond the SPR, at longer wavelengths, the reflectance reaches a plateau with a reflectance value of 0.7 - 0.8. The plateau effect can primarily be explained by two key factors. First, beyond the SPR wavelength, the momentum mismatch between the incident light and the surface plasmons increases, leading to a significant reduction in resonance coupling. This mismatch results in diminished interaction between the light and plasmons, thereby stabilizing the reflectance values. Additionally, at longer wavelengths, the real part of the metal's dielectric function gains prominence over its absorptive (imaginary) component. Consequently, the metal absorbs less energy and reflects more, contributing further to the stabilization of the reflectance, seen as a plateau in the spectrum. Note that in thinner gold nanofilms, the broader FWHM of the SPR peak causes reflectance to stabilize at longer wavelengths. This broader resonance spreads the effects over a wider wavelength range, delaying the onset of the stabilization plateau compared to thicker films.

The dependence of the reflectance spectrum on the angle of incidence is shown in Figure 4.2. To compare the theoretical analysis with the experimental findings, the angles of incidence were selected according to the experimental parameters. Figure 4.2a illustrates the reflectance for *p* polarized light (R_p) as a function of wavelength. Three curves are depicted, corresponding to angles of incidence at 67° , 70° , and 73° . As the angle of incidence increases, there is a noticeable redshift in the resonance wavelength. The redshift with increasing angle of incidence is due to changes in the coupling conditions between the incident photons and the surface plasmons. As the angle moves away from the critical angle, the momentum transfer to the surface plasmons increases, requiring a longer wavelength to meet the resonance condition.

Figure 4.2b presents the reflectance for *s* polarized light (R_s). The absence of a distinct plasmonic dip in the reflectance spectrum signifies that SPR is not excited by *s* polarized light, which is consistent with the theoretical understanding of SPR phenomena.

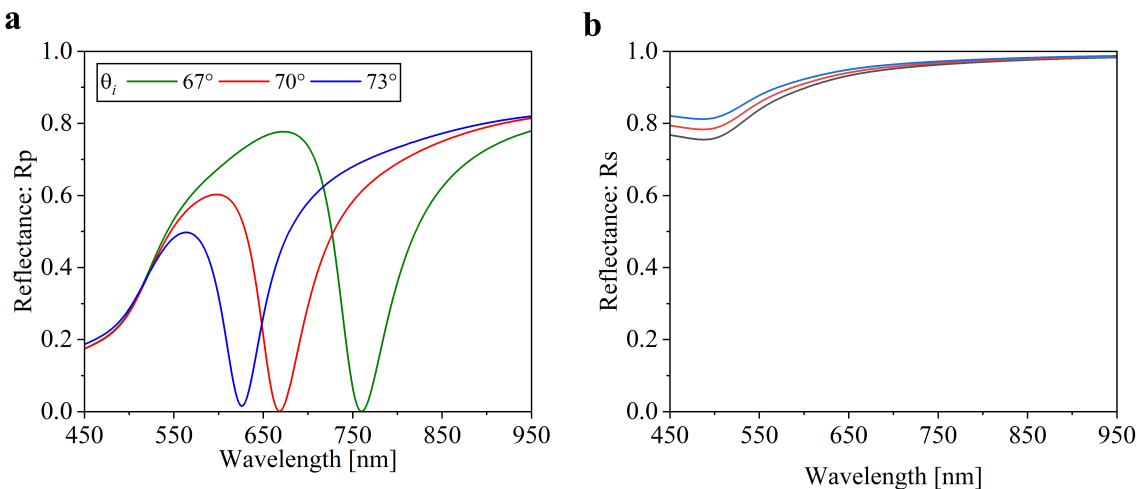


Figure 4.2: Calculated reflectance spectrum under **a.** *p* and **b.** *s* polarized electric field for different angles of incidence

4.1.3 Experimental measurements

The experimental reflectance spectra of Au NFs of the varying thickness were measured. The inherent problem of poor adhesion between gold and silicate glass necessitated the introduction of a Ti NF as an adhesion layer. A monolayer of 1 nm Ti NF was sputter-deposited

onto the glass substrate, followed by the deposition of Au NFs onto this intermediary Ti layer. The experimental setup was configured in the Kretschmann configuration (as detailed in Section 3.4.2) operating in intensity interrogation mode at an angle of incidence set to 70°.

Figure 4.3a presents the reflectance spectra of Au NFs with varied thicknesses, incrementally scaled from 50 nm to 58 nm in 2 nm steps. The spectra exhibit an initial increase in reflectance with wavelength, peaking at 540 nm. Then, an abrupt decrease in reflectance occurs reaching its minimum at the resonance wavelength. Following this, the reflectance increases plateauing at approximately 0.75.

Subsequent quantification of the resonance wavelength and the FWHM for each Au NF thickness is depicted in Figure 4.3b. The plot of the resonance wavelength, indicated by black circles, shows a general trend of shifting towards longer wavelengths, as the Au NF thickness increases. The FWHM, shown in red, varies across the range of thicknesses measured; it does not follow a clear trend but it is the narrowest for the Au NF with a thickness of 54 nm, suggesting a sharper resonance, and the widest is observed for the 56 nm thick Au NF.

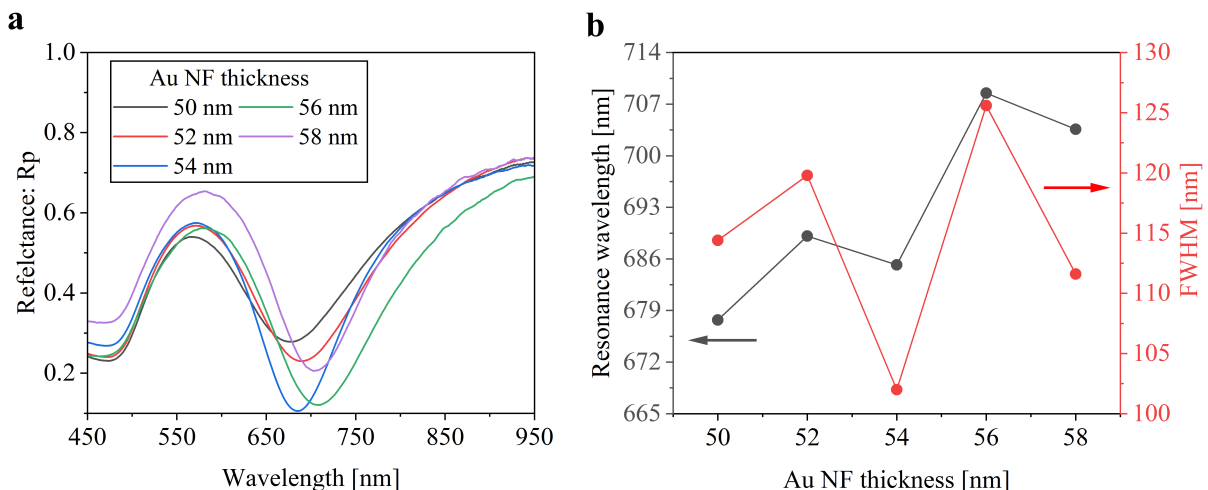


Figure 4.3: **a.** Experimental reflectance spectrum of Au NF for different thickness under *p* polarized light. **b.** Resonance wavelength and FWHM of the Au NF reflectance spectrum. The angle of incidence is 70°

The reflectance spectrum's angular dependence for a 50 nm thick Au NF has been measured and is presented in Figure 4.4. The incidence angle spanned from slightly above the critical angle to the experimentally feasible maximum, covering a range between 67° and 73°.

For the *p* polarized light across all examined incident angles (Figure 4.4a), the plasmonic dip is consistently observed. Notably, with increasing angles of incidence, a redshift in the resonance wavelength occurs along with a broadening of the plasmonic dip. Close to the critical angle, the resonance wavelength shifts into the region beyond 1000 nm, which is outside of the detection range of our spectrometer.

Meanwhile, Figure 4.4b shows the reflectance spectra for *s* polarized light. In accordance with theoretical predictions, the characteristic plasmonic dip is absent under *s* polarized conditions, reaffirming the polarization-dependent nature of surface plasmon excitation.

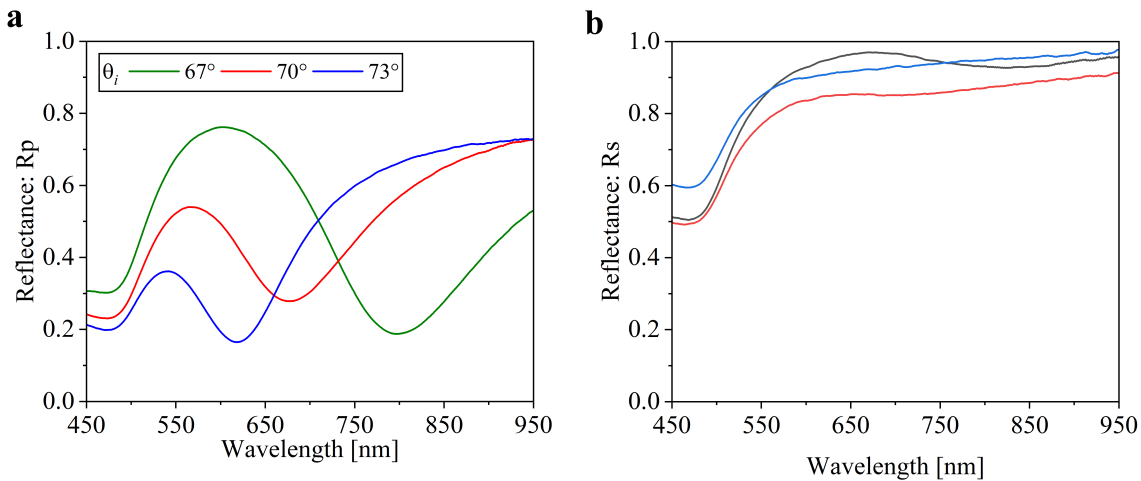


Figure 4.4: Experimental reflectance spectrum of a 50 nm Au NF with different angles of incidence under **a.** p and **b.** s polarized incident light

4.1.4 Discussion

For sensing applications, it is crucial to design an SPR transducer that maximizes *i*) resonance strength, *ii*) the narrowness of the resonance dip, and *iii*) the tunability of the resonance wavelength. The theoretical and experimental results obtained facilitate such optimization.

The optimal thickness of Au NF for SPR, where maximum resonance strength is observed, is dictated by the skin depth of gold. The skin depth defines the scale at which the electromagnetic field decays inside the metal; only electrons within this region significantly contribute to the SPR phenomenon. For films thinner than the skin depth, the electromagnetic field may not be sufficiently attenuated, leading to a suboptimal SPR response. In this scenario, the field extends beyond the film, reducing the interaction with the electrons responsible for plasmonic oscillations and thus dampening the resonance strength. Conversely, when the Au NF is much thicker than the skin depth, the interior of the film contributes little to the plasmonic activity due to rapid field attenuation. The excess material only increases absorption and scattering losses without enhancing the SPR signal, resulting in unnecessary damping and energy dissipation.

The skin depth of gold at a 633 nm wavelength is expected to be around 42 nm at 520 nm.^[144] The optimal thickness of the Au NF for SPR should closely align with the skin depth to ensure efficient field confinement and plasmon excitation. Experiment shows that a 54 nm thick film provides better resonance strength, suggests that factors such as interfacial quality, grain structure within the film, and fabrication-induced stresses may significantly affect the plasmonic properties. Additionally, the real thickness of the Au NF may deviate from the expected value due to fluctuations in the deposition process. Variations in factors such as sputtering power, working gas pressure, or wear of the Au target can affect the deposition rate and thus introduce errors in film thickness estimation. All these factors could contribute to the deviation from the theoretical prediction, underscoring the importance of experimental validation in the design of SPR systems.

Another notable difference between the experimental and analytical reflectance spectra of the 50 nm Au NF is that the reflectance at resonance is nearly zero for analytical spectra, while it measures around 0.41 for the best experimental sample (with 54 nm thickness). This inconsistency between the analytical and experimental reflectance values may be due to the

losses introduced by Ti NF intended to enhance adhesion to Au NF. Additional simulations demonstrated that a slightly thicker Ti NF on the glass substrate could significantly prevent critical coupling.

Theoretical results have demonstrated that increasing the thickness of Au NFs leads to a smaller FWHM, resulting in a narrower resonance dip. This effect is partially due to reduced material damping in thicker films, which allows for more sustained plasmonic oscillations and thereby narrows the FWHM. Additionally, as the film thickness increases, the impact of surface roughness is mitigated by favoring the bulk properties over surface imperfections, leading to a more uniform and stable plasmonic field.

However, the experimental dependence of FWHM on film thickness does not exhibit a clear trend, with an average FWHM of approximately 115 nm. This contrasts with the widest FWHM of 90 nm observed for the 40 nm thick Au NF in the analytical reflectance spectrum. The discrepancies observed may likely be attributed to variations in the actual thicknesses of the two metal films, titanium and gold. The origin of uncontrolled variations in the thickness of the Au NF has been discussed previously. Determining the actual thickness of a Ti NF expected to be around 1 nm is particularly challenging, as such thin films may not consistently form a continuous layer. This necessitates reliance on controlling the deposition time to manage thickness accurately. However, the deposition time for TiNF is typically brief, making precise control challenging without specialized automated timing solutions. This limitation introduces significant uncertainty in film thickness control, potentially affecting the experimental results.

Both experimental and theoretical analysis of the dependence of resonance wavelength on Au NF thickness reveal some discrepancies. Analytically, the resonance wavelength remains relatively constant as the Au NF thickness varies, whereas experimentally, it exhibits a considerable redshift (about 30 nm). We hypothesize that the larger shift in experimental resonance wavelength could be due to systematic errors in setting the incidence angle at very oblique angles. Indeed, both experimental and theoretical results indicate that minor variations in the angle of incidence lead to significant changes in resonance wavelength: a 6° change in incidence angle results in more than a 150 nm shift in resonance wavelength. Therefore, to maintain changes in wavelength within 1 nm, the angle should be controlled with a precision of better than 0.01°, which is not feasible with the rotary stage used in our experiment.

4.2 Bulk refractive index sensitivity of Au NFs using the intensity interrogation mode

To determine the RIS of Au NFs, the refractive index of the surrounding medium is systematically varied. The refractive index values were selected based on experimental parameters, specifically corresponding to water and NaCl solutions of varying concentrations, ranging from 2% to 10% in increments of 2%. The refractive index values used in theoretical simulation are outlined in Table 3.1.

4.2.1 Theoretical calculations

In this section, the SPR response of AuNF to changes in the refractive index of the surrounding media will be theoretically evaluated to determine key transducer performance parameters—namely, RIS, FWHM, and FOM. Previous sections have demonstrated that

the plasmonic response is significantly influenced by both the film thickness and the angle of incidence. Therefore, to optimize conditions for maximum transducer performance, the analysis will be conducted across three different angles of incidence and a range of film thicknesses from 40 to 58 nm, in increments of 2 nm.

An example of RIS determination for a 50 nm thick Au NF at an angle of incidence of 70° is shown in Figure 4.5. Figure 4.5a presents the reflectance spectra of Au NF in an ATR configuration for various refractive indices of the surrounding medium, highlighting a redshift in the resonance wavelength as the refractive index increases. Figure 4.5b depicts the relative changes in the resonance wavelength when compared to water. As previously discussed, the slope of this graph represents the RIS, which was found to be 3600 nm RIU⁻¹.

Furthermore, the RIS was also calculated for angles of incidence of 67° and 73°. Figure 4.5c illustrates that the RIS increases as the angle of incidence approaches the critical angle, indicating enhanced sensitivity under these conditions.

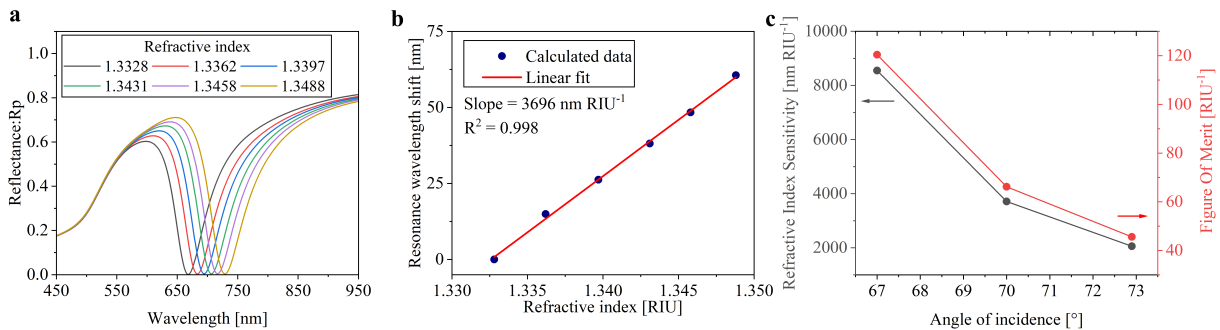


Figure 4.5: **a.** Calculated reflectance spectrum of a four-layer system (glass–1 nm Ti NF–50 nm Au NF–surrounding medium) for different refractive index of the surrounding medium. The angle of incidence is 70°. **b.** Resonance wavelength changes relative to water. **c.** RIS of Au NF for different angles of incidence

Following this, the angle of incidence was fixed at 70°, and the RIS for Au NFs of varying thicknesses was calculated. Figure 4.6 illustrates the dependence of RIS on Au NF thickness.

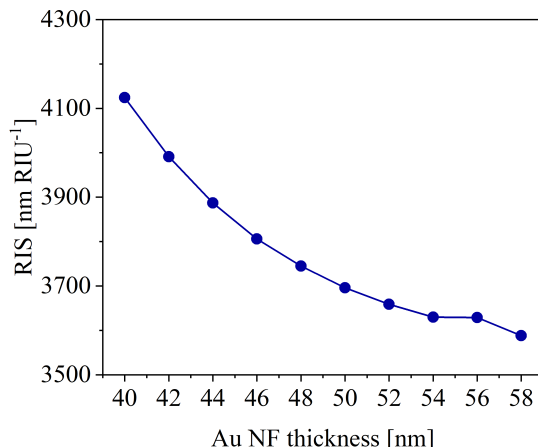


Figure 4.6: RIS of a four-layer system (glass–1 nm Ti NF–Au NF–surrounding medium) for different Au NF thickness in the refractive index range from 1.3328 to 1.3410. The angle of incidence is 70°

It is observed that as the thickness of the AuNF increases, the RIS decreases. The highest RIS recorded at this angle of incidence was 4124 nm RIU^{-1} , achieved with an AuNF thickness of 40 nm.

This procedure was repeated across all thicknesses and angles. The main findings regarding the plasmonic characteristics and the sensing performance parameters of the AuNFs are summarized in Table 4.1. From the table, a trend can be observed where the FOM tends to peak for Au NFs at angles approaching the critical angle. Specifically, the Au NF with a thickness of 58 nm exhibits the highest FOM, which is a desirable trait for high-performance sensing applications. The maximum value observed is 163 RIU^{-1} , which indicates an optimized balance between RIS and FWHM.

On the other hand, the Au NF of 40 nm thickness shows an exceptionally high RIS of 9087 nm RIU^{-1} , suggesting an excellent sensitivity to changes in the refractive index of the surrounding medium. However, this is counterbalanced by a relatively broad reflectance spectrum, as indicated by the FWHM of 129.0 nm, which results in a reduced FOM of 70 RIU^{-1} . This reflects the trade-off between achieving high sensitivity and maintaining a narrow linewidth for the peak resonance.

The approach to enhance the FOM appears straightforward: increase the RIS by adjusting the angle of incidence closer to the critical angle. However, this adjustment tends to broaden the FWHM, as indicated in Figure 4.2a, which in turn could negatively impact the FOM. Therefore, a balance must be struck between RIS and FWHM to achieve an Au NF reflectance spectrum that optimizes the FOM.

In conclusion, following the theoretical analysis of the plasmonic properties of Au NFs, the optimal parameters for the four-layered system and the angle of incidence for sensing purposes were determined. The recommended angle of incidence is 67° (or as close as feasible), with an Au NF thickness of 58 nm.

4.2.2 Experimental measurements

Spectral reflectance measurements in ATR configurations for Au NF of varying thicknesses at different angles of incidence were performed, with a plasmonic dip consistently observed in the R_p spectrum. These characteristics were analyzed to determine the transducer's performance characteristics.

Figure 4.7a illustrates the reflectance spectra for an Au NF of 50 nm thickness across a range of surrounding media from water to a 10 % NaCl solution. The angle of incidence is maintained at 70.0° . The resonance wavelength is approximately 680 nm with water as the medium, showing a distinct redshift as the medium is changed to NaCl solutions.

Figure 4.7b presents the sensor response over time, typically referred to as a sensogram. Here, the resonance wavelength is tracked for around 100 seconds to determine an average value at each sensogram step. Consistent with previous observations, an increase in the refractive index of the surrounding medium leads to a corresponding increase in the resonance wavelength. Subsequently, the relative shifts in the resonance wavelength from the baseline water measurement are plotted against the refractive index of the surrounding medium, as shown in Figure 4.7c. The slope derived from linear fitting of these changes against the refractive index indicates the RIS, calculated to be 5184 nm RIU^{-1} .

Table 4.1: Au NF thickness, resonance wavelength, RIS, FWHM, and FOM at different incident angles

Au NF thickness [nm]	Resonance wavelength [nm]	RIS [nm RIU ⁻¹]	FWHM [nm]	FOM [RIU ⁻¹]
40	772.1 669.8	619.7 9087 4124 2177	67° 70° 73° 67° 73° 70° 73°	129.0 90.2 57.9 70.4 45.7 37.6
42	768.3 669.0	621.4 8919 3991 2137	112.8 80.8 55.3 79.1 49.4 38.6	
44	765.4 668.6	622.9 8790 3887 2106	99.0 73.1 52.7 88.8 53.2 40.0	
46	763.1 668.5	624.2 8688 3806 2082	88.1 66.3 49.9 98.6 57.4 41.7	
48	761.4 668.4	625.3 8605 3745 2064	79.0 60.5 47.3 108.9 61.9 43.6	
50	760.0 668.4	626.2 8538 3696 2049	70.9 55.8 44.9 120.4 66.2 45.6	
52	759.0 668.5	626.9 8482 3659 2038	64.7 51.7 42.6 131.1 70.8 47.8	
54	758.2 668.7	627.6 8436 3630 2030	59.4 48.1 40.7 142.0 75.5 49.9	
56	757.6 668.8	628.7 8397 3629 2024	54.7 45.1 38.6 153.5 80.5 52.4	
58	757.1 668.9	628.7 8364 3588 2019	51.2 42.9 37.0 163.4 83.6 54.7	

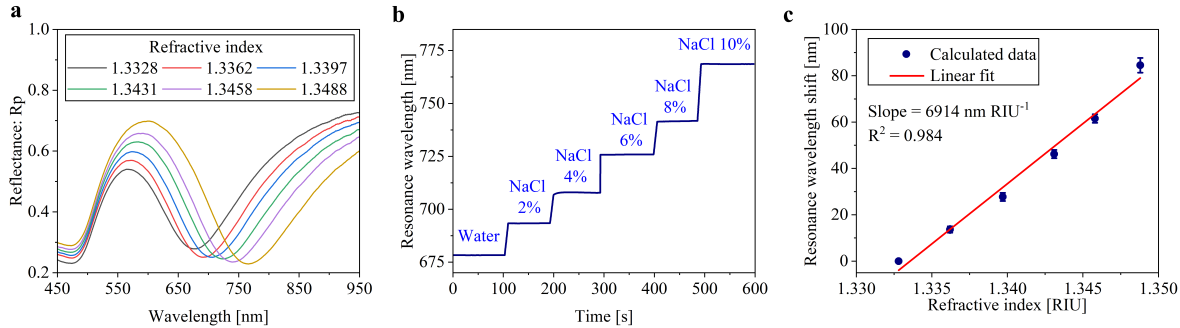


Figure 4.7: Principle of SPR wavelength detection. **a.** Experimental reflectance spectrum of Au NF of 50 nm thickness when varying the refractive index of the surrounding medium. **b.** Sensogram of the resonance wavelength detection. **c.** Resonance wavelength changes versus refractive index change relative to water. The angle of incidence is 70°

Subsequent experiments involved assessing the RIS for an Au NF with thickness of 50 nm at incidence angles of 67° and 73° . As demonstrated in Figure 4.8, the RIS notably increases as the angle of incidence nears the critical angle, with the maximal RIS reaching 9970 nm RIU^{-1} at an angle of 67° . This pattern aligns with analytical predictions discussed earlier.

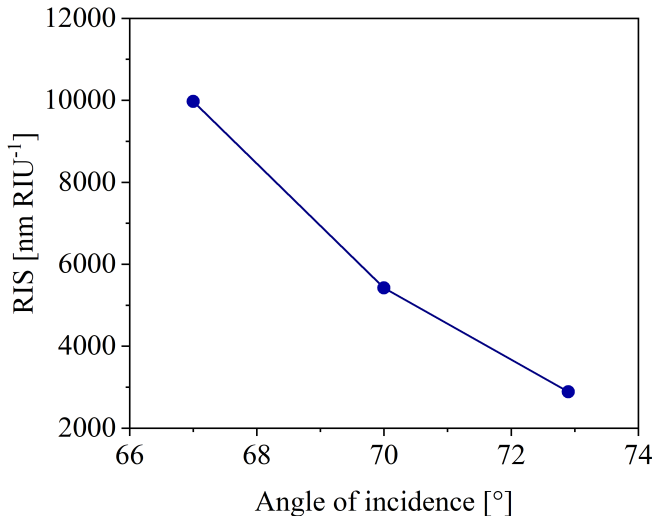


Figure 4.8: RIS of Au NF of 50 nm thickness under different angles of incidence

Despite the maximum RIS occurring at an incidence angle of 67° , the RIS for other Au NF samples was determined at an incidence angle of 70° . This particular angle was selected to manage the trade-off with the FWHM, which tends to broaden at lower angles of incidence. In Figure 4.9 it is seen that there is a noticeable reduction in RIS with increased thickness of the Au NF. The 50 nm thick Au NF sample exhibits the highest RIS at 5424 nm RIU^{-1} . For thicker Au NFs, particularly when the surrounding medium is a 10% NaCl solution, the resonance wavelength approaches the edge of the white light source spectrum, which hampers the detection of the resonance wavelength.

In the final phase of characterization focused on the sensing capabilities of the Au NF, the refractive index resolution is evaluated. The precision of the experimental setup in wavelength interrogation is quantified by measuring the standard deviation while water is

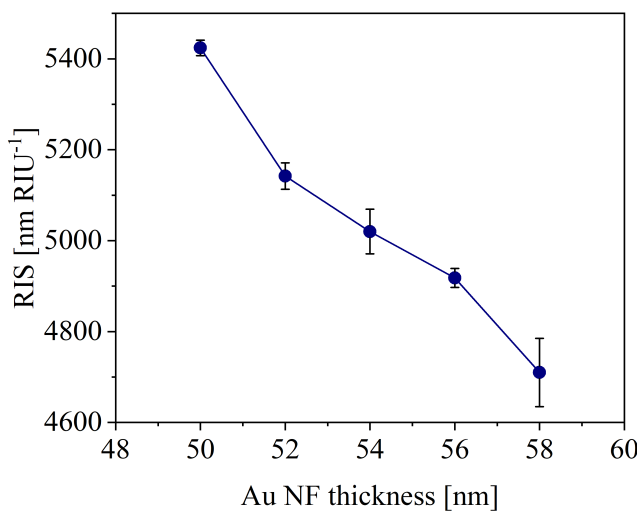


Figure 4.9: RIS of Au NFs with different thickness for an angle of incidence of 70°

on the Au NF and monitoring the resonance wavelength for 5 minutes. The sensogram post-processing reveals the standard deviation to be 4.2×10^{-3} nm. Among the samples, the 50 nm Au NF exhibits the most favorable RIR, calculated to be 4.2×10^{-7} RIU.

Table 4.2 summarizes the sensing characteristics of the transducers based on Au NFs. The 50 nm thick Au NF presents the highest FOM (48.0 RIU^{-1}), although it shows the widest reflectance spectrum (FWHM of 207.5 nm). This is due to the highest RIS (9970 nm RIU^{-1}).

Therefore, the optimal configuration for the transducer and the experimental arrangement for wavelength interrogation sensing experiments is an Au NF with a 50 nm thickness, paired with an incidence angle that approximates the critical angle, 67° in our case. This setup yields the highest RIS and an advantageous balance of FOM and RIR, positioning it as the superior choice for precise refractive index measurements.

Table 4.2: Experimental plasmonic behavior and biosensing performance of a transducer composed of a 50 nm Au NF deposited onto a 1 nm Ti NF at an angle of incidence of 70°

Au NF thickness [nm]	Angle of incidence [°]	Resonance wavelength [nm]	FWHM [nm]	RIS [nm RIU ⁻¹]	FOM [RIU ⁻¹]	RIR [10^{-7} RIU]
50	67	798.2	207.5	9970	48.0	4.2
	70	677.6	143.9	5424	37.7	7.7
	73	618.4	72.6	2887	39.8	14.5
52	70	677.7	114.4	5142	24.8	8.2
54	70	689.1	119.8	5020	24.2	8.4
56	70	685.2	102.0	4918	23.7	8.5
58	70	708.5	125.6	4710	22.7	8.9

4.2.3 Discussion

Although some discrepancies were observed between the theoretical and experimental reflectance spectra of the Au NF, the trends in their sensing properties consistently align across both analytical and experimental findings. In both scenarios, an increase in Au NF thickness leads to a decrease in RIS performance. Additionally, the angle of incidence is critical for achieving an enhanced RIS. Our experiments confirmed that the angle should be as close as possible to the critical angle. This finding aligns with the predictions made by Homola, J. and subsequently supported by Roh, S. et al. They established that longer resonance wavelengths increase the RIS of an SPR sensor, achievable by reducing the angle of incidence. This effect occurs because a smaller incident angle results in greater penetration of the evanescent field into the sensing medium, thereby heightening the sensor's sensitivity to refractive index changes.

In the theoretical analysis, the FOM is observed to monotonically increase with the thickness of the Au NF. This trend is primarily due to the significant decrease in FWHM, which narrows approximately threefold as the thickness increases. Concurrently, there is only a slight reduction in RIS, diminishing marginally from 9087 to 8364 nm RIU⁻¹. Such a decline in FWHM with increasing thickness is anticipated to outweigh the decrease in RIS, resulting in the overall increase in the theoretical FOM. As a result, Table 4.1 indicates that, from an analytical standpoint, the Au NF with a 58 nm thickness is optimal for sensing applications in wavelength interrogation mode: although it exhibits the lowest RIS (8364 nm RIU⁻¹), its narrow FWHM (51.2 nm) compensates for this, resulting in a highest FOM (163.4 RIU⁻¹).

In contrast, the experimental FOM does not follow a monotonic increase with the thickness of the Au NF. Instead, it displays a relatively constant value across different thicknesses, except for the 50 nm sample. This constancy suggests that the experimentally observed decrease in RIS with increasing thickness is almost directly counterbalanced by a corresponding narrowing in FWHM. The fact that these two parameters change at nearly the same rate experimentally ensures that the FOM remains stable, demonstrating that the experimental setup and real-world imperfections introduce factors that moderate the impact of thickness on the sensor's performance. The notable exception is the 50 nm sample, which stands out with a significantly higher RIS and, consequently, a higher FOM, underscoring the unique sensitivity of this thickness in the experimental setup.

For this reason, and after several experiments with different conditions, the optimal transducer was found to be double metallic bilayer composed by a 1 nm thick Ti NF and 50 nm thick Au NF at the angle of incidence 67°.

4.3 Experimental measurements of bulk refractive index sensitivity using the phase interrogation mode

In this section, we examine the phase interrogation mode for detecting changes in the refractive index. The Au NF with a 50 nm thickness, which previously demonstrated the highest RIS in wavelength interrogation mode, is now assessed using the ATR configuration in phase interrogation mode. Due to phase retrieval constraints at lower angles of incidence, the angle of incidence is set at 68°.

The typical output of the common path spectral interferometer is a wavelength-dependent interference pattern known as a spectral interferogram, exemplified in Figure 4.10a. The

spectral interferogram with water as the surrounding medium (black line) displays a significant decrease in fringe contrast around 760 nm, which constitutes the resonance zone. When the surrounding medium is switched to a 2 % NaCl solution (red line), there is a notable redshift in the resonance zone. The phase of the fringes within the resonance zone undergoes a change, while the fringes outside this zone remain consistent in phase.

Figure 4.10b presents the differential phase for each spectral interferogram against various refractive index values of the surrounding medium. An abrupt phase jump is evident at the resonance wavelength, while the phase stays nearly unchanged outside of the resonance zone. To pinpoint the exact location of the resonance wavelength—the point where the phase response is steepest—the wavelength derivative of the phase is taken, as illustrated in Figure 4.10c.

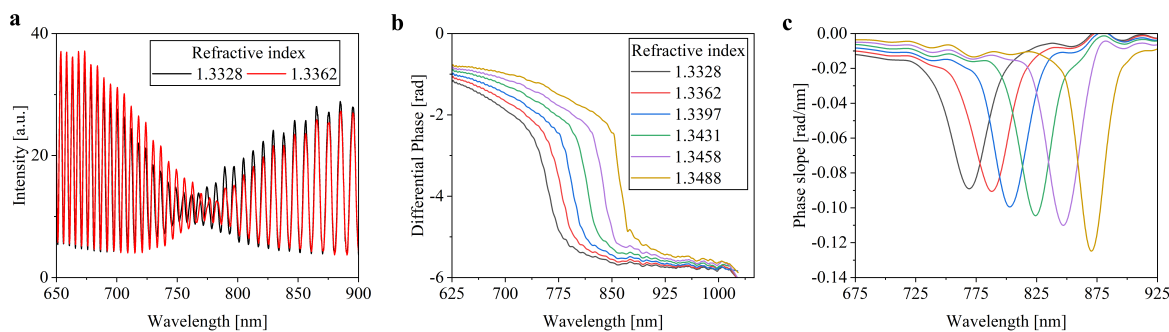


Figure 4.10: Experimental plasmonic response of the common path spectral interferometer. **a.** Spectral interferogram, **b.** differential phase of the interferogram and its **c.** phase derivative when varying the refractive index of the surrounding medium

In phase interrogation mode, we identify three distinct variables for sensing purposes simultaneously. The first is the peak position of each phase derivative, indicating the differential's resonance wavelength. The second variable relates to the phase value's alteration at the resonance wavelength. Lastly, the amplitude of the phase derivative (the phase slope at resonance) is also tracked in response to refractive index variations.

For determining the RIS associated with the wavelength, phase, and phase derivative at resonance in phase interrogation mode, we utilized a custom LabVIEW interface outlined in Section 3.5. This interface acquires the signal from the spectrometer, processes it, extracts differential phase spectra, evaluates the resonance wavelength, differential phase shift, and amplitude of the phase derivative at resonance, and finally, displays all three parameters in real time. The first column of Figure 4.11 exhibits a sensogram for the wavelength, phase, and phase derivative at resonance for each refractive index tested. In all three cases, the sensing parameters demonstrated an approximately linear increase with the refractive index.

Changes in wavelength, phase, and phase derivative at resonance relative to water are illustrated in the second column of Figure 4.11. The methodology for ascertaining the RIS for each parameter parallels that of the wavelength interrogation mode. Linear fits applied to the experimental data points on each graph yield the RIS; the slope of these linear fits is indicative of the RIS values. The RIS calculated for the resonance wavelength is 6360 nm RIU^{-1} , and for the phase derivative, it is -0.95 RIU^{-1} .

In the case of phase detection, two separate linear fits were performed over different refractive index intervals: the first spanning from 1.3328 to 1.3362, and the second from 1.3362 to 1.3488. Within the first interval, the phase changes remained inside the dynamic range, whereas in the second interval, they exceeded it. As a result, the RIS for the first

refractive index interval was calculated at 271 rad RIU^{-1} , and for the second interval, it reduced to 113 rad RIU^{-1} .

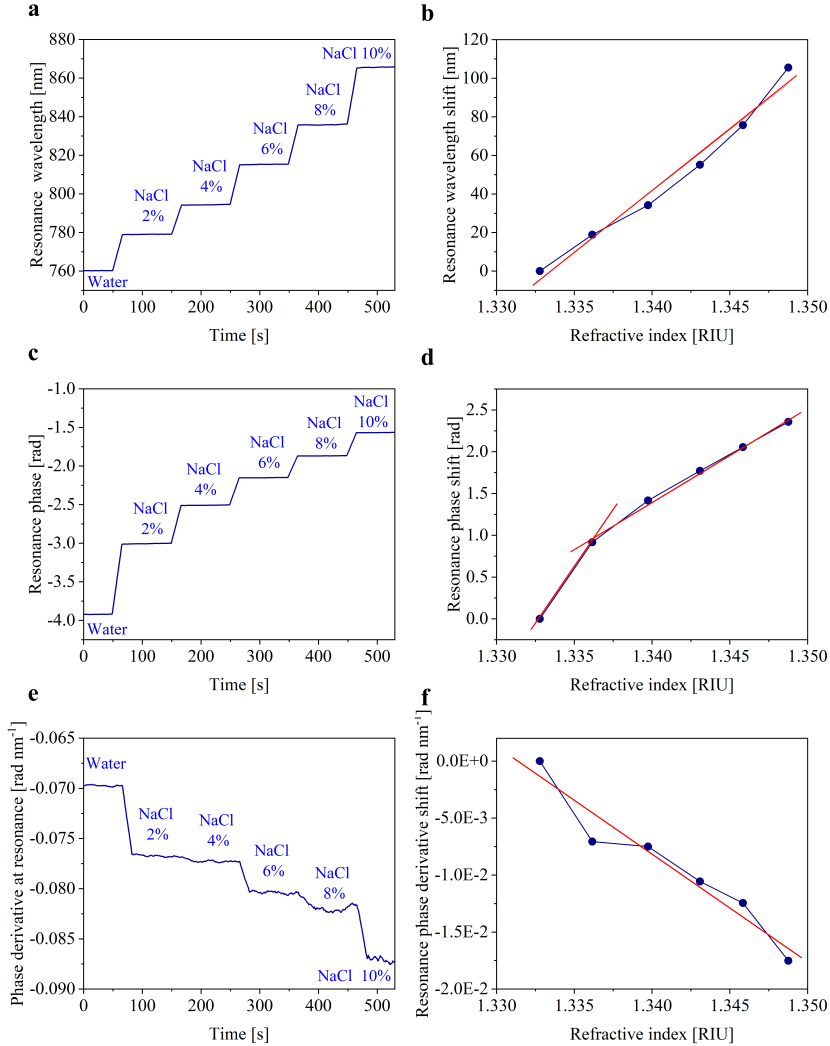


Figure 4.11: Determination of the RIS of a SPR transducer using phase interrogation mode. (First column) Sensogram of the **a.** wavelength, **c.** phase and **e.** phase derivative at resonance when the surrounding medium is varied using NaCl solutions. (Second column) Relative changes to water of the **b.** wavelength, **d.** phase and **f.** phase derivative at resonance. The red plot represents a linear fitting

To enable a comparison of the three sensing approaches within the phase interrogation method, the RIR must be established. Assessing the standard deviation in the three detection modes—wavelength, phase, and phase derivative—involved recording the LSPR signal continuously for 5 minutes while the microfluidic device was filled with water. The subsequent data processing allowed for the calculation of both the mean and the standard deviation. This analysis produced a wavelength standard deviation of $3.3 \times 10^{-4} \text{ nm}$, a phase standard deviation of $6.0 \times 10^{-5} \text{ rad}$, and a phase derivative standard deviation of $3.5 \times 10^{-6} \text{ rad nm}^{-1}$. Consequently, the RIR values were determined to be $5.2 \times 10^{-8} \text{ RIU}$ for wavelength detection, $4.3 \times 10^{-7} \text{ RIU}$ for phase detection, and $3.7 \times 10^{-6} \text{ RIU}$ for phase derivative detection mode.

4.3.1 Discussion

First, we compare two methods that utilize the resonance wavelength as a marker in ATR configuration: *i*) the resonance wavelength extracted from the intensity spectra, identified as the minimum position of reflectance spectra, and *ii*) the resonance wavelength derived from the phase spectra, identified at the maximum position in the spectral phase derivative. We observed that method *i*) achieves a higher RIS of 9970 nm RIU^{-1} compared to method *ii*), where it is measured at 6360 nm RIU^{-1} . However, the phase interrogation mode (method *ii*) demonstrates a smaller standard deviation, which contributes to enhanced refractive index resolution.

When comparing measurements with three different resonance markers within the phase interrogation mode, the data suggest that wavelength detection offers the highest resolution (lowest RIR), potentially making it the preferred choice for applications requiring the highest sensitivity. Note, however, that as we will demonstrate in the following section, phase detection achieves the highest sensitivity when amplitude is minimal, i.e., in the so-called topological darkness regime. This regime is challenging to achieve in SPR mode; however, we will show that it can be accomplished in LSPR mode using a random metasurface.

Note that the phase dependence on refractive index is nonlinear, as evidenced by the significant disparity in RIS between two refractive index intervals 271 rad RIU^{-1} in the first and 113 rad RIU^{-1} in the second, which may indicate saturation at higher analyte concentrations. The dynamic range comparison between the two interrogation modes reveals that the wavelength interrogation mode has a wider dynamic range of 0.045 RIU , while the phase interrogation mode has a more limited range of 0.0021 RIU . Nevertheless, in biosensing applications, small changes in the SPR phase signal are expected, and they typically fall within the dynamic range of phase interrogation. Consequently, phase interrogation was preferred for conducting sensing experiments with different analytes.

4.4 SPR sensing of various analytes

In the previous section, we examined the response of the SPR transducer to changes in bulk refractive index and its performance characteristics such as RIS, FWHM, FOM, and RIR. In this section we explore the fundamentally different response when the sensor detects specific biomolecular binding events between an analyte and a bioreceptor, in particular those discussed in Section 3.7. Based on the characterization of the sensing performance parameters of the Au NFs, an Au NF with a thickness of 50 nm , deposited atop a 1 nm thick Ti NF, was utilized as the transducer for these biosensing experiments. The experimental setup was the spectral interferometer, which employed an angle of incidence as close as possible to the critical angle for the glass-water interface.

4.4.1 Polyelectrolytes LbL system detection

When transitioning from detecting bulk refractive index changes to sensing specific biomolecular binding events, the dynamics and the nature of the response can differ significantly. Binding events lead to local changes at the sensor surface rather than bulk refractive index changes. This localized change affects the surface plasmon waves differently because the interaction is confined to the immediate vicinity of the bound molecules. The sensitivity might not only depend on the refractive index change but also on the mass, size, and the specific orientation of the biomolecules attached to the sensor surface.

One effective method to characterize the sensor response to molecular binding events is through the use of multilayer or LbL systems employing polyelectrolytes. These systems can build up a precisely controlled nanostructured film on the sensor surface. The polyelectrolytes are prepared in solutions, such as a 1:1 ratio in an aqueous solution with a NaCl concentration of 0.3 M, to ensure proper layer formation and stability.

Figure 4.12 show the sensogram for detecting polyelectrolytes LbL binding events using three different resonance markers in phase interrogation mode: resonance wavelength, phase, and phase derivative. The process begins with establishing a stable baseline (area marked by blue color) by monitoring the resonance wavelength in the presence of a buffer solution for 2.5 minutes. This baseline phase is crucial as it sets a reference point for detecting shifts induced by biomolecular interactions.

Upon the addition of the PAH polyelectrolyte, there is a notable redshift in the resonance wavelength by approximately 3 nm, indicating the initial layer's successful adsorption onto the Au NF. It is important to ensure that the SPR signal stabilizes following each polyelectrolyte deposition. Initially, upon the introduction of a polyelectrolyte, the resonance wavelength experiences a sharp increase, indicative of the first layer's interaction with the sensor surface. After this, the resonance wavelength continues to gradually increase. This ongoing change, although less pronounced, suggests a continuing adjustment of the molecular layers on the sensor surface. After approximately 15 minutes, the resonance wavelength reaches a stable state, indicating that the interactions at the sensor surface have equilibrated and the system is ready for the next layer's deposition.

Following the deposition of PAH on the Au NF, the subsequent addition of the PSS polyelectrolyte, as depicted in the first red column of Figure 4.12, induces a notable redshift in the resonance wavelength, this time by approximately 11 nm. This larger shift could be attributed to the different molecular structure and density of the PSS layer compared to PAH, suggesting a significant alteration in the local refractive index at the interface. This change represents the formation of the first bilayer (PAH-PSS). After this, PAH and PSS are alternately deposited, with each deposition consistently resulting in further redshifts of the resonance wavelength, systematically building up the multilayer structure.

Figure 4.12b and Figure 4.12c demonstrate the sensogram of the polyelectrolyte deposition process using phase and phase derivative detection modes, respectively. These figures show analogous behavior to that observed with the wavelength detection mode.

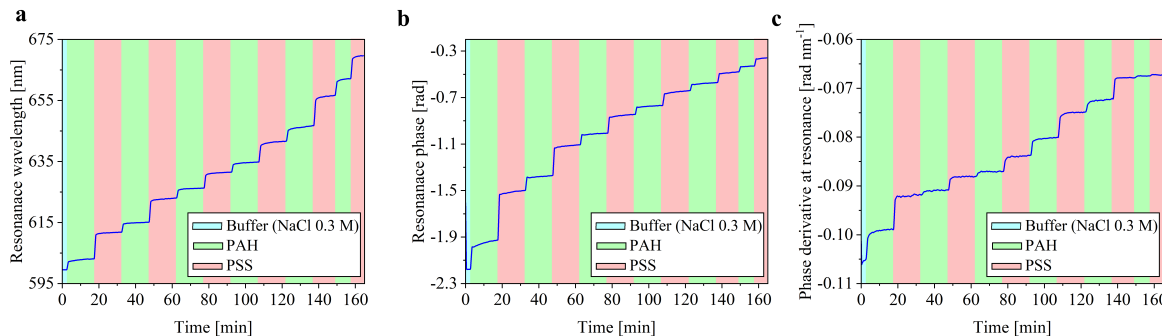


Figure 4.12: Sensogram of the polyelectrolytes deposition on a Au NF using **a.** wavelength, **b.** phase and **c.** phase derivative detection modes. Blue columns represent the SPR signal when running the buffer, while green and red column corresponds to PAH and PSS deposition, respectively. The angle of incidence of 68°

After the deposition of each polyelectrolyte layer, the surface is rinsed with buffer solution

to remove any unbound molecules. The stability of the resonance wavelength post-washing indicates that the polyelectrolytes are firmly attached to the surface.

To further investigate the LbL assembly of polyelectrolytes on Au NF surfaces, the experiment was conducted across various NaCl concentrations in the buffer solution. The aim was to discern the impact of NaCl concentration on the polyelectrolyte bilayer's thickness. Employing NaCl concentrations of 0.1 M, 0.3 M, and 1.0 M—while maintaining the polyelectrolytes in a 1:1 ratio—the RIS of the Au NFs was evaluated. Post five bilayer depositions, the relative shifts in resonance wavelength compared to the buffer is depicted in Figure 4.13a. In the wavelength detection mode, a clear linear trend is observed in the response to the number of polyelectrolyte layers deposited. A steeper slope in the resonance wavelength shifts correspond to the buffer solution with higher NaCl concentration. This steeper slope implies that increased optical thickness of the individual layers.

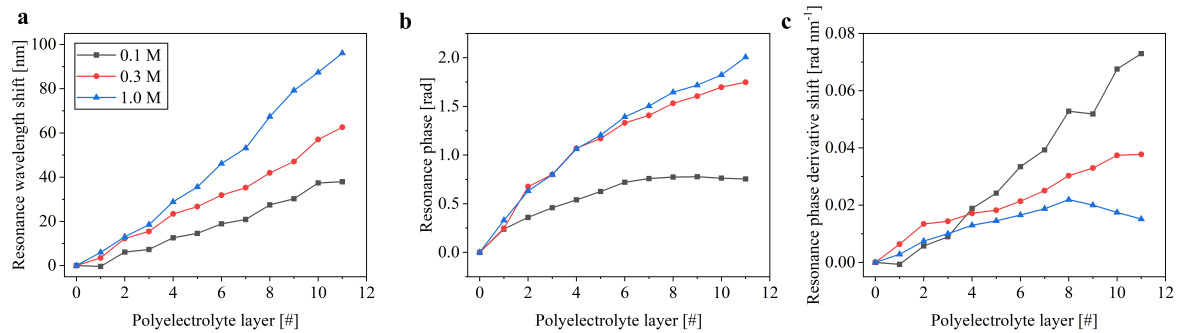


Figure 4.13: Relative changes of **a.** wavelength, **b.** phase and **c.** phase derivative at resonance to buffer when PAH and PSS polyelectrolytes are alternatively deposited on the Au NF

The equation to compute the change in the effective refractive index Δn_{eff} due to thin-layer adsorption takes into account the thickness of the adsorbed layer d_l , the refractive indices of the layer n_l and the buffer n_b , and the penetration depth of the evanescent field L_{pd} [145]

$$\Delta n_{\text{eff}} = \frac{2d_l}{L_{\text{pd}}} (n_l - n_b). \quad (4.1)$$

Using the changes in the resonance wavelength resulting from polyelectrolyte adsorption in tandem with the calibrated bulk RIS, the thickness of each bilayer can be derived from the above equation. The computed average thickness for each bilayer is 2.1 nm at 0.1 M NaCl, 3.5 nm at 0.3 M, and 5.0 nm at 1.0 M concentration. These results are corroborated by previous studies such as those by Kedem, O. et al. [146], who observed similar trends using metallic nanoparticles on a glass substrate as the sensing platform.

The increase in bilayer thickness at higher NaCl concentration can be explained by two factors: changes in macromolecule conformation and effect of bilayer swelling. At higher ionic strengths, the increased concentration of NaCl in the buffer solution leads to a greater screening of the electrostatic charges on the polyelectrolyte chains. This screening effect reduces the mutual repulsion between similarly charged segments of the polymer, allowing the chains to transition from a more extended (coil-like) configuration to a more compact (globular) one. However, this compaction is not just a simple collapse; it allows for a certain degree of expansion perpendicular to the substrate, contributing to the overall thickness of the adsorbed layer.

Furthermore, the presence of more ions from the added salt contributes to the osmotic pressure differential between the polyelectrolyte layer and the surrounding solution. This

differential causes the layer to absorb more water, leading to osmotic swelling. The polyelectrolyte layer acts like a sponge, with the polyelectrolyte chains acting as a network that traps water molecules. This process further increases the volume and thickness of the polyelectrolyte layer.

Note, that the phase and phase derivative detection modes, see Figure 4.13b and c, exhibit a nonlinear response to the increase in overall thickness of the adsorbed macromolecules layer. This suggests that phase and phase derivative measurements have a limited dynamic range and are more suited to detecting very thin layers.

4.4.2 Streptavidin-biotin binding event detection

In this section, the experiment for detecting the binding event of the streptavidin-biotin system was conducted. A 50 nm thick Au NF was functionalized with streptavidin, followed by biotin binding. The preparation procedures for both molecules are outlined in Section 3.7.3. To achieve a higher SPR shift due to streptavidin-biotin interactions, the angle of incidence was reduced to 65°, closer to the critical angle.

Figure 4.14 illustrates the sensogram of the functionalization and binding processes in the streptavidin-biotin detection using phase interrogation in both wavelength and phase detection modes. Initially, the reference SPR response was obtained by introducing a buffer solution (where streptavidin and biotin are diluted in the subsequent steps). The wavelength and phase at resonance were monitored for several minutes until the response stabilized (blue column in Figures 4.14).

Subsequently, the functionalization of the Au NF was achieved by circulating streptavidin through the microfluidic device at a controlled flow rate of 0.5 mL min⁻¹, as shown in the green columns of Figures 4.14a and 4.14b. The SPR response becomes higher significantly until reaching a plateau, which indicates the completion of the surface functionalization. It is noteworthy that the interaction dynamics of streptavidin with the Au NF are notably slower compared to those of polyelectrolytes, as illustrated in Figure 4.12. This suggests a more intricate binding mechanism, potentially attributable to the steric and specific binding characteristics inherent to the AuNF-streptavidin configuration. It is assumed that streptavidin is attached to the surface of the Au NF via electrostatic interactions. At pH 7, the surface charge of the Au NF is negative, which facilitates the electrostatic attachment of the positively charged lysine or histidine amino groups on the streptavidin surface, as reported in previous studies. [147]

Following this, water is injected into the microfluidic device to wash away any unbound streptavidin from the Au NF, leading to a slight increase in the SPR signal. To ensure complete functionalization of the Au NF surface, streptavidin is introduced followed by a buffer wash on two additional occasions. The gradual reduction in the redshift of the SPR signal from the first to the third streptavidin injection indicates a decrease in the available surface area on the Au NF for functionalization. In Figures 4.14a and 4.14b, the fourth blue column represents the resonance wavelength and phase, respectively, after the Au NF has been washed. The SPR response remains relatively stable, indicating that the Au NF surface remains covered with streptavidin.

Subsequently, biotin is injected to interact with the functionalized Au NF surface using the injection pump. The changes in the SPR response, illustrated in Figures 4.14a and 4.14b, correspond to the introduction of biotin into the microfluidic device. Given biotin's small size, the alterations in the SPR response are relatively minor compared to the initial functionalization process depicted by the green columns.

Biotin is injected into the microfluidic system on two additional occasions, with each subsequent injection resulting in progressively smaller changes in the SPR response. This pattern suggests that the availability of sites for binding with biotin decreases with each injection. The hybridization process concludes with a buffer wash of the Au NF surface. Following this wash, the SPR response stabilizes, indicating that neither streptavidin nor biotin detaches from the surface.

The LOD is then determined based on the SPR shift's dependence on successive biotin depositions. By calculating the RIS for the initial deposition of biotin and applying Equation (2.89), the LOD is determined to be 6.6 nM.

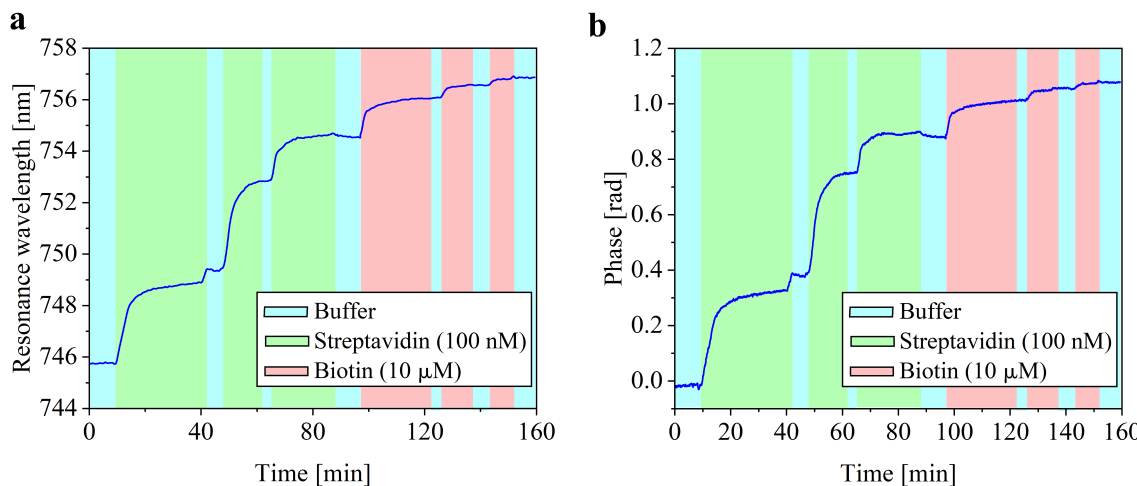


Figure 4.14: Sensogram of **a.** wavelength and **b.** phase at resonance using phase interrogation mode. The functionalization of the Au NF surface using an aqueous solution of 100 nM streptavidin is indicated by the green columns. While the hybridization process with an aqueous solution of 10 μ M biotin is represented by red columns. The washing of the Au NF using the buffer is shown with blue columns

4.4.3 Conjugated oligonucleotides binding event detection

The final experiment involves the detection of binding between two complementary RNA strands specific to SARS-CoV-2. The oligonucleotide used to functionalize the Au NF surface is thiolated, whereas the complementary strand for hybridization is not. Both oligonucleotides are diluted in nuclease-free water, with the preparation procedure detailed in Section 3.7.4. Due to the unavailability of the standard 50 nm Au NF, a transducer comprising a 1 nm Ti NF and a 54 nm Au NF was utilized. The angle of incidence was set at 65°.

Figure 4.15 presents a sensogram of the functionalization and hybridization processes of the conjugated oligonucleotides using phase interrogation mode. The SPR baseline response is first established by flowing the buffer through the system for approximately three minutes while monitoring the resonance wavelength and phase (first blue column in Figures 4.15a and 4.15b, respectively). Subsequently, the surface of the Au NF is functionalized by introducing the thiolated oligonucleotides at a concentration of 10 μ M into the microfluidic device (red column in Figure 4.15). To ensure complete functionalization, the thiolated oligonucleotides are reinjected at the same concentration. The stability in the position of the SPR wavelength and phase after this step confirms the complete functionalization of the Au NF.

Due to the inherent fragility of RNA strands, the stability of the bioreceptors (thiolated oligonucleotides) on the Au NF surface may be influenced by environmental factors such as

temperature or the pH of the buffer solution. Additionally, the random orientation of bioreceptors can hinder their effective binding to the analytes (complementary oligonucleotides). Following the method described by Qiu et al. [45], the complementary oligonucleotides were prepared at a reduced concentration of 5 nM to optimize hybridization efficiency.

The hybridization process is initiated by injecting these complementary oligonucleotides into microfluidic camber atop of the functionalized Au NF surface. The resultant increase in the SPR signal, as shown in both the wavelength and phase sensograms (green column in Figures 4.15a and 4.15b, respectively), indicates successful binding of the complementary oligonucleotides to the thiolated oligonucleotides already attached to the surface.

Hybridization is repeated until the SPR wavelength and phase stabilize, signifying saturation of the bioreceptors' binding capacity. Subsequently, the Au NF surface is washed with nuclease-free water to remove unbound material. Although the SPR wavelength and phase slightly decrease after washing, they remain elevated compared to the initial reference (blue column) and the functionalization step (green column). This stable, elevated signal reflects changes in the refractive index due to the hybridization of the analytes with the bioreceptors.

The RIS is calculated by assessing the SPR shifts resulting from successive injections of 5 nM complementary oligonucleotides onto the functionalized Au NF surface. The LOD is then determined using Equation (2.89), yielding a value of 5.2 pM.

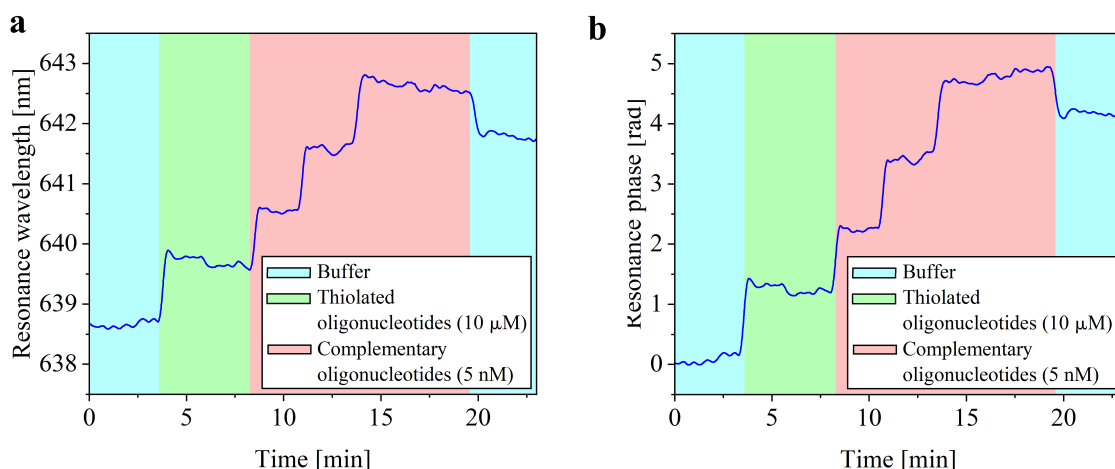


Figure 4.15: Sensogram of complementary SARS-CoV-2 oligonucleotides detection. **a.** Wavelength and **b.** phase sensogram of the functionalization of the surface of a Au NF with thiolated oligonucleotides (green columns) and hybridization with complementary oligonucleotides (green columns) using a common path spectral interferometer. The baseline and the washing at the end of the experiment is represented by blue columns

4.4.4 Discussion

This study successfully detected various biomolecular systems. Initially, the polyelectrolyte LbL system was deposited on the Au NF surface using buffers with different NaCl concentrations. It was observed that increasing the saline concentration led to an increase in the thickness of the polyelectrolytes. The presence of salt induced electrostatic screening, causing the polyelectrolyte chains to transition from an extended to a more globular conformation as the salt concentration increased. [148, 149] The maximum thickness, measuring

5.0 nm, was achieved with a buffer containing 1.0 M of NaCl. A total of 6 bilayers were deposited, resulting in a consistent redshift of the SPR wavelength with each deposition, as depicted in Figure 4.12. Considering a resonance wavelength of 612 nm, the penetration depth of the evanescent field into the dielectric medium was estimated using Equation (2.63), yielding approximately 161 nm. Therefore, the SPR signal did not saturate following the deposition of 30 nm thick layers of polyelectrolytes on the Au NF surface. Accurately measuring the SPP penetration length would require the deposition of at least 26 additional bilayers, corresponding to roughly 12 hours of experimentation.

The second system investigated was the streptavidin-biotin binding interactions. Notably, streptavidin is significantly larger than biotin, with dimensions of approximately 4.2 nm × 4.2 nm × 5.8 nm according to Li, Y. and Zhang, H. [150] This difference is evident in the sensogram (Figure 4.14), where the SPR shifts are more pronounced during the functionalization process (Au NF-streptavidin interaction) compared to the hybridization process (streptavidin-biotin interaction). The LOD for biotin was determined to be 6.6 nM, which aligns with findings from similar studies. [151–153]

Finally, the functionalization-hybridization process using conjugated oligonucleotides was evaluated. The LOD achieved was 5.2 pM, surpassing the values reported in previous studies utilizing conjugated oligonucleotides [154–156] and is comparable to other similar works. [113] This demonstrates the high sensitivity and specificity of the detection system employed in this research.

Chapter 5 |

LSPR: Results and Discussion

This chapter presents the theoretical and experimental study of the LSPR phenomenon in random metasurfaces based on Au NI onto a glass substrate.

Initially, the morphological characterization of the fabricated nanoparticles was performed using SEM and AFM methods. These analyses yielded the main parameters of the Au NI, including its shape, dimensions, degree of embedding into the glass substrate, and the surface coverage of the Au NI array.

The island film theory was used to calculate the modified Fresnel coefficients of a three-layered system, which is composed of a glass substrate, the Au NI array, and the surrounding medium. The calculations were conducted under ATR condition and for both p and s polarization components.

To explore the scope of theoretical model, the reflectance spectra of spherical and spheroidal shaped nanoparticle arrays were calculated under different angles of incidence and wavelengths. Following this, and using the size parameters of the fabricated nanoparticles, the transmittance spectrum at normal incidence was analytically obtained, complemented by experimental measurements under identical conditions.

Further, theoretical R_p and R_s spectra of the Au NI were computed for two angles of incidence, assuming water as surrounding medium. Experimental measurements of reflectance spectra of the Au NI using the Kretschmann configuration for both p and s polarization components provided validity of the theoretical findings.

Additionally, the theoretical and experimental dependence of LSPR wavelength on the refractive index of the surrounding medium were explored, focusing on determining the RIS in both theoretical and experimental scenarios. Furthermore, the experimental dependence of LSPR response was obtained using the phase interrogation mode.

Lastly, the topological darkness phenomenon was theoretically predicted and experimentally demonstrated in a random array of Au NI using the phase interrogation mode.

To enhance clarity and coherence, the subsequent sections of this chapter are structured into three distinct parts: first, the presentation of theoretical calculations utilizing the island film theory model, followed by experimental measurements, and finishing in a discussion of the findings.

5.1 Morphological characterization of the Au NI arrays

5.1.1 SEM analysis of Au NI arrays

As detailed in Section 3.1.2, Au NI were fabricated by deposition of ultra-thin Au NF on a glass substrate, followed by a thermal annealing at 530° for 3 hours. Figure 5.1a to Figure 5.1h depicts SEM micrographs of the fabricated Au NI arrays. The initial thickness of the Au NF is indicated in the left top corner of each SEM image, which range from 3 nm to 17 nm. Note that the scale bar is different for each SEM image. A photograph of the real sample is shown in the left down corner of the SEM images.

Arrays obtained from ultra-thin Au NF with initial thicknesses of 3 nm and 5 nm, demonstrate Au NI with a uniform circular morphology as depicted in Figure 5.1a and Figure 5.1b. The rest of the Au NI arrays present more and more elongated nanostructures as the Au NF nominal thickness increases, resembling an ellipse. Particularly, the sample fabricated with nominal thickness of 13 nm shows various nanostructures with hexagonal shape, see Figure 5.1f.

Concerning the size of the Au NI, SEM micrographs reveal a diverse range of sizes within the same array. Subsequently, a statistical analysis of the processed SEM images yields the size distribution of the Au NI, which exhibit a Gaussian behaviour. The mean radius of the Au NI is determined by Gaussian fitting the size distribution and regarding the position of the centre of the peak.

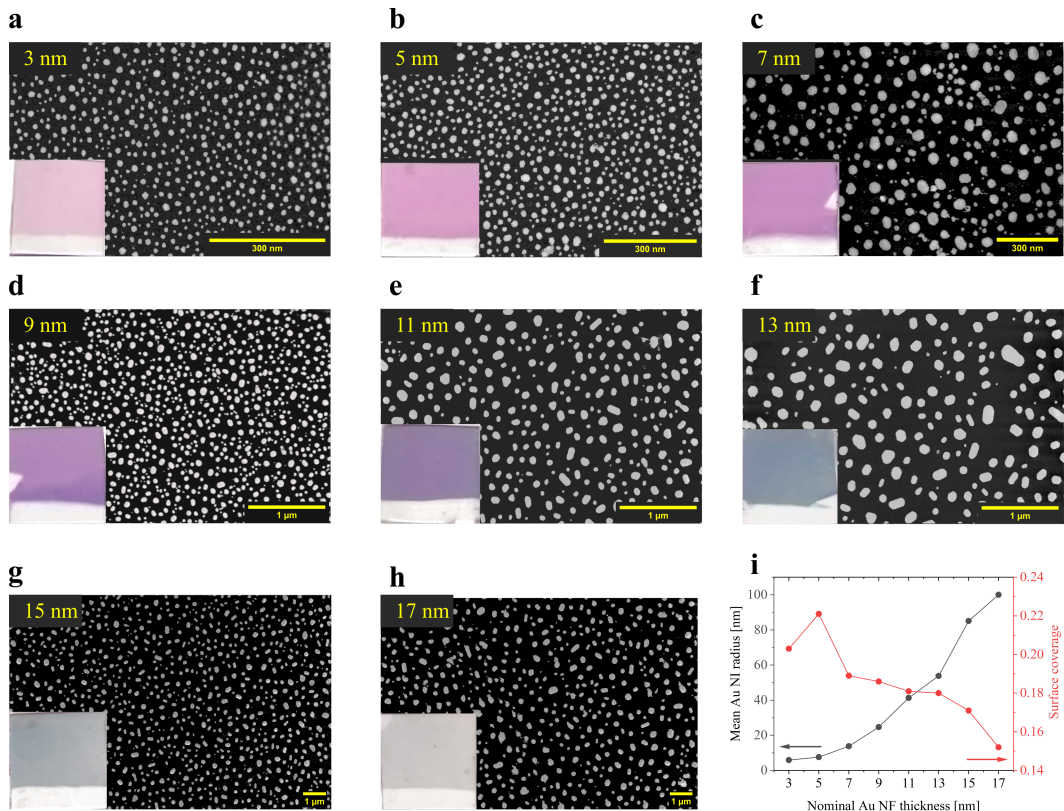


Figure 5.1: a-h. Processed SEM micrographs of Au NI arrays for different nominal thickness of the initial Au NF, marked in the upper left corner of each image. i. Mean Au NI radius (black) and surface coverage (black) dependence on the initial Au NF thickness. A photograph of each fabricated Au NI arrays is shown in the lower left corner of the SEM micrographs. Note that the scale bar is in general different for each micrograph

The dark plot in Figure 5.1i illustrates the relationship between the mean radius of the Au NI and the initial thickness of the Au NF. It reveals a strong influence of the Au NF thickness on the size of the Au NI. Particularly noteworthy is the power-law growth of Au NI size with the initial thickness of the Au NF, resulting in Au NI ranging from 5.9 nm to 100.0 nm in radius. Furthermore, the proportion of the substrate occupied by the Au NI, also referred to as surface coverage (Θ) is evaluated through SEM micrograph analysis. In this study, the surface coverage is quantified by values between 0 and 1, where 0 represents no coverage and 1 represents complete coverage. Additionally, the surface density (ρ) is defined as the amount of Au NI per unit of area on the substrate. Considering circular shaped nanoparticles, the surface coverage and the surface density are related by the expression $\Theta = \rho\pi a^2$.

The red plot in Figure 5.1i illustrates the surface coverage dependence on the initial Au NF thickness. It indicates a slight decrease in surface coverage as the initial Au NF thickness increases. However, Au NI arrays obtained from initial Au NF thicknesses ranging 7 nm to 13 nm, show nearly constant surface coverage, averaging at 0.184. Overall, the surface coverage of the samples obtained ranges from 0.152 to 0.203.

5.1.2 AFM analysis of Au NI arrays

Next, the main topographic features of the Au NI were obtained through AFM images. To facilitate the comprehension of the results, a representative AFM image of the sample with a mean radius of 24.7 nm is provided in Figure 5.2. For smaller Au NI ($r < 13.8$ nm), measuring the height and the crater depth becomes challenging due to the diameter of the AFM tip, which is 10 nm, rendering it impossible to spatially resolve the height of the Au NI as well as its crater depth.

In Figure 5.2a, a $4 \mu\text{m}^2$ AFM image illustrates the height of the Au NI supported on the substrate. The colour bar indicates the distance from the substrate (dark – 0.0 nm) to the top of the Au NI (white – 37.3 nm).

Figure 5.2b shows a topographic image of the substrate after removal of the Au NI from its surface. Residual craters can be appreciated in the image, providing experimental evidence of the partial embedding of the Au NI into the substrate. In this case, the crater depth is represented by negative values on the colour bar. This convention is because the reference, indicated by the orange colour in the colour bar, represents the substrate plane, while the distance from the substrate to the maximum crater depth is depicted by the darker colours.

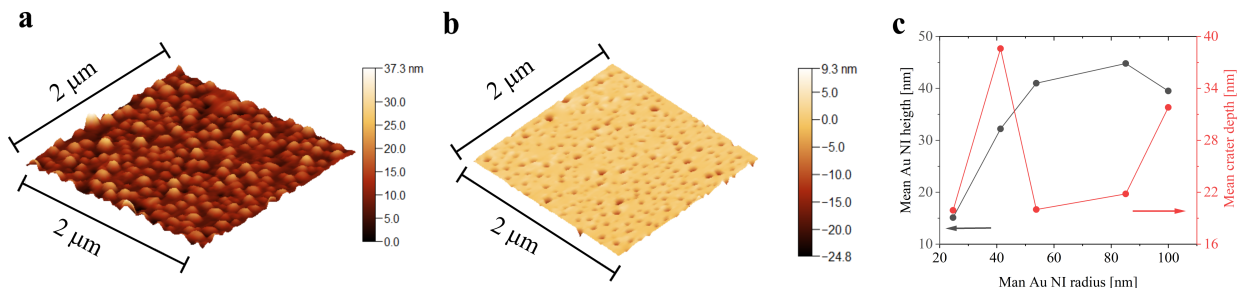


Figure 5.2: Representative AFM from the Au NI **a.** heights and the **b.** crater depth after removing Au NI from the substrate. **c.** Au NI height and crater depth dependence on the Au NI size

The relationship between the Au NI height and its size is illustrated in Figure 5.2c (black

circles). Initially, the height increases rapidly with the Au NI radius, then, it saturates and even decreases for largest nanoparticles (radius of 100 nm). This means that for largest nanoparticles the aspect ratio (in a cross-section which is perpendicular to the substrate plane) is increasing for larger nanoparticles.

The red circles in Figure 5.2c depicts the crater depth as a function of the Au NI radius. Except for the sample with a radius of 41.3 nm, the trend of crater depth is to increase as the radius of the Au NI increases.

5.1.3 Discussion

Table 5.1 summarizes the morphological characteristics of the Au NI arrays obtained from statistical analysis of SEM and AFM micrographs. SEM analysis shows a wide range of mean radii for the resulting Au NI, spanning from 5.9 nm to 100.0 nm. This demonstrates the capability of achieving diverse Au NI dimensions through controlled variation of the Au NF thickness using the dewetting technique.

To calculate the total height of the Au NI, representing the distance from the bottom of the crater to the top of the Au NI, the values from the "Mean Au NI height" and "Mean crater depth" columns are summed. As mentioned previously, Table 5.1 contains incomplete data on the height of Au NI and its crater depth due to equipment limitations. However, AFM measurements reveal that the total height of Au NI ranges from 35.0 nm to 71.3 nm for Au NI arrays obtained from depositions of the Au NF with thickness from 9 nm to 17 nm. Additionally, Au NI with radius of 24.7 nm and 41.3 nm, a greater portion of the Au NI is embedded in the substrate compared to the portion protruding above the substrate. Conversely, for the remaining samples, the opposite trend is observed.

To determine the shape of the Au NI, the aspect ratio was determined as the ratio between mean Au NI radius and total height, resulting in values ranging from 1.41 to 2.53. It is observed that as the radius of the Au NI increases, the spheroidal shape becomes more pronounced.

5.2 Island film theory-based analysis of reflectance spectra for Au NI arrays

5.2.1 General remarks

The analytical reflectance spectra of the Au NI arrays are modelled using island film theory in the low coverage limit. The metasurface is considered as a three-layer system, which consists of glass, Au NI, and a surrounding medium. Within this model, the Au NI are identical and randomly distributed on top of the glass layer, immersed within the ambient medium.

The reflectance spectra of Au NI arrays are calculated for a wide range of angles of incidence, as well as wavelength. For this reason, the reflectance spectra will be presented as a grayscale map the horizontal axis represents the wavelength of incidence, while the vertical axis represent the angles of incidence. The grey level represents the value of the reflectance at specific angle and wavelength of incidence. It is expressed in values from 0 to 1, corresponding to black to white colours, where black indicates zero reflection and white complete reflection of the incident electric field. In particular, when total internal reflection is achieved, the critical angle will be marked with a dashed cyan line.

Table 5.1: Summary of the morphological characterization of Au NI arrays extracted from the SEM and AFM analysis. The Au NI arrays were fabricated by depositing an ultra-thin Au NF, followed by a thermal annealing at 550°C for 3 hours

Initial Au NF thickness [nm]	Mean Au NI radius [nm]	Mean Au NI height [nm]	Mean crater depth [nm]	Total Au NI height [nm]	Aspect ratio of Au NI	Surface coverage	Surface density [$\text{Au NI } \mu\text{m}^{-2}$]
3	5.9	—	—	—	—	0.203	1856
5	7.6	—	—	—	—	0.221	1218
7	13.8	—	—	—	—	0.189	316
9	24.7	15.1	19.9	35.0	1.41	0.186	99
11	41.3	32.2	38.6	70.8	1.17	0.181	34
13	53.8	41.0	20.0	61.0	1.76	0.180	20
15	85.1	44.8	21.8	66.6	2.56	0.171	8
17	100.0	39.5	31.8	71.3	2.81	0.152	5

The format for the presentation of the spectra allows to simultaneously visualize the reflectance spectra under angular and wavelength interrogation modes.

5.2.2 Size and shape influence on the reflectance spectra of Au NI

The primary objective of this analysis is to gain an understanding of the reflectance spectra of the metasurfaces, with a focus on the effects of particle shape (spheres vs. spheroids) and size.

Figure 5.3 presents a wavelength- and angle-dependent analysis of the investigated reflectance spectra of both Au NI shapes, which is indicated on the left of each gray map. The first row of Figure 5.3 shows a case of spherical particles, while the subsequent rows represent spheroids of increasing sizes. The left and right columns correspond to p and s polarized incident electric field, respectively. The p polarization of the electric field is indicated by vertical black arrows, while the s polarization component is indicated by black circles, indicating the arrowhead. For the angles above the critical, the LSPR minima are discernible as darker regions on the graymap, with their exact locations demarcated by dashed yellow lines.

Initially, the R_p and R_s spectra of a Au nanospheres array with radius of 20.0 nm and surface coverage of 0.175 are calculated employing Equations (2.77) and (2.78), respectively.

Notably, for R_p (Figure 5.3a) and R_s (Figure 5.3b), a LSPR plasmonic mode is observed, and it remains constant regardless of the angle of incidence. This is expected due to the spherical symmetry of the Au NI. However, the position of the LSPR dip for p polarization is located at ~ 534.7 nm, while for s polarization is located at ~ 535.4 nm. The slight redshift in the s polarization LSPR dip position can be attributed to the influence of the substrate.

Following that, the reflectance of an Au nanospheroids array was calculated using Equation (2.79) and Equation (2.80), as show in the second and third row of Figure 5.3. The main parameters defining the nanospheroids include a major semi-axis of 20.0 nm, a minor semi-axis of 11.0 nm. Additionally, larger nanospheroids are considered, with major semi-axes of 50.0 nm and minor semi-axes of 27.8 nm. The aspect ratio (major semi axis/minor semiaxis) of both nanospheroid arrays remains constant at a value of 1.8, as well as the surface coverage, which remains at a value of 0.2.

In this case, several key observations can be made: *i*) The R_p spectrum exhibits two plasmonic modes, whereas the R_s spectrum shows only one; *ii*) the s polarization LSPR dip is redshifted relative to the p polarization; *iii*) the position of the LSPR is now dependent on the angle of incidence (from 552 nm to 611 nm); *iv*) as the size of the spheroids increases, keeping the aspect ratio, the p polarization LSPR dips become deeper, while the s polarization LSPR dip redshifts and tend to disappear.

Next, the reflectance of Au nanospheroids with similar characteristics to those Au NI fabricated was calculated, as shown in Figure 5.4. The main parameters are major semis axis of 50.2 nm, minor semi axis of 38.1 nm and surface coverage of 0.157.

In Figure 5.4a two plasmonic modes are observed when the Au nanospheroids are illuminated under p polarized electric field. The first one, marked with dashed yellow line, appears close to the critical angle, and it extends from 500 nm to 585 nm, while the second one (marked with dashed violet line) is located at angles above 65° and it extends from 608 nm to 662 nm. In both cases, the resonance position redshifts with increasing angle. At an angle of $\sim 74^\circ$ both plasmonic modes combine forming a single and broad plasmonic mode.

In contrast, for s polarization component (Figure 5.4b) a plasmonic mode is rather broad

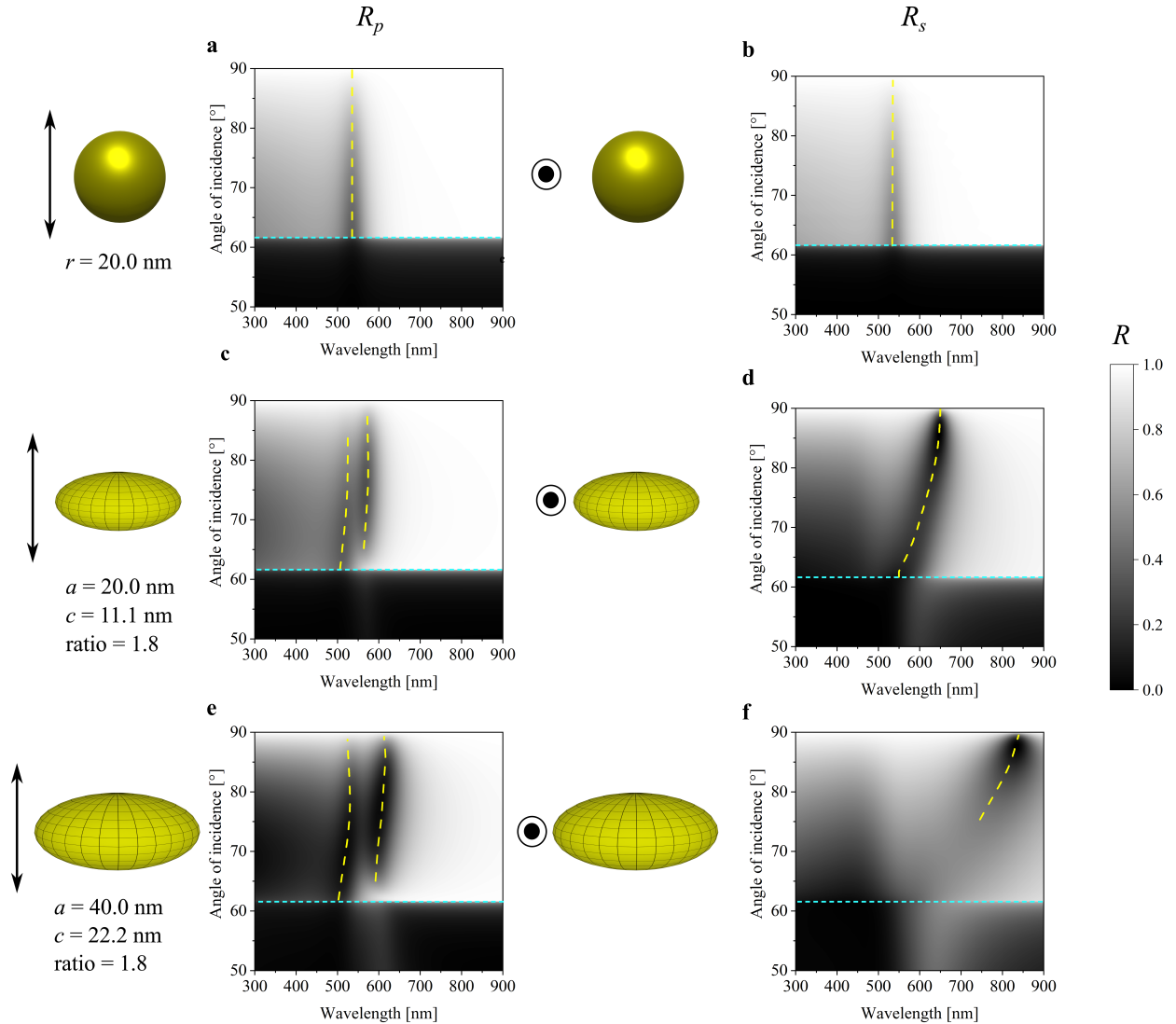


Figure 5.3: Angle- and wavelength- dependent reflectance of an Au nanoparticles array supported on a glass substrate for p (first column) and s (second column) polarization component under internal incidence. Sphere and spheroid shaped nanoparticles were studied. The first row shows the reflectance of the spheres random array, with radius $r = 20.0 \text{ nm}$. The second row displays the reflectance of the spheroids random array, with major and minor semi-axes of 4 nm and $b = 11.0 \text{ nm}$, respectively. The reflectance of larger spheroids with the same ratio is shown in the third row. The dimensions of this spheroid array are $a = 40.0 \text{ nm}$ and $b = 22.2 \text{ nm}$. The surface coverage of all the nanoparticle array is 0.2 In all the cases the yellow dashed line indicates the resonance position, while the blue short-dashed line indicates the critical angle (62.5°) considering the glass-water interface. The vertical black line to the left indicates the parallel polarization component of the electric field, considering the plane of incidence parallel to the page; the black circle indicates the perpendicular polarization component of the electric field. The grey bar indicates the reflectance value

and shallow for larger wavelengths.

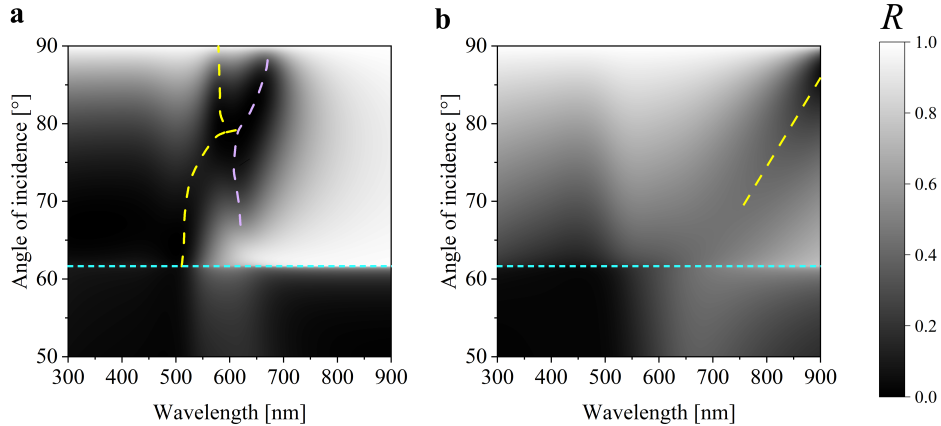


Figure 5.4: Angle- and wavelength- dependent reflectance of an Au nanospheroids under **a.** p and **b.** s polarization component of the incident electric field. The main characteristics of the nanospheroids array are a major semi-axis of 50.0 nm, minor semiaxis of 38.0 nm and surface coverage of 0.16

To better illustrate the differences of the reflectance spectra of Au nanoparticle arrays composed of spheres or spheroids, line profiles were extracted from their respective grey maps. Figure 5.5a and Figure 5.5b show the reflectance spectrum of Au nanoparticle arrays under p and s polarization, respectively, with an angle of incidence of 70°.

The dark line in Figure 5.5 corroborates the presence of a well-defined plasmonic modes for both polarization states, with redshifted resonance positions for s polarized light. Furthermore, the LSPR dip under s polarized light appears deeper compared to that under p polarized light.

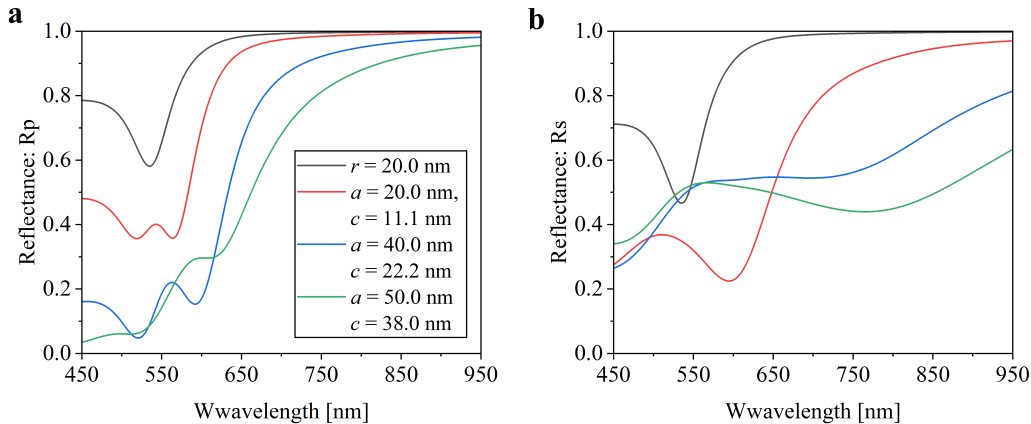


Figure 5.5: Angle- and wavelength- dependent reflectance of an Au nanospheroids under **a.** p and **b.** s polarization of the incident electric field. The main characteristics of the nanospheroid array are a major semi-axis of 50.0 nm, minor semiaxis of 38.0 nm and surface coverage of 0.16

For spheroids with a major semi-axis equal to the radius of spheres (red plot in Figure 5.5), the reflectance spectrum under p polarized light shows two distinct plasmonic modes, whereas under s polarized light, it shows a single, broad plasmonic mode.

As the size of the nanospheroids increases, the two plasmonic modes in the reflectance of p polarized light, separate and become deeper. The first plasmonic mode remains constant,

while the second plasmonic mode has a redshift. Conversely, in the reflectance under s polarized light, the plasmonic mode becomes very broad, making it less discernible.

5.2.3 Discussion

The observation of a plasmonic dip in both R_p and R_s calculated spectra for an Au nanosphere array, using island film theory, aligns qualitative by calculations for other theoretical models such as the dipolar model and coherent scattering model. This consistency validates the model employed in this study for subsequent calculations.

In case of spheroids, the difference in plasmonic modes between p and s polarization states arises from their inherent anisotropy. Specifically, p polarized light, with its electric field oscillating parallel to the plane of incidence, perceives the elliptical cross-section of spheroids, thereby exciting two distinct plasmonic modes corresponding to the spheroid's major and minor axes. Conversely, s polarized light, oscillating parallel to the substrate, encounters a symmetrical circular cross-section equivalent to the spheroid's long axis, thus showing a single plasmonic mode.

The observed redshift in the LSPR dip for s polarized light versus p polarized light can be ascribed to the effective dimensional disparity, the s polarized regime interacts with a geometrically larger cross-section, leading to longer plasmon oscillation wavelengths. The same dimensional effect underpins the shift of LSPR peaks toward longer wavelength as spheroid size increases for both polarization states. Larger spheroids support slower plasmonic oscillation, thus producing redshifted resonances.

5.3 Transmittance spectrum of Au NI arrays at normal incidence

The optical properties of the Au NI arrays with sizes similar to those experimentally fabricated are further studied. Table 5.2 shows the main parameters used as an input for theoretical model to calculate the transmittance and reflectance spectrum of the Au NI.

Table 5.2: Major and minor semi-axes values of the analytical oblate spheroids based on the morphological characterization of the fabricated Au NI. The surface density as well as the surface coverage are also presented

Major semi-axis (a) [nm]	Minor semi-axis (b) [nm]	Surface density [Au NI μm^{-2}]	Surface coverage
6.3	5.1	1790	0.223
8.3	6.5	1240	0.268
14.4	11.6	330	0.215
25.8	18.9	95	0.199
42.4	29.1	29	0.164
50.0	38.0	20	0.160
78.0	44.0	7	0.134
91.0	54.0	4	0.104

5.3.1 Theoretical calculations

The transmission spectrum of the Au NI analytically obtained using island film theory at normal incidence and air as the ambient matrix, are presented in Figure 5.6a.

For Au NI with major semi-axes of 6.3 nm, 8.3 nm, and 14.4 nm, a pronounced plasmonic absorption band is centred around 545 nm. Further, the plasmonic resonance wavelength exhibits a redshift with increasing major semi-axis of the Au NI, as shown in Figure 5.6b. The depth of the plasmonic absorption band — indicative of plasmonic resonance strength — gradually increases with the Au NI size and reaches a maximum value for the Au NI array with a major semi-axis of 50.0 nm, suggesting enhanced plasmonic resonance coupling. For Au NI arrays with major semi-axes of 78.0 nm and 98.0 nm, the absorption band depth decreases, indicating a reduction in resonance efficiency. Additionally, the bandwidth, characterized by the FWHM, broadens from 44.1 nm for the smallest Au NI array (6.3 nm major semi-axis) to 344.2 nm for the largest one (91.0 nm major semi-axis).

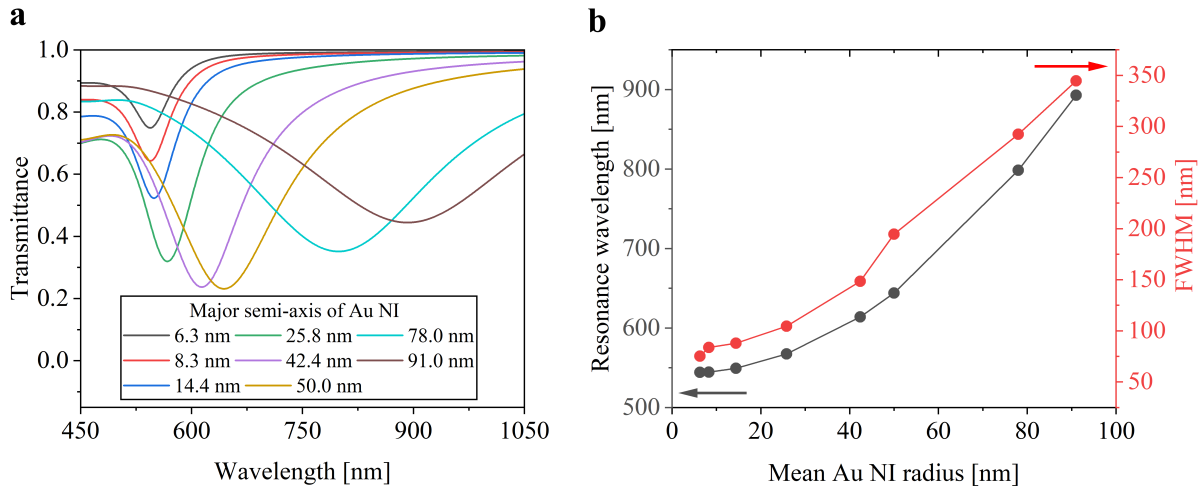


Figure 5.6: a. Analytical transmittance spectrum of Au NI arrays at normal incidence. b. Dependence of LSPR wavelength (navy blue) and FWHM (red) of the transmittance spectrum on the mean major semi-axis of Au NI. The ambient medium is air

5.3.2 Experimental measurements

The transmission spectra of the fabricated Au NI based metasurfaces were experimentally obtained under normal incidence with air as the ambient medium, as shown in Figure 5.7a. The spectra display distinctive plasmonic absorption bands, and with increasing Au NI mean radius, these bands exhibit a redshift in their resonance wavelength and an increase in bandwidth, as illustrated in Figure 5.7b. For the Au NI arrays with radius ranging from 5.9 nm to 41.3 nm, the absorption band depth becomes more pronounced, indicating stronger plasmonic resonance, as the size of the Au NI increases. However, for Au NI arrays with radii beyond 41.3 nm, the depth of the absorption band reaches a plateau, maintaining a relatively constant value of around 0.42 in the transmittance. For largest nanoparticles the depth of the plasmonic dip slightly decrease.

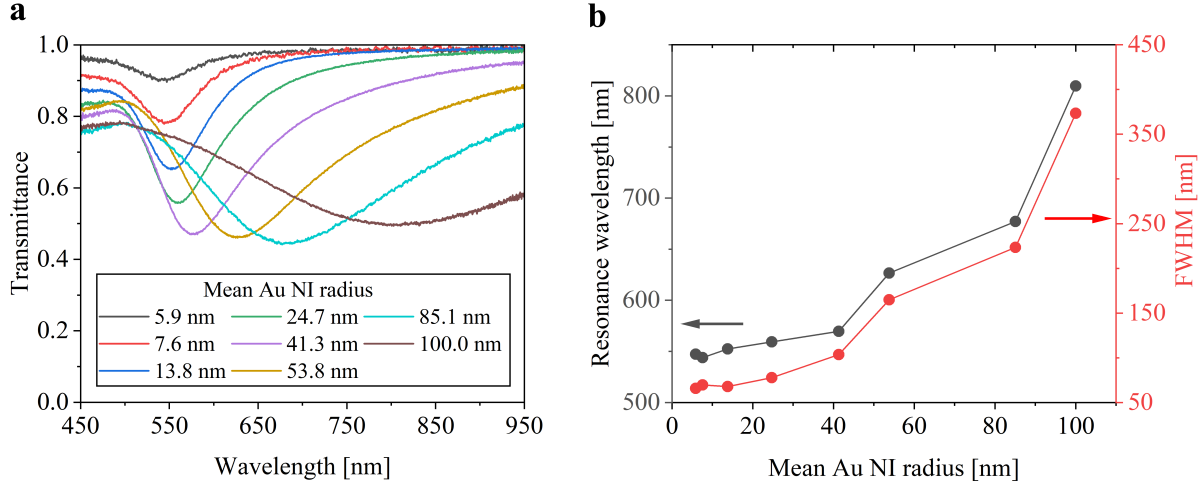


Figure 5.7: a. Experimental transmittance spectrum of Au NI arrays under normal illumination. b. Wavelength position of the plasmonic peak of the transmission spectrum

5.3.3 Discussion

The comparative analysis of the island thin film model, which utilizes the MLWA for polarizability calculations, and the experimental data shows a strong agreement. This agreement is notably visible in the transmission spectra features with the increased Au NI size: resonance position, strength, and bandwidth.

In the case of smaller Au NIs, specifically those below 10-20 nm in diameter, absorption predominates their interaction with light. This observation is in line with predictions from both the island thin film model and classical Mie theory. Due to their size being significantly smaller than the wavelength of light, the resonance wavelength of these smaller particles remains relatively unchanged, characteristic of the Rayleigh scattering regime. The resonance strength increases with the size due to higher surface-to-volume ratio, which enhances the local electromagnetic field. The bandwidth of the plasmonic resonance in this size range is narrow, indicating minimal radiative losses.

As the size of the Au NIs increases, particularly when transitioning to sizes between 30 nm to 50 nm, the mixed mechanism take place with shift from absorption towards scattering. This shift is more pronounced as the size of the nanoparticles approaches the wavelength of the incident light. The island thin film model, with its reliance on MLWA, effectively captures the complexities of this size-dependent behaviour, unlike traditional models such as Mie theory which fully account for spherical shapes. The transition towards a scattering-dominated interaction is marked by a size-dependent shift in the resonance wavelength. This transition is marked also by an increase in resonance strength as the larger volume of the nanoislands can support stronger plasmonic oscillations. However, this increase in resonance strength comes with a broadening of the bandwidth due to enhanced radiative losses, which are significant in this size range.

Experimental data further corroborate this transition to a scattering-dominated regime, particularly noticeable as Au NI sizes increase from 50 nm to 100 nm. Within this range, the bandwidth of the plasmonic resonance is observed to expand significantly, reflecting the theoretical anticipation based on the radiation damping's dependence on size, which can be approximated by the formula $\Gamma_{\text{rad}} \propto k^3 R^3$, where Γ_{rad} is the radiative damping rate, k is the wave number of the incident light, and R is the radius of the nanoparticle. For very large particles the plasmonic resonance strength ceases to increase due to enhanced radiative

damping and the excitation of multipolar modes. These factors lead to energy dispersion across various channels and a broadening of the resonance peak, diluting the peak intensity and limiting the resonance strength.

5.4 Reflectance spectrum of Au NI arrays under ATR condition

5.4.1 Theoretical calculations

The reflectance of the Au NI arrays was calculated using the modified Fresnel coefficients [Equation (2.79) and Equation (2.80) for two angles of internal incidence: close to the critical angle (65°) and oblique angle (73°). These angles of incidence were specifically selected for direct comparation with experiment measurements.

In Figure 5.8a, the R_p spectrum of the Au NI exhibits a plasmonic feature for all the Au NI arrays under an angle of incidence of 65° . The reflectance spectra for the metasurface composed of spheroidal Au NIs show that with an increase in the Au NI radius, both the shoulder of the spectra around 450 nm and the depth of the plasmonic resonance dip decrease. Notably, for the Au NIs with a radius of 50.0 nm, the reflectance at the resonance wavelength diminishes significantly, approaching nearly zero reflectance ($R_p \approx 0.001$) at 501 nm, indicating a highly pronounced plasmonic effect at this particular size.

In Figure 5.8b, the R_s spectra exhibit distinct plasmonic modes for Au NI arrays with smaller radii, specifically 6.3 nm, 8.3 nm, and 14.4 nm. For these sizes, the plasmonic mode is pronounced, with the 8.3 nm radius Au NI array displaying the most marked feature: the reflectance R_s reaches its minimum, approximately 9.4×10^{-4} , at a wavelength of 545 nm. This indicates a strong plasmonic absorption for the nanoislands of this particular size. However, for larger Au NI arrays, beyond a radius of 14.4 nm, the spectra do not show a well-defined plasmonic mode. The resonance features become less distinct, suggesting that the size increase leads to a diminution or even absence of the characteristic plasmonic behaviour that is prominent in smaller nanoislands.

Figure 5.8c presents the R_p spectra for Au NI arrays at an angle of incidence of 73° . The spectra reveal well-defined plasmonic modes for Au NI arrays with major semi-axes smaller than 25.8 nm. For these smaller sizes, the LSPR wavelength remains constant at approximately 535 nm, indicating a size-independent behaviour.

For the Au NI array with a major semi-axis of 42.4 nm, two plasmonic modes emerge, one at 539 nm and a second, less intense mode around 590 nm. As the semi-axis increases to 50.0 nm, the metasurface response continues to display two plasmonic modes; however, the depths of these modes are similar and modest, with the first mode appearing at 540 nm and the second at 607 nm. Larger Au NI arrays with major semi-axes of 78.0 nm and 91.0 nm also exhibit two modes. Consistent with the smaller arrays, the first mode does not deviate significantly in position, while the second mode is both deeper and broader, indicating a stronger plasmonic response. These second modes are located at longer wavelengths.

Following this, the reflectance spectrum of the Au NI under s polarization illumination is calculated, as depicted in Figure 5.8d. Clear plasmonic modes are present for Au NI arrays with major semi-axes of 6.3 nm, 8.3 nm, and 14.4 nm.

For the larger Au NI arrays, the plasmonic resonance becomes broader and less pronounced, manifesting as a broad, shallow dip in the reflectance spectra. This broadening is accompanied by a redshift in the LSPR wavelength as the major semi-axis of the Au NIs

increases. The reflectance spectra for the largest arrays, those with major semi-axes of 78.0 nm and 91.0 nm, are notably wide and the LSPR wavelengths extend into the near-infrared region.

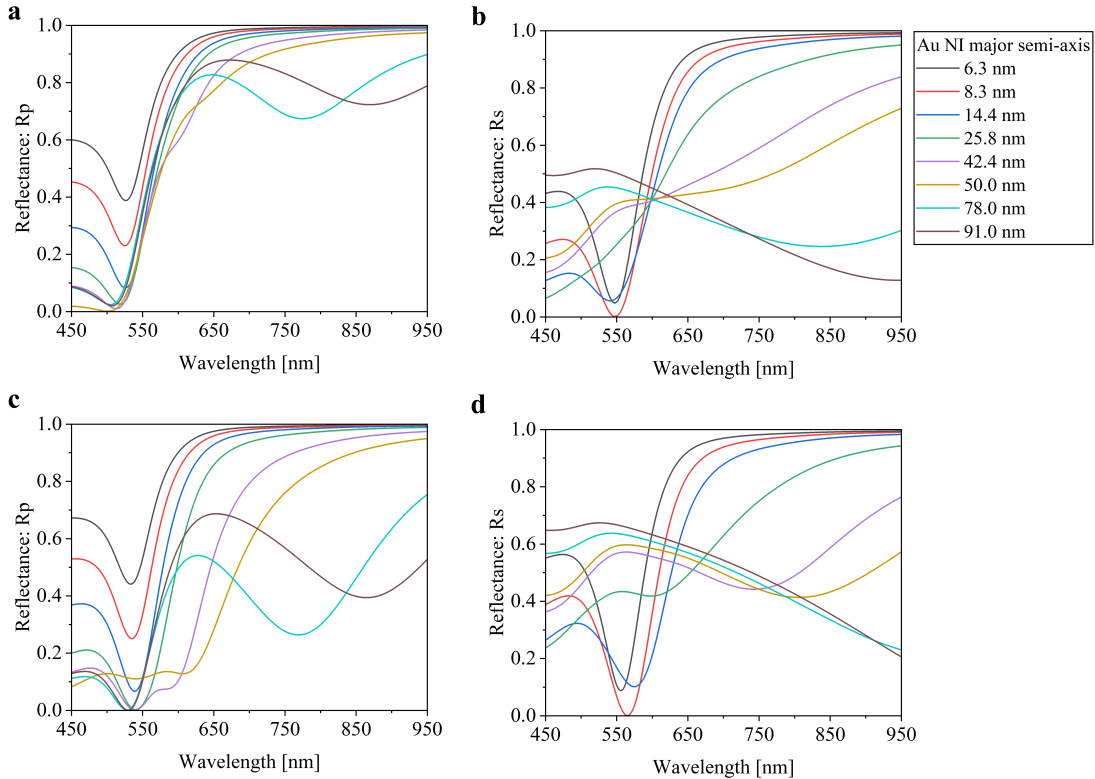


Figure 5.8: Analytical reflectance spectrum of Au NI under **a**, **c**. *p* and **b**, **d**. *s* polarized illumination. The ambient matrix is water, and the angle of incidence is **a**, **b**. 65° and **c**, **d**. 73°

5.4.2 Experimental measurements

Subsequently, the reflectance spectrum of the Au NI was experimentally obtained using the Kretschmann configuration in the intensity mode (see Section 3.4.2) employing both *p* and *s* polarized light and considering two angles of incidence. The choice of this angles of incidence is determined by the following. The first angle of incidence has to be as close as possible to the critical angle for the glass-water interface; and the other one is the maximal experimentally possible angle of incidence.

Figure 5.9 depicts the R_p spectrum of Au NI arrays at an angle of incidence of 65° . Across the spectrum for all tested samples, there is a notable plasmonic dip at the LSPR wavelength. For smaller Au NI, the LSPR position remains constant at 504 nm, indicating that the resonance position is size-independent for these samples. However, as the size of the Au NI increases beyond a radius of 53.8 nm, the LSPR wavelength undergoes a redshift.

As the radius of the Au NIs increases, both reflectance values decrease, reaching their lowest point for Au NIs with a radius of 53.8 nm. For this radius, the spectrum shows an almost complete suppression of reflected light at the resonance wavelength. Beyond this size, both the initial reflectance at 450 nm and the minimum reflectance at the resonance wavelength begin to increase.

In the red-NIR region of the reflectance spectra each curve exhibits a trend where the reflectance levels off to a constant value towards the longer wavelengths. This saturation

point, indicative of the limit where the Au NI arrays cease to strongly absorb or scatter light, shows a dependence on the size of the Au NI: as the size increases, the reflectance at this plateau decreases. Additionally, the wavelength at which this saturation occurs shifts towards the red for larger Au NIs, further illustrating the size-dependent optical response of the arrays.

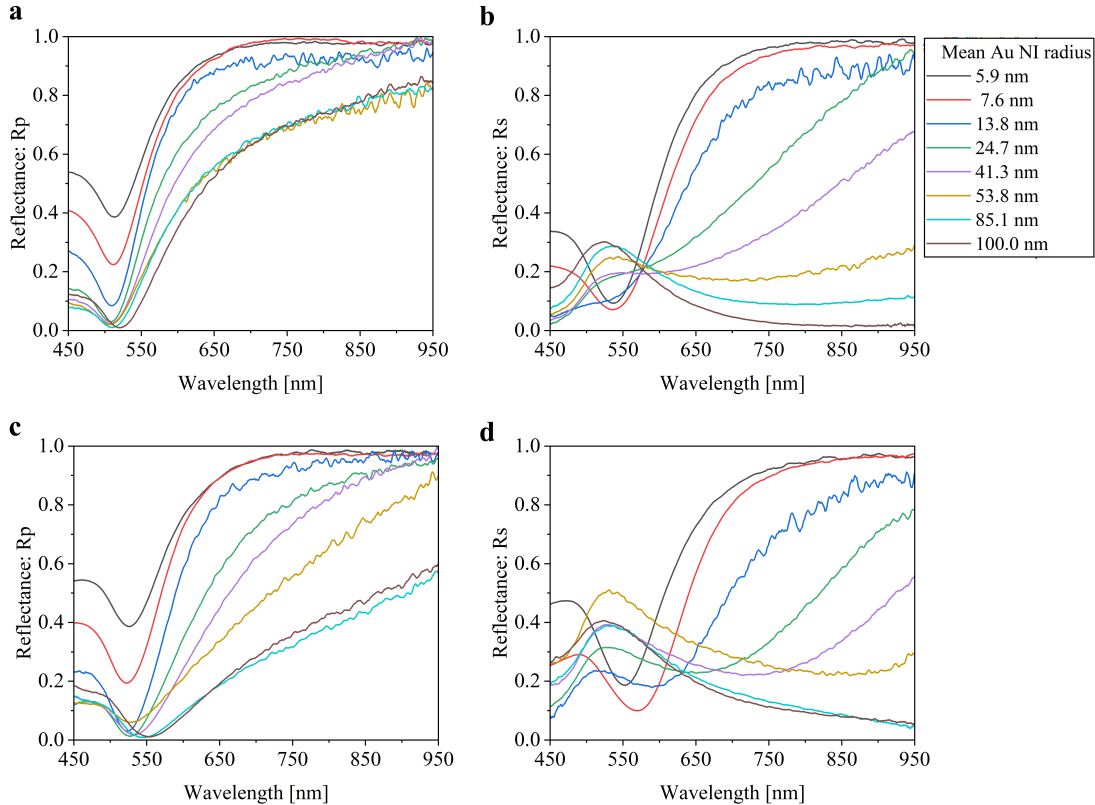


Figure 5.9: Experimental reflectance spectrum of Au NI under **a, c.** p and **b,d.** s polarized light. The angle of incidence are **a, b.** 65° and **c, d.** 73° . The surrounding medium is water

On the other hand, the reflectance of Au NI for s polarized light (Figure 5.9b) shows a well-defined plasmonic dip, specifically at a wavelength of 538 nm, but only for the Au NI arrays with a radius of 5.9 nm and 7.6 nm. Notably, LSPR excited by s polarized light is redshifted respected to the LSPR induced by p polarized light. For larger Au NI, instead of a plasmonic dip, a peak is observed at approximately 530 nm. The behaviour in the red and near-infrared regions of the spectrum for smaller Au NI, is similar to that seen with p polarized light: the reflectance initially increases after the LSPR dip and then levels off. However, as the size of the Au NI increases, this trend changes—rather than continuing to increase or leveling off, the reflectance begins to decrease. Notably, for the largest particles in the array, the reflectance significantly decreases, dropping towards zero in the near-infrared region.

In Figure 5.9c, the R_p spectra at a larger angle of incidence show qualitative similarities to those previously discussed for a smaller angle (in Figure 5.9a). A key feature across these spectra is the near-zero reflection observed for Au NI with a radius of 85.1 nm, indicating a strong plasmonic absorption at this size. Compared to the smaller angle of incidence, larger nanoparticles exhibit a broader plasmonic dip in the R_p spectra, which becomes increasingly pronounced with particle size.

Additionally, in the near-infrared region, rather than converging to a single saturation

level as seen at the smaller angle, the reflectance displays a range of saturation levels, each corresponding to a different size of the Au NIs. The saturation wavelength—the point at which the reflectance ceases to change significantly with wavelength—also varies, shifting towards the longer wavelengths for larger nanoparticles.

5.4.3 Discussion

Analytical calculations based on the island film theory for a three-layered system (glass-Au NI-ambient medium) demonstrate a generally good agreement with experimental measurements of the reflectance spectrum of fabricated Au NI arrays. The theoretical analysis revealed distinct plasmonic features in the reflectance spectra under both *p* and *s* polarized illumination for different angles of incidence.

The analytical R_p spectra demonstrated the presence of well-defined plasmonic mode for all Au NI arrays. Notably, the amplitude of these plasmonic dips exhibited a decreasing trend with increasing Au NI radius. Similarly, experimental results corroborated these findings, demonstrating pronounced plasmonic dips in the reflectance spectra for *p* polarized light.

At an angle of incidence of 65°, both experimental and analytical reflectance spectrum for the sample of radius of 53.8 nm and 50.0 nm respectively, shows a nearly zero reflected light at the resonance wavelength, indicating efficient plasmonic coupling and strong light-matter interaction. However, for larger spheroid arrays which have major semi-axes of 78.0 nm and 90.0 nm, a second plasmonic mode is observed at approximately 780 nm and 870, respectively. Although the second plasmonic mode is very broad, the experimental reflectance measurements cannot resolve it. Only a rather considerable decrease in intensity is observed in this wavelength region, compared to the other reflectance spectra.

The presence of a second plasmonic mode in the R_p spectra is more evident when the Au nanospheroid arrays are illuminated with a larger angle of incidence. In this case, the second plasmonic mode is observed for spheroids with major semi-axis greater than 43.3 nm. Again, in the experimental R_p spectra, this second plasmonic mode is not observed.

In the other hand, in both experimental and theoretical spectra, R_s spectrum does not exhibit a well-defined plasmonic dip for Au NI with radii greater than 7.6 nm for experiment and major semi-axis of 14.4 nm for analytical calculations. Furthermore, both theoretical calculations and experimental measurements demonstrated the broadening of plasmonic dips in the reflectance spectra as the size of the Au NI increased.

Additionally, the theoretical calculations predict that for the nanospheroid arrays with major semi-axis of 8.3 nm, the reflectance at the resonance wavelength for the R_s spectrum has a value of 9.4×10^{-4} . However, in the experimental R_s spectrum, the reflectance at the resonance wavelength is far from nearly zero reflection.

The discrepancies observed between the theoretical and experimental results in the reflectance spectrum could be attributed to several factors: *i*) firstly, the island film theory assumes identical sizes of nanoparticles, whereas the fabricated Au NI exhibit a size distribution; *ii*) secondly, the theoretical model assumes that the nanoparticles are perfectly supported on the substrate, whereas the Au NI are partially embedded in the substrate; *iii*) thirdly, the fabricated Au NI have in reality an ellipsoidal shape with three different semi-axes. While the theory considers the projection of the nanoparticle on the interface plane as a circle.

5.5 Bulk refractive index sensitivity of Au NI arrays

To determine the RIS of the Au NI arrays, both analytical and experimental approaches were employed, involving a variation in the refractive index of the ambient medium within the interval $n_a = 1.3328 - 1.3488$. Experimentally, these refractive index values correspond to different concentrations of aqueous saline solutions, ranging from 0 % to 10 % NaCl concentration, as detailed in Table 3.1.

The RIS was calculated using its definition [Equation (2.85)], where the numerator represents the resonance wavelength shift relative to water, denoted as $\Delta\lambda_R = \lambda_{R,n_a} - \lambda_{R,n_{\text{water}}}$. Here, λ_R stands for the resonance wavelength of the R_p and R_s spectra for each refractive index of the ambient medium.

Both analytical and experimental analyses were performed for angles of incidence set at 65° and 73°.

5.5.1 Theoretical calculations

Figure 5.10 a shows the resonance wavelength shift respect to water for different refractive index values for an angle of incidence of 65°. Notably, the resonance wavelength of all the Au NI arrays, moves towards shorter wavelength (blueshift) as the refractive index increases in a linear way. Furthermore, as the size of the Au NI increases, the shifts become more pronounced. For the Au NI with major semi-axis of 42.4 nm, 50 nm, 78.0 nm and 91.0 nm, the resonance wavelength shifts approximately in the same manner.

The dependence of the R_s spectrum on the refractive index was calculated only for the Au NI arrays where the plasmonic dip is observed, which are the 6.3 nm, 8.3 nm and 14.4 nm sized Au NI. As shown in Figure 5.10b, the resonance wavelength also blueshifts as the major semi-axis of the Au NI increases. Moreover, the shifts are more pronounced under s polarized illuminations compared to p polarization for the same Au NI array.

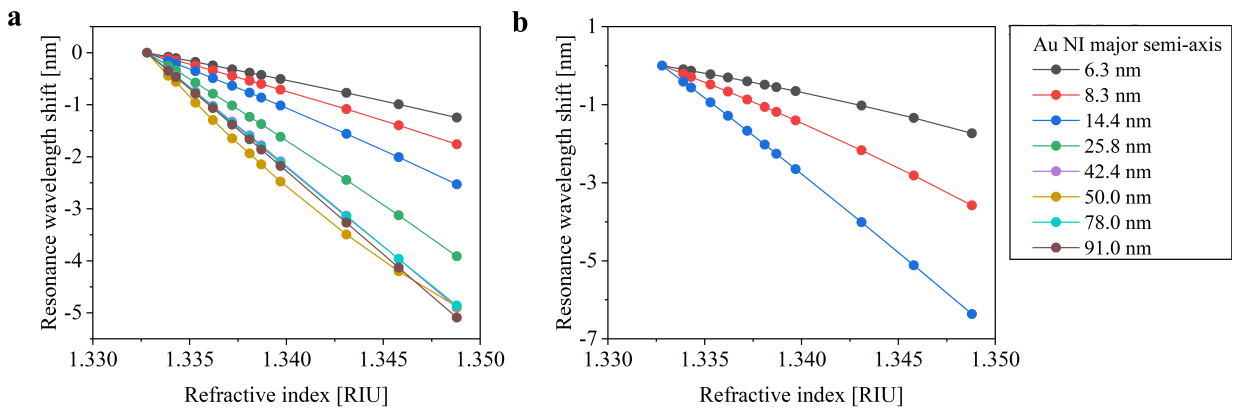


Figure 5.10: Resonance wavelength shift by increasing the refractive index of the ambient medium under **a.** p and **b.** s polarized light. The angle of incidence is 65°

Then, the RIS values of each Au NI were determined by linear fitting their respectively resonance wavelength shifts as a function of the refractive index, plots in Figure 5.10. As the resonance wavelength of the R_p and R_s spectra experiences a blueshift with increments in the refractive index, according to the definition provided in Equation (2.85), the RIS shows negative values.

Figure 5.11a shows the analytical RIS dependence on the size of the Au NI when they are illuminated under *p* polarized light. The smaller Au NI (major semi-axis of 6.3 nm) shows the lowest RIS with a value of $-73.6 \text{ nm RIU}^{-1}$, while the highest RIS is demonstrated by the Au NI with a major semi-axis of 50 nm, with a value of $-338.6 \text{ nm RIU}^{-1}$.

On the other hand, when the Au NI are illuminated with *s* polarized light, the RIS improves, as depicted in Figure 5.11b. The Au NI arrays with major semi-axis of 14.4 nm shows the highest RIS with a value of $-384.4 \text{ nm RIU}^{-1}$.

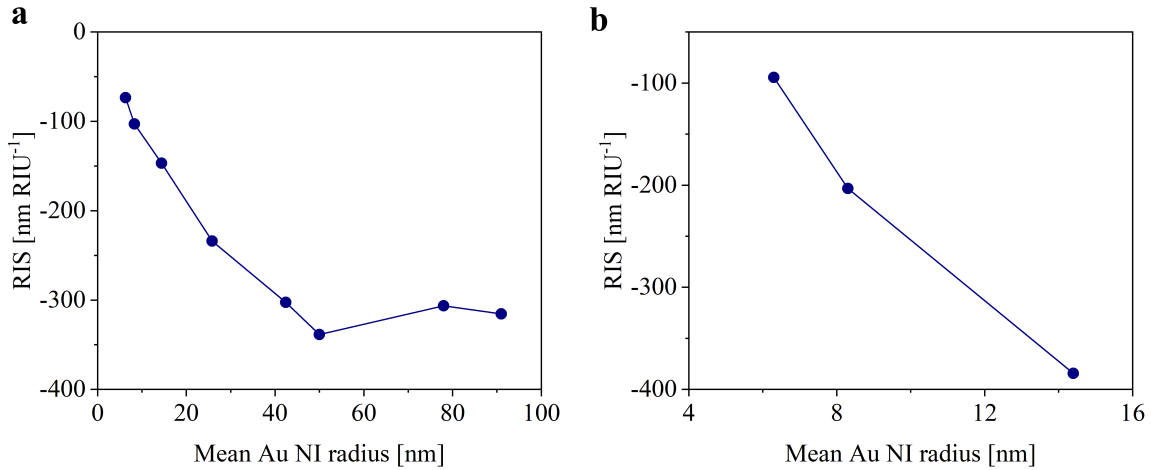


Figure 5.11: Analytical RIS in function of Au NI size when the arrays are illuminated under **a.** *p* and **b.** *s* polarization light. The angle of incidence is 65°

The same analysis was then performed to determine the RIS of the Au NI arrays, but this time for an angle of incidence of 73° .

As previously observed for the angle of incidence of 65° and under *p* polarized illumination, the resonance wavelength experiences a blueshift as the refractive index of the surrounding medium increases, see Figure 5.12a. In this case, the resonance wavelength shows a non-linear dependence on the refractive index. The Au NI with major semi-axis of 42.4 nm presents the most pronounced shift while increasing the refractive index.

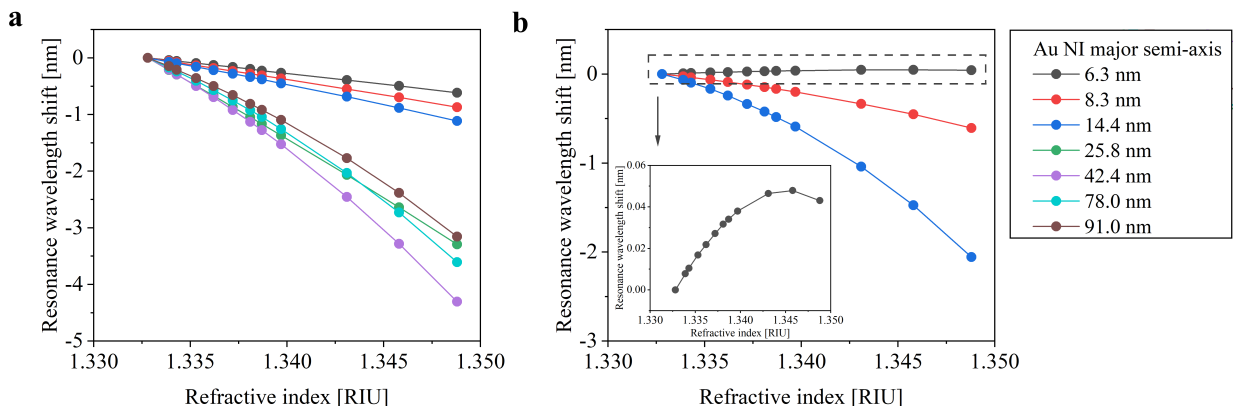


Figure 5.12: Analytical resonance wavelength shift by increasing the refractive index of the ambient medium under **a.** *p* and **b.** *s* polarized light. The angle of incidence is 73° . Inset in **b.** better illustrates the resonance wavelength dependence on the refractive index for the Au NI array with major semi-axis of 6.3 nm

It is important to note that the resonance wavelength shift due to refractive index variations for the 50.0 nm sized Au NI cannot be determined because the plasmonic dip is very shallow and as the refractive index increases, it becomes less defined.

On the other hand, Figure 5.12b illustrates the blueshift in resonance wavelength, for *s* polarization component, when increasing the refractive index. The smallest Au NI array (major semi-axis of 6.3 nm) shows a particular behaviour of the resonance wavelength in function of the refractive index. However, due to high values of the vertical scale this behaviour is not clearly appreciated. To address this, the plot for this Au NI is represented by zooming in on Figure 5.12b. Unlike in all the above cases, the resonance wavelength redshifts in the refractive index range from $n_a = 1.3328$ to 1.3441. Then, for $n_a = 1.3458$, the resonance wavelength remains nearly constant. Subsequently, for $n_a = 1.3488$ the resonance blueshifts.

Lastly, the Au NI array with major semi-axis of 14.4 nm shows the highest resonance wavelength shifts among the arrays studied.

The RIS cannot be directly determined by linear fitting of the resonance wavelength shifts with increasing refractive index, as this dependency is non-linear. Therefore, the RIS is calculated within two refractive index intervals: the first ranging from 1.3328 to 1.3397, and the second from 1.3397 to 1.3488. In these refractive index ranges, the resonance wavelength shifts exhibit an approximately linear dependence on the refractive index, as shown in Figure 5.12.

The first row of Figure 5.13 shows the analytical values of the RIS of each Au NI array within each refractive index range, considering *p* polarized incident light.

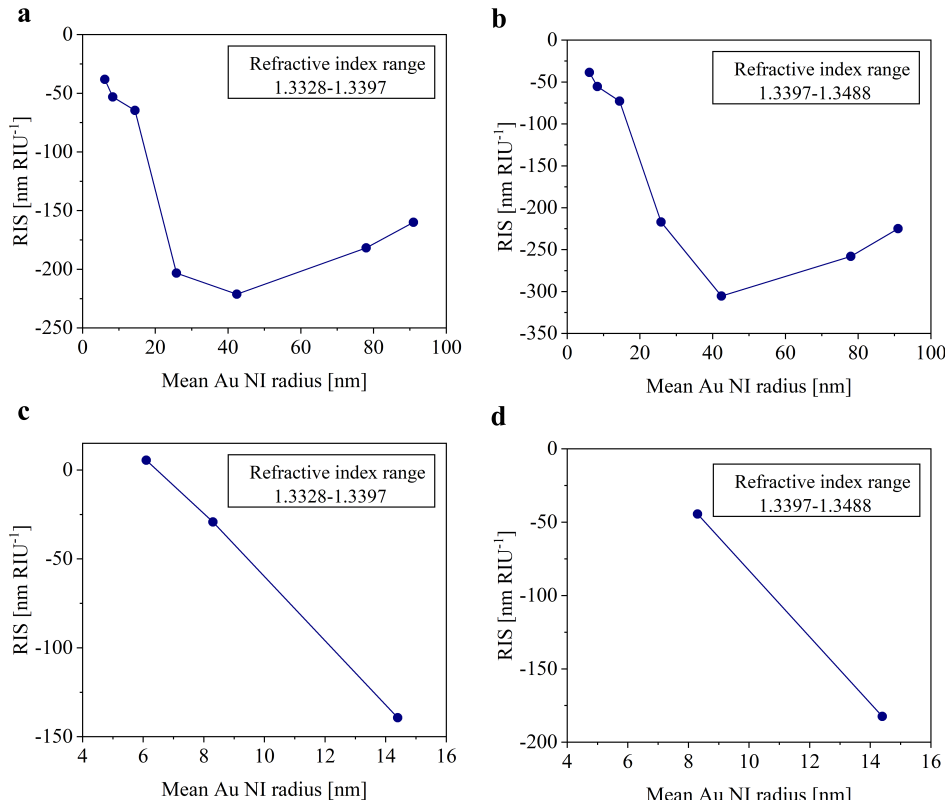


Figure 5.13: Calculated RIS in function of the Au NI major semi-axis under **a**, **b**. *p* and **c**, **d**. *s* polarization light within two refractive index ranges. The first goes from 1.3328 to 1.3397 (left column) and the second one from 1.3397 to 1.3488 (right column)

The Au NI arrays with major semi-axis of 6.3 nm, 8.3 nm and 14.4 nm, shows the lowest RIS values in both refractive index ranges. Whereas the 42.4 nm Au NI array presents the highest RIS value in the second refractive index range, reaching $-305.4 \text{ nm RIU}^{-1}$.

On the other hand, the second row of Figure 5.13 shows the RIS values when the incident beam is *s* polarized. In this case, the RIS values are lower compared to those observed with *p* polarized incident light. Due to the resonance wavelength behaviour during refractive index increments (refer to the zoomed-in Figure 5.13), the RIS cannot be determined for the 6.3 Au NI array in the refractive index range from 1.3397 to 1.3488.

5.5.2 Experimental measurements

The sensing properties of the metasurfaces were investigated by measuring the LSPR shift while varying the refractive index of the surrounding medium. Firstly, the bulk RIS of the Au NI arrays was explored at an angle of incidence of 65° , closely approximating the critical angle for the glass-water interface.

Figure 5.14 shows the change of resonance wavelength with respect to water, for both *p* and *s* polarized light. Notably, this dependency exhibits a non-linear behaviour, and it strongly depends on the size of the Au NI.

Figure 5.14a shows the LSPR wavelength shift versus the refractive index for the Au NI arrays with different sizes and when they are illuminated under *p* polarized light and an angle of incidence of 65° . For the smallest Au NI array (radius of 5.9 nm), an increase in the refractive index of the surrounding medium initially induces a slight redshift in the resonance wavelength. Subsequently, the resonance wavelength shifts to smaller wavelengths (blueshift) as the refractive index continues increasing. This non-linear dependence of the relative resonance wavelength on the refractive index is consistent across the remaining Au NI arrays, leading to a blueshift as the refractive index increases.

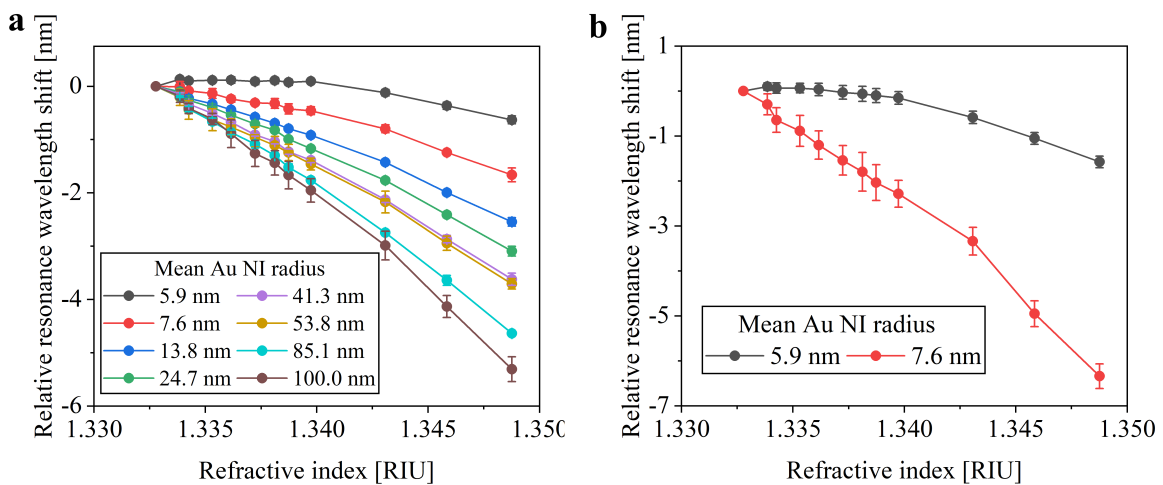


Figure 5.14: Resonance wavelength changes relative to water under **a.** *p* and **b.** *s* polarization light. The angle of incidence is 65° . The RIS were obtained by linear fitting in two refractive index intervals

As depicted in Figure 5.9b, the Au NI arrays which show a well-defined plasmonic dip under *s* polarized illumination are those with Au NI mean radii of 5.9 nm and 7.6 nm. For this reason, the relative resonance wavelength dependence versus the refractive index of the surrounding media could only be measured for these Au NI arrays, see Figure 5.14b. Similar

to the p polarized case, the resonance wavelength exhibits a non-linear dependence on the refractive index, resulting also in a blueshift.

The RIS was determined in two refractive index intervals: the first ranging from 1.3328 to 1.3397 and the second goes from 1.3397 to 1.3488, as was done in the theoretical analysis.

Figure 5.15a and Figure 5.15b show the RIS values of the Au NI arrays when illuminated with p polarized light for the first and second refractive index interval, respectively. As expected, the RIS gradually increases as the Au NI size does. The maximum RIS was observed for the largest Au NI (radius of 100.0 nm) in the second refractive index interval, yielding a value of -375 nm RIU^{-1} .

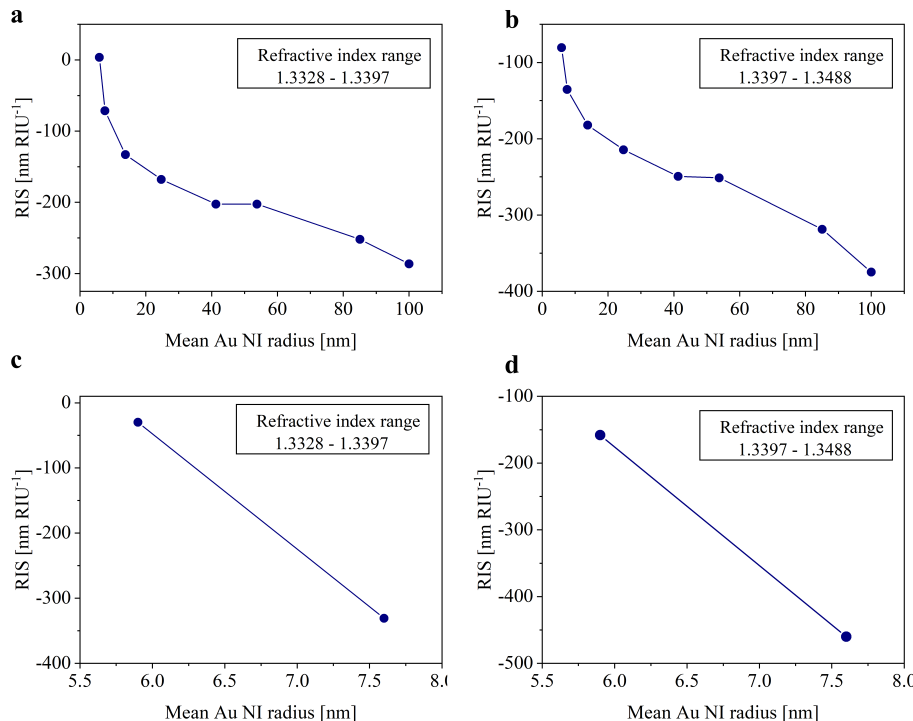


Figure 5.15: Experimental RIS in function of Au NI mean radius under **a**, **b**. p and **c**, **d**. s polarization light. The angle of incidence is 65°

The RIS of the Au NI when illuminated with s polarization light was also obtained, see Figure 5.15c and Figure 5.15d. The AuNI array with radius of 7.6 nm demonstrates the maximum slope in the resonance wavelength shift with the refractive index, achieving a RIS of -460 nm RIU^{-1} .

Subsequently, the LSPR shift associated with a change in the refractive index of the surrounding medium were determined, considering the maximum experimental angle of incidence, $\theta_i = 73^\circ$.

Figure 5.16a shows the relative resonance wavelength to water when the Au NI arrays when illuminated under p polarization light. For the Au NI with a radius of 5.9 nm, the resonance wavelength initially redshifts in the refractive index interval from 1.3328 to 1.3353. Then, as the refractive index of the surrounding medium increases the resonance wavelength slowly decreases. In the same way, the Au NI with radius of 7.6 nm redshifts in a short refractive index interval (1.3328 to 1.3339), followed by a blueshift in the resonance wavelength. The rest of the Au NI arrays non-linearly blueshifts in the whole refractive index interval.

The Au NI arrays with radius of 5.6 nm and 7.6 nm were subsequently illuminated with *s* polarized light and the refractive index of the surrounding medium was varied within the previously mentioned refractive index interval. For the smallest Au NI (radius of 5.6 nm), the dependence of the resonance wavelength with the refractive index shows a particular behaviour, as depicted in Figure 5.16b. The resonance wavelength gradually redshifts as the refractive index increase in the interval from 1.3328 to 1.3381, then, the resonance wavelength practically does not change in the interval from 1.3381 to 1.3431 and finally, experiences a rapid blueshift in the interval from 1.3431 to 1.3488.

In contrast, for the Au NI with radius of 7.6 nm, the resonance wavelength redshifts in the interval from 1.3328 to 1.3339, and then, the LSPR wavelength undergoes a non-linear blueshift.

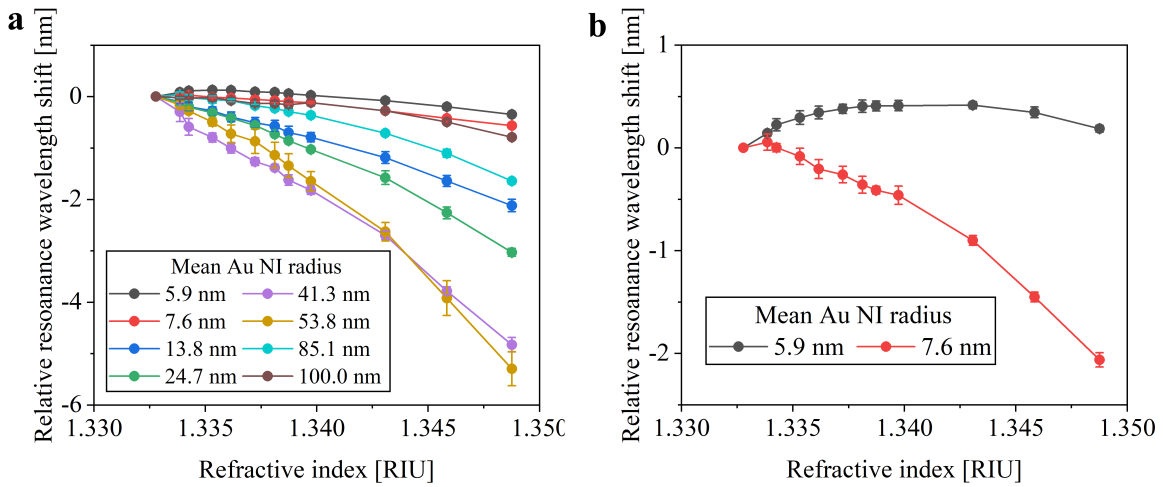


Figure 5.16: Experimental resonance wavelength changes relative to water under **a.** *p* and **b.** *s* polarization light. The angle of incidence is 73° . The RIS were obtained by linear fitting in two refractive index intervals: from 1.3328 to 1.3397 and the second goes from 1.3397 to 1.3488

The RIS was subsequently determined by linear fitting the plots in Figure 5.16 where the LSPR dependence on the refractive index is linear.

Figure 5.17a and Figure 5.17b show the RIS when the Au NI are illuminated under *p* polarized light. As previously discussed, the LSPR shift of smallest Au NI (radius of 5.6 nm) initially redshifts and then blueshifts in the refractive index interval from 1.3328 to 1.339, for this reason the RIS is undetermined for this specific case.

For this angle, the RIS dependence on the Au NI size is not the same for the angle of 65° , see Figure 5.15. Notably, an optimum Au NI size can be observed, where the RIS reaches its maximum. For the first refractive index interval (1.3328 to 1.3397) the maximum RIS was found in the Au NI array with radius of 41.3 nm with a value of -254 nm RIU^{-1} . However, the Au NI arrays with radius of 53.8 nm presents a RIS of -234 nm RIU^{-1} which is a value very close to the maximum found. For the second refractive index interval (1.3328 to 1.3397) the Au NI with radius of 53.8 nm shows the maximum RIS of -409 nm RIU^{-1} . Counterintuitively, the largest Au NI (radius of 85.1 nm and 100.0 nm) shows a small RIS values -142 nm RIU^{-1} and -74 nm RIU^{-1} , respectively.

Figure 5.17c and Figure 5.17d show the RIS dependence on the Au NI size when the arrays are illuminated under *s* polarized light. In the first refractive index interval, the Au NI with radius of 5.6 nm shows a positive RIS with value of 55 nm RIU^{-1} and the Au NI array with radius of 7.6 nm, shows a negative RIS with value of $-79.5 \text{ nm RIU}^{-1}$. The maximum

RIS of the Au NI under *s* polarized illumination is observed in the second refractive index range for the Au NI with a radius of 7.6 nm, having a value of -179 nm RIU^{-1} .

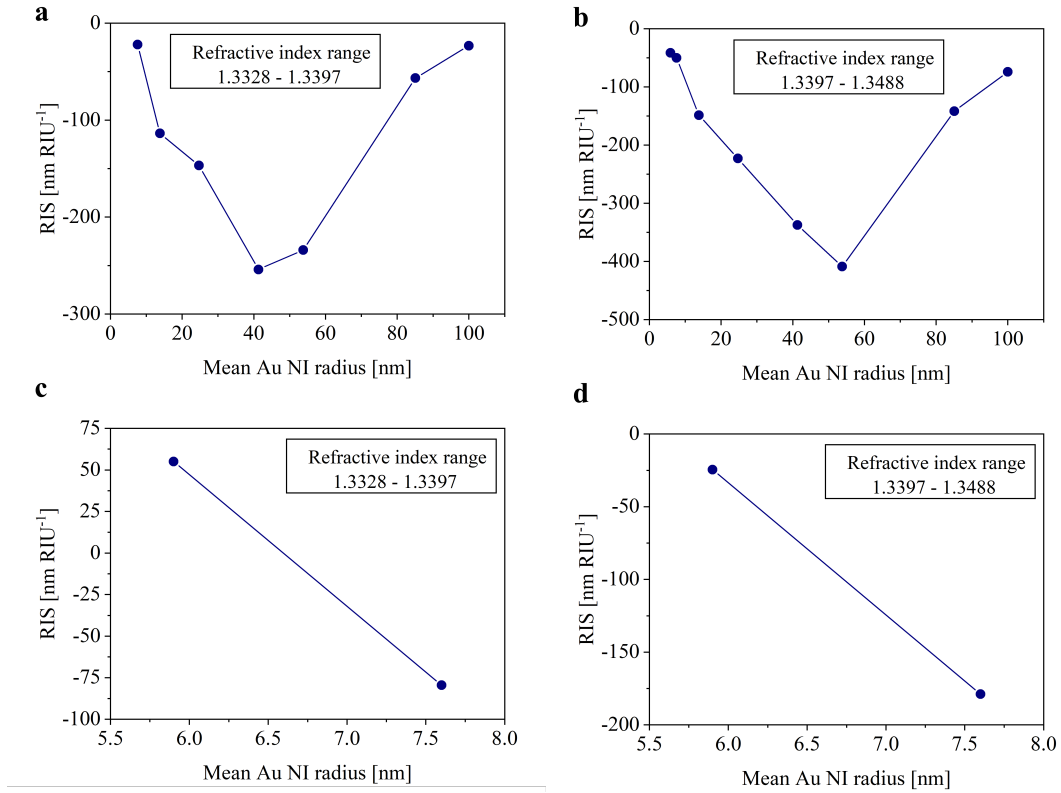


Figure 5.17: Experimental RIS in function of the Au NI mean radius under **a**, **b**. *p* and **c**, **d**. *s* polarization light. The angle of incidence is 73° .

5.5.3 Discussion

5.5.3.1 Non-linear dependence of resonance wavelength on refractive index

The resonance wavelength dependence on the refractive index shows distinct behaviors between propagating SPR and LSPR. [145] For SPR, involving oscillations across extended metal-dielectric interfaces λ_R typically scales linearly with the medium's refractive index. This predictable variation arises from the uniform interaction of the incident light wave with the metal film, leading to straightforward sensing applications.

In contrast, LSPR manifests a non-linear, λ_R dependency due to the electromagnetic field enhancement around each particle. [145, 157] When the refractive index of the surrounding medium changes, the localized field around the nanoparticle can experience nonlinear shifts due to changes in the electronic polarization within the metal, which does not always behave proportionally to the changes in the environment. This non-linearity is further complicated by the presence of a substrate, which influences the nanoparticles' field enhancement and introduces asymmetry in the electric field distribution. Consequently, the LSPR shift may not be strictly proportional to refractive index changes, especially as the size, shape, and material properties of the nanoparticles contribute to the complex response.

This effect can make the interpretation of the LSPR-based sensing data more complex as the relationship between λ_R and refractive index changes becomes less predictable and may vary significantly with the nanoparticle's size, shape, and material properties.

Notably, the study reveals a predominantly blueshifted LSPR wavelength (specially for angles close to critical) when the arrays are subjected to illumination under total internal reflectance conditions—a finding that, to our knowledge, has not been previously documented.

Interesting, for more oblique angles and small NI size the dependence is more complex. Thus, Au NI array with a 5.9 nm radius shows initially LSPR redshift with the increased n and then blueshifts, a phenomenon captured in Figure 5.16. A corresponding trend is mirrored analytically for an Au NI with a major semi-axis of 6.3 nm, detailed in Figure 5.12.

In SPR the redshift of λ_R with increasing refractive index is a well-documented phenomenon. This phenomenon is rooted in the dispersion relationship of surface plasmons, which dictates how their wavevector (and hence the resonance condition) depends on the dielectric properties of the materials involved. As the refractive index of the dielectric increases, the wavevector of the surface plasmons must adjust to satisfy this relationship, resulting in the observed redshift in the resonance wavelength.

The conventional LSPR bulk RIS sensitivity measurements are usually performed at normal incidence. The redshift of the LSPR wavelength with the increasing refractive index at normal incidence it is also very well known in literature. The explanation is as follows. When the refractive index of the surrounding medium increases, it alters the local dielectric constant around the nanoparticle, affecting the conditions under which the collective oscillations of electrons resonate with the incident light. This change in the dielectric environment affects the polarizability of the nanoparticle, requiring a shift in the resonance frequency to re-establish the resonant condition for the localized surface plasmons.

The observation of a blueshift in the LSPR resonance wavelength in ATR configuration above the critical angle could be attributed to the unique interaction between the evanescent wave and the nanoparticles. In ATR, the evanescent wave's penetration depth into the medium where nanoparticles reside is influenced by the angle of incidence. Above the critical angle, the evanescent field becomes more confined near the interface, potentially altering the local dielectric environment experienced by the nanoparticles. This confinement can affect the plasmon resonance condition, leading to a blueshift in the LSPR wavelength.

5.5.3.2 Bulk refractive index sensitivity

The experimental and analytical investigations of sensitivity show a strong dependence of the RIS on several factors, including the Au NI size and the angle of the incident beam.

Under *p* polarized light at an incident angle of 65°, RIS values for Au NI arrays increase with nanoparticle size, as confirmed by both analytical and experimental evidence, aligning with predictions from Mie theory.^[157] This size-related sensitivity enhancement is due to the expanding field enhancement region surrounding larger nanoparticles (Figure 5.15), allowing for a more extensive interaction with the surrounding medium and a stronger response to refractive index changes—the greatest RIS noted for an Au NI with a 100 nm radius.

Conversely, under *s* polarized illumination, smaller Au NIs, specifically those with a 7.6 nm radius, demonstrate the highest experimental RIS values, reaching -460 nm RIU⁻¹, with analytical results for 14.4 nm particles at -384 nm RIU⁻¹. This increased sensitivity is likely related to the pronounced plasmonic resonance strength for *s* polarized light at these particle sizes, with potential effects from particle-substrate interactions further influencing the sensitivity.

As the incidence angle increases, the RIS values decrease, for both polarizations. Both analytical and experimental data indicate an optimal size for Au NI arrays in sensing con-

texts. Experimentally, the array with a 53.8 nm radius shows an RIS of -409 nm RIU^{-1} within a refractive index range of 1.3397 to 1.3488. Analytically, a 42.4 nm radius Au NI array displays the greatest RIS, at -305 nm RIU^{-1} for the same index range. It is notable that the RIS for the 50.0 nm semi-axis sample was indeterminable analytically due to a shallow dip in the R_p spectrum.

The reduction in RIS at more oblique angles, as well as the identification of an optimum Au NI size, can be explained by the penetration depth of the evanescent wave, which is angle dependent. The penetration depth measures 112 nm at a 532 nm wavelength and a 65° incidence angle, reducing to 71 nm at a 73° angle. Maximum sensitivity is achieved when the nanoparticle height is comparable to the evanescent wave's penetration depth. Additionally, diminished sensitivity for larger particles may also result from increased radiative losses, as previously discussed.

5.5.4 Experimental measurements of bulk refractive index sensitivity using the phase interrogation mode

The plasmonic behavior of metasurfaces based on randomly distributed Au NI and its corresponding RIS was characterized in phase interrogation mode using the ATR setup integrated with a spectral interferometer.

Figure 5.18 displays selected interferograms that are representative of the three distinct size categories of Au NI metasurfaces: small (5.9 and 7.6 nm), intermediate (13.8 nm, 24.7 nm, 41.3 nm), and large (53.8 nm, 85.1 nm and 100 nm) nanoparticles. These interferograms were chosen to illustrate the contrasting plasmonic phase responses attributable to each size group when probed at an incidence angle of 65° with water as the surrounding medium.

In Figure 5.18, panels *a* through *c* display the spectral interferograms for three samples of Au NI arrays with radii of 5.9 nm, 13.8 nm, and 53.8 nm, respectively. For the 5.9 nm radius Au NI sample (Figure 5.18a), the resonance region appears at approximately 540 nm, indicated by a reduction in the contrast of the spectral fringes while maintaining a nonzero amplitude. The sample with 13.8 nm radius Au NIs (Figure 5.18b) presents a less distinct resonance zone around 520 nm, where a subtle diminishment in fringe contrast can be observed. Conversely, the 53.8 nm radius Au NI sample (Figure 5.18c) features a clear and well-defined resonance zone at roughly 515 nm, followed by a rapid increase in the amplitude of the interference fringes post-resonance, indicating a strong resonance effect at this size.

In Figure 5.18, panels *d* and *e* show the differential phase and its derivative for the Au NI samples. The most pronounced feature in panel *d* corresponds to the sample with a radius of 53.8 nm, showcasing the steepest change in the differential phase at the resonance zone. This steepness is indicative of a strong plasmonic effect, aligning with the almost zero contrast observed in the resonance region of the corresponding interferograms. Panel *e* further elucidates these observations by presenting the derivatives of the differential phase, offering a clearer visualization of the phase behaviour. The sample with a radius of 53.8 nm exhibits a notably sharp peak in the derivative, underscoring the significant optical phase shift at the plasmonic resonance. This is in contrast with the broader and less pronounced features for the smaller Au NI samples, reflecting their weaker and more spread out phase modulation across the spectrum.

For the larger Au NI samples with radii of 85.1 nm and 100.0 nm, the interferograms exhibit trends similar to those observed for the 53.8 nm radius sample. Nonetheless, the resonance zones in these larger samples are less sharply defined compared to the distinct

resonance region displayed in Figure 5.18c. This results in a differential phase profile where the slope of the linear region, although similar, does not exceed the steepness captured in Figure 5.18d. The less pronounced definition of the resonance zone for these larger nanoislands suggests a broader spectral response.

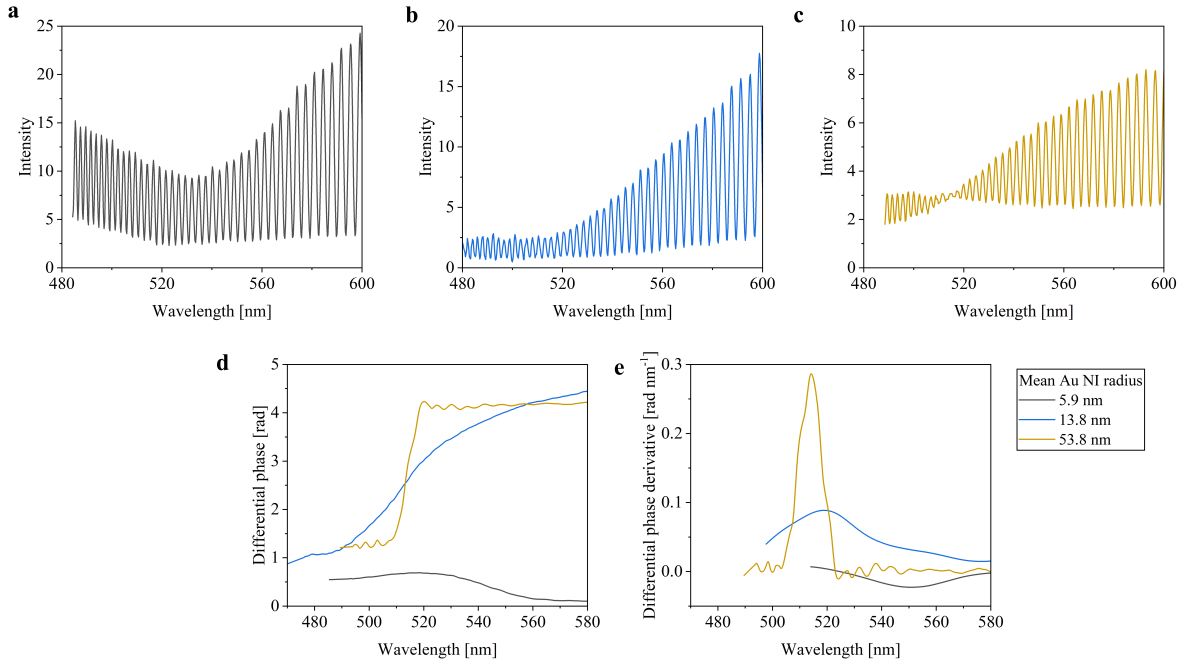


Figure 5.18: Spectral interferograms of Au NI samples with radius of a. 5.9 nm, b. 13.8 nm and c. 53.8 nm. d. Differential phase and its e. derivative obtained from their spectral interferograms. The angle of incidence is 65° and the surrounding medium is water

After analysing the spectral interferograms of the Au NI arrays, the RIS was measured for each Au NI array. The aim of these experiments is to compare the RIS values between the wavelength and phase interrogations, and to determine the best characteristics of an Au NI arrays which presents the maximum RIS and RIR. The procedure to measure the RIS is the same as previously described; the refractive index of the surrounding medium is varied and the LSPR is determined using the LabView interface shown in Figure 3.12.

Figure 5.19 shows the LSPR shift due to variations in the refractive index of the surrounding medium for the wavelength, phase and phase derivative detection modes. The LSPR shift is determined with respect to the position of LSPR of the water as the surrounding medium.

In Figure 5.19a it is shown that the resonance wavelength blueshifts in a nonlinear way as the refractive index of the surrounding medium increases. The Au NI arrays with radius of 5.9 nm shows the minimum change of the resonance wavelength due to refractive index variations, while the sample with Au NI with radius of 53.8 nm shows the maximum change of the resonance wavelength.

Figure 5.19b shows the modulus of the LSPR phase shift. It presents a linear dependence on the refractive index. Here, the maximum phase shift was found for the sample with Au NI radius of 85.1 nm, while the sample with radius of 5.9 nm shows the minimum shift.

For the phase derivative mode, a nonlinear dependence of the phase derivative shifts on the refractive index was observed, see Figure 5.19c. The Au NI arrays with radius of 53.8 nm shows the maximum phase derivative shift among all the samples.

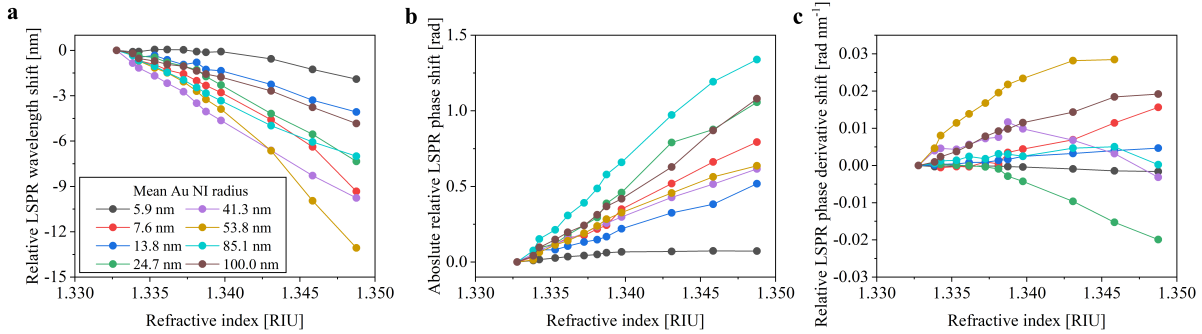


Figure 5.19: LSPR **a.** wavelength, **b.** phase and **c.** phase derivative shift due to refractive index variations. The angle of incidence is 65°

Similarly to the intensity interrogation, LSPR response due to refractive index variations reveals a non-linear dependence of the LSPR wavelength on the refractive index, using the phase interrogation. Consequently, the RIS was determined in two refractive index intervals: *i*) from 1.3328 to 1.3397 and *ii*) from 1.3397 to 1.3488. The dependence of the RIS on the size of the Au NI is depicted in Figure 5.20.

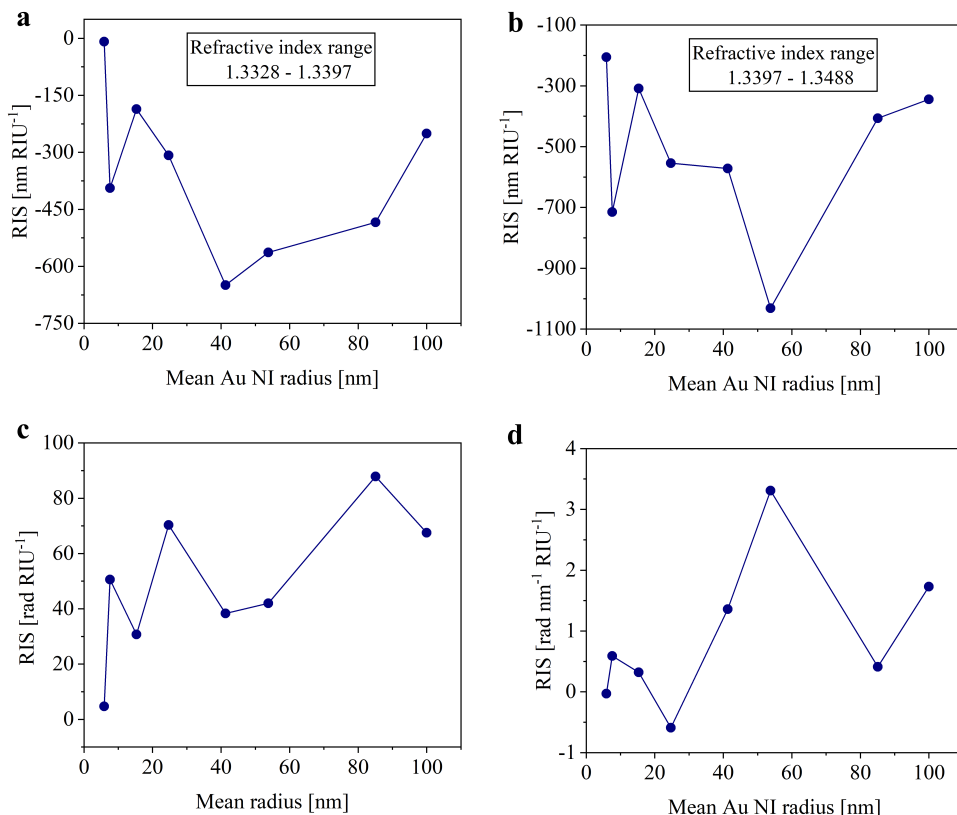


Figure 5.20: RIS dependence on the Au NI size for **a, b.** wavelength in two refractive index intervals, **c.** phase and **d.** phase derivative detection modes. The angle of incidence is 65°

For the first refractive index interval, the RIS increases as the Au NI radius does (Figure 5.20), until the Au NI reaches the value of 41.3 nm, except for the sample with radius of 7.6 nm that deviates from this trend. The RIS is maximal for the Au NI with radius of 41.3 nm with a value of -649 nm RIU^{-1} . Then, the RIS diminishes as the radius of the Au NI

increases. For the second refractive index interval, the RIS shows a very similar dependence on the Au NI size, see Figure 5.20b. Nevertheless, the maximum RIS is found in the Au NI array with radius of 53.8 nm with a value of $-1031 \text{ nm RIU}^{-1}$.

For the phase detection mode, Figure 5.20c, no clear trend as a function of nanoparticle size is observed, however the Au NI with radius of 85.1 nm shows the maximum RIS with value of $87.9 \text{ rad RIU}^{-1}$. Similarly, for the phase derivative detection mode, Figure 5.20d does not show a clear dependence on the Au NI size, but the maximum RIS is found for the sample with radius of 53.8 nm with a value of $3.31 \text{ nm rad}^{-1} \text{ RIU}^{-1}$.

5.5.5 Discussion

We have successfully demonstrated the ability to measure refractive index changes using three different resonance markers: resonance wavelength, phase change, and changes in phase steepness (phase derivative). In comparing RIS for Au NIs at a 65° angle of incidence, phase interrogation typically exhibits superior sensitivity over intensity interrogation ($-1031 \text{ nm RIU}^{-1}$ vs -409 nm RIU^{-1}). This is attributed to the phase of light's inherent stability, rendering it less prone to variations from instrumental and environmental factors, unlike intensity, which can fluctuate with changes in the light source and detector attributes. Hence, phase interrogation is particularly good for detecting small changes in refractive index, that may be less discernible through intensity measurement alone.

Differences in size-dependent RIS between the two interrogation modes also reveal distinct underlying physical mechanisms. Intensity interrogation shows a continuous sensitivity enhancement with nanoparticle size, aligning with the increasing sensing volume, as discussed in previous section. In contrast, phase interrogation identifies an optimal Au NI size (41.3 and 53.8 nm) that yields highest RIS. This is believed to be associated with near-zero reflectance at resonance exhibited by these Au NI (Figure 5.9), known as topological darkness, where phase singularities enable ultra-sensitive refractive index detection. The concept of topological darkness, along with phase singularities, will be explored in detail in the subsequent section to understand how these phenomena contribute to the observed sensitivity peak.

Table 5.3 summarizes the main studies on LSPR sensing employing various nanostructure geometries and interrogation modes. In wavelength interrogation, the resonance wavelength was determined from transmission or reflection spectra, whereas in phase interrogation, the LSPR signal was acquired using ellipsometry techniques or a spectral interferometer.

A comparison of the sensing parameters between the published values and our best values reveals that our technique, utilizing wavelength interrogation, surpasses typical RIS values of hundreds of nm RIU^{-1} .^[40, 58, 63, 116, 158] However, our sensing parameter values are surpassed by theoretical or experimental works employing more complex nanostructure shapes.^[42, 63, 117, 159] In case of the sensing values using the phase interrogation, our work exceeds the values reported in [119, 120, 158], but are exceeded by the values reported in [62, 121].

5.6 Zero reflectance and phase singularity in a random array of Au NI

The parameters of the metasurface used in the simulations were: oblate spheroids with major semi-axis a of 50.0 nm and a minor semi-axis b of 38.0 nm; and a surface density of

Table 5.3: Comparation of bulk RIS and RIR of LSPR based sensors between published works and our work

Nanostructure	Interrogation mode	Performance (RIS /RIR)	Bulk sensing medium	Reference
Au nanospheres	Wavelength	190 nm RIU $^{-1}$	Glycerol solutions	Huang et al. [63]
Au nanostars	Wavelength	318 nm RIU $^{-1}$		
Au nanocubes	Wavelength	94.5 nm RIU $^{-1}$	Glucose solutions	Hegde et al. [40]
Au nanorods	Wavelength	108.3 nm RIU $^{-1}$		
Au nanocone	Wavelength	300 nm RIU $^{-1}$	Theoretical work	Guo, Y.B. et al. [158]
Au cone-on-plate	Wavelength	433 nm RIU $^{-1}$		
Au nanobipyramids	Wavelength	362 nm RIU $^{-1}$	Glycerol solutions	Li, Q et al. [116]
Au square nanorings	Wavelength	893 nm RIU $^{-1}$	Theoretical	Zhang et al. [159]
Au nanorings	Wavelength	880 nm RIU $^{-1}$	Ethylene glycol solutions	Larsson et al. [42]
Ag triangles	Wavelength	1116.8 nm RIU $^{-1}$	Glucose solutions	Song et al. [117]
Au nanodots	Wavelength	1.3×10^{-4} RIU	Glycerol solutions	Tselikov et al. [58]
Au crossed-bowties	Wavelength	1753 nm RIU $^{-1}$	Theoretical work	Das, A. et al. [118]
Au nanodisk	Phase	172.34 nm RIU $^{-1}$		
Au nanorod	Phase	9.89 rad RIU $^{-1}$	Glucose solutions	CT, Li. et al. [119]
Au nanosphere	Phase	194.18 nm RIU $^{-1}$		
X shaped Au nanoislands	Phase	6.05 rad RIU $^{-1}$		
Au nanoislands	Phase	190 rad RIU $^{-1}$	Glycerol solutions	Huang, F. et al. [63]
Au nanorods	Phase	17.6 rad RIU $^{-1}$	Sucrose solutions	CT, Li. et al. [120]
Au nanoislands	Wavelength	9.75×10^{-8}	Saline solutions	Qiu et al. [121]
Au nanoislands	Phase	135 000 ° RIU $^{-1}$	Theoretical work	Yan, C. et al. [62]
Au nanoislands	Wavelength	-409 nm RIU $^{-1}$	NaCl solutions	This work
Au nanoislands	Phase	-1031 nm RIU $^{-1}$	NaCl solutions	This work

20 Au NI per μm^2 or surface coverage of $\Theta = 0.16$. These values are consistent with the morphological characteristics of the fabricated random Au NI metasurface. The dielectric function of gold was taken from Johnson and Christy. [77]

The reflectance spectra of a three-layer system in an ATR configuration were computed using Equations (2.79) and (2.80). This system comprises a glass substrate (BK7, $n = 1.515$), a thin gold island film, and water as the ambient matrix.

5.6.1 Reflectance spectra under p and s polarized light for different angles of incidence

The experimental R_p spectra, Figure 5.21a, illustrate a distinct reflectance dip, characterized by a redshift of the resonance wavelength from 504 nm to 530 nm while increasing the angle of incidence. Notably, at an angle of incidence of 65° , close to the critical angle, the reflectance at resonance wavelength reaches a minimum value of 0.017. At larger incidence angles, the reflectance at resonance increases from 0.017 to 0.080. Thus, the angle of incidence of 65° was used for the subsequent measurements because it ensures total internal reflection conditions on the whole refractive index range.

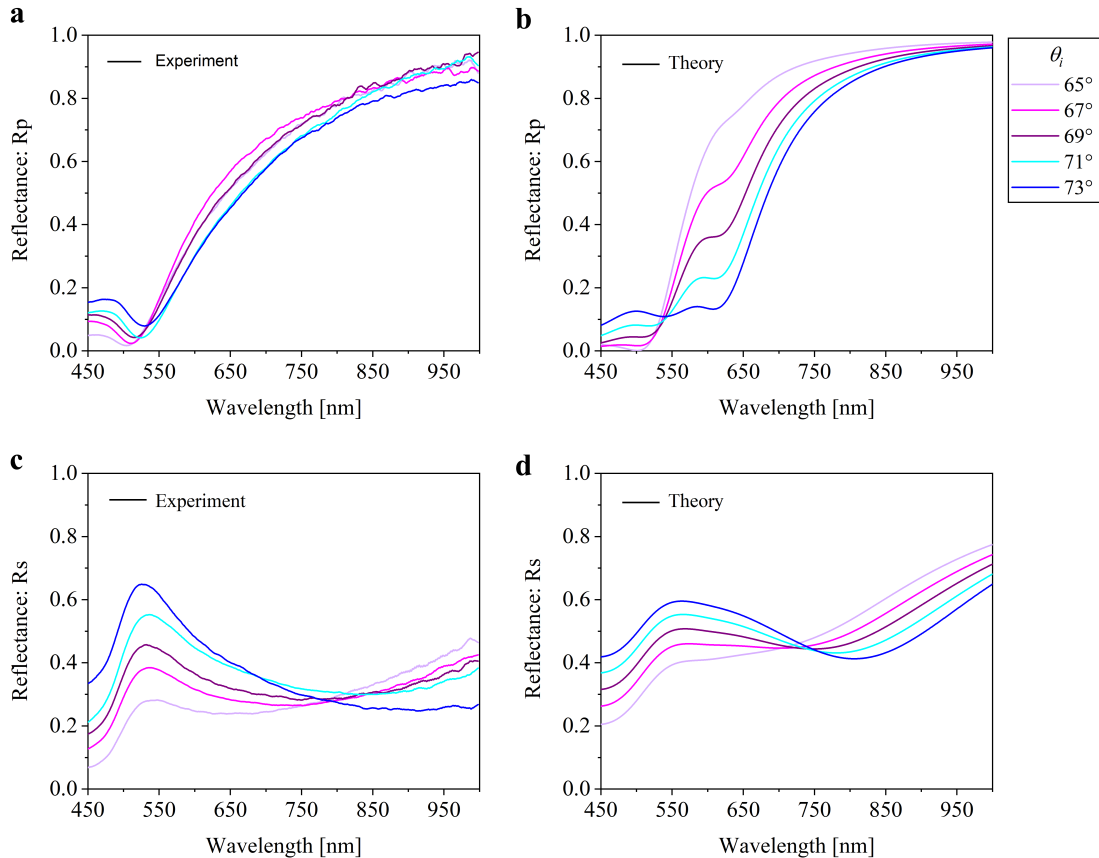


Figure 5.21: Experimental (first column) and theoretical (second column) reflectance spectra of a three-layer glass—thin gold island film—water system in ATR configuration for **a**, **b**. p and **c**, **d**. s polarization components, for different angles of incidence

From the theoretical side, Figure 5.21b displays the calculated R_p spectra, which shows similar features with a plasmonic dip which redshifts within the range of approximately

501–539 nm, as the angle of incidence increases. Most importantly, a near-zero reflectance ($R_p \approx 0.001$) is observed at resonance wavelength (501 nm) for an incidence angle of 65°.

Alongside the plasmonic dip, a shoulder is observed at approximately 650 nm in the theoretical R_p which is absent in the experimental spectra. This difference is likely attributed to several factors not accounted for in the theoretical model. Firstly, the island film theory model assumes an array of identical metallic nanospheroids supported onto a glass substrate. However, in our case, the fabricated Au NI arrays exhibit a wide size distribution. Secondly, AFM analysis reveals a partially embedding of the Au NI into the substrate.

For the experimental R_s spectra, a peak is observed at the wavelength of 530 nm, and its position remains independent of the angle of incidence, see Figure 5.21c. In the theoretical R_s spectra, Figure 5.21d, the peak is observed at 550 nm. After this peak, there is a broad and shallow LSPR valley with resonance wavelengths redshifting as the angle of incidence increases.

5.6.2 Reflectance spectra for p and s polarized light for different refractive indices

Next, we analyze the plasmonic response for p and s polarizations by varying the refractive index of the ambient medium, from 1.3328 to 1.3591. As shown in the experimental and analytical R_p spectra, Figure 5.22a and Figure 5.22b, respectively, a blueshift of the resonance wavelength is observed as the refractive index increases. The refractive index sensitivity, RIS, defined as $\Delta\lambda/\Delta n$, was determined to be -269 nm RIU⁻¹ experimentally, whereas the theoretical prediction yielded -263 nm RIU⁻¹. However, for s polarization (see Figures 5.22c and 5.22d), measuring the RIS is meaningless due to the broad plasmonic dip.

5.6.3 Phase response

Figures 5.23a and 5.23b display the experimental and theoretical differential phase spectral dependence on the refractive index of the medium surrounding the Au NI, respectively, and as predicted by Grigorenko et al. the steepest phase change occurs at the resonance wavelength. At low refractive indices ($n_a < 1.3397$) of the ambient medium, the phase increases monotonically with wavelength. As the refractive index increases further, the differential phase slope becomes steeper, until a phase singularity occurs at around $n_a = 1.3397$ - $n_a = 1.3431$, and after this value the sign of the differential phase slope reverses. Then, the phase becomes non-monotonic and the phase slope at resonance decreases while increasing the refractive index. It is important to note that in the experiment, the change in slope sign renders the measured phase indeterminate causing signal instability.

To effectively visualize the trends in phase dependence, the differential phase derivative, $\Delta\phi'_{LSPR}$, which characterizes the steepness of the phase response at resonance was experimentally and theoretically obtained, as shown in Figures 5.23c and 5.23d, respectively.

The peak position corresponds to the resonance wavelength, while the peak amplitude represents the steepness of the phase slope. Figures 5.23c and 5.23d demonstrate the blueshift of the resonance position as the refractive index increases, which was previously observed in the reflectance spectra dependence (see Figures 5.22a and 5.22b). As the refractive index increases from $n_a = 1.3328$ to $n_a = 1.3397$, the FWHM decreases from 11.4 to 10.9. Additionally, the peak amplitude increases with the refractive index, reaching its maximum at $n_a = 1.3397$, indicating the steepest phase response. Beyond this point, in the refractive index range $n_a = 1.3397$ –1.3431, a sign change in the derivative occurs, indicating

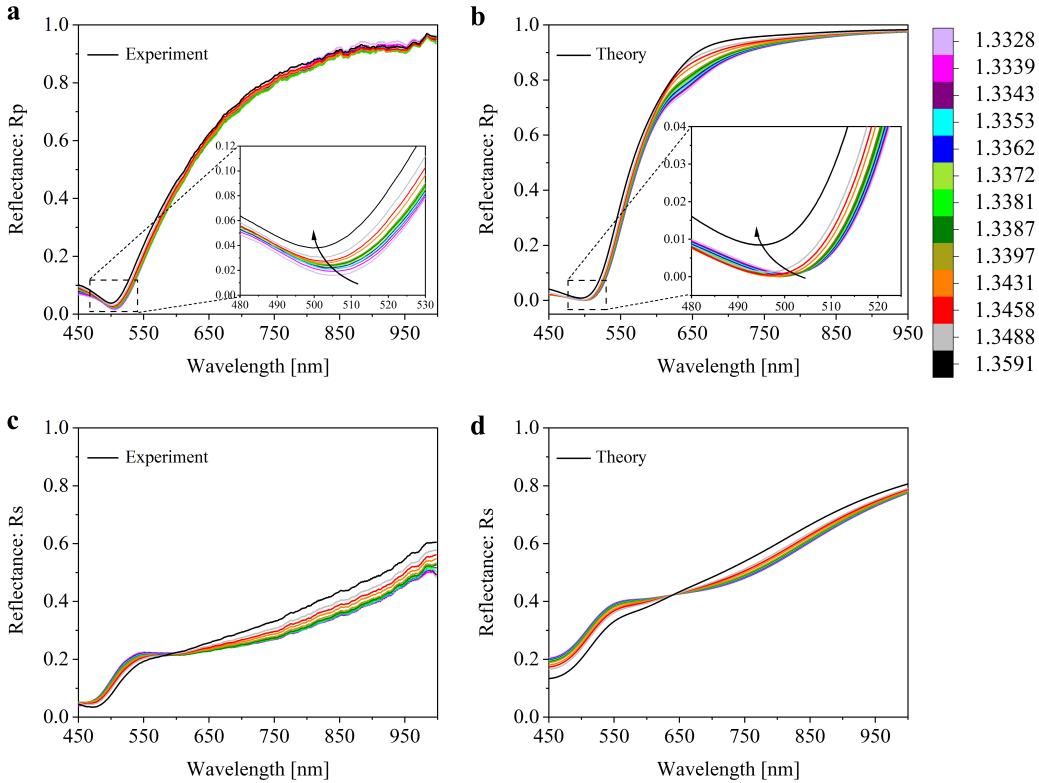


Figure 5.22: Reflectance spectra of Au NI metasurface in contact with saline solutions of different concentrations for **a**, **b**. *p* and **c**, **d**. *s* polarization components for experimental measurements (first column) and theoretical calculations (second column). The inset in R_p spectra clearly shows a blueshift of the resonance wavelength while increasing the refractive index of the ambient medium.

a phase singularity. As the refractive index continues increasing, a reduction in the peak amplitude and its broadening can be observed.

The phase behavior illustrated in Figure 5.23 corresponds to three distinct coupling regimes: *i*) the phase singularity region, characterized by an abrupt π phase jump (see Figures 5.23a and 5.23b), describes the critical coupling region, which occurs when all the energy of the incident field is completely transferred to the Au NI at its resonance frequency, resulting in a near-zero reflectance. [160, 161] *ii*) In the region characterized by a negative phase slope, the coupling between the Au NI and the incident field is weak (under coupling regime), resulting in an insufficient absorption. *iii*) In the region characterized by the positive phase slope, the Au NI reradiates the incident field into the ambient matrix medium (over coupling regime). [160, 161]

5.6.4 Localized surface plasmon resonance phase sensitivity

The bulk refractive index sensitivity, RIS, of the metasurface was determined both experimentally (Figures 5.24a and 5.24b) and theoretically (Figures 5.24c and 5.24d) using changes in the differential phase and its steepness. Figures 5.24a and 5.24b show the experimental and theoretical relationship between the LSPR differential phase shift ($\Delta\Phi$), respectively. Initially, the differential phase difference increases with the refractive index ($n_a = 1.3328$ to $n_a = 1.3397$). Subsequently, an abrupt change is observed in the singularity region ($n_a = 1.3397$ to $n_a = 1.3431$), followed by a decrease in amplitude with further increase in the refractive index ($n_a = 1.3431$ to $n_a = 1.3591$).

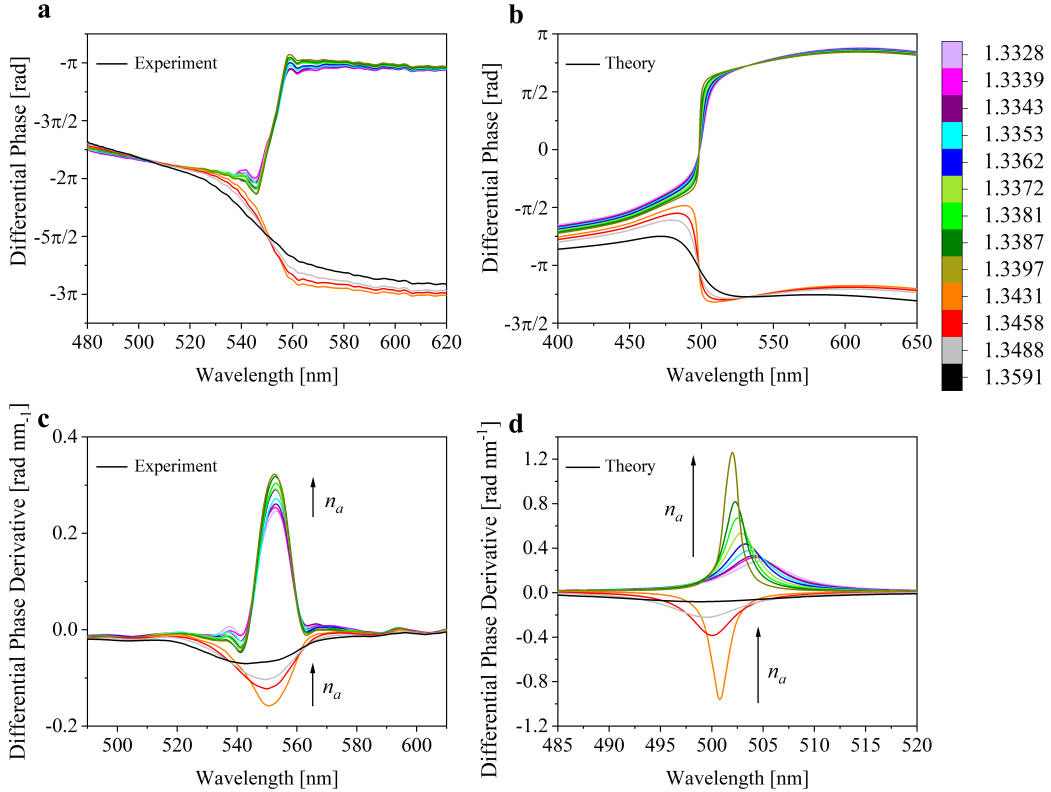


Figure 5.23: Experimental and analytical wavelength dependence of the **a, c.** differential phase between *s* and *p* polarization components and its **b, d.** derivative for different refractive indices of the ambient media

Figures 5.24c and 5.24d present the experimental and theoretical dependence of the phase spectral derivative ($\Delta\Phi'$) on the refractive index, respectively. As the refractive index increases, the phase derivative also increases, passes through the singularity region, and then decreases with an opposite sign.

Due to the nonlinear dependence of the phase shift and its derivative on the refractive index, the determination of the RIS defined as $\Delta\Phi/\Delta n$ and $\Delta\Phi'/\Delta n$, respectively, is not straightforward. Thus, it was conducted in four distinct refractive index intervals (two for each side before and after the phase singularity) approximated by a linear relationship of $\Delta\Phi$ and $\Delta\Phi'$ with n . The maximum phase RIS for experiments is 28 rad RIU^{-1} , while for the theoretical RIS is 198 rad nm^{-1} . In the phase derivative measurement mode, the maximum experimental RIS is $13 \text{ rad nm}^{-1} \text{ RIU}^{-1}$, while the maximum theoretical RIS is $290 \text{ rad nm}^{-1} \text{ RIU}^{-1}$.

Taking into consideration the experimental standard deviation of $6.0 \times 10^{-5} \text{ rad}$ for the differential phase measurements mode and $3.5 \times 10^{-6} \text{ rad nm}^{-1}$ for phase derivative measurements mode, we determined the corresponding refractive index resolution (RIR), which is calculated as the ratio of the standard deviation to the RIS. The resulting RIR values are $2.1 \times 10^{-6} \text{ RIU}$ (for the differential phase detection) and $2.7 \times 10^{-7} \text{ RIU}$ (for phase derivative mode).

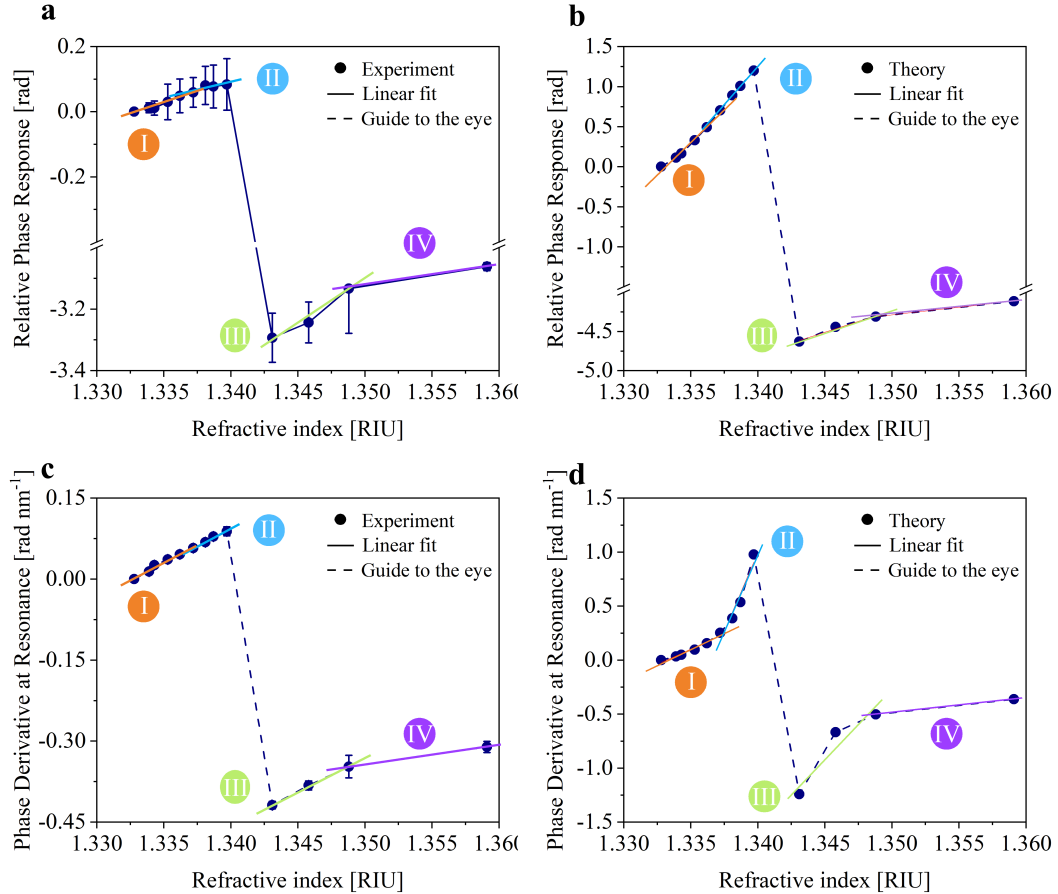


Figure 5.24: a, c. Relative LSPR phase and a, d. steepness of the LSPR phase response for different refractive indices for experiment (first row) and theoretical calculations (second row). The solid lines correspond to linear fits used to determine the RIS within distinct refractive index intervals

5.6.5 Discussion

The comparison between the experimental findings and the theoretical predictions of the plasmonic response for the metasurface based on a random Au NI array shows a good agreement between them. In particular, the main features of the experimental reflectance spectra for both polarization components are well described by the theoretical model under different angles of incidence (see Figure 5.21) and refractive index variations (see Figure 5.22). Specifically, when varying the refractive index, both the experimental and simulated R_p spectra exhibit a consistent trend: the resonance wavelength experiences a blueshift as the refractive index of the ambient medium for the Au NI increases. It is noteworthy that the measurements of the transmittance spectra at normal incidence for varying the refractive index show a redshift of the LSPR wavelength with the increasing n_a , consistent with results reported in literature

Most importantly, our study revealed that the metasurface characterized by a random distribution of Au NI exhibited a near-zero reflection for the p polarization component, with $R_p \approx 10^{-2}$. Our experimental phase spectra manifested a phase singularity and the associated flip of the phase slope, thus confirming the presence of topological darkness. This behavior aligns with the predictions made by Kravets et al. , showing that the phase exhibits bifurcational behaviour with a 2π round trip around the topological darkness. The

Table 5.4: Experimental (E) values of phase and phase derivative RIS and RIR obtained for different refractive index intervals around the phase singularity. The theoretical (T) RIS values were obtained through an estimation using the island film theory

Refractive index interval	RIS $\Delta\Phi$		RIR $\Delta\Phi$		RIS $\Delta\Phi'$		RIR $\Delta\Phi'$	
	[rad RIU $^{-1}$]	E	[RIU] $\times 10^{-6}$	E	[rad nm $^{-1}$ RIU $^{-1}$]	T	[RIU] $\times 10^{-7}$	E
I 1.3328 - 1.3372	14 ± 1.2	162	4.3±0.37	13 ± 0.8	56	2.7±0.17		
II 1.3372 - 1.3397	9 ± 3.9	198	6.7±2.9	13 ± 1.0	290	2.7±0.21		
III 1.3431 - 1.3488	28 ± 5.2	70	2.1±0.40	13 ± 0.5	213	2.7±0.1		
IV 1.3488 - 1.3591	7 ± 0.5	23	8.6±0.61	4 ± 0.1	21	8.8±0.22		

predicted topological stability associated with this effect was clearly manifested in our experiment through multiple observations. Remarkably, as mentioned above, we experimentally observed the presence of a phase singularity, even though the formal criteria for achieving topological darkness were partially fulfilled. Additionally, despite the wide distribution of Au NI sizes and positional disorder within our metasurface, we still achieved a near-zero reflection condition and the corresponding phase singularity. Furthermore, we noticed that variations in the refractive index had a negligible impact on the minimum reflectance value at the resonance wavelength.

As expected, the maximum sensitivity is found in the region near the phase singularity in both phase and phase derivative detection modes. Therefore, it is advantageous to focus on sensing refractive index changes within this specific region. Conversely, as we move away from the phase singularity region, the sensitivity gradually decreases, which limits the dynamic range.

A summary of the experimental and analytical RIS in both phase and phase derivative measurement modes, as well as the RIR, is provided in Table 5.4. Note that the obtained value of RIR exceeds typical values reported in the literature for the LSPR sensing mode and it is comparable with record values reported for SPR sensing mode

It is important to note that the rapid phase jumps in the phase singularity region poses a challenge, as even slight variations in the refractive index can lead to significant changes in the LSPR differential phase slope. Consequently, the highest sensitivity regime in our measurements was not achieved. However, this issue can be solved by enhancing the thermal and mechanical stability of our experimental setup and/or employing advanced signal processing tools.

There are also certain limitations associated with topological darkness in 2D metasurfaces. One limitation is the restricted operational range within which the topological darkness phenomenon occurs. The phase slope responses and minimal reflectance are only observed within a specific refractive index range, and beyond this range, the performance of the metasurface deteriorates. This limitation requires careful selection of the operating conditions and consideration of the target refractive index range for a given sensing application.

5.7 Polyelectrolytes binding detection using LSPR effect

The sample of Au NI with radius of 41.3 nm was selected for detecting the binding event of polyelectrolytes due to its maximum RIS in the first refractive index interval, as illustrated in Figure 5.20a. Since there was a shortage of reagents for manufacturing microfluidic

devices, a microfluidic device intended for calibration purposes, as shown in Figure 3.7b, was used. Both analytical and experimental findings have demonstrated a reduction in RIS as the angle of incidence deviates from the critical angle under ATR condition. However, due to technical issues, the angle of incidence chosen for this experiment was 73°.

Figure 5.25 shows the sensogram of the detection of polyelectrolytes using the phase interrogation mode in both wavelength (blue line) and phase derivative (red line) detection modes. Initially, in the wavelength detection mode, the LSPR wavelength is located at approximately 544 nm when the buffer is placed on the Au NI. Subsequently, upon careful removal of the buffer using a pipette and deposition of the PAH polyelectrolyte, the LSPR wavelength redshifts due to changes in the local refractive index. Then, the remaining material is retired from the Au NI and the PSS polyelectrolyte is followed deposited. Here, the LSPR wavelength significantly blueshifts, approximately 3 nm. After consecutive and alternating deposition of both PAH and PSS polyelectrolytes, the LSPR wavelength remains nearly constant.

The red line in Figure 5.25 shows the sensogram of the polyelectrolytes' detection using the phase derivative detection mode, acquired simultaneously with the LSPR wavelength detection mode. The LSPR phase derivative is positioned at approximately $-0.019 \text{ rad nm}^{-1}$ when the buffer is placed on the Au NI. Upon alternating depositions of PAH and PSS, the phase derivative gradually decreases, with each polyelectrolyte deposition inducing a smaller change compared to the previous one. Notably, for the third deposition of PSS (last red column), the LSPR phase derivative remains nearly constant compared to the third PAH deposition (third green column).

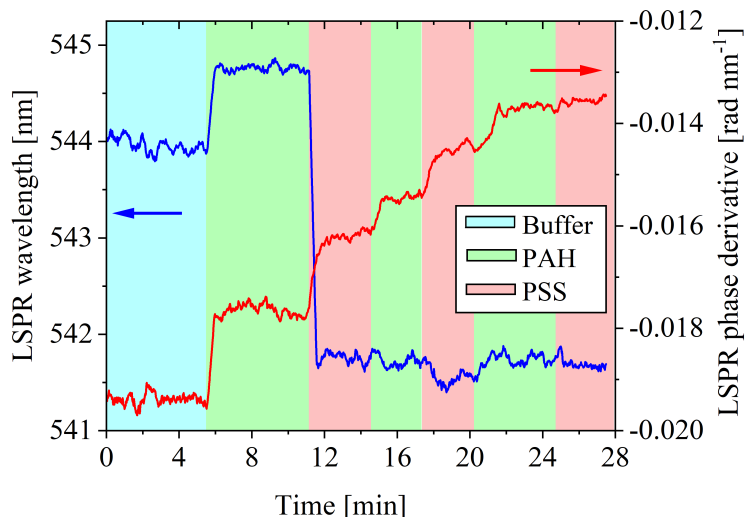


Figure 5.25: Sensogram of the LbL polyelectrolytes detection in the phase interrogation mode. The detection modes used are the LSPR wavelength (blue) and phase derivative (red). The angle of incidence is 73°.

5.7.1 Discussion

The sensogram showed in Figure 5.25 demonstrates the detection of three bilayers (PAH-PSS) of polyelectrolytes using a metasurface composed by Au NI with mean radius of 41.3 nm using phase interrogation mode. In the wavelength detection mode, a redshift is

observed during the first PAH deposition, followed by a considerable blueshift with the PSS deposition, completing the first bilayer. This LSPR wavelength behaviour was previously observed for the metasurface composed by Au NI with radius of 5.9 nm radius (see Figure 5.19b) when the refractive index of the surrounding medium is changed. Then, observing a redshift and then a blueshift as the refractive index increases is not uncommon.

Afterwards, two more bilayers were deposited on the Au NI; however, the LSPR wavelength does not shift anymore. Conversely, using the phase derivative detection mode, all three bilayers of polyelectrolytes could be successfully detected. This demonstrates the high sensitivity of the phase derivative mode for detecting binding events, compared to the wavelength detection mode. As expected, the LSPR near field is saturated with low deposition of polyelectrolytes compared to SPR experiments, due to the localized nature of plasmons.

Multiple experiments for detecting the binding events using the streptavidin-biotin system, were conducted using different Au NI arrays, different conditions of the experimental setup and different conditions for the streptavidin-biotin preparation. However, they could not be successfully detected, the signal in the corresponding sensogram is very weak and is comparable to the intrinsic noise of the experimental detection. This is attributed to the low RIS of the Au NI compared to the RIS found for the Au NFs, were both functionalization and hybridization were successfully performed. The RIS of the Au NI array is at least an order of magnitude smaller compared to the Au NF.

Similarly, multiple experiments for the detection of the conjugated oligonucleotides were performed without successfully detecting them, for the same reasons. Therefore, our metasurfaces must be optimized to enhance sensitivity and detect binding events for the streptavidin-biotin and conjugated oligonucleotide systems.

Chapter 6 | Conclusions

SPR and LSPR transducers were theoretically and experimentally investigated in intensity and phase interrogation mode using different resonance markers.

- The transfer matrix method and the thin island film theory were computationally implemented for theoretical analysis for calculating the intensity and phase response of the reflectance spectra.
- The fabrication of random metasurfaces composed of gold nanoislands was achieved through thermal annealing of ultrathin gold films.
- The experimental setup based on Kretschmann configuration was implemented to perform the measurements for both intensity and phase interrogation modes.
- A custom LabVIEW interface was developed for acquisition, processing and display of the signal in real time.

6.1 Surface Plasmon Resonance Approach

- The experimental and analytical reflectance spectrum demonstrated a satisfactory agreement.
- The experimental conditions for achieving maximum sensitivity were optimized.
- Gold nanofilms with thickness of 50 nm exhibited the highest experimental sensitivity (9970 nm RIU^{-1}) at an angle of incidence of 67° .
- The refractive index resolution was enhanced by using the phase interrogation mode with values of $5.2 \times 10^{-8} \text{ RIU}$ for wavelength marker, 4.3×10^{-7} for phase marker and $3.7 \times 10^{-6} \text{ RIU}$ for phase derivative marker.
- The detection and characterization of various biological systems was successfully performed, highlighting versatility and reliability of surface plasmon resonance-based biosensors.
 - The thickness of the polyelectrolyte layers was controlled by varying saline concentration of the buffer, resulting in layer thicknesses ranging from 2.1 nm to 5.0 nm.
 - Low limit of detection values were obtained: 6.6 nM for biotin detection and 5.2 pM for oligonucleotides detection.

Phase interrogation techniques have shown to offer advantages over traditional methods in monitoring biomolecular interactions.

6.2 Localized Surface Plasmon Resonance Approach

- The fabricated gold nanoislands arrays exhibited a broad size distribution and various shapes (quasi-spherical, hexagonal, ellipsoidal), with partial embedding into the glass substrate ensuring mechanical stability.
- The reflectance spectra in attenuated total reflectance condition under both *s* and *p* polarization components closely resembled experimental results, validating island film theory.
- The gold nanoislands arrays displayed blueshifted resonance wavelength and nonlinear response to changes in refractive index, with highest sensitivity achieved close to near-zero reflectance.
- An improvement in sensitivity was demonstrated using a common path spectral interferometer, surpassing the sensitivity reported in previous studies.
- Two alternative phase sensing markers were introduced and compared:
 - The phase detection marker demonstrated high refractive index resolution with value of 2.1×10^{-6} RIU.
 - The phase derivative detection marker achieved high sensitivity with value of 2.7×10^{-7} RIU.
- The topological darkness phenomenon was observed in a random metasurface supported on a glass substrate:
 - The differential phase spectrum displays abrupt $\pm\pi$ phase jumps for certain refractive index values, indicating the presence of phase singularities associated with topological darkness.
 - The observed behaviour of reflectance spectra and differential phase was validated by a theoretical model based on the island film theory, demonstrating qualitative agreement with the experimental data.
 - The sensitivity values achieved near the phase singularity surpassed those reported in previous studies, with values reaching up to 198 rad RIU^{-1} and $290 \text{ rad nm}^{-1} \text{ RIU}^{-1}$ for phase and phase derivative markers, respectively, highlighting the remarkable performance of the proposed sensing approach.
 - This achievement demonstrates the potential of exploiting topological darkness for advanced sensing applications.

The findings provide valuable guidance for the design and optimization of gold nanoislands arrays supported on a glass substrate for advanced sensing applications.

6.3 Perspectives

Even though an extensive study of gold nanoislands arrays supported on a glass substrate have been conducted, avenues for future investigation remain open.

- Sensitivity enhancement:

- Exploration of alternative nanoparticle geometries to improve sensitivity. Preliminary results indicates that gold nanorods arrays supported on a glass substrate show improved sensitivity compared to quasi-spherical nanoislands arrays.
- Investigation of other manufacturing methods, like the chemical synthesis of metallic nanoparticles using the Turkevich technique, to facilitate further exploration in enhancing sensitivity.
- Sensing challenges:
 - Implementation of a temperature controller to mitigate undesired shifts in the resonance signal induced by the thermal equilibrium process between the transducer and aqueous solutions.
 - Consideration for employing a differential scheme for multiplexing sensing, where one spot monitors the plasmonic response of a buffer reference, while another spot monitors the plasmonic shift due to binding events.
- Biomolecular detection:
 - Exploration of the thermoplasmonic effect to enhance the detection of conjugated oligonucleotides, which locally elevates the temperature near nanoparticles, creating optimal conditions for the hybridization process of complementary oligonucleotides and enabling discrimination of similar oligonucleotides.
 - Expansion of the scope of biological systems for developing plasmonic biosensors tailored for specific applications in medical diagnostics.

Appendix A |

Derivation of the dielectric function using the Lorentz-Drude model

The optical properties of a dielectric medium are mainly described by the dielectric function. The Lorentz-Drude model is the theory more complete to describe the dielectric-light interaction. Let us assume electrons with mass m_e bounded to atomic nucleus by an imaginary string with a restitutive constant ω_0^2 . The electron motion is attenuated by a force proportional to their velocity, the proportionality constant also known as damping constant is represented by Γ . The whole system is under an external electric field \vec{E} , with frequency ω .

The analysis of forces using Newton's second law is then

$$\vec{F}_{\text{electric}} + \vec{F}_{\text{restoring}} + \vec{F}_{\text{damping}} = \vec{F}_{\text{net}}, \quad (\text{A.1})$$

by explicitly writing the value of each of the forces we obtain

$$-q\vec{E} - m_e\omega_0^2\vec{r} - m_e\Gamma\frac{\partial\vec{r}}{\partial t} = m_e\frac{\partial^2\vec{r}}{\partial t^2}, \quad (\text{A.2})$$

where q is the charge of the electron. Solving the second-order differential equation, the displacement vector \vec{r} is found,

$$\vec{r}(\omega) = -\frac{q}{m_e}\frac{\vec{E}(\omega)}{\omega_0^2 - \omega^2 - i\Gamma\omega}, \quad (\text{A.3})$$

Here, the equation shows that the electron oscillates with the phase and frequency of the \vec{E} . The offset of the negative and positive charges is known as dipole moment, defined as $\vec{p} = -q\vec{r}$. Then

$$\vec{p}(\omega) = -\frac{q^2}{m_e}\frac{\vec{E}(\omega)}{\omega_0^2 - \omega^2 - i\Gamma\omega}. \quad (\text{A.4})$$

The ratio between the induced dipole moment and the electric field is defined as the electric polarizability and it is given by

$$\alpha = \frac{\vec{p}}{\epsilon_0\epsilon_d\vec{E}_0}. \quad (\text{A.5})$$

Furthermore, assuming that the metal has an atomic density of N , the polarizability function is

$$\vec{P} = N\langle\vec{p}\rangle = -Nq\vec{r} = \frac{Nq^2}{m_e}\frac{\vec{E}(\omega)}{(\omega_0^2 - \omega^2 - i\Gamma\omega)}, \quad (\text{A.6})$$

where $\langle \rangle$ represents average over all atoms in the material. By relating Equation (A.6) with the polarizability [Equation (2.7)], we obtain

$$\chi = \frac{Nq^2}{m_e} \frac{1}{\omega_0^2 - \omega^2 - i\Gamma\omega}. \quad (\text{A.7})$$

The dielectric permittivity of the medium and the electric susceptibility are related by

$$\varepsilon = 1 + \chi, \quad (\text{A.8})$$

then, the dielectric function of the medium is

$$\varepsilon_m(\omega) = 1 + \frac{\omega_p^2}{\omega_0^2 - \omega^2 - i\Gamma\omega}. \quad (\text{A.9})$$

where $\omega_p^2 = \frac{N_e q^2}{\varepsilon_0 m_e}$ is known as plasma frequency of the free electron gas. The term m_e stands for the effective mass of the electron, while N_e stands for the electron density.

The plasma frequency can be interpreted as the angular frequency at which electrons in the metal respond to oscillating electric fields. Equation (A.9) is the core of the Lorentz model because the dielectric permittivity depends on the electric field frequency as well as the optical properties of the metal. Evidently, the dielectric permittivity is a complex function which can be separated into its real and imaginary parts, as $\varepsilon_m(\omega) = \varepsilon_{m,1} + i\varepsilon_{m,2}$. After some algebra, the real part of the dielectric permittivity function is

$$\varepsilon_{m,1} = \frac{\omega_p^2(\omega_0^2 - \omega^2)}{(\omega_0^2 - \omega^2)^2 + \Gamma^2\omega^2}, \quad (\text{A.10})$$

and the imaginary part is given by

$$\varepsilon_{m,2} = \frac{\omega_p^2\Gamma\omega}{(\omega_0^2 - \omega^2)^2 + \Gamma^2\omega^2}. \quad (\text{A.11})$$

The physical meaning of these equations is described as follows. The real part of the dielectric function [Equation (A.10)] is related to the refractive index, while the imaginary part [Equation (A.11)] influences the attenuation of light as it propagates through the material, i.e., it represents losses. Figure A.1 depicts the real and the imaginary parts of the dielectric function (A.9). The real and imaginary parts of the dielectric function are centered on the resonant frequency of the atom, while the width of the real part is determined by the damping constant.

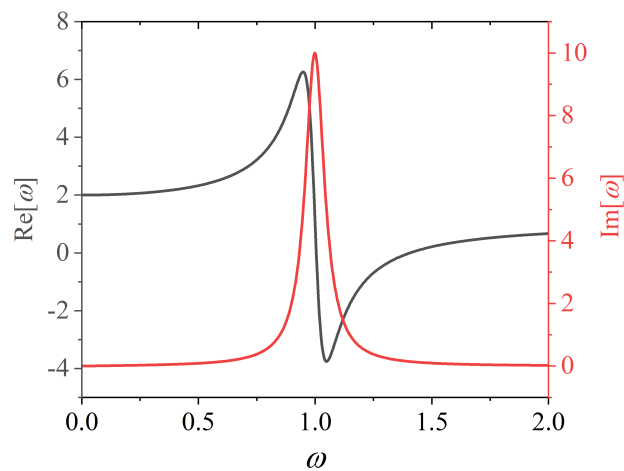


Figure A.1: Real and imaginary part of the dielectric function analytically obtained through the Lorentz-Drude model

Appendix B |

Derivation of SPPs dispersion relation

The derivation of the dispersion relation for SPPs is based on solving the boundary conditions at the interface between a metal and a dielectric interface. We now shall consider a propagating wave along the x direction on interface composed by a thin metallic film with a dielectric function ε_m and a non-absorbing dielectric medium with dielectric constant ε_d , as shown in Figure 2.10. The electric and magnetic waves can be mathematically described as $\vec{E}(\vec{r}) = \vec{E}(z)e^{ik_x x}$ and $\vec{H}(\vec{r}) = \vec{H}(z)e^{ik_x x}$, respectively. By replacing this equation in the Helmholtz equation [Equation (2.16)], this leads to

$$\frac{\partial^2 E(z)}{\partial z^2} + (k_0 \varepsilon - k_x^2) E(z) = 0. \quad (\text{B.1})$$

Similarly, for the magnetic field, which is oscillating in the xy plane

$$\frac{\partial^2 H(z)}{\partial z^2} + (k_0 \varepsilon - k_x^2) H(z) = 0. \quad (\text{B.2})$$

By expanding the curl in the Ampère equation [Equation (2.4)] in the spatial coordinates; and using the spatial and temporal derivative relations [Equation (2.12)], we obtain

$$\frac{\partial E_z}{\partial y} - \frac{\partial E_y}{\partial z} = i\omega \mu_0 H_x, \quad (\text{B.3})$$

$$\frac{\partial E_x}{\partial z} - \frac{\partial E_z}{\partial x} = i\omega \mu_0 H_y, \quad (\text{B.4})$$

$$\frac{\partial E_y}{\partial x} - \frac{\partial E_x}{\partial y} = i\omega \mu_0 H_z. \quad (\text{B.5})$$

In a similar way, after operating the Faraday equation [Equation (2.3)] we obtain

$$\frac{\partial H_z}{\partial y} - \frac{\partial H_y}{\partial z} = -i\omega \varepsilon_0 \varepsilon E_x, \quad (\text{B.6})$$

$$\frac{\partial H_x}{\partial z} - \frac{\partial H_z}{\partial x} = -i\omega \varepsilon_0 \varepsilon E_y, \quad (\text{B.7})$$

$$\frac{\partial H_y}{\partial x} - \frac{\partial H_x}{\partial y} = -i\omega \varepsilon_0 \varepsilon E_z. \quad (\text{B.8})$$

For an electromagnetic wave propagating in the xz plane, the magnitudes of the phasor fields are dependent on the coordinates x and z , but constant along the y direction, i.e., $\frac{\delta}{\delta y} = 0$. Then, the above set of equations are transformed to

$$\frac{\partial E_y}{\partial z} = -i\omega\mu_0 H_x, \quad (\text{B.9})$$

$$\frac{\partial E_x}{\partial z} - ik_x E_z = i\omega\mu_0 H_y, \quad (\text{B.10})$$

$$ik_x E_y = i\omega\mu_0 H_z, \quad (\text{B.11})$$

$$\frac{\partial H_y}{\partial z} = i\omega\varepsilon_0\varepsilon E_x, \quad (\text{B.12})$$

$$\frac{\partial H_x}{\partial z} - ik_x H_z = -i\omega\varepsilon_0\varepsilon E_y, \quad (\text{B.13})$$

$$ik_x H_y = -i\omega\varepsilon_0\varepsilon H_x. \quad (\text{B.14})$$

For p polarized light, the electric field components are in the xz plane and the magnetic field components are in the xy plane. Then, the equations that describe this mode are

$$\begin{aligned} E_x &= -i\frac{1}{\omega\varepsilon_0\varepsilon}\frac{\partial H_y}{\partial z}, \\ E_z &= \frac{k_x}{\omega\varepsilon_0\varepsilon}H_y, \\ \frac{\partial^2 H_y}{\partial z^2} + (k_0\varepsilon - k_x^2)H_y &= 0. \end{aligned} \quad (\text{B.15})$$

The remaining equations correspond to s polarized light, where the electric field component being nonzero is E_y and for the magnetic field is H_x, H_y . Then

$$\begin{aligned} H_x &= i\frac{1}{\omega\mu_0}\frac{\partial E_y}{\partial z}, \\ H_z &= \frac{k_x}{\omega\mu_0}E_y, \\ \frac{\partial^2 E_y}{\partial z^2} + (k_0\varepsilon - k_x^2)E_y &= 0. \end{aligned} \quad (\text{B.16})$$

Now, propagating wave solutions confined to the interface are looked. First, let's analyze the case where the light is p polarized. Using the set of Equations (B.15), the electric and magnetic fields components for $z > 0$ are

$$E_x(z) = iA_2\frac{1}{\omega\varepsilon_0\varepsilon_d}k_2e^{ik_xx}e^{-k_dz}, \quad (\text{B.17})$$

$$E_z(z) = -A_1\frac{k_x}{\omega\varepsilon_0\varepsilon_d}e^{ik_xx}e^{-k_dz}, \quad (\text{B.18})$$

$$H_y(z) = A_2e^{ik_xx}e^{-k_dz}, \quad (\text{B.19})$$

and for $z < 0$

$$E_x(z) = iA_2 \frac{1}{\omega \varepsilon_0 \varepsilon_m} k_1 e^{ik_x x} e^{k_m z}, \quad (\text{B.20})$$

$$E_z(z) = -A_1 \frac{k_x}{\omega \varepsilon_0 \varepsilon_m} e^{ik_x x} e^{k_m z}, \quad (\text{B.21})$$

$$H_y(z) = A_1 e^{ik_x x} e^{k_m z}. \quad (\text{B.22})$$

The continuity of the normal and transversal field components on this interface is fulfilled if the amplitudes, A_1 and A_2 , are equal, so

$$\frac{k_d}{k_m} = -\frac{\varepsilon_d}{\varepsilon_m}. \quad (\text{B.23})$$

This equation is satisfied only if ε_m is negative. Additionally, the expression for H_y must satisfy the wave equation, then

$$k_m^2 = -k_0^2 \varepsilon_m, \quad (\text{B.24})$$

$$k_d^2 = k_x^2 - k_0^2 \varepsilon_d. \quad (\text{B.25})$$

Combining Equations from (B.23) to (B.25) and solving from k_x , we obtain the relation [48, 76]

$$k_{\text{SPP}} = \frac{\omega}{c} \sqrt{\frac{\varepsilon_m \varepsilon_d}{\varepsilon_m + \varepsilon_d}}, \quad (\text{B.26})$$

The propagation constant is known as the SPP dispersion relation.

Now, let's analyze the case where the interface is illuminated under s polarized incident light. Using a similar procedure, the electric and magnetic fields components for $z > 0$ are

$$E_y(z) = A_2 e^{ik_x x} e^{-k_2 z}, \quad (\text{B.27})$$

$$H_x(z) = -A_2 \frac{1}{\omega \mu_0} k_2 e^{ik_x x} e^{-k_2 z}, \quad (\text{B.28})$$

$$H_z(z) = A_2 \frac{\beta}{\omega \mu_0} e^{ik_x x} e^{-k_2 z}, \quad (\text{B.29})$$

and for $z < 0$

$$E_y(z) = A_1 e^{ik_x x} e^{k_1 z}, \quad (\text{B.30})$$

$$H_x(z) = iA_1 \frac{1}{\omega \mu_0} k_1 e^{ik_x x} e^{k_1 z}, \quad (\text{B.31})$$

$$H_z(z) = A_1 \frac{\beta}{\omega \mu_0} e^{ik_x x} e^{k_1 z}. \quad (\text{B.32})$$

Now, the condition of continuity for the normal and transversal field components on this interface requires

$$A_1(k_1 + k_2) = 0. \quad (71) \quad (\text{B.33})$$

This condition is only satisfied if the amplitude is null, $A_1 = 0$.

Although Equation (B.23) appears trivial, it is a relevant result because it says that SPPs cannot be excited under s polarized light; they are observed only under p polarized incident light.

Bibliography

- [1] P. V. Markov *et al.*, “The evolution of SARS-CoV-2,” *Nature Reviews Microbiology*, vol. 21, no. 6, pp. 361–379, Apr. 2023, ISSN: 1740-1534. DOI: [10.1038/s41579-023-00878-2](https://doi.org/10.1038/s41579-023-00878-2).
- [2] B. Bhushan, “Introduction to nanotechnology,” *Springer Handbooks*, pp. 1–19, 2017, ISSN: 25228706. DOI: [10.1007/978-3-662-54357-3__1/FIGURES/11](https://doi.org/10.1007/978-3-662-54357-3__1/FIGURES/11).
- [3] S. Bayda, M. Adeel, T. Tuccinardi, M. Cordani, and F. Rizzolio, “The History of Nanoscience and Nanotechnology: From Chemical–Physical Applications to Nanomedicine,” *Molecules*, vol. 25, no. 1, p. 112, Dec. 2019, ISSN: 1420-3049. DOI: [10.3390/MOLECULES25010112](https://doi.org/10.3390/MOLECULES25010112).
- [4] “‘Plenty of room’ revisited,” *Nature Nanotechnology* 2009 4:12, vol. 4, no. 12, pp. 781–781, 2009, ISSN: 1748-3395. DOI: [10.1038/nnano.2009.356](https://doi.org/10.1038/nnano.2009.356).
- [5] N. Taniguchi, “On the basic concept of’nano-technology,” Proc. Intl. Conf. Prod. Eng. Tokyo, Part II, 1974, 1974.
- [6] J. T. Lue, “Physical Properties of Nanomaterials,” *Encyclopedia of Nanoscience and Nanotechnology*, vol. 10, 2007.
- [7] J. M. Gonzalez Estevez, J. Antonio Sánchez-Gil, A. Ali, A. Mitra, and B. Aïssa, “Metamaterials and Metasurfaces: A Review from the Perspectives of Materials, Mechanisms and Advanced Metadevices,” *Nanomaterials*, vol. 12, no. 6, p. 1027, Mar. 2022, ISSN: 2079-4991. DOI: [10.3390/NANO12061027](https://doi.org/10.3390/NANO12061027).
- [8] N. Meinzer, W. L. Barnes, and I. R. Hooper, “Plasmonic meta-atoms and metasurfaces,” *Nature Photonics*, vol. 8, no. 12, pp. 889–898, Nov. 2014, ISSN: 1749-4893. DOI: [10.1038/nphoton.2014.247](https://doi.org/10.1038/nphoton.2014.247).
- [9] S. Boroviks, R. A. Deshpande, N. A. Mortensen, and S. I. Bozhevolnyi, “Multifunctional Metamirror: Polarization Splitting and Focusing,” *ACS Photonics*, vol. 5, no. 5, pp. 1648–1653, May 2018, ISSN: 23304022. DOI: [10.1021/ACSPHOTONICS.7B01091](https://doi.org/10.1021/ACSPHOTONICS.7B01091).
- [10] F. Cheng, J. Gao, S. T. Luk, and X. Yang, “Structural color printing based on plasmonic metasurfaces of perfect light absorption,” *Scientific Reports*, vol. 5, no. 1, pp. 1–10, Jun. 2015, ISSN: 2045-2322. DOI: [10.1038/srep11045](https://doi.org/10.1038/srep11045).
- [11] N. Destouches *et al.*, “Laser-Empowered Random Metasurfaces for White Light Printed Image Multiplexing,” *Advanced Functional Materials*, vol. 31, no. 18, p. 2010 430, May 2021, ISSN: 1616-3028. DOI: [10.1002/ADFM.202010430](https://doi.org/10.1002/ADFM.202010430).
- [12] N. Liu, M. Mesch, T. Weiss, M. Hentschel, and H. Giessen, “Infrared perfect absorber and its application as plasmonic sensor,” *Nano Letters*, vol. 10, no. 7, pp. 2342–2348, Jul. 2010, ISSN: 15306984. DOI: [10.1021/NL9041033](https://doi.org/10.1021/NL9041033).

- [13] H. X. Xu *et al.*, “Polarization-insensitive 3D conformal-skin metasurface cloak,” *Light: Science & Applications*, vol. 10, no. 1, pp. 1–13, Apr. 2021, ISSN: 2047-7538. DOI: [10.1038/s41377-021-00507-8](https://doi.org/10.1038/s41377-021-00507-8).
- [14] Z. Wang *et al.*, “Plasmonic Metasurfaces for Medical Diagnosis Applications: A Review,” *Sensors*, vol. 22, no. 1, p. 133, Dec. 2021, ISSN: 1424-8220. DOI: [10.3390/S22010133](https://doi.org/10.3390/S22010133).
- [15] S. Sim and N. K. Wong, “Nanotechnology and its use in imaging and drug delivery (Review),” *Biomedical reports*, vol. 14, no. 5, 2021, ISSN: 2049-9434. DOI: [10.3892/BR.2021.1418](https://doi.org/10.3892/BR.2021.1418).
- [16] J. K. Patra *et al.*, “Nano based drug delivery systems: recent developments and future prospects,” *Journal of Nanobiotechnology 2018 16:1*, vol. 16, no. 1, pp. 1–33, Sep. 2018, ISSN: 1477-3155. DOI: [10.1186/S12951-018-0392-8](https://doi.org/10.1186/S12951-018-0392-8).
- [17] L. Li *et al.*, “A review of nanomaterials for biosensing applications,” *Journal of Materials Chemistry B*, vol. 12, no. 5, pp. 1168–1193, Jan. 2024, ISSN: 2050-7518. DOI: [10.1039/D3TB02648E](https://doi.org/10.1039/D3TB02648E).
- [18] H. Altug, S. H. Oh, S. A. Maier, and J. Homola, “Advances and applications of nanophotonic biosensors,” *Nature Nanotechnology*, vol. 17, no. 1, pp. 5–16, Jan. 2022, ISSN: 1748-3395. DOI: [10.1038/s41565-021-01045-5](https://doi.org/10.1038/s41565-021-01045-5).
- [19] D. Bera, L. Qian, T. K. Tseng, and P. H. Holloway, “Quantum Dots and Their Multimodal Applications: A Review,” *Materials*, vol. 3, no. 4, pp. 2260–2345, Mar. 2010, ISSN: 1996-1944. DOI: [10.3390/MA3042260](https://doi.org/10.3390/MA3042260).
- [20] N. Bhalla, P. Jolly, N. Formisano, and P. Estrela, “Introduction to biosensors,” *Essays in Biochemistry*, vol. 60, no. 1, pp. 1–8, Jun. 2016, ISSN: 0071-1365. DOI: [10.1042/EBC20150001](https://doi.org/10.1042/EBC20150001).
- [21] P. Damborský, J. Švitel, and J. Katrlík, “Optical biosensors,” *Essays in Biochemistry*, vol. 60, no. 1, pp. 91–100, Jun. 2016, ISSN: 0071-1365. DOI: [10.1042/EBC20150010](https://doi.org/10.1042/EBC20150010).
- [22] C. Chen and J. Wang, “Optical biosensors: an exhaustive and comprehensive review,” *Analyst*, vol. 145, no. 5, pp. 1605–1628, Mar. 2020, ISSN: 1364-5528. DOI: [10.1039/C9AN01998G](https://doi.org/10.1039/C9AN01998G).
- [23] D. Dey and T. Goswami, “Optical biosensors: A revolution towards quantum nanoscale electronics device fabrication,” *Journal of Biomedicine and Biotechnology*, vol. 2011, 2011, ISSN: 11107243. DOI: [10.1155/2011/348218](https://doi.org/10.1155/2011/348218).
- [24] P. Talarzka, M. Boruczkowski, and J. Żurawski, “Current Knowledge of Silver and Gold Nanoparticles in Laboratory Research—Application, Toxicity, Cellular Uptake,” *Nanomaterials*, vol. 11, no. 9, p. 2454, Sep. 2021, ISSN: 2079-4991. DOI: [10.3390/NANO11092454](https://doi.org/10.3390/NANO11092454).
- [25] R. Wood, “XLII. On a remarkable case of uneven distribution of light in a diffraction grating spectrum,” *The London, Edinburgh, and Dublin Philosophical Magazine and Journal of Science*, vol. 4, no. 21, pp. 396–402, Sep. 1902, ISSN: 1941-5982. DOI: [10.1080/14786440209462857](https://doi.org/10.1080/14786440209462857).
- [26] U. Fano, “The Theory of Anomalous Diffraction Gratings and of Quasi-Stationary Waves on Metallic Surfaces (Sommerfeld’s Waves),” *JOSA*, vol. 31, no. 3, pp. 213–222, Mar. 1941, ISSN: 0030-3941. DOI: [10.1364/JOSA.31.000213](https://doi.org/10.1364/JOSA.31.000213).

- [27] E. Kretschmann and H. Raether, “Radiative Decay of Non Radiative Surface Plasmons Excited by Light,” *Zeitschrift fur Naturforschung - Section A Journal of Physical Sciences*, vol. 23, no. 12, pp. 2135–2136, Dec. 1968, ISSN: 18657109. DOI: [10.1515/ZNA-1968-1247/MACHINEREADABLECITATION/RIS](https://doi.org/10.1515/ZNA-1968-1247).
- [28] A. Otto, “Excitation of nonradiative surface plasma waves in silver by the method of frustrated total reflection,” *Zeitschrift für Physik*, vol. 216, no. 4, pp. 398–410, Aug. 1968, ISSN: 14346001. DOI: [10.1007/BF01391532/METRICS](https://doi.org/10.1007/BF01391532).
- [29] B. Liedberg, C. Nylander, and I. Lunström, “Surface plasmon resonance for gas detection and biosensing,” *Sensors and Actuators*, vol. 4, no. C, pp. 299–304, Jan. 1983, ISSN: 0250-6874. DOI: [10.1016/0250-6874\(83\)85036-7](https://doi.org/10.1016/0250-6874(83)85036-7).
- [30] S. G. Patching, “Surface plasmon resonance spectroscopy for characterisation of membrane protein–ligand interactions and its potential for drug discovery,” *Biochimica et Biophysica Acta (BBA) - Biomembranes*, vol. 1838, no. 1, pp. 43–55, Jan. 2014, ISSN: 0005-2736. DOI: [10.1016/J.BBAMEM.2013.04.028](https://doi.org/10.1016/J.BBAMEM.2013.04.028).
- [31] C. C. Fong, W. P. Lai, Y. C. Leung, S. C. Lo, M. S. Wong, and M. Yang, “Study of substrate–enzyme interaction between immobilized pyridoxamine and recombinant porcine pyridoxal kinase using surface plasmon resonance biosensor,” *Biochimica et Biophysica Acta (BBA) - Protein Structure and Molecular Enzymology*, vol. 1596, no. 1, pp. 95–107, Apr. 2002, ISSN: 0167-4838. DOI: [10.1016/S0167-4838\(02\)00208-X](https://doi.org/10.1016/S0167-4838(02)00208-X).
- [32] C. H. Wong and F. S. Liang, “Surface Plasmon Resonance Study of RNA–Aminoglycoside Interactions,” *Methods in Enzymology*, vol. 362, pp. 340–353, Jan. 2003, ISSN: 0076-6879. DOI: [10.1016/S0076-6879\(03\)01024-3](https://doi.org/10.1016/S0076-6879(03)01024-3).
- [33] A. D. Dursun, B. A. Borsa, G. Bayramoglu, M. Y. Arica, and V. C. Ozalp, “Surface plasmon resonance aptasensor for Brucella detection in milk,” *Talanta*, vol. 239, p. 123 074, Mar. 2022, ISSN: 0039-9140. DOI: [10.1016/J.TALANTA.2021.123074](https://doi.org/10.1016/J.TALANTA.2021.123074).
- [34] H. Miyoshi *et al.*, “Binding analyses for the interaction between plant virus genome-linked protein (VPg) and plant translational initiation factors,” *Biochimie*, vol. 88, no. 3-4, pp. 329–340, Mar. 2006, ISSN: 0300-9084. DOI: [10.1016/J.BIOCHI.2005.09.002](https://doi.org/10.1016/J.BIOCHI.2005.09.002).
- [35] A. Gade, A. Sharma, N. Srivastava, and S. J. Flora, “Surface plasmon resonance: A promising approach for label-free early cancer diagnosis,” *Clinica Chimica Acta*, vol. 527, pp. 79–88, Feb. 2022, ISSN: 0009-8981. DOI: [10.1016/J.CCA.2022.01.023](https://doi.org/10.1016/J.CCA.2022.01.023).
- [36] P. I. Nikitin, A. A. Beloglazov, V. E. Kochergin, M. V. Valeiko, and T. I. Ksenevich, “Surface plasmon resonance interferometry for biological and chemical sensing,” *Sensors and Actuators B: Chemical*, vol. 54, no. 1-2, pp. 43–50, Jan. 1999, ISSN: 0925-4005. DOI: [10.1016/S0925-4005\(98\)00325-6](https://doi.org/10.1016/S0925-4005(98)00325-6).
- [37] A. V. Kabashin and P. I. Nikitin, “Interferometer based on a surface-plasmon resonance for sensor applications,” *Quantum Electronics*, vol. 27, no. 7, pp. 653–654, Jul. 1997, ISSN: 1063-7818. DOI: [10.1070/QE1997V027N07ABEH001013/XML](https://doi.org/10.1070/QE1997V027N07ABEH001013/XML).
- [38] A. N. Grigorenko, S. Patskovsky, and A. V. Kabashin, “Phase and amplitude sensitivities in surface plasmon resonance bio and chemical sensing,” *Optics Express*, vol. 17, no. 23, pp. 21 191–21 204, Nov. 2009, ISSN: 1094-4087. DOI: [10.1364/OE.17.021191](https://doi.org/10.1364/OE.17.021191).

- [39] M. O. Hunault *et al.*, “Thirteenth-century stained glass windows of the Sainte-Chapelle in Paris: an insight into medieval glazing work practices,” *Journal of Archaeological Science: Reports*, vol. 35, p. 102753, Feb. 2021, ISSN: 2352409X. DOI: [10.1016/J.JASREP.2020.102753](https://doi.org/10.1016/J.JASREP.2020.102753).
- [40] H. R. Hegde, S. Chidangil, and R. K. Sinha, “Refractive index sensitivity of Au nanostructures in solution and on the substrate,” *Journal of Materials Science: Materials in Electronics*, vol. 33, no. 7, pp. 4011–4024, Mar. 2022, ISSN: 1573482X. DOI: [10.1007/s10854-021-07593-9](https://doi.org/10.1007/s10854-021-07593-9).
- [41] J. R. Krenn, P. Kvasnička, J. Homola, N. Galler, and M. Piliarik, “Local refractive index sensitivity of plasmonic nanoparticles,” *Optics Express*, Vol. 19, Issue 10, pp. 9213–9220, vol. 19, no. 10, pp. 9213–9220, May 2011, ISSN: 1094-4087. DOI: [10.1364/OE.19.009213](https://doi.org/10.1364/OE.19.009213).
- [42] E. M. Larsson, J. Alegret, M. Käll, and D. S. Sutherland, “Sensing characteristics of NIR localized surface plasmon resonances in gold nanorings for application as ultrasensitive biosensors,” *Nano Letters*, vol. 7, no. 5, pp. 1256–1263, May 2007, ISSN: 15306984. DOI: [10.1021/nl0701612](https://doi.org/10.1021/nl0701612).
- [43] M. K. Omrani, H. Mohammadi, and H. Fallah, “Ultrahigh sensitive refractive index nanosensors based on nanoshells, nanocages and nanoframes: effects of plasmon hybridization and restoring force,” *Scientific Reports*, vol. 11, no. 1, pp. 1–9, Jan. 2021, ISSN: 2045-2322. DOI: [10.1038/s41598-021-81578-w](https://doi.org/10.1038/s41598-021-81578-w).
- [44] L. Malassis *et al.*, “Topological darkness in self-assembled plasmonic metamaterials,” *Advanced Materials*, vol. 26, no. 2, pp. 324–330, Jan. 2014, ISSN: 09359648. DOI: [10.1002/adma.201303426](https://doi.org/10.1002/adma.201303426).
- [45] G. Qiu, Z. Gai, Y. Tao, J. Schmitt, G. A. Kullak-Ublick, and J. Wang, “Dual-Functional Plasmonic Photothermal Biosensors for Highly Accurate Severe Acute Respiratory Syndrome Coronavirus 2 Detection,” *ACS nano*, vol. 14, no. 5, pp. 5268–5277, May 2020, ISSN: 1936-086X. DOI: [10.1021/ACSNANO.0C02439](https://doi.org/10.1021/ACSNANO.0C02439).
- [46] J. R. Krenn, P. Kvasnička, J. Homola, H. Šípová, N. Galler, and M. Piliarik, “High-resolution biosensor based on localized surface plasmons,” *Optics Express*, Vol. 20, Issue 1, pp. 672–680, vol. 20, no. 1, pp. 672–680, Jan. 2012, ISSN: 1094-4087. DOI: [10.1364/OE.20.000672](https://doi.org/10.1364/OE.20.000672).
- [47] T. H. Lee, S. W. Lee, J. A. Jung, J. Ahn, M. G. Kim, and Y. B. Shin, “Signal Amplification by Enzymatic Reaction in an Immunosensor Based on Localized Surface Plasmon Resonance (LSPR),” *Sensors*, vol. 10, no. 3, pp. 2045–2053, Mar. 2010, ISSN: 1424-8220. DOI: [10.3390/S100302045](https://doi.org/10.3390/S100302045).
- [48] S. A. Maier, *Plasmonics: Fundamentals and applications*. Springer US, 2007, pp. 1–223, ISBN: 0387331506. DOI: [10.1007/0-387-37825-1](https://doi.org/10.1007/0-387-37825-1).
- [49] X. Wang, T. Hou, H. Lin, W. Lv, H. Li, and F. Li, “In situ template generation of silver nanoparticles as amplification tags for ultrasensitive surface plasmon resonance biosensing of microRNA,” *Biosensors and Bioelectronics*, vol. 137, pp. 82–87, Jul. 2019, ISSN: 0956-5663. DOI: [10.1016/J.BIOS.2019.05.006](https://doi.org/10.1016/J.BIOS.2019.05.006).
- [50] L. Rodríguez-Lorenzo, R. De La Rica, R. A. Álvarez-Puebla, L. M. Liz-Marzán, and M. M. Stevens, “Plasmonic nanosensors with inverse sensitivity by means of enzyme-guided crystal growth,” *Nature Materials*, vol. 11, no. 7, pp. 604–607, May 2012, ISSN: 1476-4660. DOI: [10.1038/nmat3337](https://doi.org/10.1038/nmat3337).

- [51] S. Zhu, C. L. Du, and Y. Fu, “Localized surface plasmon resonance-based hybrid Au–Ag nanoparticles for detection of *Staphylococcus aureus* enterotoxin B,” *Optical Materials*, vol. 31, no. 11, pp. 1608–1613, Sep. 2009, ISSN: 0925-3467. DOI: [10.1016/J.OPTMAT.2009.03.009](https://doi.org/10.1016/J.OPTMAT.2009.03.009).
- [52] D. Shi, F. Sheng, X. Zhang, and G. Wang, “Gold nanoparticle aggregation: Colorimetric detection of the interactions between avidin and biotin,” *Talanta*, vol. 185, pp. 106–112, Aug. 2018, ISSN: 0039-9140. DOI: [10.1016/J.TALANTA.2018.02.102](https://doi.org/10.1016/J.TALANTA.2018.02.102).
- [53] T. Xu and Z. Geng, “Strategies to improve performances of LSPR biosensing: Structure, materials, and interface modification,” *Biosensors and Bioelectronics*, vol. 174, p. 112850, Feb. 2021, ISSN: 0956-5663. DOI: [10.1016/J.BIOS.2020.112850](https://doi.org/10.1016/J.BIOS.2020.112850).
- [54] A. N. Grigorenko, P. I. Nikitin, and A. V. Kabashin, “Phase jumps and interferometric surface plasmon resonance imaging,” *Applied Physics Letters*, vol. 75, no. 25, pp. 3917–3919, Dec. 1999, ISSN: 00036951. DOI: [10.1063/1.125493](https://doi.org/10.1063/1.125493).
- [55] P. Wang, “Phase-sensitive surface plasmon resonance sensors for highly sensitive bioanalysis,” *Comprehensive Analytical Chemistry*, vol. 95, pp. 55–88, Jan. 2021, ISSN: 0166-526X. DOI: [10.1016/BS.COAC.2021.09.001](https://doi.org/10.1016/BS.COAC.2021.09.001).
- [56] B. Ran and S. G. Lipson, “Comparison between sensitivities of phase and intensity detection in surface plasmon resonance,” *Optics Express*, Vol. 14, Issue 12, pp. 5641–5650, vol. 14, no. 12, pp. 5641–5650, Jun. 2006, ISSN: 1094-4087. DOI: [10.1364/OE.14.005641](https://doi.org/10.1364/OE.14.005641).
- [57] V. G. Kravets *et al.*, “Singular phase nano-optics in plasmonic metamaterials for label-free single-molecule detection,” *Nature Materials*, vol. 12, no. 4, pp. 304–309, Apr. 2013, ISSN: 14761122. DOI: [10.1038/nmat3537](https://doi.org/10.1038/nmat3537).
- [58] G. I. Tselikov, A. Danilov, V. O. Shipunova, S. M. Deyev, A. V. Kabashin, and A. N. Grigorenko, “Topological Darkness: How to Design a Metamaterial for Optical Biosensing with Ultrahigh Sensitivity,” *ACS Nano*, vol. 17, no. 19, pp. 19338–19348, Oct. 2023, ISSN: 1936086X. DOI: [10.1021/ACSNANO.3C06655](https://doi.org/10.1021/ACSNANO.3C06655).
- [59] G. Ermolaev *et al.*, “Topological phase singularities in atomically thin high-refractive-index materials,” *Nature Communications*, vol. 13, no. 1, pp. 1–9, Apr. 2022, ISSN: 2041-1723. DOI: [10.1038/s41467-022-29716-4](https://doi.org/10.1038/s41467-022-29716-4).
- [60] K. V. Sreekanth, P. Mahalakshmi, S. Han, M. S. Mani Rajan, P. K. Choudhury, and R. Singh, “Brewster Mode-Enhanced Sensing with Hyperbolic Metamaterial,” *Advanced Optical Materials*, vol. 7, no. 21, p. 1900680, Nov. 2019, ISSN: 2195-1071. DOI: [10.1002/ADOM.201900680](https://doi.org/10.1002/ADOM.201900680).
- [61] K. V. Sreekanth *et al.*, “Biosensing with the singular phase of an ultrathin metal-dielectric nanophotonic cavity,” *Nature Communications*, vol. 9, no. 1, pp. 1–8, Jan. 2018, ISSN: 2041-1723. DOI: [10.1038/s41467-018-02860-6](https://doi.org/10.1038/s41467-018-02860-6).
- [62] C. Yan, T. V. Raziman, and O. J. Martin, “Phase Bifurcation and Zero Reflection in Planar Plasmonic Metasurfaces,” *ACS Photonics*, vol. 4, no. 4, pp. 852–860, Apr. 2017, ISSN: 23304022. DOI: [10.1021/ACSPHOTONICS.6B00914](https://doi.org/10.1021/ACSPHOTONICS.6B00914).
- [63] F. Huang *et al.*, “Zero-Reflectance Metafilms for Optimal Plasmonic Sensing,” *Advanced Optical Materials*, vol. 4, no. 2, pp. 328–335, Feb. 2016, ISSN: 2195-1071. DOI: [10.1002/ADOM.201500424](https://doi.org/10.1002/ADOM.201500424).

- [64] C. Coutant, S. Ravaïne, X. Wang, J. Toudert, V. Ponsinet, and P. Barois, “Plasmonic metamaterials for ultra-sensitive sensing: topological darkness,” *Rendiconti Lincei*, vol. 26, no. 2, pp. 175–182, Aug. 2015, ISSN: 17200776. DOI: [10.1007/S12210-015-0404-7](https://doi.org/10.1007/S12210-015-0404-7).
- [65] Y. Chen, “Nanofabrication by electron beam lithography and its applications: A review,” *Microelectronic Engineering*, vol. 135, pp. 57–72, Mar. 2015, ISSN: 0167-9317. DOI: [10.1016/J.MEE.2015.02.042](https://doi.org/10.1016/J.MEE.2015.02.042).
- [66] L. J. Guo, “Nanoimprint Lithography: Methods and Material Requirements,” *Advanced Materials*, vol. 19, no. 4, pp. 495–513, Feb. 2007, ISSN: 1521-4095. DOI: [10.1002/ADMA.200600882](https://doi.org/10.1002/ADMA.200600882).
- [67] J. del Barrio and C. Sánchez-Somolinos, “Light to Shape the Future: From Photolithography to 4D Printing,” *Advanced Optical Materials*, vol. 7, no. 16, p. 1900598, Aug. 2019, ISSN: 2195-1071. DOI: [10.1002/ADOM.201900598](https://doi.org/10.1002/ADOM.201900598).
- [68] C. V. Thompson, “Solid-State Dewetting of Thin Films,” *Annual Review of Materials Research*, vol. 42, pp. 399–434, Jul. 2012, ISSN: 15317331. DOI: [10.1146/ANNREV-MATSCI-070511-155048](https://doi.org/10.1146/ANNREV-MATSCI-070511-155048).
- [69] M. Born *et al.*, “Principles of Optics: Electromagnetic Theory of Propagation, Interference and Diffraction of Light,” *Cambridge University Press*, Oct. 1999. DOI: [10.1017/CBO9781139644181](https://doi.org/10.1017/CBO9781139644181).
- [70] T. Wakamatsu and K. Aizawa, “Penetration-depth characteristics of evanescent fields at metal attenuated total reflection,” *Japanese Journal of Applied Physics, Part 1: Regular Papers and Short Notes and Review Papers*, vol. 44, no. 6 A, pp. 4272–4274, Jun. 2005, ISSN: 00214922. DOI: [10.1143/JJAP.44.4272/XML](https://doi.org/10.1143/JJAP.44.4272/XML).
- [71] A. Yariv, P. Yeh, and C.-S. Hong, “Electromagnetic propagation in periodic stratified media. I. General theory*,” *JOSA*, vol. 67, no. 4, pp. 423–438, Apr. 1977, ISSN: 0030-3941. DOI: [10.1364/JOSA.67.000423](https://doi.org/10.1364/JOSA.67.000423).
- [72] J. T. Guske, *Modeling and Prediction of Surface Plasmon Resonance Spectroscopy*. Jun. 2013.
- [73] P. Drude, “Zur Elektronentheorie der Metalle,” *Annalen der Physik*, vol. 306, no. 3, pp. 566–613, Jan. 1900, ISSN: 1521-3889. DOI: [10.1002/ANDP.19003060312](https://doi.org/10.1002/ANDP.19003060312).
- [74] *The theory of electrons and its applications to the phenomena of light and radiant heat : Lorentz, H. A. (Hendrik Antoon), 1853-1928 : Free Download, Borrow, and Streaming : Internet Archive*.
- [75] M. R. Querry, M. A. Ordal, R. J. Bell, L. L. Long, and R. W. Alexander, “Optical properties of fourteen metals in the infrared and far infrared: Al, Co, Cu, Au, Fe, Pb, Mo, Ni, Pd, Pt, Ag, Ti, V, and W.,” *Applied Optics*, vol. 24, no. 24, pp. 4493–4499, Dec. 1985, ISSN: 2155-3165. DOI: [10.1364/AO.24.004493](https://doi.org/10.1364/AO.24.004493).
- [76] J. Homola and M. Piliarik, *Surface Plasmon Resonance (SPR) Sensors*. 2006, pp. 45–67. DOI: [10.1007/5346014](https://doi.org/10.1007/5346014).
- [77] P. B. Johnson and R. W. Christy, “Optical Constants of the Noble Metals,” *Physical Review B*, vol. 6, no. 12, p. 4370, Dec. 1972, ISSN: 01631829. DOI: [10.1103/PhysRevB.6.4370](https://doi.org/10.1103/PhysRevB.6.4370).

- [78] E. J. Zeman and G. C. Schatz, “An accurate electromagnetic theory study of surface enhancement factors for Ag, Au, Cu, Li, Na, Al, Ga, In, Zn, and Cd,” *Journal of Physical Chemistry*, vol. 91, no. 3, pp. 634–643, 1987, ISSN: 00223654. DOI: [10.1021/J100287A028](https://doi.org/10.1021/J100287A028).
- [79] J. Zhang, L. Zhang, and W. Xu, “Surface plasmon polaritons: physics and applications,” *Journal of Physics D: Applied Physics*, vol. 45, no. 11, p. 113 001, Feb. 2012, ISSN: 0022-3727. DOI: [10.1088/0022-3727/45/11/113001](https://doi.org/10.1088/0022-3727/45/11/113001).
- [80] M. Elsherif *et al.*, “Optical Fiber Sensors: Working Principle, Applications, and Limitations,” *Advanced Photonics Research*, vol. 3, no. 11, p. 2 100 371, Nov. 2022, ISSN: 2699-9293. DOI: [10.1002/ADPR.202100371](https://doi.org/10.1002/ADPR.202100371).
- [81] V. Naresh and N. Lee, “A Review on Biosensors and Recent Development of Nanosstructured Materials-Enabled Biosensors,” *Sensors*, vol. 21, no. 4, p. 1109, Feb. 2021, ISSN: 1424-8220. DOI: [10.3390/S21041109](https://doi.org/10.3390/S21041109).
- [82] K. Ladutenko, U. Pal, A. Rivera, and O. Peña-Rodríguez, “Mie calculation of electromagnetic near-field for a multilayered sphere,” *Computer Physics Communications*, vol. 214, pp. 225–230, May 2017, ISSN: 0010-4655. DOI: [10.1016/J.CPC.2017.01.017](https://doi.org/10.1016/J.CPC.2017.01.017).
- [83] K. L. Kelly, E. Coronado, L. L. Zhao, and G. C. Schatz, “The optical properties of metal nanoparticles: The influence of size, shape, and dielectric environment,” *Journal of Physical Chemistry B*, vol. 107, no. 3, pp. 668–677, Jan. 2003, ISSN: 10895647. DOI: [10.1021/JP026731Y](https://doi.org/10.1021/JP026731Y).
- [84] M. Meier and A. Wokaun, “Enhanced fields on large metal particles: dynamic depolarization,” *Optics Letters*, vol. 8, no. 11, pp. 581–583, Nov. 1983, ISSN: 1539-4794. DOI: [10.1364/OL.8.000581](https://doi.org/10.1364/OL.8.000581).
- [85] A. Moroz, “Depolarization field of spheroidal particles,” *JOSA B*, vol. 26, no. 3, pp. 517–527, Mar. 2009, ISSN: 1520-8540. DOI: [10.1364/JOSAB.26.000517](https://doi.org/10.1364/JOSAB.26.000517).
- [86] D. Bedeaux and J. Vlieger, “Optical Properties of Surfaces,” *Optical Properties of Surfaces*, Jul. 2004. DOI: [10.1142/P327](https://doi.org/10.1142/P327).
- [87] R. Lazzari and I. Simonsen, “GRANFILM: a software for calculating thin-layer dielectric properties and Fresnel coefficients,” *Thin Solid Films*, vol. 419, pp. 124–136, 2002. DOI: [10.1016/S0040-6090\(02\)00679-X](https://doi.org/10.1016/S0040-6090(02)00679-X).
- [88] D. Bedeaux and J. Vlieger, “A phenomenological theory of the dielectric properties of thin films,” *Physica*, vol. 67, no. 1, pp. 55–73, Jul. 1973, ISSN: 0031-8914. DOI: [10.1016/0031-8914\(73\)90022-0](https://doi.org/10.1016/0031-8914(73)90022-0).
- [89] L. Haiping, W. Jiangyue, M. Fanping, and L. Aifeng, “Immunochemical assay for the detection of antibiotics in animal-derived foods: A review,” *Food Control*, vol. 130, p. 108 356, Dec. 2021, ISSN: 0956-7135. DOI: [10.1016/J.FOODCONT.2021.108356](https://doi.org/10.1016/J.FOODCONT.2021.108356).
- [90] N. Boonham *et al.*, “Methods in virus diagnostics: From ELISA to next generation sequencing,” *Virus Research*, vol. 186, pp. 20–31, Jun. 2014, ISSN: 0168-1702. DOI: [10.1016/J.VIRUSRES.2013.12.007](https://doi.org/10.1016/J.VIRUSRES.2013.12.007).
- [91] J. Baranwal, B. Barse, G. Gatto, G. Broncova, and A. Kumar, “Electrochemical Sensors and Their Applications: A Review,” *Chemosensors*, vol. 10, no. 9, p. 363, Sep. 2022, ISSN: 2227-9040. DOI: [10.3390/CHEMOSENSORS10090363](https://doi.org/10.3390/CHEMOSENSORS10090363).

- [92] M. Ju *et al.*, “Piezoelectric Materials and Sensors for Structural Health Monitoring: Fundamental Aspects, Current Status, and Future Perspectives,” *Sensors*, vol. 23, no. 1, p. 543, Jan. 2023, ISSN: 1424-8220. DOI: [10.3390/S23010543](https://doi.org/10.3390/S23010543).
- [93] B. G. Gorshkov *et al.*, “Scientific Applications of Distributed Acoustic Sensing: State-of-the-Art Review and Perspective,” *Sensors*, vol. 22, no. 3, p. 1033, Jan. 2022, ISSN: 1424-8220. DOI: [10.3390/S22031033](https://doi.org/10.3390/S22031033).
- [94] F. C. Dudak and I. H. Boyaci, “Rapid and label-free bacteria detection by surface plasmon resonance (SPR) biosensors,” *Biotechnology Journal*, vol. 4, no. 7, pp. 1003–1011, Jul. 2009, ISSN: 1860-7314. DOI: [10.1002/BIOT.200800316](https://doi.org/10.1002/BIOT.200800316).
- [95] J. W. Chung, S. D. Kim, R. Bernhardt, and J. C. Pyun, “Application of SPR biosensor for medical diagnostics of human hepatitis B virus (hHBV),” *Sensors and Actuators B: Chemical*, vol. 111-112, no. SUPPL. Pp. 416–422, Nov. 2005, ISSN: 0925-4005. DOI: [10.1016/J.SNB.2005.03.055](https://doi.org/10.1016/J.SNB.2005.03.055).
- [96] M. Park, J. Jose, and J. C. Pyun, “SPR biosensor by using E. coli outer membrane layer with autodisplayed Z-domains,” *Sensors and Actuators B: Chemical*, vol. 154, no. 2, pp. 82–88, Jun. 2011, ISSN: 0925-4005. DOI: [10.1016/J.SNB.2010.03.039](https://doi.org/10.1016/J.SNB.2010.03.039).
- [97] A. Olaru, C. Bala, N. Jaffrezic-Renault, and H. Y. Aboul-Enein, “Surface Plasmon Resonance (SPR) Biosensors in Pharmaceutical Analysis,” *Critical Reviews in Analytical Chemistry*, vol. 45, no. 2, pp. 97–105, Apr. 2015, ISSN: 15476510. DOI: [10.1080/10408347.2014.881250](https://doi.org/10.1080/10408347.2014.881250).
- [98] Y. F. Chang *et al.*, “Simple Strategy for Rapid and Sensitive Detection of Avian Influenza A H7N9 Virus Based on Intensity-Modulated SPR Biosensor and New Generated Antibody,” *Analytical Chemistry*, vol. 90, no. 3, pp. 1861–1869, Feb. 2018, ISSN: 15206882. DOI: [10.1021/ACS.ANALCHEM.7B03934](https://doi.org/10.1021/ACS.ANALCHEM.7B03934).
- [99] M. Focsan *et al.*, “A simple and efficient design to improve the detection of biotin-streptavidin interaction with plasmonic nanobiosensors,” *Biosensors and Bioelectronics*, vol. 86, pp. 728–735, Dec. 2016, ISSN: 0956-5663. DOI: [10.1016/J.BIOS.2016.07.054](https://doi.org/10.1016/J.BIOS.2016.07.054).
- [100] K. M. Mayer *et al.*, “A label-free immunoassay based upon localized surface plasmon resonance of gold nanorods,” *ACS Nano*, vol. 2, no. 4, pp. 687–692, Apr. 2008, ISSN: 19360851. DOI: [10.1021/NN7003734](https://doi.org/10.1021/NN7003734).
- [101] T. Lee *et al.*, “Label-free localized surface plasmon resonance biosensor composed of multi-functional DNA 3 way junction on hollow Au spike-like nanoparticles (HAuSN) for avian influenza virus detection,” *Colloids and Surfaces B: Biointerfaces*, vol. 182, p. 110341, Oct. 2019, ISSN: 0927-7765. DOI: [10.1016/J.COLSURFB.2019.06.070](https://doi.org/10.1016/J.COLSURFB.2019.06.070).
- [102] S. Y. Yoo, D. K. Kim, T. J. Park, E. K. Kim, E. Tamiya, and S. Y. Lee, “Detection of the most common corneal dystrophies caused by BIGH3 gene point mutations using a multispot gold-capped nanoparticle array chip,” *Analytical Chemistry*, vol. 82, no. 4, pp. 1349–1357, Feb. 2010, ISSN: 00032700. DOI: [10.1021/AC902410Z](https://doi.org/10.1021/AC902410Z).
- [103] M. Moros, M. E. Kyriazi, A. H. El-Sagheer, T. Brown, C. Tortiglione, and A. G. Kanaras, “DNA-Coated Gold Nanoparticles for the Detection of mRNA in Live Hydra Vulgaris Animals,” *ACS Applied Materials and Interfaces*, vol. 11, no. 15, pp. 13905–13911, Apr. 2019, ISSN: 19448252. DOI: [10.1021/ACSAM.8B17846](https://doi.org/10.1021/ACSAM.8B17846).

- [104] P. P. Austin Suthanthiraraj and A. K. Sen, “Localized surface plasmon resonance (LSPR) biosensor based on thermally annealed silver nanostructures with on-chip blood-plasma separation for the detection of dengue non-structural protein NS1 antigen,” *Biosensors and Bioelectronics*, vol. 132, pp. 38–46, May 2019, ISSN: 0956-5663. DOI: [10.1016/J.BIOS.2019.02.036](https://doi.org/10.1016/J.BIOS.2019.02.036).
- [105] M. A. Ortega *et al.*, “In situ LSPR sensing of secreted insulin in organ-on-chip,” *Biosensors*, vol. 11, no. 5, p. 138, May 2021, ISSN: 20796374. DOI: [10.3390/BIOS11050138/S1](https://doi.org/10.3390/BIOS11050138).
- [106] M. Soler and L. M. Lechuga, “Principles, technologies, and applications of plasmonic biosensors,” *Journal of Applied Physics*, vol. 129, no. 11, Mar. 2021, ISSN: 10897550. DOI: [10.1063/5.0042811/1025364](https://doi.org/10.1063/5.0042811/1025364).
- [107] M. E. Hamza, M. A. Othman, and M. A. Swillam, “Plasmonic Biosensors: Review,” *Biology*, vol. 11, no. 5, p. 11, May 2022, ISSN: 20797737. DOI: [10.3390/BIOLOGY11050621](https://doi.org/10.3390/BIOLOGY11050621).
- [108] B. A. Prabowo, A. Purwidyantri, and K. C. Liu, “Surface Plasmon Resonance Optical Sensor: A Review on Light Source Technology,” *Biosensors*, vol. 8, no. 3, p. 80, Aug. 2018, ISSN: 2079-6374. DOI: [10.3390/BIOS8030080](https://doi.org/10.3390/BIOS8030080).
- [109] G. G. Politano and C. Versace, “Spectroscopic Ellipsometry: Advancements, Applications and Future Prospects in Optical Characterization,” *Spectroscopy Journal*, vol. 1, no. 3, pp. 163–181, Dec. 2023, ISSN: 2813-446X. DOI: [10.3390/SPECTROSCJ1030014](https://doi.org/10.3390/SPECTROSCJ1030014).
- [110] A. H. P. Ho, D. Kim, and M. G. Somekh, *Handbook of photonics for biomedical engineering*. Springer Netherlands, Jan. 2017, pp. 1–947, ISBN: 9789400750524. DOI: [10.1007/978-94-007-5052-4](https://doi.org/10.1007/978-94-007-5052-4).
- [111] Y. Tang, X. Zeng, and J. Liang, “Surface Plasmon Resonance: An Introduction to a Surface Spectroscopy Technique,” *Journal of Chemical Education*, vol. 87, no. 7, pp. 742–746, 2010, ISSN: 00219584. DOI: [10.1021/ED100186Y](https://doi.org/10.1021/ED100186Y).
- [112] R. K. Sinha, “Wavelength modulation based surface plasmon resonance sensor for detection of cardiac marker proteins troponin I and troponin T,” *Sensors and Actuators A: Physical*, vol. 332, p. 113104, Dec. 2021, ISSN: 0924-4247. DOI: [10.1016/J.SNA.2021.113104](https://doi.org/10.1016/J.SNA.2021.113104).
- [113] Y. C. Li *et al.*, “Sensitive detection of unlabeled oligonucleotides using a paired surface plasma waves biosensor,” *Biosensors and Bioelectronics*, vol. 35, no. 1, pp. 342–348, May 2012, ISSN: 0956-5663. DOI: [10.1016/J.BIOS.2012.03.014](https://doi.org/10.1016/J.BIOS.2012.03.014).
- [114] W. C. Law, C. Lin, S. Y. Wu, H. P. Ho, and S. K. Kong, “Highly sensitive differential phase-sensitive surface plasmon resonance biosensor based on the Mach–Zehnder configuration,” *Optics Letters*, vol. 29, no. 20, pp. 2378–2380, Oct. 2004, ISSN: 1539-4794. DOI: [10.1364/OL.29.002378](https://doi.org/10.1364/OL.29.002378).
- [115] D. Monzón-Hernández and J. Villatoro, “High-resolution refractive index sensing by means of a multiple-peak surface plasmon resonance optical fiber sensor,” *Sensors and Actuators B: Chemical*, vol. 115, no. 1, pp. 227–231, May 2006, ISSN: 0925-4005. DOI: [10.1016/J.SNB.2005.09.006](https://doi.org/10.1016/J.SNB.2005.09.006).
- [116] Q. Li, X. Zhuo, S. Li, Q. Ruan, Q. H. Xu, and J. Wang, “Production of Monodisperse Gold Nanobipyramids with Number Percentages Approaching 100% and Evaluation of Their Plasmonic Properties,” *Advanced Optical Materials*, vol. 3, no. 6, pp. 801–812, Jun. 2015, ISSN: 2195-1071. DOI: [10.1002/ADOM.201400505](https://doi.org/10.1002/ADOM.201400505).

- [117] H. Song, H. Zhang, Z. Sun, Z. Ren, X. Yang, and Q. Wang, “Triangular silver nanoparticle U-bent fiber sensor based on localized surface plasmon resonance,” *AIP Advances*, vol. 9, no. 8, p. 85307, Aug. 2019, ISSN: 21583226. DOI: [10.1063/1.5111820](https://doi.org/10.1063/1.5111820).
- [118] A. Das, K. Kumar, and A. Dhawan, “Periodic arrays of plasmonic crossed-bowtie nanostructures interspaced with plasmonic nanocrosses for highly sensitive LSPR based chemical and biological sensing,” *RSC Advances*, vol. 11, no. 14, pp. 8096–8106, Feb. 2021, ISSN: 2046-2069. DOI: [10.1039/DORA09012C](https://doi.org/10.1039/DORA09012C).
- [119] C.-T. Li *et al.*, “Study of optical phase transduction on localized surface plasmon resonance for ultrasensitive detection,” *Optics Express*, vol. 20, no. 3, pp. 3250–3260, Jan. 2012, ISSN: 1094-4087. DOI: [10.1364/OE.20.003250](https://doi.org/10.1364/OE.20.003250).
- [120] C.-T. Li, H.-C. Lee, T.-J. Yen, and H.-F. Chen, “Demonstration of an ultrasensitive refractive-index plasmonic sensor by enabling its quadrupole resonance in phase interrogation,” *Optics Letters*, vol. 40, no. 22, pp. 5152–5155, Nov. 2015, ISSN: 1539-4794. DOI: [10.1364/OL.40.005152](https://doi.org/10.1364/OL.40.005152).
- [121] G. Qiu, S. P. Ng, and C. M. L. Wu, “Differential phase-detecting localized surface plasmon resonance sensor with self-assembly gold nano-islands,” *Optics Letters*, vol. 40, no. 9, pp. 1924–1927, May 2015, ISSN: 1539-4794. DOI: [10.1364/OL.40.001924](https://doi.org/10.1364/OL.40.001924).
- [122] A. I. Aristov *et al.*, “3D plasmonic crystal metamaterials for ultra-sensitive biosensing,” *Scientific Reports*, vol. 6, May 2016, ISSN: 20452322. DOI: [10.1038/srep25380](https://doi.org/10.1038/srep25380).
- [123] H. Song *et al.*, “Dispersion Topological Darkness at Multiple Wavelengths and Polarization States,” *Advanced Optical Materials*, vol. 5, no. 12, Jun. 2017, ISSN: 21951071. DOI: [10.1002/adom.201700166](https://doi.org/10.1002/adom.201700166).
- [124] G. Ma *et al.*, “Topologically protected phase singularities in TMDCs monolayers,” Dec. 2022. DOI: [10.21203/RS.3.RS-2272184/V1](https://doi.org/10.21203/RS.3.RS-2272184/V1).
- [125] M. Svedendahl, R. Verre, and M. Käll, “Refractometric biosensing based on optical phase flips in sparse and short-range-ordered nanoplasmonic layers,” *Light: Science & Applications*, vol. 3, no. 11, e220–e220, Nov. 2014, ISSN: 2047-7538. DOI: [10.1038/lsa.2014.101](https://doi.org/10.1038/lsa.2014.101).
- [126] G. Habibullah, J. Viktorova, and T. Rumí, “Current Strategies for Noble Metal Nanoparticle Synthesis,” *Nanoscale Research Letters*, vol. 16, no. 1, pp. 1–12, Mar. 2021, ISSN: 1556-276X. DOI: [10.1186/S11671-021-03480-8](https://doi.org/10.1186/S11671-021-03480-8).
- [127] D. Wang and P. Schaa, “Solid-state dewetting for fabrication of metallic nanoparticles and influences of nanostructured substrates and dealloying,” *physica status solidi (a)*, vol. 210, no. 8, pp. 1544–1551, Aug. 2013, ISSN: 1862-6319. DOI: [10.1002/PSSA.201200895](https://doi.org/10.1002/PSSA.201200895).
- [128] S. F. Guerra Hernández, “Estudio del proceso de fabricación de películas delgadas y nanoestructuras de Au por sputtering para aplicaciones como transductor plasmónico en biosensores,” Instituto Nacional de Astrofísica, Óptica y Electrónica, Instituto Nacional de Astrofísica, Óptica y Electrónica, 2022.
- [129] I. Gazga Gurrión, “Desarrollo de nanoestructuras de Au para aplicaciones en biosensor plasmónico,” Instituto Nacional de Astrofísica, Óptica y Electrónica, Instituto Nacional de Astrofísica, Óptica y Electrónica, 2023.

- [130] W. Zhou, R. Apkarian, Z. L. Wang, and D. Joy, “Fundamentals of scanning electron microscopy (SEM),” in *Scanning Microscopy for Nanotechnology: Techniques and Applications*, Springer New York, 2007, pp. 1–40, ISBN: 0387333258. DOI: [10.1007/978-0-387-39620-0_1](https://doi.org/10.1007/978-0-387-39620-0_1).
- [131] H. J. Butt, B. Cappella, and M. Kappl, “Force measurements with the atomic force microscope: Technique, interpretation and applications,” *Surface Science Reports*, vol. 59, no. 1-6, pp. 1–152, Oct. 2005, ISSN: 0167-5729. DOI: [10.1016/J.SURFREP.2005.08.003](https://doi.org/10.1016/J.SURFREP.2005.08.003).
- [132] S. Pang Ng *et al.*, “Common-path spectral interferometry with temporal carrier for highly sensitive surface plasmon resonance sensing,” *Optics Express*, vol. 21, no. 17, pp. 20 268–20 273, Aug. 2013, ISSN: 1094-4087. DOI: [10.1364/OE.21.020268](https://doi.org/10.1364/OE.21.020268).
- [133] A. Savitzky and M. J. Golay, “Smoothing and Differentiation of Data by Simplified Least Squares Procedures,” *Analytical Chemistry*, vol. 36, no. 8, pp. 1627–1639, Jul. 1964, ISSN: 15206882. DOI: [10.1021/AC60214A047](https://doi.org/10.1021/AC60214A047).
- [134] Díaz-Failach. Cristina-Isabel, “Funcionalización de nanopelículas de oro con oligonucleótidos de SARS-CoV-2 para uso en un biosensor óptico,” Instituto Nacional de Astrofísica, Óptica y Electrónica, 2021.
- [135] A. Ramírez-Cordero, “Estudio de la funcionalización de un chip plasmónico para la detección de SARS-CoV-2,” Instituto Nacional de Astrofísica, Óptica y Electrónica, Instituto Nacional de Astrofísica, Óptica y Electrónica, 2023.
- [136] K. Büscher, K. Graf, H. Ahrens, and C. A. Helm, “Influence of Adsorption Conditions on the Structure of Polyelectrolyte Multilayers,” *Langmuir*, vol. 18, no. 9, pp. 3585–3591, Apr. 2002, ISSN: 07437463. DOI: [10.1021/LA011682M](https://doi.org/10.1021/LA011682M).
- [137] P. Bertrand, A. Jonas, A. Laschewsky, and R. Legras, “Ultrathin polymer coatings by complexation of polyelectrolytes at interfaces: suitable materials, structure and properties Scheme of the electrostatic layer-by-layer self-assembly (ESA),” *Macromol. Rapid Commun.*, vol. 21, pp. 319–348, 2000. DOI: [10.1002/\(SICI\)1521-3927\(20000401\)21:7<319::AID-MARC319>3.0.CO;2-7](https://doi.org/10.1002/(SICI)1521-3927(20000401)21:7<319::AID-MARC319>3.0.CO;2-7).
- [138] C. M. Dundas, D. Demonte, and S. Park, “Streptavidin-biotin technology: Improvements and innovations in chemical and biological applications,” *Applied Microbiology and Biotechnology*, vol. 97, no. 21, pp. 9343–9353, Nov. 2013, ISSN: 01757598. DOI: [10.1007/S00253-013-5232-Z](https://doi.org/10.1007/S00253-013-5232-Z).
- [139] C. S. Neish, I. L. Martin, R. M. Henderson, and J. M. Edwardson, “Direct visualization of ligand-protein interactions using atomic force microscopy,” *British Journal of Pharmacology*, vol. 135, no. 8, pp. 1943–1950, Apr. 2002, ISSN: 1476-5381. DOI: [10.1038/SJ.BJP.0704660](https://doi.org/10.1038/SJ.BJP.0704660).
- [140] T. C. Roberts, R. Langer, and M. J. Wood, “Advances in oligonucleotide drug delivery,” *Nature Reviews Drug Discovery*, vol. 19, no. 10, pp. 673–694, Aug. 2020, ISSN: 1474-1784. DOI: [10.1038/s41573-020-0075-7](https://doi.org/10.1038/s41573-020-0075-7).
- [141] L. Moumné, A. C. Marie, and N. Crouvezier, “Oligonucleotide Therapeutics: From Discovery and Development to Patentability,” *Pharmaceutics*, vol. 14, no. 2, p. 260, Jan. 2022, ISSN: 1999-4923. DOI: [10.3390/PHARMACEUTICS14020260](https://doi.org/10.3390/PHARMACEUTICS14020260).
- [142] J. T. Guske, *SPR XPhase - File Exchange - MATLAB Central*.

- [143] R. Bower *et al.*, “Temperature stability of thin film refractory plasmonic materials,” *Optics Express*, vol. 26, no. 12, pp. 15 726–15 744, Jun. 2018, ISSN: 1094-4087. DOI: [10.1364/OE.26.015726](https://doi.org/10.1364/OE.26.015726).
- [144] S. G. Rodrigo, F. J. García-Vidal, and L. Martín-Moreno, “Influence of material properties on extraordinary optical transmission through hole arrays,” *Physical Review B - Condensed Matter and Materials Physics*, vol. 77, no. 7, p. 075 401, Feb. 2008, ISSN: 10980121. DOI: [10.1103/PHYSREVB.77.075401](https://doi.org/10.1103/PHYSREVB.77.075401).
- [145] J. Jatschka, A. Dathe, A. Csáki, W. Fritzsche, and O. Stranik, “Propagating and localized surface plasmon resonance sensing — A critical comparison based on measurements and theory,” *Sensing and Bio-Sensing Research*, vol. 7, pp. 62–70, Mar. 2016, ISSN: 2214-1804. DOI: [10.1016/J.SBSR.2016.01.003](https://doi.org/10.1016/J.SBSR.2016.01.003).
- [146] O. Kedem, A. B. Tesler, A. Vaskevich, and I. Rubinstein, “Sensitivity and optimization of localized surface plasmon resonance transducers,” *ACS Nano*, vol. 5, no. 2, pp. 748–760, Feb. 2011, ISSN: 19360851. DOI: [10.1021/NN102617D](https://doi.org/10.1021/NN102617D).
- [147] M. Mahmoudi, I. Lynch, M. R. Ejtehadi, M. P. Monopoli, F. B. Bombelli, and S. Laurent, “Protein-nanoparticle interactions: Opportunities and challenges,” *Chemical Reviews*, vol. 111, no. 9, pp. 5610–5637, Sep. 2011, ISSN: 00092665. DOI: [10.1021/CR100440G](https://doi.org/10.1021/CR100440G).
- [148] S. Dodoo, R. Steitz, A. Laschewsky, and R. Von Klitzing, “Effect of ionic strength and type of ions on the structure of water swollen polyelectrolyte multilayers,” *Physical Chemistry Chemical Physics*, vol. 13, no. 21, pp. 10 318–10 325, May 2011, ISSN: 1463-9084. DOI: [10.1039/C0CP01357A](https://doi.org/10.1039/C0CP01357A).
- [149] C. C. Buron *et al.*, “Surface morphology and thickness of a multilayer film composed of strong and weak polyelectrolytes: Effect of the number of adsorbed layers, concentration and type of salts,” *Thin Solid Films*, vol. 517, no. 8, pp. 2611–2617, Feb. 2009, ISSN: 0040-6090. DOI: [10.1016/J.TSF.2008.10.036](https://doi.org/10.1016/J.TSF.2008.10.036).
- [150] Y. Li and H. Zhang, “Binding of streptavidin to surface-attached biotin with different spacer thicknesses,” *Journal Wuhan University of Technology, Materials Science Edition*, vol. 30, no. 6, pp. 1304–1309, Dec. 2015, ISSN: 10002413. DOI: [10.1007/S11595-015-1312-5](https://doi.org/10.1007/S11595-015-1312-5).
- [151] H. Vaisocherová *et al.*, “Investigating oligonucleotide hybridization at subnanomolar level by surface plasmon resonance biosensor method,” *Biopolymers*, vol. 82, no. 4, pp. 394–398, Jul. 2006, ISSN: 1097-0282. DOI: [10.1002/BIP.20433](https://doi.org/10.1002/BIP.20433).
- [152] J. S. Mitchell, Y. Wu, C. J. Cook, and L. Main, “Sensitivity enhancement of surface plasmon resonance biosensing of small molecules,” *Analytical Biochemistry*, vol. 343, no. 1, pp. 125–135, Aug. 2005, ISSN: 0003-2697. DOI: [10.1016/J.AB.2005.05.001](https://doi.org/10.1016/J.AB.2005.05.001).
- [153] Y. K. Lee, D. H. Jang, K. S. Lee, W. M. Kim, and Y. S. Sohn, “Enhancing performance of a miniaturized surface plasmon resonance sensor in the reflectance detection mode using a waveguide-coupled bimetallic chip,” *Nanoscale Research Letters*, vol. 8, no. 1, pp. 1–8, Aug. 2013, ISSN: 1556276X. DOI: [10.1186/1556-276X-8-344](https://doi.org/10.1186/1556-276X-8-344).
- [154] R. Sierpe, M. J. Kogan, and S. Bollo, “Label-Free Oligonucleotide-Based SPR Biosensor for the Detection of the Gene Mutation Causing Prothrombin-Related Thrombophilia,” *Sensors*, vol. 20, no. 21, p. 6240, Oct. 2020, ISSN: 1424-8220. DOI: [10.3390/S20216240](https://doi.org/10.3390/S20216240).

- [155] Y. Huang *et al.*, “Development of a Portable SPR Sensor for Nucleic Acid Detection,” *Micromachines*, vol. 11, no. 5, p. 526, May 2020, ISSN: 2072-666X. DOI: [10.3390/MI11050526](https://doi.org/10.3390/MI11050526).
- [156] S. Fathi *et al.*, “Surface plasmon resonance-based oligonucleotide biosensor for *Salmonella Typhi* detection,” *Analytical Biochemistry*, vol. 677, p. 115 250, Sep. 2023, ISSN: 0003-2697. DOI: [10.1016/J.AB.2023.115250](https://doi.org/10.1016/J.AB.2023.115250).
- [157] P. Kvasnička, ; J. Homola, and J. Homola, “Optical sensors based on spectroscopy of localized surface plasmons on metallic nanoparticles: Sensitivity considerations,” *Biointerphases*, vol. 3, no. 3, FD4–FD11, Sep. 2008, ISSN: 1934-8630. DOI: [10.1116/1.2994687](https://doi.org/10.1116/1.2994687).
- [158] Y. B. Guo, J. Zhu, G. J. Weng, J. J. Li, and J. W. Zhao, “Multipole Plasmonic Optical Properties of the Au Cone-On-Plate Nanostructure: Change the Effective Mean Free Path to Improve Refractive Index Sensing,” *Plasmonics*, vol. 18, no. 1, pp. 407–420, Feb. 2023, ISSN: 15571963. DOI: [10.1007/S11468-022-01771-Z](https://doi.org/10.1007/S11468-022-01771-Z).
- [159] R. X. Zhang *et al.*, “Individual Split Au Square Nanorings for Surface-Enhanced Raman and Hyper-Raman Scattering,” *Plasmonics*, vol. 17, no. 3, pp. 965–971, Jun. 2022, ISSN: 15571963. DOI: [10.1007/S11468-021-01582-8](https://doi.org/10.1007/S11468-021-01582-8).
- [160] J. Yoon *et al.*, “Critical coupling in dissipative surface-plasmon resonators with multiple ports,” *Optics Express*, vol. 18, no. 25, pp. 25 702–25 711, Dec. 2010, ISSN: 1094-4087. DOI: [10.1364/OE.18.025702](https://doi.org/10.1364/OE.18.025702).
- [161] S. Balci, C. Kocabas, and A. Aydinli, “Critical coupling in plasmonic resonator arrays,” *Optics Letters*, vol. 36, no. 15, pp. 2770–2772, Aug. 2011, ISSN: 1539-4794. DOI: [10.1364/OL.36.002770](https://doi.org/10.1364/OL.36.002770).